ISSN 2408-2384 (ONLINE)

Environment and Natural Resources Journal

Volume 24 Number 2 March - April 2026

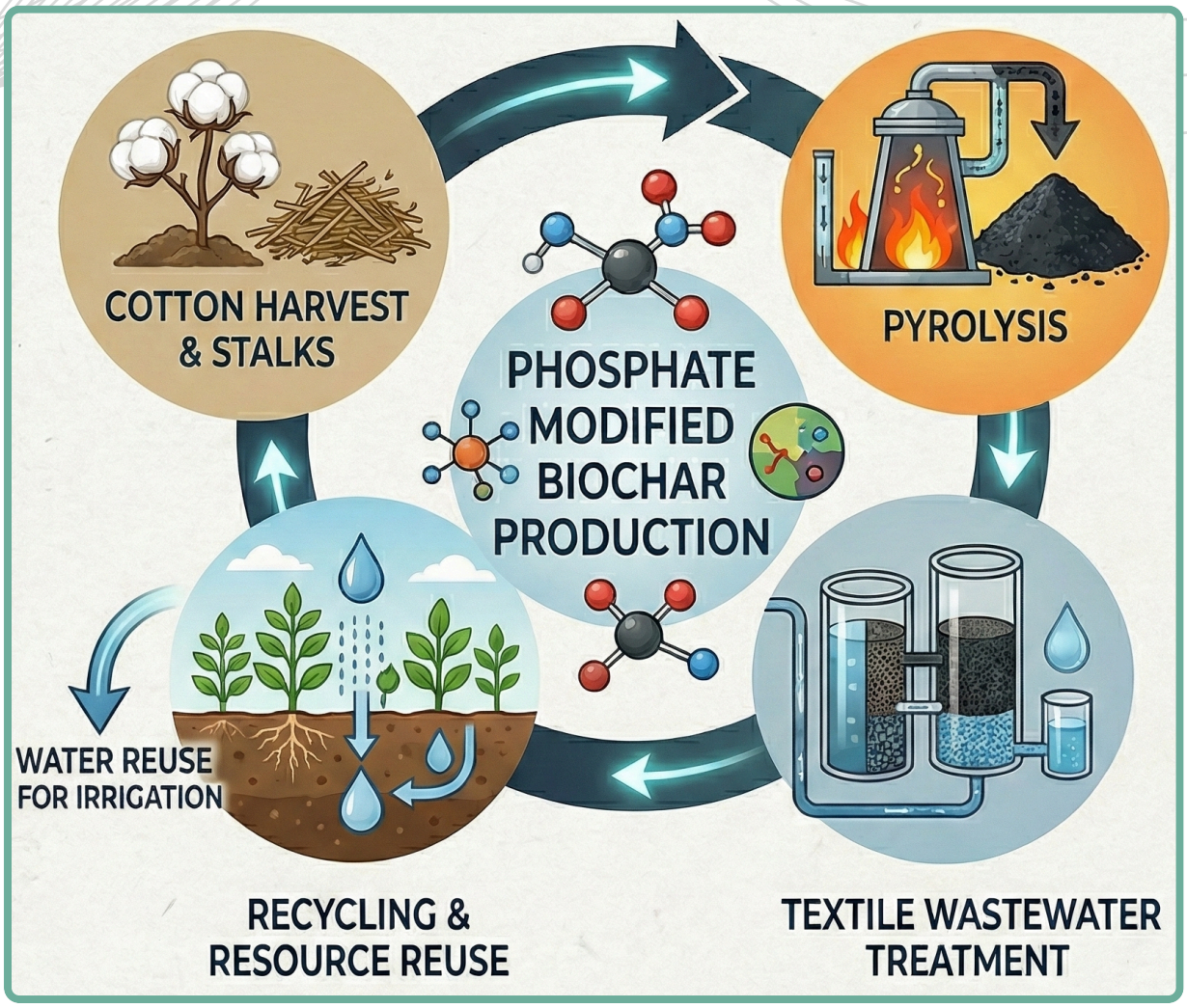

Cotton stalk from Gujarat, India, was pyrolyzed to produce functional biochar for textile wastewater treatment. This valorization approach offers significant pollutant removal and mitigates environmental challenges posed by agricultural waste and open burning.

Source: Shah VV and Patel NM. Circular Economy Pathway: Valorization of Cotton Stalk into Biochar for Textile Wastewater Treatment. Environ. Nat. Resour. J. 2026; 24(2): 250-267.

Environment and Natural Resources Journal (EnNRJ)
Volume 24, Number 2, March - April 2026 ISSN: 2408-2384 (Online)

FOCUS AND SCOPE

Environment and Natural Resources Journal (EnNRJ) is a peer-reviewed journal which provides a platform for exchanging and distributing knowledge and cutting-edge research in environmental science and natural resource management to academicians, scientists, and researchers.

The scope of the journal covers the integration of multidisciplinary sciences for prevention, control, treatment, environmental clean-up, and restoration. The study of existing or emerging problems related to the environment and natural resources in Southeast Asia and the development of innovative knowledge and/or creative recommendations for mitigation measures and sustainable development are emphasized. The subject areas are diverse, but specific topics of interest include:

- Biodiversity
- Climate change
- Detection and monitoring of pollutants and their sources (e.g., agriculture, industry, mining, urban activities, accidents)
- Disaster (e.g., forest fires, flooding, earthquakes, tsunamis or tidal waves)
- Ecological/Environmental modelling
- Emerging contaminants/hazardous wastes investigations and remediation
- Environmental dynamics (e.g., coastal erosion, rising sea levels)
- Environmental assessment tools, policy, and management [e.g., GIS, remote sensing, and Environmental Management Systems (EMS)]
- Pollution control and innovative solutions for pollution reduction
- Remediation technology in contaminated environments
- Transboundary pollution
- Waste and wastewater treatments and disposal technology

Schedule
Environment and Natural Resources Journal (EnNRJ) is published 6 issues per year in January-February, March-April, May-June, July-August, September-October, and November-December.

Publication Fees
An article publication fee in the Environment and Natural Resources Journal is set at a rate of 250 USD per article, payable after the final acceptance of the manuscript.

Ethics in publishing
EnNRJ follows closely a set of guidelines and recommendations published by Committee on Publication Ethics (COPE).

Environment and Natural Resources Journal (EnNRJ)

Volume 24, Number 2, March - April 2026 ISSN: 2408-2384 (Online)

Editorial Office Address
Research and Academic Service, Research Management Unit,
Faculty of Environment and Resource Studies, Mahidol University
999, Phutthamonthon Sai 4 Road, Salaya, Phutthamonthon, Nakhon Pathom, Thailand, 73170
Phone +662 441 5000 ext. 2108
Website: https://ph02.tci-thaijo.org/index.php/ennrj/index
E-mail: ennrjournal@gmail.com

Environment and Natural Resources Journal (EnNRJ)

Volume 24, Number 2, March - April 2026 ISSN: 2408-2384 (Online)

CONTENT

Environment and Natural Resources Journal

Volume 24
Issue 2
2026

The Invisible Threat: Assessing Microplastic Contamination in Beef and Its Implications for Food Safety

Inneke Hantoro*, Mellia Harumi, Katharina Ardanareswari, Bernadeta Soedarini, and Budi Widianarko

Faculty of Agricultural Technology, Soegijapranata Catholic University, Indonesia

ARTICLE INFO

Received: 28 Dec 2024
Received in revised: 10 Oct 2025
Accepted: 15 Oct 2025 Published online: 7 Jan 2026
DOI: 10.32526/ennrj/24/20240348

Keywords:
Microplastics/ Beef/ Food safety/ Market/ FTIR

*** Corresponding author:**
E-mail:
inneke.hantoro@unika.ac.id

ABSTRACT

Microplastics (MPs) have been widely found in various food products cultivated on land, including meat. This study focuses on detecting the presence of MPs in beef available at traditional markets, specialty meat shops, and retail stores in the city of Semarang. The samples were digested using a combination of KOH solution, hydrogen peroxide, Fenton's reagent, and identified using micro-FTIR. All samples were analyzed in duplicate. MPs were found in all beef samples. The highest concentration of MPs was found in beef from the traditional market ($2.57\times10^6\pm3.35\times10^6$ MPs/kg WB), followed by samples taken from the meat shop ($7.51\times10^5\pm1.58\times10^5$ MPs/kg WB), and supermarket ($6.78\times10^5\pm2.41\times10^5$ MPs/kg WB). Samples from traditional markets contained predominantly polyethylene (PE, 94.1%), while those from supermarkets and meat shops were mainly polyvinyl chloride (PVC), at 47.5% and 38.8% respectively. Polyvinyl alcohol (PVAL) was often found in supermarket samples (27.1%), and ethylene vinyl alcohol (EVOH) was commonly observed in meat shop samples (20.4%). Most of the MPs in fragment form were frequently found in supermarket and meat shop samples (62.5% and 65.9%, respectively), while foam MPs dominated traditional market samples (62.3%). Film MPs were also common in supermarket (25.3%) and traditional market (26.6%) samples. Most MPs across all samples measured >100-≤300 µm (33.4% to 37.7%). The intake of MPs from beef consumption for the Indonesian population is considered high, ranging from 1,866,750 MP/person/year to 6,733,400 MP/person/year based on national beef consumption data. Therefore, MP contamination still needs to be monitored to prevent food safety issues.

HIGHTLIGHTS

- MPs in beef from traditional markets are three times higher than in other markets.
- PVC, PET, EVOH, and PVAL are the dominant types of polymers found in beef samples.
- MP intake from beef consumption among Indonesians is considered high.

1. INTRODUCTION

Microplastics (MPs) are tiny plastic particles, ranging from 1 to 5,000 µm, (GESAMP, 2019), originating from primary sources, intentionally produced for industrial or commercial use, and secondary sources formed by the breakdown of larger plastic debris through environmental processes (Andrady, 2017). MPs are commonly found in the air, water, and soil due to various human activities, such as improper disposal of plastic waste, industrial processes, fishing and maritime activities, the use of personal products and synthetic textiles, transportation and urban runoff, and improper wastewater treatment (Sharma and Chatterjee, 2017; Lundebye et al., 2022). Once present in the environment, MPs can enter both aquatic and terrestrial food chains and contaminate

Citation: Hantoro I, Harumi M, Ardanareswari K, Soedarini B, Widianarko B. The invisible threat: Assessing microplastic contamination in beef and its implications for food safety. Environ. Nat. Resour. J. 2026;24(2):140-148. (https://doi.org/10.32526/ennrj/24/20240348)

numerous food and beverage products consumed by humans (Gündogdu et al., 2023; Prata and Dias-Pereira, 2023; Sewwandi et al., 2023).

It is possible for MPs to enter the human body, with evidence of their presence found in feces (Luqman et al., 2021), the colon (Ibrahim et al., 2020), the placenta (Ragusa et al., 2021), blood (Leslie et al., 2022), lungs (Jenner et al., 2022), and breast milk (Ragusa et al., 2022). Concerns about the potential health impacts of MPs include inflammation, oxidative stress, and toxicity, as demonstrated in both in vitro and in vivo studies (Emenike et al., 2023; Mattioda et al., 2023). However, our understanding of the risks posed by MPs to human health remains limited, particularly regarding realistic human exposure (Zhao et al., 2024).

Studies have identified MPs in seafood (Hantoro et al., 2019), freshwater fish (Li et al., 2018), various food products like salt, honey, and beer (Peixoto et al., 2019; Toussaint et al., 2019), drinking water (Kirstein et al., 2016; Oßmann, 2021), poultry including chicken meat, eggs (up to 12 particles per egg) (Liu et al., 2022; Zhao et al., 2024), and livestock (Chen et al., 2023; Bahrani et al., 2024), indicating their widespread presence. A study in Iran reported an average of 0.14 and 0.13 particles/g in cattle and goats, respectively, with the highest concentration in beef tissue at 0.19 particles/g, mainly comprising nylon and fiber polymers (Bahrani et al., 2024). Likewise, Visentin et al. (2024) demonstrated the occurrence of MPs in beef hamburgers in Italy. Furthermore, analysis on top sirloin steaks from a USA supermarket showed 25±38 MP particles/serving (Milne et al., 2024). These findings provide the initial evidence of MPs in beef.

Research on MP contamination in livestock meat, particularly beef, in Indonesia is limited, despite its importance as a protein source. Although beef consumption in Indonesia, is relatively low (approximately 2.62 kg/capita/year in 2022, compared to the world average of 6.4 kg/capita/year), it has been increasing over the past five years (Chafid, 2024).

MPs enter livestock through the environment, water, and feed. Some low-income populations in Indonesia rear cattle near or inside municipal garbage disposal sites due to limited grazing areas, increasing the risk of MP exposure. MPs have also been detected in meat, with post-slaughter contamination linked to the use of plastic cutting boards during preparation for customers (Habib et al., 2022a). Habib et al. (2022a) further demonstrated that plastic cutting boards are a source of MPs contamination in raw cut fish and livestock, and that washing cutting boards before meat preparation increases MP release into wastewater sinks.

Thus, further research is needed to understand the extent of MP contamination in beef and its potential impact on consumer health. This study aims to investigate the occurrence of MPs in beef from traditional markets, specialty meat shops, and retail stores in Semarang.

2. METHODOLOGY

2.1 Sampling and sample preparation

2.1.1 Study area

This study was conducted in Semarang City, Central Java Province, and focused on butchers from a traditional market, a meat shop, and a supermarket who met specific criteria: the beef must be sourced from Semarang City and consist of sirloin and brisket.

2.2.2 Sample collection and preparation

A total of 1 kg sample consisting of each 500 g of brisket and sirloin cuts were collected from each location and wrapped in aluminum foil before being transported to the laboratory. A disinfected cooler box (wiped with 70% ethanol) was used to transport the samples to the laboratory. For each location, those cuts were divided into smaller pieces before being ground and homogenized. The homogenized sample was weighed at 5 grams, wrapped in aluminum foil, placed in glass containers, labeled, and stored in a freezer at -18°C. As for the digestion process, samples were removed from the freezer and thawed until they reached room temperature.

2.2 Microplastics detection

2.2.1 Quality assurance of analysis

Before sample analysis, laboratory quality assurance was performed in accordance with Dehaut et al. (2019). All equipment and work surfaces were sterilized with 70% ethanol. The floor and working areas were vacuumed, and an air purifier was turned on during the analysis. To prevent external microplastic contamination, only non-plastic equipment such as glass, stainless steel, and wood were employed. The entire operation was carried out while wearing laboratory coats and nitrile gloves. Each glassware was washed and rinsed with ethanol and aquabidest, then wrapped in aluminum foil and dried in the oven. The solutions were initially filtered using Whatman filter paper. Moreover, blank analysis and air contamination control checks were conducted to correct the results of MPs analysis on the samples.

2.2.2 Sample digestion

The method for identifying microplastics in beef was derived from Milne et al. (2024). Five grams of homogenized sample were digested in a 10% KOH solution and incubated at 40°C for 24 hours. The materials were then filtered with Whatman filter paper 541. In addition, 120 mL of 30% H_2O_2 solution was added to the sample and left for another 24 hours to remove any organic matter. The digestion process continued with wet peroxide oxidation (WPO), which used iron sulfate ($Fe(II)SO_4$) as a catalyst in conjunction with 30% H_2O_2 at a 1:5 ratio. To keep the temperature below 50°C and reduce microplastic loss, an ice bath was used. The sample was filtered through PTFE filter paper, before the identification step, and placed in a Petri plate and dried.

2.2.3 Characterization and identification of MPs

The characterizations were based on quantity, form, and size. The shapes were classified as fragments, fibers, films, foams, and pellets. The types of microplastic polymers were evaluated using micro-FTIR (IR Tracer100 & AIM 9000, Shimadzu) in the wavenumber range of 4,000-400 cm^{-1}, resolution of 4 cm^{-1}, utilizing reflection mode and %transmission measurement mode. A total of 50 scans were completed. From the total surface area of the filter paper in contact with the sample, 5% of the area was taken for identification. Sixteen points, each measuring 2 × 2 mm^2 on the membrane filter surface, were randomly selected for analysis. The number of particles found was extrapolated to cover the entire surface area of the membrane filter.

Polyamide (PA) was used as a reference material to ensure the accuracy of the spectral observations. The spectra from the samples were compared to known plastic polymer spectra from many reference spectral libraries from Shimadzu. To determine the types of polymers present, the examined spectrum data were matched to the reference database using a matching threshold of more than 65% (Corami et al., 2020).

To determine the shape and size of MP particles identified from micro-FTIR analysis results, the program ImageJ Version 1.54 was used. The image analysis was conducted through a series of systematic procedures. Initially, microplastic (MP) images obtained from the micro-FTIR instrument were imported into the ImageJ software for further analysis. Scale calibration was then performed to ensure accurate measurement. In cases where particle images appeared unclear, brightness and contrast adjustments were applied to enhance visual clarity. The particle size was subsequently determined based on the axial diameter, defined as the maximum linear distance measured from one end of the particle to the opposite end. The morphology of microplastic particles was determined by comparing visual images with shape classification criteria reported in previous studies (Rochman et al., 2019; Lusher et al., 2020).

2.3 Data analysis

Microplastic concentrations were presented as mean value data (MPs/kg, WB). The MP concentration in the samples was corrected using the average of blank controls and airborne contaminants found in the laboratory. The characteristics of MPs, including shape, size, and type of polymer, are presented in the graphs.

3. RESULTS AND DISCUSSION

3.1 MP concentration in the beef samples

The average concentration of MPs in beef obtained (MPs/kg, WB) is displayed in Table 1. MPs were detected in all analyzed samples, confirming their ubiquitous presence in markets. Beef from the traditional market exhibited the highest concentration ($2.57\times10^6\pm3.35\times10^6$ MPs/kg, WB), followed by the meat shop ($7.51\times10^5\pm1.58\times10^5$ MPs/kg WB) and the supermarket ($6.78\times10^5\pm2.41\times10^5$ MPs/kg WB). However, statistical analysis using the Kruskal-Wallis test revealed no significant differences among the markets ($\chi^2=2.000$, df=2, p=0.368), indicating relatively similar contamination levels across sampling sites. The observed variations in mean values may be associated with differences in post-slaughter handling practices. Field observations show that meat sold in traditional market is transported from slaughterhouses in plastic sacks and displayed on plastic trays or wrapped in plastic. Meanwhile, meat from the supermarket and the meat shop is transported in plastic but displayed differently: hung on hooks over ceramic tables or placed on melamine trays and wrapped in cling wrap. Furthermore, the highly open condition of traditional market increases the likelihood of microplastic contamination from the surrounding environment.

The findings of this study are significantly higher than the MP levels found in beef hamburgers produced in Italy, where the contamination density ranges from 200 to 30,000 MP/kg of sample (Visentin et al., 2024). Compared to the highest MP density in beef burger samples, the contamination level in fresh beef from this study is 24 to 86 times higher.

Table 1. The concentration of MPs in beef obtained from different markets

Location	MP concentration ((MP/kg, WB)
Supermarket	$6.78\times10^{5}\pm2.41\times10^{5}$
Meat shop	$7.51\times10^{5}\pm1.58\times10^{5}$
Traditional market	$2.57\times10^{6}\pm3.35\times10^{6}$

Compared to MP findings in other types of meat measured in France—such as 1.1±1.9 and 10.8±6.0 MP/kg in packaged meat (Kedzierski et al., 2020) and 0.03±0.04 to 1.19±0.72 MP/g in meat cut on plastic cutting board (Habib et al., 2022a)—this study also shows significantly higher concentrations. This significant difference may be attributed to variations in identification methods, such as the hit quality index used, and the extrapolation method employed in this study, which could have led to an overestimation of MP concentrations. Although microscopic observations revealed an even distribution of MP particles on the membrane filter, this indicates a high density of MPs in the beef samples. Additionally, differences in location may also play a role.

MP contamination in beef can start from cattle production on farms and extend through to market sales (Velebit et al., 2023). MPs can enter the meat supply chain primarily through livestock feed. If cows ingest contaminated water, feed, or fodder, MPs can accumulate in their tissues. Additionally, the use of plastic containers and packaging during beef handling and display contributes to MP contamination.

3.2 The characteristics of MPs in the beef samples

Figure 1 shows that the dominant particles in beef samples from the traditional market were polyethylene (PE, 94.1%). In contrast, samples from the supermarket and the meat shop were predominantly composed of polyvinyl chloride (PVC), at 47.5% and 38.8% respectively. The type of polymer polyvinyl alcohol (PVAL) was frequently found in samples from the supermarket (27.1%, while ethylene vinyl alcohol (EVOH) was commonly found in samples from the meat shop (20.4%). The diversity of MP polymer types in meat samples is much less than in the supermarket and the meat shop. The infrared spectra of the most dominant MPs are presented in Figure 2.

To identify the identic functional group of polymers, FTIR spectra was recorded. Figure 2 represents the functional group of two most dominant polymer types which were found in beef samples. Characteristic of PE are shown at peak 1,465 cm^{-1} which represents to bending vibration of C-H_2 and 2,924 cm^{-1} of C-H stretching vibration. Peak at 599 cm^{-1} is attributed to stretching vibration of C-Cl from PVC spectra. The spectra also has the same signal at 2,908 cm^{-1} as C-H stretching vibration.

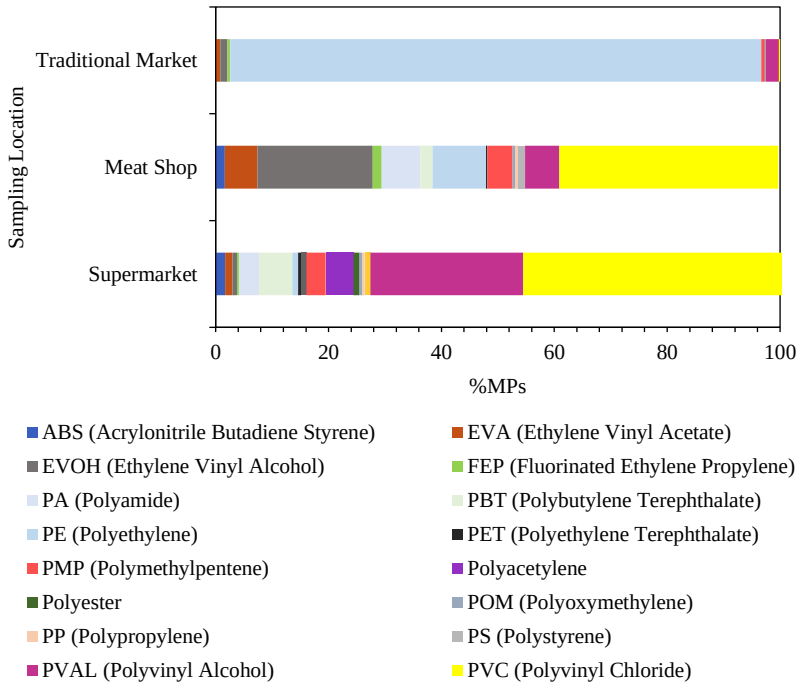

Figure 1. Polymer type of MPs found in beef samples

PVC (740)

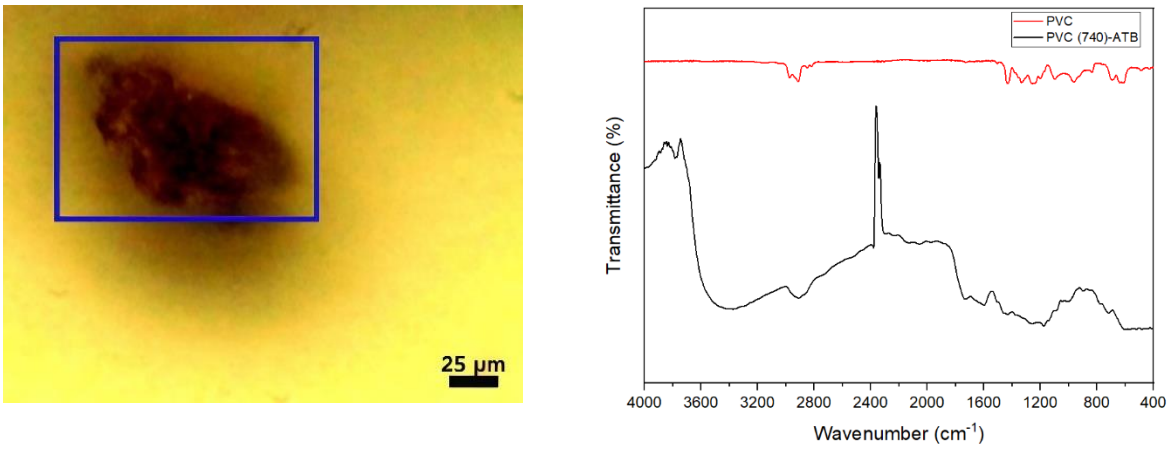

PE (803)

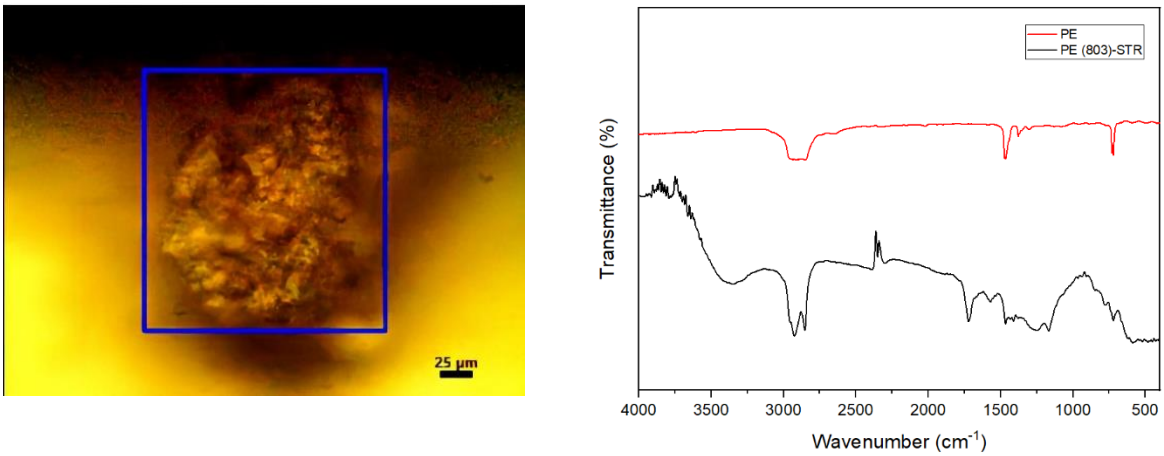

Figure 2. The shape and size of the most abundant identified MPs in beef samples (PVC and PE) analyzed with ImageJ and the FTIR spectra of detected MP particles.

The PE plastic found in the meat samples, particularly prevalent in traditional markets, is most likely from the plastic wrapping bags commonly used in these markets and throughout the beef supply chain. The study by Katsara et al. (2022) also found that the most common plastic in cured beef product samples was LDPE. The presence of PE has also been reported in chicken meat, as demonstrated by Habib et al. (2022a), who identified PE originating from cutting boards. This study demonstrates that LDPE from plastic packaging can be transferred to meat products during distribution and storage. PE could also originate from cling wrap, which is commonly used in supermarkets. However, the PE polymer found in beef samples from supermarkets is relatively low compared to other samples.

The detection of PVC in beef is supported by previous findings from Van Der Veen et al. (2022), who successfully identified PVC in several meat samples. PVC is predominantly found in meat samples from the meat shop and the supermarket. PVC with the addition of plasticizers is commonly used as food packaging material (Carlos et al., 2018), which, in this case, is likely a source of MP exposure to beef. PVAL is frequently detected in beef samples from the supermarket. PVAL is widely used in food packaging because it is biodegradable, non-toxic, has excellent film-forming capabilities, good absorbency, ready availability, and low processing costs (Channa et al., 2022; Uysal-Unalan et al., 2024). EVOH is commonly found in beef samples from the meat shop. EVOH is a plastic polymer commonly used in food packaging due to its exceptional barrier resistance to gases, aroma, water hydrocarbon permeation and chemical resistance (Luzi et al., 2020; Uysal-Unalan et al., 2024), making it ideal for preserving food with 70% crystalline structure. The presence of hydroxyl groups make EVOH is frequently used as a copolymer with

hydrophobic materials as a good barrier coating system. Blending this material with compounds or monomers will ease the process of decomposition (Tyagi et al., 2021).

Figure 3 shows that fragments were frequently found in samples from supermarkets and meat shops (62.5% and 65.9%, respectively), while MPs in foam form were prevalent in beef samples from traditional markets (62.3%). MPs in film form were also commonly found in samples from supermarkets (25.3%) and traditional markets (26.6%). Fragments were also found to be the most prevalent form in beef hamburgers, and the other MP forms were fibers and beads (Visentin et al., 2024). The cutting board used by markets contributed to the generation of the fragment shape of MPs (Habib et al., 2022a). It was estimated that every gram of cut meat will release 2.2 mg of plastic (Habib et al., 2022b). Considering that fragment form of MPs has been detected in supermarket samples, the source of this shape can come from the usage of cutting boards as the result of field observation during this research. Research on MPs in meat or meat products is very limited, and previous studies have not found the presence of MPs in the form of foam.

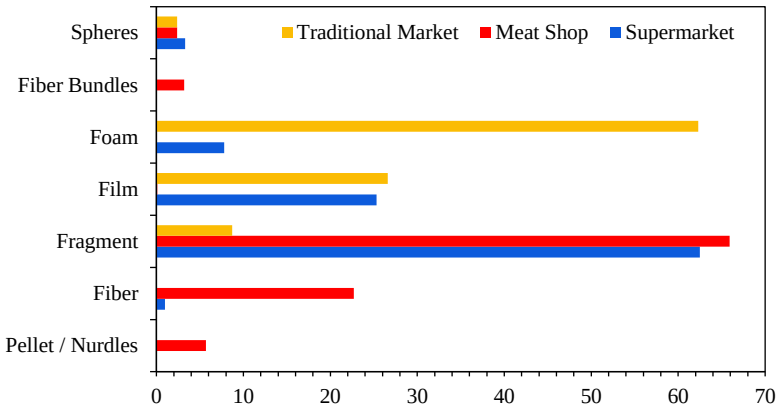

Figure 3. The morphotypes of MPs found in beef samples

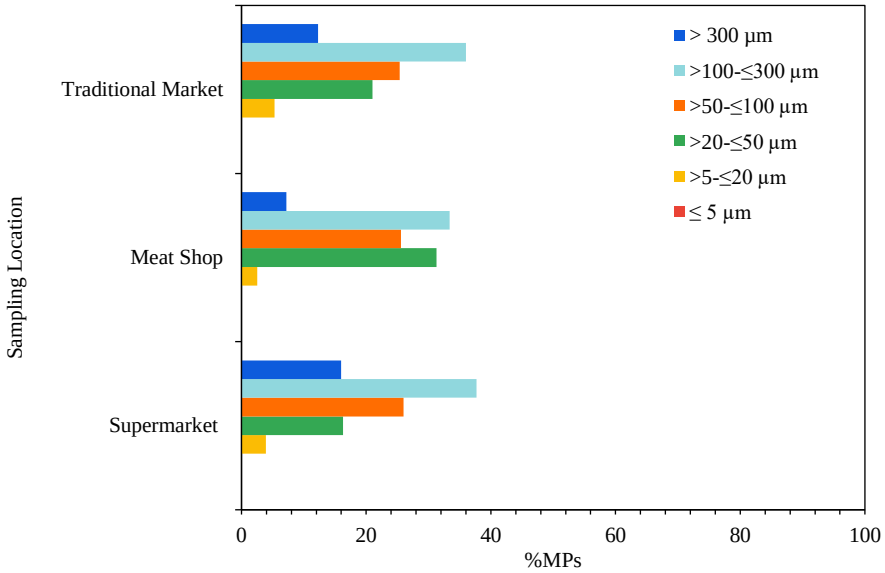

Figure 4. The size of MPs found in beef samples

The most common size of MPs found in all samples was >100-≤300 µm, followed by size range >50-≤100 µm and >20-≤50 µm (Figure 4). Particles smaller than 20 µm and larger than 300 µm were found in lower proportions in all beef samples. A similar range of MP sizes has also been found in other related studies (Kedzierski et al., 2020). Meanwhile, the study by

Visentin et al. (2024) showed that the most common polymers were in the size range of 51-100 µm.

3.3 Implications for food safety

Beef available in markets, meat shops, and retail stores shows high levels of MP contamination. Consequently, beef becomes a significant pathway for human exposure to MPs. Although beef consumption in Indonesia is relatively low compared to other countries, the high contamination levels can still result in substantial MP intake.

MP contamination in beef may pose health risks, given that beef and its products are essential sources of protein and other nutrients in the Indonesian diet. However, assessing the potential health risks of MPs in beef requires an understanding of the extent of human exposure through its consumption. Based on the average beef consumption in Indonesia in 2022, which was approximately 2.62 kg/capita/year (Chafid, 2024), the annual intake of MPs could range from 1,866,750 MPs/capita/year to 6,733,400 MPs/capita/year. This intake level is much higher compared to the annual MP intake through green mussel consumption, which range from 218,400-775,180 MPs/capita/year in Indonesia (Irnidayanti et al., 2023). It's worth noting that green mussels are known to be one of the seafood products with high levels of MP contamination. However, as determined by this study, MP exposure from beef consumption is still lower than intake from drinking water, which can reach 12,273,490 MPs/capita/year (Rubio-Armendariz et al., 2022).

Even though the concentration of MPs in beef is very high, it does not necessarily imply a greater health risk, as factors such as the shape, size, and type of polymer of MPs also play a role (Hantoro et al., 2024). The smaller-sized MPs showed greater toxicity reactions in in-vitro studies (Pelegrini et al., 2023). Furthermore, another study indicated that toxicity is influenced by the composition of polymer monomers (Yuan et al., 2022).

MP contamination in meat can be influenced by various stages along the supply chain, including production on farms, slaughtering, transportation, and distribution to different types of market. Therefore, implementing good practices throughout the food supply chain is essential to reduce the likelihood of MPs entering beef. The use of various plastic equipment and plastic packaging needs to be minimized throughout the food supply chain. Consumers should also avoid using plastic cutting boards, as their use has been shown to contribute to the entry of MPs into meat (Habib et al., 2022a). Despite the health effects of MPs on humans are not yet fully understood, precautionary measures suggest avoiding MP intake and highlight the importance of proper beef handling to reduce risks.

4. CONCLUSION

The high levels of MP contamination detected in beef from markets in Semarang highlight a potential route of MP exposure to consumers. Although the contamination observed in this study is most likely linked to post-slaughter handling practices, such as displaying, cutting, weighing, and packaging, the possibility of pre-slaughter contamination cannot be ruled out, as it was beyond the study's scope. Variations in MP concentrations and characteristics among market types suggest that handling practices along the supply chain, from slaughter to retail, may influence the degree of MP contamination in beef available to the consumers.

Future research should focus on elucidating the fate and dynamics of microplastic contamination across pre- and post-slaughter stages of the meat supply chain. Considering the potential health risks associated with MP-contaminated beef, it is crucial to broaden research on human exposure pathways and the toxicity of MPs. There is an urgent need for mitigation measures in beef handling and processing to lower human exposure risks. Future studies should also focus on improving risk assessments and creating effective strategies to reduce MP contamination along the beef supply chain and safeguard public health.

ACKNOWLEDGEMENTS

Acknowledgments are extended to the Ministry of Education, Culture, and Technology of the Republic of Indonesia for funding this research through the BIMA Regular Fundamental Research Grant scheme, contract number 108/E5/PG.02.00.PL/2024. The authors also would like to thank Angel Swasti Herista, Gracesella Kurniawan, Janice Carissa Marvell Wijaya, and Felix Sholeh Kuntoro for their assistance in field sampling and laboratory analysis.

AUTHOR CONTRIBUTIONS

Conceptualization, Hantoro I, Widianarko B; Methodology, Hantoro I, Harumi M, Ardanareswari K, Soedarini B, Widianarko B; Validation, Hantoro I; Formal Analysis, Hantoro I and Widianarko B; Investigation, Hantoro I, Harumi M, Ardanareswari K, Soedarini B, Widianarko B; Data Curation Hantoro I, Harumi M,

Ardanareswari K, Soedarini B, Widianarko B; Writing-Original Draft Preparation, Hantoro I, Harumi M, Ardanareswari K; Writing-Review and Editing, Soedarini B, Widianarko B; Visualization, Hantoro I; Supervision, Widianarko B; Project Administration, Hantoro I.

DECLARATION OF CONFLICT OF INTEREST

The authors declare that they have no known competing financial interests or personal relationships that could have appeared to influence the work reported in this paper.

REFERENCES

Andrady AL. The plastic in microplastics: A review. Marine Pollution Bulletin 2017;119(1):12-22.

Bahrani F, Mohammadi A, Dobaradaran S, De-la Torre GE, Arfaeinia H, Ramavandi B, et al. Occurrence of microplastics in edible tissues of livestock (cow and sheep). Environmental Science and Pollution Research 2024;31(14):22145-57.

Carlos KS, de Jager LS, Begley TH. Investigation of the primary plasticisers present in polyvinyl chloride (PVC) products currently authorised as food contact materials. Food Additives and Contaminants: Part A 2018;35(6):1214-22.

Chafid M. Outlook Daging Sapi. In: Susanti AA, Putra RK, editors. Sekretariat Jendral - Kementrian Pertanian. Jakarta: Pusat Data dan Sistem Informasi Pertanian; 2024.

Channa IA, Ashfaq J, Gilani SJ, Chandio AD, Yousuf S, Makhdoom MA, et al. Sustainable and eco-friendly packaging films based on poly (Vinyl Alcohol) and glass flakes. Membranes 2022;12(7):1-14.

Chen J, Chen G, Peng H, Qi L, Zhang D, Nie Q, et al. Microplastic exposure induces muscle growth but reduces meat quality and muscle physiological function in chickens. Science of the Total Environment 2023;882:Article No. 163305.

Corami F, Rosso B, Roman M, Picone M, Gambaro A, Barbante C. Evidence of small microplastics (<100 Mm) ingestion by Pacific Oysters (*Crassostrea gigas*): A novel method of extraction, purification, and analysis using micro-FTIR. Marine Pollution Bulletin 2020;160:Article No. 111606.

Dehaut A, Hermabessiere L, Duflos G. Current frontiers and recommendations for the study of microplastics in seafood. TrAC-Trends in Analytical Chemistry 2019;116:346-59.

Emenike EC, Okorie CJ, Ojeyemi T, Egbemhenghe A, Iwuozor KO, Saliu OD, et al. From oceans to dinner plates: The impact of microplastics on human health. Heliyon 2023;9(10): e20440.

Joint Group of Experts on the Scientific Aspects of Marine Environmental Protection (GESAMP). Guidelines for the Monitoring and Assessment of Plastic Litter in the Ocean. Reports and Studies GESAMP No. 99. United Nations Environment Programme (UNEP); 2019.

Gündogdu S, Rathod N, Hassoun A, Jamróz E, Kulawik P, Gokbulut C, et al. The impact of nano/micro-plastics toxicity on seafood quality and human health: facts and gaps. Critical Reviews in Food Science and Nutrition 2023;63(23):6445-63.

Habib RZ, Al Kindi R, Al Salem F, Al Siyabi M, Al Shaibi T, Soussi A, et al. Microplastic contamination of chicken meat and fish through plastic cutting boards. International Journal of Environmental Research and Public Health 2022a;19(20):1-13.

Habib RZ, Poulose V, Alsaidi R, al Kendi R, Iftikhar SH, Mouraad AHI, et al. Plastic cutting boards as a source of microplastics in meat. Food Additives and Contaminants: Part A 2022b;39(3):609-19.

Hantoro I, Löhr AJ, Van Belleghem FG, Widianarko B, Ragas AMJ. Microplastics in coastal areas and seafood: Implications for food safety. Food Additives and Contaminants: Part A 2019;36(6):860-74.

Hantoro I, Löhr A, Van Belleghem FG, Widianarko B, Ragas AMJ. Characteristics of microplastics pollution in important commercial coastal seafood of central java, indonesia. Environmental Advances 2024;17:Article No. 100574.

Ibrahim YS, Anuar ST, Azmi AA, Mohd Khalik WMAW, Lehata S, Hamzah SR, et al. Detection of microplastics in human colectomy specimens. Journal of Hepatology and Hepatology Foundation 2020;5(1):116-21.

Irnidayanti Y, Soegianto A, Brabo AH, Abdilla FM, Indriyasari KN, Rahmatin NM, et al. Microplastics in green mussels (*Perna viridis*) from jakarta bay, indonesia, and the associated hazards to human health posed by their consumption. Environmental Monitoring and Assessment 2023;195(7):1-12.

Jenner LC, Rotchell JM, Bennett RT, Cowen M, Tentzeris V, Sadofsky. Detection of microplastics in human lung tissue using MFTIR spectroscopy. Science of the Total Environment 2022;831:Article No. 154907.

Katsara K, Kenanakis G, Alissandrakis E, Papadakis VM. Low-density polyethylene migration from food packaging on cured meat products detected by micro-raman spectroscopy. Microplastics 2022;1(3):428-39.

Kedzierski M, Lechat B, Sire O, Le Maguer G, Le Tilly V, Bruzaud S. Microplastic contamination of packaged meat: occurrence and associated risks. Food Packaging and Shelf Life 2020;24:Article No. 100489.

Kirstein IV, Kirmizi S, Wichels A, Garin-Fernandez A, Erler R, Löder M, et al. Dangerous hitchhikers? evidence for potentially pathogenic *Vibrio* spp. on microplastic particles. Marine Environmental Research 2016;120:1-8.

Leslie HA, van Velzen MJM, Brandsma SH, Vethaak AD, Garcia-Vallejo JJ, Lamoree MH. Discovery and quantification of plastic particle pollution in human blood. Environment International 2022;163:Article No. 107199.

Li J , Liu H, Chen JP. Microplastics in freshwater systems: Aa review on occurrence, environmental effects, and methods for microplastics detection. Water Research 2018;137:362-74.

Liu Q, Chen Z, Yang F, Yao W, Xie Y. Microplastics contamination in eggs: Detection, occurrence and status. Food Chemistry 2022;397:Article No. 133771.

Lundebye AK, Lusher AL, Bank MS. Marine microplastics and seafood: Implication for food security. In: Bank MS, editor. Microplastic in the Environment: Pattern and Process. Environmental Contamination Remediation and Management. Cham: Springer; 2022. p. 131-53.

Luqman A, Nugrahapraja H, Wahyuono RA, Islami I, Haekal MH, Fardiansyah Y, et al. Microplastic contamination in human stools, foods, and drinking water associated with indonesian coastal Population. Environments 2021;8(12):Article No. 138.

Lusher AL, Bråte IL, Munno K, Hurley RR, Welden NA. Is it or isn't: The importance of visual classification in microplastic characterization. Applied Spectroscopy 2020;74(9):1139-53.

Luzi F, Torre L, Puglia D. Antioxidant packaging films based on ethylene vinyl alcohol copolymer (EVOH) and caffeic acid. Molecules 2020;25(17):Article No. 3953.

Mattioda V, Benedetti V, Tessarolo C, Oberto F, Favole A, Gallo M, et al. Pro-inflammatory and cytotoxic effects of polystyrene microplastics on human and murine intestinal cell lines. Biomolecules 2023;13(1):Article No. 140.

Milne MH, De Frond H, Rochman CM, Mallos NJ, Leonard GH, Baechler BR. Exposure of US adults to microplastics from commonly-consumed proteins. Environmental Pollution 2024;343:Article No. 123233.

Oßmann BE. Microplastics in drinking water? Present state of knowledge and open questions. Current Opinion in Food Science 2021;41:44-51.

Peixoto D, Pinheiro C, Amorim J, Olivia-Teles L, Guilhermino L, Vieira MN. Microplastic pollution in commercial salt for human consumption: A review. Estuarine, Coastal and Shelf Science 2019;219:161-8.

Pelegrini K, Pereira TC, Maraschin TG, Teodoro LD, Basso NR, De Galland GL, et al. Micro- and nanoplastic toxicity: A review on size, type, source, and test-organism implications. Science of the Total Environment 2023;878:1-14.

Prata JC, Dias-Pereira P. Microplastics in terrestrial domestic animals and human health: Implications for food security and food safety and their role as sentinels. Animals 2023;13(4): Article No. 661.

Ragusa A, Svelato A, Santacroce C, Cantalano P, Notarstefano V, Carnevalli O, et al. Plasticenta: First evidence of microplastics in human placenta. Environment International 2021;146: Article No. 106274.

Ragusa A, Notarstefano V, Svelato A, Belloni A, Gioacchini G, Blondee C, et al. Raman microspectroscopy detection and characterisation of microplastics in human breastmilk. Polymers 2022;14(13):Article No. 2700.

Rochman CM, Brookson C, Bikker J, Djuric N, Earn A, Bucci K, et al. Rethinking microplastics as a diverse contaminant suite. Environmental Toxicology and Chemistry 2019;38(4):703-11.

Rubio-Armendariz C, Alejandro-Vega S, Paz-Montelongo S, Gutierrez-Fernandez AJ, Carrascos-Iruzubieta CJ, Hardisson-de la Torre A. Microplastics as emerging food contaminants: A challenge for food safety. International Journal of Environmental Research and Public Health 2022;19(3):Article No. 1174.

Sharma S, Chatterjee S. Microplastic pollution, a threat to marine ecosystem and human health: A short review. Environmental Science and Pollution Research 2017;24(27):21530-47.

Sewwandi M, Wijesekara H, Rajapaksha AU, Soysa S, Vithanage M. Microplastics and plastics-associated contaminants in food and beverages; global trends, concentrations, and human exposure. Environmental Pollution 2023;317:Article No. 120747.

Toussaint B, Raffael B, Angers-Loustau A, Gilliland D, Kestens V, Petrillo M, et al. Review of micro- and nanoplastic contamination in the food chain. Food Additives and Contaminants: Part A 2019;36(5):639-73.

Tyagi P, Salem KS, Hubbe MA, Pal L. Advances in barrier coatings and film technologies for achieving sustainable packaging of food products: A review. Trends in Food Science and Technology 2021;115:461-85.

Uysal-Unalan I, Sogut E, Realini CE, Cakmak H, Oz E, Espinosa E, et al. Bioplastic packaging for fresh meat and fish: Current status and future direction on mitigating food and packaging waste. Trends in Food Science and Technology 2024;152:Article No. 104660.

Van Der Veen I, Van Mourik LM, Van-Velzen MJ, Groenewoud QR, Leslie HA. Plastic Particles in Livestock Feed, Milk, Meat and Blood. The Netherlands: Department of Environment and Health, Plastic Soup Foundation; 2022.

Velebit B, Janković V, Milojević L, Baltić T, Cirić J. Overview of microplastics in the meat: Occurrence, detection methods and health effects. Meat Technology 2023;64(2):36-41.

Visentin E, Niero G, Benetti F, Perini A, Zanella M, Pozza M, et al. Preliminary characterization of microplastics in beef hamburgers. Meat Science 2024;217:Article No. 109626.

Yuan Z, Nag R, Cummins E. Human health concerns regarding microplastics in the aquatic environment - From Marine to food systems. Science of the Total Environment 2022;823: Article No. 153730.

Zhao B, Rehati P, Yang Z, Cai Z, Guo C, Li Y. The potential toxicity of microplastics on human health. Science of the Total Environment 2024;912:Article No. 168946.

Environment and Natural Resources Journal

Volume 24
Issue 2
2026

Life Cycle Assessment of Sugarcane Bagasse Takeout Containers: A Case Study in Laibin, Guangxi, China

Meng Fan*, and Chokeanand Bussracumpakorn

School of Architecture and Design, King Mongkut's University of Technology Thonburi (KMUTT), Bangkok, Thailand

ARTICLE INFO

Received: 20 Apr 2025
Received in revised: 21 Oct 2025
Accepted: 31 Oct 2025
Published online: 18 Nov 2025
DOI: 10.32526/ennrj/24/20250100

Keywords:
Biomass-based packaging/ Life cycle assessment (LCA)/ Carbon footprint/ Environmental optimization/ Renewable materials/ Low-carbon innovation/ Circular economy

*** Corresponding author:**
E-mail: fanmeng90@outlook.com

ABSTRACT

With growing global concerns over climate change, resource depletion, and environmental degradation, the packaging industry is under increasing pressure to shift toward low-carbon and sustainable alternatives. This study applies a Life Cycle Assessment (LCA) framework to evaluate the environmental impacts of sugarcane bagasse-based takeout containers using a representative enterprise in Laibin, Guangxi, China—a major sugarcane production hub. The system boundary spans from raw material acquisition to end-of-life disposal. Six environmental impact categories—Global Warming Potential (GWP), Acidification Potential (AP), Eutrophication Potential (EP), Abiotic Depletion Potential (ADP), Ozone Depletion Potential (ODP), and Photochemical Ozone Formation Potential (POFP)—were assessed using the CML 2001 method and compared with plastic, starch, and composite starch containers. The results show that bagasse containers significantly outperform conventional materials, especially in GWP and ADP, reducing total environmental burden by over 70%. Sensitivity analysis identifies bamboo pulp input, additives, and boiler fuel as key contributors. Optimization strategies include adopting cleaner pulping technologies, using green additives, and improving low-carbon logistics. The integrated "sugar mill-pulp mill-container factory" model in Laibin demonstrates high replicability in other agricultural regions of southern China and Southeast Asia. This study provides theoretical insights for promoting biomass packaging as part of the circular economy and sustainable material innovation.

HIGHLIGHTS

1. Cradle-to-grave LCA evaluates sugarcane-bagasse takeout containers in Laibin.
2. CML 2001 covers six impacts; compares bagasse, plastic, starch, and composite.
3. Bagasse cuts total life-cycle impacts by >70%, notably for GWP and ADP.
4. Sensitivity identifies hotspots: bamboo pulp, chemical additives, boiler fuel.
5. Actions proposed: carbon capture and storage, bio-based additives, and electrified logistics.

1. INTRODUCTION

1.1 Research background and objectives

The global packaging industry is under mounting pressure to transition toward low-carbon and sustainable solutions due to intensifying challenges related to climate change, resource depletion, and environmental degradation (Arfelli et al., 2024). As one of the largest packaging consumers globally, China generates enormous quantities of packaging waste, particularly from the fast-growing food delivery sector (Lu et al., 2025). A total of 1.6 million tons of plastic waste was generated by China's takeaway food services in 2020, accounting for 3% of plastic waste within the country's municipal solid waste, exacerbating resource inefficiency and plastic pollution (Zhang and Wen, 2022). In response, the Chinese government has introduced a series of environmental policies—such as the "14th Five-Year Plan for Plastic Pollution Control"—to promote degradable, recyclable, and low-carbon packaging alternatives and phase out conventional plastic products (Fürst and Feng, 2022).

Among the promising substitutes, biomass-based materials have received considerable attention due to their renewable, biodegradable, and carbon-neutral characteristics (Cruz et al., 2022). Sugarcane bagasse, a

Citation: Fan M, Bussracumpakorn C. Life cycle assessment of sugarcane bagasse takeout containers: A case study in Laibin, Guangxi, China. Environ. Nat. Resour. J. 2026;24(2):149-161. (https://doi.org/10.32526/ennrj/24/20250100)

by-product of the sugar industry, stands out for its environmental potential (Janika et al., 2024). Its high cellulose content makes it suitable for molded pulp packaging, while its use does not require additional land or compete with food production—hence, it is widely regarded as a "zero-land-use, zero-carbon-source" green material (Hossam and Fahim, 2023).

Although bagasse-based packaging has gained initial traction in the marketplace, current research primarily focuses on mechanical properties and forming processes. There is a lack of comprehensive environmental evaluation based on standardized Life Cycle Assessment (LCA), which is essential for quantifying its true sustainability performance. LCA enables a cradle-to-grave analysis of resource use and emissions throughout all life cycle stages, providing objective and comparable insights.

This study aims to fill these gaps by conducting a cradle-to-grave LCA (ISO 14040/14044) of sugarcane bagasse takeout containers produced in Laibin, Guangxi—one of China's key sugarcane production hubs. It evaluates the environmental impacts across six key categories using the CML 2001 method: Global Warming Potential (GWP), Acidification Potential (AP), Eutrophication Potential (EP), Abiotic Depletion Potential (ADP), Ozone Depletion Potential (ODP), and Photochemical Ozone Formation Potential (POFP). The environmental performance of bagasse containers is compared with conventional materials including plastic, starch, and composite starch containers.

The objectives of this study are fourfold: (1) to construct an LCA model for bagasse-based takeout containers and quantify their environmental impacts across life cycle stages; (2) to identify environmental hotspots and key contributing factors through sensitivity analysis; (3) to compare the environmental performance of bagasse containers with other materials and assess their substitution potential; and (4) to propose targeted strategies for material optimization, green processing, and policy support.

By achieving these objectives, this study not only offers robust evidence for the environmental advantages of sugarcane bagasse packaging, but also aligns with broader efforts in promoting sustainable materials and advancing the circular economy.

1.2 Development status and research gaps of bagasse-based packaging

Bagasse, a cellulose-rich agricultural by-product, has a considerable global resource base (Thongsomboon et al., 2023). Taking Laibin City in Guangxi, China as an example—a major national sugarcane production area—the sugarcane planting area reached 1.8302 million mu in 2023, with a total yield exceeding 11.45 million tons (Table 1). The annual output of bagasse, as a by-product, is approximately 3.44 million tons, providing a sufficient and stable raw material foundation for bagasse-based packaging production. Traditionally, bagasse has mostly been used as boiler fuel, livestock feed, or directly discarded, resulting in low resource utilization efficiency (Barasa Kabeyi, 2023). In recent years, with the tightening of environmental regulations and the rising awareness of green consumption, bagasse has attracted increasing attention in the packaging industry due to its natural biodegradability, renewability, and low carbon emissions (Debnath et al., 2022; Liu et al., 2020).

In international markets, several countries have promoted the large-scale application of bagasse-based packaging products. Major sugarcane-producing countries such as the United States, Brazil, and India have widely adopted bagasse for producing disposable biodegradable tableware, food trays, and fast-food packaging containers, and have preliminarily formed industrial chains in the food, airline, and medical packaging sectors (Grand View Research, 2024; Hossam and Fahim, 2023; Stroescu et al., 2024). With the growing stringency of environmental regulations and the continued promotion of green consumption concepts, bagasse has become a key pathway for the resource utilization of agricultural waste in the food packaging sector (Singh et al., 2022; Fan and Bussracumpakorn, 2025). Particularly under the joint influence of "plastic restriction" and "dual-carbon" policies, bagasse-based containers have emerged as an ideal alternative to single-use plastic packaging, owing to their renewability, biodegradability, and low carbon footprint (Varghese et al., 2023). Currently, some domestic enterprises have mastered the core technology of molded bagasse pulp and have preliminarily achieved industrial-scale production. The products are widely applied in scenarios such as food delivery, fast food, and airline catering, with market acceptance continuously improving (Semple et al., 2022).

Despite the promising development momentum of the bagasse-based packaging industry, existing studies and industry practices still reveal several critical issues and research gaps:

(1) Lack of quantitative research on environmental impact from a complete life cycle

perspective. Most existing studies focus on the physical properties, molding processes, or mechanical optimization of bagasse packaging materials. However, there is a lack of systematic Life Cycle Assessment (LCA) analysis. Especially across the entire process—from raw material acquisition and manufacturing to transportation and end-of-life disposal—the environmental impacts of each stage lack comparative data support, making it difficult to provide comprehensive quantitative evidence for its green credentials.

(2) Lack of environmental comparison with other alternative materials (e.g., plastic, starch, composite packaging). Current research mostly takes a single-product perspective and rarely conducts full-process environmental performance comparisons between bagasse packaging and mainstream materials. As a result, it remains unclear how bagasse performs in terms of carbon emissions, resource consumption, and other indicators, limiting its wider promotion and policy endorsement.

(3) Lack of sensitivity analysis and optimization pathway research based on key process parameters. Although bagasse packaging holds strong potential for sustainability, its environmental performance is highly dependent on factors such as raw material composition, energy structure, and transportation methods. There is currently a lack of systematic sensitivity analysis to identify key influencing factors in the life cycle, and no multi-parameter coordinated optimization framework aimed at low-carbon improvement has been established, making it difficult to efficiently manage environmental burdens in real-world applications.

Table 1. Sugarcane planting data table for Laibin City, Guangxi

Year	Sugarcane Price (Yuan/Ton)	Cultivation Cost (Yuan/Mu)	Sugarcane Farmer's Income (Yuan/Mu)	Planting area (10,000 Mu)	Yield (Ton/Mu)	Total output (10,000 tons)	Sugarcane residue output (10,000 tons)	Government subsidy (Yuan/Mu)
2012	470	1,813.42	311	267.96	4.52	1,211.09	363.327	0
2013	475	1,992.61	154.39	260.43	4.52	1,267.47	380.241	0
2014	445	2,016.62	195.03	249.615	4.97	1,241.78	372.534	0
2015	400	2,122.29	13.71	225.315	5.34	1,204.78	361.434	0
2016	440	2,198.8	194.8	219.36	5.44	1,193.22	357.966	0
2017	480	2,317.47	548.13	205.83	5.97	1,229.11	368.733	0
2018	500	2,439.49	615.51	181.545	6.11	1,108.72	332.616	0
2019	490	2,394.37	589.73	177.975	6.09	1,083.20	324.96	0
2020	490	2,433.42	1,003.58	179.1	6.30	1,128.03	338.409	350
2021	490	2,545.46	720.04	178.89	5.95	1,066.25	319.875	350
2022	490	2,582.16	629.44	181.41	5.84	1,059.16	317.748	350
2023	510	2,615.00	907.6	183.015	6.26	1,145.73	343.719	330

2. METHODOLOGY

2.1 Life cycle assessment method and system boundary definition

Life Cycle Assessment (LCA) is a standardized environmental management tool used to quantify the potential environmental impacts of a product, process, or service throughout its entire life cycle (Hauschild et al., 2018). This study adopts the Life Cycle Assessment (LCA) method based on ISO 14040 and ISO 14044 standards to systematically evaluate the environmental impacts of sugarcane bagasse-based takeout containers throughout their entire life cycle, from raw material acquisition to final disposal. A representative manufacturing enterprise located in Laibin, Guangxi, China was selected as the case study. In LCA research, the definition of the system boundary is a fundamental step to ensure the integrity and scientific rigor of the assessment. It determines which processes, activities, and resource flows are included in the analytical scope, thereby directly influencing the accuracy and comparability of the environmental impact results. In accordance with ISO 14040 and ISO 14044, this study adopts a cradle-to-grave system boundary, comprehensively covering the resource inputs and environmental emissions involved in the entire process of bagasse takeout container production—from raw material extraction, manufacturing, and transportation to end-of-life disposal.

In Life Cycle Assessment (LCA), clearly defining the system boundary is essential for ensuring the completeness and accuracy of the environmental

evaluation, as it determines the scope of all included processes and flows (El Haouat et al., 2025). The system boundary includes four main stages (Figure 1). The first stage, raw material acquisition, covers the procurement and transportation of sugarcane bagasse, bamboo pulp, water-repellent agents, and oil-repellent agents. Sugarcane bagasse, as a by-product of sugar processing, is sourced from local sugar mills with a transportation distance set at 30 kilometers. The acquisition of bamboo pulp and chemical additives is also included in the evaluation of resource consumption and emissions. The second stage, production, involves pulp preparation, molding, hot pressing, trimming, drying, disinfection, and packaging, as well as the consumption of water and biomass fuel. The third stage, distribution, is represented by the delivery of takeout containers from the factory to the city center, with a transportation distance set at 10 kilometers. The fourth stage, disposal, adopts incineration as the main method of end-of-life treatment, in line with China's ongoing policy of restricting landfill usage, and includes the evaluation of greenhouse gases and other pollutants generated during the incineration process (Liu and Zheng, 2023).

Throughout all stages, the study considers inputs such as material flows (including raw materials, water resources, and biomass fuels) and energy flows (e.g., thermal energy), with outputs primarily consisting of the final product and environmental emissions (e.g., CO_2, SO_2, NO_x, particulate matter). Additionally, Figure 1 presents the system boundary as a flowchart, clearly outlining key activities and data collection points at each stage. The figure also indicates the six characterization indicators—Global Warming Potential (GWP), Acidification Potential (AP), Abiotic Depletion Potential (ADP), Eutrophication Potential (EP), Ozone Depletion Potential (ODP), and Photochemical Ozone Formation Potential (POFP)—and adopts the CML 2001 method for normalization and weighting to ensure that environmental impacts across each life cycle stage can be quantitatively and systematically assessed.

The functional unit of this study is defined as the production and disposal of "10,000 standard sugarcane bagasse takeout containers," a unit that reflects a practical production scale and serves as the basis for normalizing all input and output data. This functional unit was selected for its strong representativeness and operability, making it well-suited for actual production contexts and facilitating horizontal comparison with other types of containers such as those made from plastic, starch, or composite materials.

In Life Cycle Assessment (LCA), characterization translates inventory flows into environmental impacts, normalization contextualizes these impacts against a reference system, and weighting aggregates them based on relative importance, while sensitivity analysis identifies the parameters most influencing the results—together forming a robust basis for environmental decision-making (Heijungs and Huijbregts, 2004; Pizzol et al., 2017). To achieve a comprehensive environmental assessment, the study incorporates characterization, normalization, and weighting analysis methods, and further conducts sensitivity analysis to identify key influencing factors, thereby enhancing the robustness of the model. This LCA study provides quantitative evidence for evaluating the environmental performance of bagasse-based packaging and offers theoretical support for its optimization in green design and life cycle management.

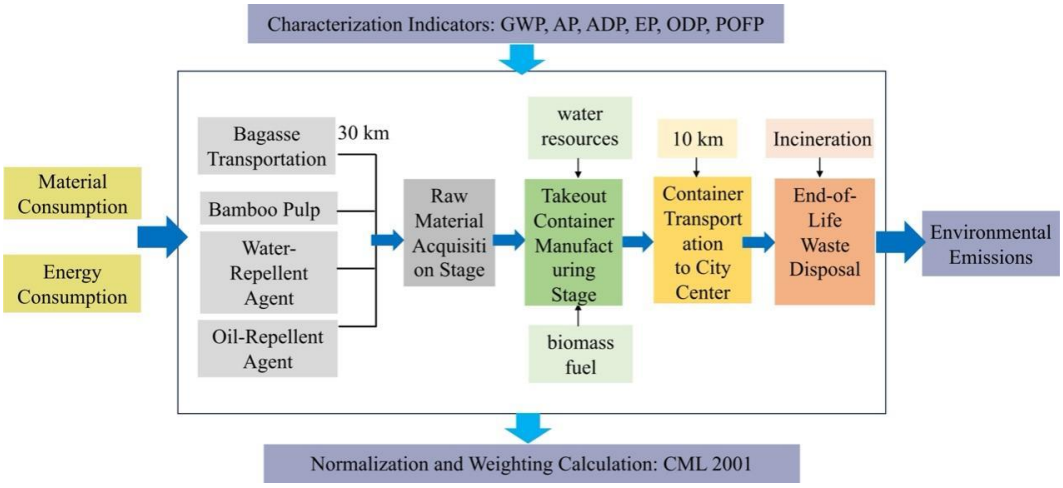

Figure 1. System boundary and life cycle flow of bagasse-based takeout container production

2.2 Life cycle inventory data

To comprehensively assess the environmental burden of bagasse containers, an LCI was developed within the cradle-to-grave boundary, covering all stages from material acquisition to final disposal. The functional unit is defined as the production and use of 10,000 sugarcane bagasse takeout containers. LCI data were primarily sourced from enterprise environmental reports, production records, and databases such as Ecoinvent and CLCD. Inputs include bagasse pulp, bamboo pulp, water-repellent and oil-repellent agents, biomass fuel, and water, as well as transport distances and emission factors. Emissions from boiler operations, including particulate matter, SO_2, and NO_x, are also considered. All data were standardized and unified in measurement units to serve as the basis for the Life Cycle Impact Assessment (LCIA) modeling. Detailed input-output data are shown in Table 2. The Life Cycle Inventory (LCI) data used in this study are primarily derived from 2024 enterprise environmental impact assessment reports, process records, and authoritative databases such as Ecoinvent and CLCD. Although no field investigation was conducted, cross-verification from multiple sources ensured the consistency and applicability of the data. As a major sugarcane-producing region, Laibin City exhibits industrial characteristics that are representative of Guangxi and other agricultural areas in southern China, making the developed model regionally applicable to a certain extent.

Table 2. Life cycle inventory of sugarcane bagasse takeout container production

Input/output	Item	Quantity
Input	Sugarcane bagasse pulp	207.83 kg
	Bamboo pulp	36.68 kg
	Biomass fuel	290.1 kg
	Water repellent agent	6.11 kg
	Oil repellent agent	2.69 kg
	Water	1,252.43 kg
	Transport distance of bagasse pulp	30 km
	Transport distance of containers	10 km
Output	Particulate matter (dust)	0.087 kg
	Sulfur dioxide (SO_2)	0.25 kg
	Nitrogen oxides (NO_x)	0.30 kg

2.3 Environmental impact assessment method and key factor identification

To enhance the systematization and comparability of the life cycle assessment, this study adopts the CML 2001 method to evaluate the environmental impacts of bagasse-based containers across six categories: Global Warming Potential (GWP), Acidification Potential (AP), Eutrophication Potential (EP), Abiotic Depletion Potential (ADP), Ozone Depletion Potential (ODP), and Photochemical Ozone Formation Potential (POFP). These categories cover key environmental burdens such as climate change, pollutant emissions, and resource depletion. Emissions data are converted into equivalent units (e.g., kg CO_2 eq) using characterization factors. Normalization and weighting are applied to improve cross-indicator comparability and interpretation. Normalization. After characterization, we normalized each impact category by dividing the LCIA result per functional unit by the CML 2001 "World" normalization factor for that category, yielding a dimensionless score that is comparable across categories (e.g., GWP=229 kg CO_2-eq per 10,000 units ÷ 4.22×10^{13} kg CO_2-eq·yr^{-1}=5.42×10^{-12}). The same procedure was applied to AP, EP, ADP, ODP, and POFP. Where an overall index is presented, we adopt equal weights (1/6 per category) for visualization only; all substantive comparisons rely on characterized and normalized results. Sensitivity analysis is also introduced to test the effects of variations in key input parameters, helping to identify major impact drivers and support low-carbon design and optimization strategies.

In the sensitivity analysis, a ±10% variation range is standard practice in LCA studies and is used to assess the model's robustness to parameter uncertainty. This range is consistent with ISO 14044's requirement to perform sensitivity analysis and with common LCA practice (Heijungs and Huijbregts, 2004), and it reflects the level of short-term variability

typically observed in industrial practice—specifically, variability in raw-material sourcing and production unit operations—which is generally on the order of 5-15%. Choosing 10% as a mid-point effectively identifies key parameters without introducing extreme bias, ensuring the practicality and comparability of the analysis. If the variation is too small (e.g., 5%), sensitivity may be underestimated; if too large (e.g., 20%), uncertainty may be overstated. The data in this study come from enterprise reports and databases, and the ±10% range is consistent with the variability observed in these sources.

3. RESULTS

3.1 Characterization results of environmental impact

To comprehensively assess the environmental impact of sugarcane bagasse-based takeout containers, this study adopts the CML 2001 method to conduct a characterization analysis across six key indicators: Global Warming Potential (GWP), Acidification Potential (AP), Eutrophication Potential (EP), Abiotic Depletion Potential (ADP), Ozone Depletion Potential (ODP), and Photochemical Ozone Formation Potential (POFP) (Figure 2).

The results show that GWP is the most significant impact, primarily due to incineration (55.56%), followed by bamboo pulp production (22.58%), both of which are closely associated with carbon emissions. The introduction of carbon capture and storage (CCS) systems and the replacement of fossil fuels with renewable energy are recommended. CCS is recommended primarily to capture and store CO_2 emissions released from the incineration stage, which is the dominant contributor to Global Warming Potential (GWP). By separating CO_2 from the flue gas and storing it underground, CCS directly mitigates greenhouse gas impacts without affecting other pollutants such as SO_2 or NO_x. In parallel, fuel substitution beyond fossil fuels is encouraged to further reduce life-cycle GWP, including the use of biomass residues from sugarcane and bamboo as boiler fuel, biogas from wastewater treatment, and electrification of low-temperature processes powered by renewable energy. These combined strategies can significantly decrease dependence on fossil fuels and enhance the overall carbon reduction potential of the production system. AP is mainly caused by boiler emissions (50%), suggesting the need for SNCR denitrification technology and real-time monitoring systems to reduce SO_2 and NO_x emissions. The SNCR (Selective Non-Catalytic Reduction) process reduces NO_x emissions by injecting ammonia or urea into the flue gas at 850-1,050°C, where it reacts with NO_x to form N_2 and H_2O. The typical removal efficiency ranges from 30-60%, depending on temperature, residence time, and mixing uniformity. Proper control of reagent dosage is essential to minimize ammonia slip and secondary pollution. The real-time monitoring system is not only for detecting emissions but also serves as a closed-loop control platform. Continuous emission monitoring systems (CEMS) with sensors for NO_x, SO_2, and O_2 provide feedback to automatically adjust reagent injection and combustion conditions, ensuring stable emission levels and reducing reagent waste. EP is concentrated in the bamboo pulping stage (28.49%), which can be mitigated through improved agricultural management and enhanced wastewater treatment. ADP is dominated by transportation (35.44%), indicating the need to adopt electric vehicles and localized production models to reduce fossil resource consumption. ODP mainly results from additives (32.52%) that may contain ozone-depleting substances like CFCs; thus, bio-based materials should be used as alternatives. POFP is driven by VOC emissions during bamboo pulp drying (33.06%), which can be addressed through VOC recovery systems and process optimization.

Incineration, bamboo pulp processing, boiler emissions, additives, and transportation are the main contributors to the environmental burden. The proposed optimization strategies—including low-carbon energy adoption, bio-based additives, cleaner production, and electric logistics—can support the sustainable and low-carbon development of bagasse-based packaging.

The optimization strategies derived from the LCA results focus on three key areas: adopting cleaner pulping and combustion technologies to reduce energy consumption and pollutant emissions identified in bamboo pulp and boiler processes; substituting bio-based and biodegradable additives to eliminate ozone-depleting substances and enhance product sustainability; and developing low-carbon logistics, including electric transport and localized supply chains, to mitigate abiotic depletion and reduce the overall carbon footprint. These targeted measures effectively address the environmental hotspots revealed by the life cycle analysis and form the foundation for the subsequent discussion.

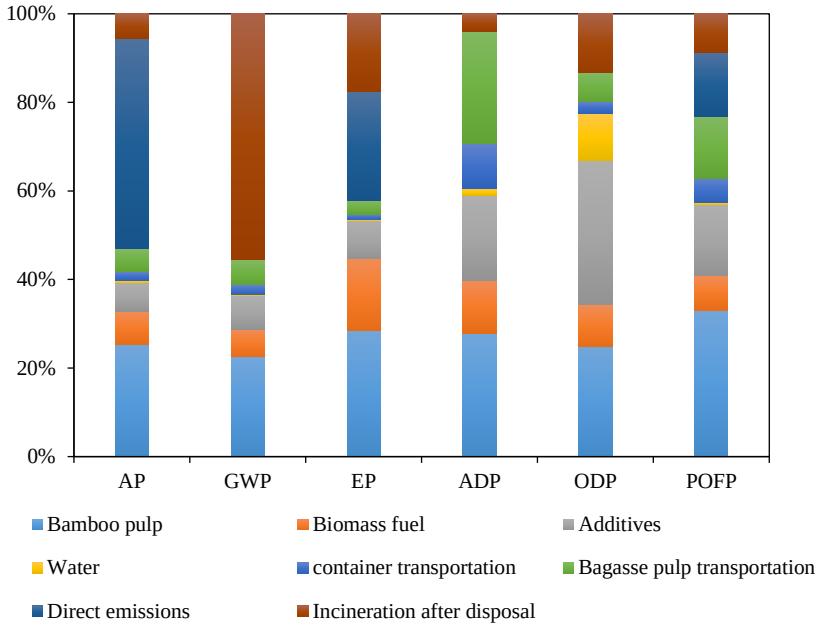

Figure 2. Contribution analysis of characterization results

3.2 Normalization and weighting analysis results

To further clarify the relative importance of different environmental impact categories in the life cycle of sugarcane bagasse takeout containers, this study conducted normalization and weighting analysis based on the CML 2001 method, aiming to identify key environmental burdens and provide optimization strategies.

The normalization results show that Global Warming Potential (GWP) is the most significant impact, with a normalized value of 5.42E-12, mainly due to CO_2 emissions from the incineration stage and fossil fuel use in bamboo pulp production. Ozone Depletion Potential (ODP) is the lowest, indicating a substantial reduction in CFC-containing additives, though residual risks in the supply chain require continued monitoring. Acidification Potential (AP) and Eutrophication Potential (EP) are mainly influenced by boiler emissions and wastewater from bamboo pulping, respectively. Abiotic Depletion Potential (ADP) and Photochemical Ozone Formation Potential (POFP) have relatively lower impacts but should still be considered in environmental optimization (Figure 3(a)).

The weighting analysis further highlights incineration (31.12%), bamboo pulp production (25.29%), and boiler emissions (15.87%) as the most critical stages in the life cycle. Although additives, fuel, and transportation showed significant differences during characterization, their impacts were balanced after weighting, revealing non-linear interactions among life cycle stages (Figure 3(b)). GWP accounted for 46.94% of the total weighted impact, making it the primary concern in environmental decision-making.

Normalization and weighting analysis revealed the environmental hotspots under current production and disposal conditions. These findings provide a scientific basis for promoting cleaner production, material substitution, and policy intervention, while further validating the environmental potential and optimization paths of sugarcane bagasse packaging in advancing low-carbon and sustainable development (Figure 3(c)).

3.3 Sensitivity analysis and key parameter identification

To identify the sensitivity of different raw materials and process parameters to the environmental impacts of sugarcane bagasse takeout containers throughout their life cycle, this study conducted a one-way sensitivity analysis by applying a ±10% variation to key input parameters. The results are shown in Figure 4.

The analysis reveals that bamboo pulp has the highest sensitivity coefficient (0.253), significantly higher than other factors, indicating that its pulping process has the most substantial impact on environmental burdens. It is therefore recommended to prioritize low-energy pulping technologies and optimize raw material sourcing to reduce its environmental footprint. Additives (0.089) and biomass fuel (0.086) follow in sensitivity. Additives

are influenced by potential ozone-depleting substances in chemical coatings, suggesting an urgent need to develop bio-based water- and oil-resistant alternatives. Biomass fuel sensitivity is linked to boiler emissions; thus, improving combustion efficiency and flue gas treatment could effectively lower environmental impacts.

(a) Comparison of normalized results for different indicators

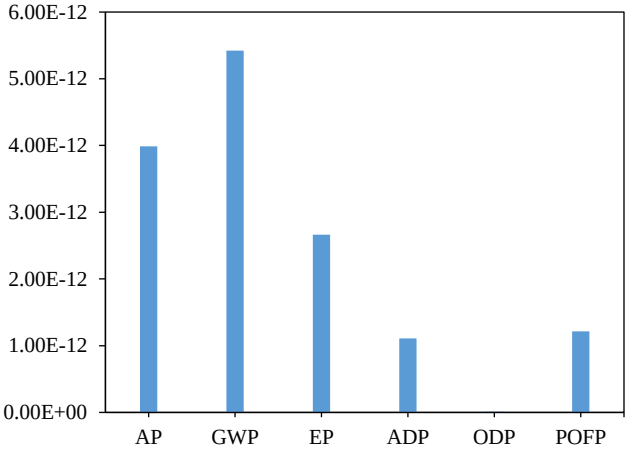

(b) Contribution of each life cycle stage to the weighted overall environmental impact

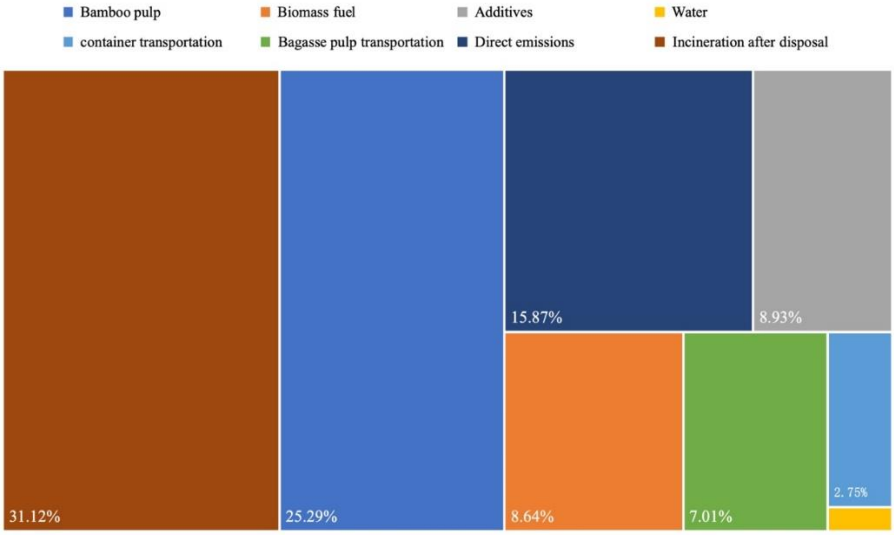

(c) Contribution of Each Impact Category to the Weighted Overall Environmental Impact

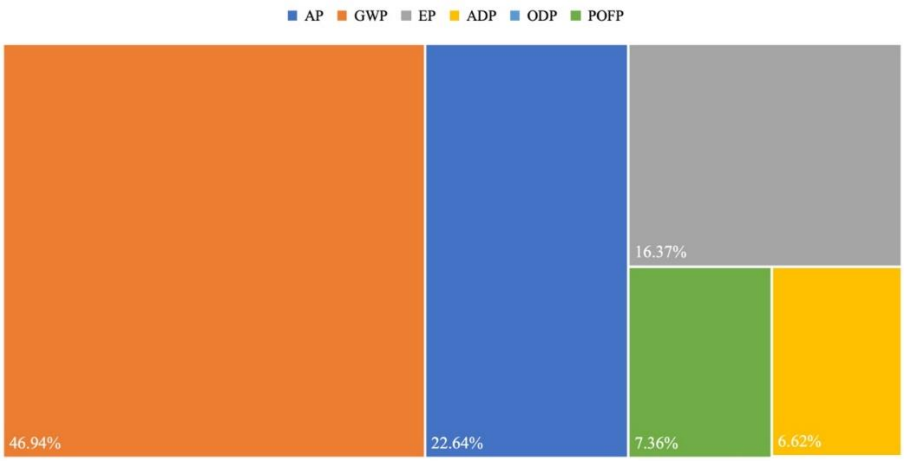

Figure 3. Normalization and weighting results

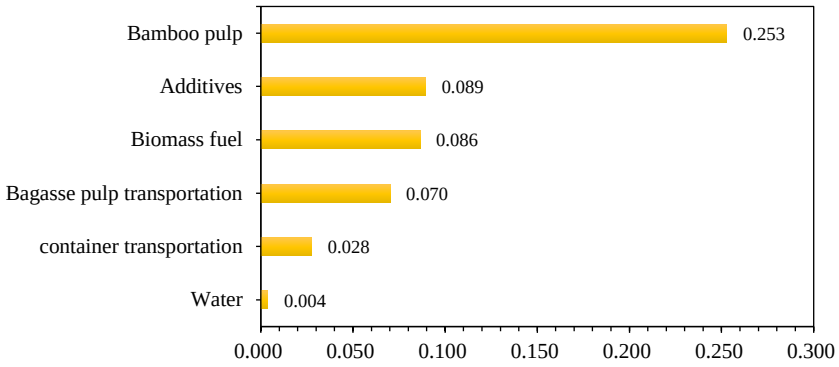

Figure 4. Sensitivity analysis results

In contrast, transport-related parameters and water use exhibit lower sensitivity (bagasse pulp transportation: 0.070; container transportation: 0.028; water use: 0.004), indicating limited optimization potential. However, improvements in these areas should still be pursued in conjunction with regional industrial planning and green logistics strategies.

The priority order for environmental optimization is: bamboo pulp processing > additive substitution > boiler emissions control > transportation and water management. This sensitivity analysis identifies the key impact factors and provides strategic guidance for process improvements and eco-design of bagasse-based packaging. In this study, the ±10% variation range for input parameters was determined based on the actual fluctuations observed in current industrial processes and raw material procurement, aligning with common variability in real-world operations. Although on-site data and authoritative databases were used as much as possible for model construction, some upstream and downstream processes—such as bamboo pulp sourcing and additive composition—still involve a degree of uncertainty. Sensitivity analysis helps assess the model's responsiveness to these variations, thereby enhancing the robustness and interpretability of the LCA results.

3.4 Comparative environmental impacts of different container materials

To clarify the environmental advantages of sugarcane bagasse takeout containers, this study conducted a comprehensive life cycle comparison with plastic, starch-based, and composite starch containers across six key environmental impact categories (Figure 5).

The results show that bagasse containers performed best in all indicators. For Global Warming Potential (GWP), the bagasse container recorded only 229 kg CO_2 eq—81.67%, 70.69%, and 82.52% lower than plastic, starch, and composite starch containers, respectively. Acidification Potential (AP) was 0.953 kg SO_2 eq, just about one-seventh of that of composite starch. Eutrophication Potential (EP) reached 0.421 kg PO_4^{3-} eq, 87.22% lower than composite starch. Regarding resource consumption, the Abiotic Depletion Potential (ADP) was only 0.401×10^{-3} kg Sb eq, significantly lower than that of other materials. In terms of Ozone Depletion Potential (ODP), bagasse containers achieved the lowest value at 0.261×10^{-5} kg CFC-11 eq. Photochemical Ozone Formation Potential (POFP) was also the lowest at 0.448×10^{-1} kg ethylene eq.

The normalization and weighting analysis (Figure 6) further confirmed the environmental superiority of bagasse containers, with an overall impact value of just 1.075×10^{-10}—81.03%, 74.20%, and 85.65% lower than that of plastic, starch, and composite starch containers, respectively. In contrast, composite starch containers, despite being labeled as "green materials," showed significantly higher impacts due to the use of high-burden inputs, highlighting the risks of "false green" alternatives.

Sugarcane bagasse containers—made from agricultural and forestry waste—demonstrate clear advantages in carbon reduction, energy efficiency, and pollution control, making them a promising solution for green transformation in the packaging industry. Future efforts should focus on technological innovation and policy incentives to expand their market adoption while remaining cautious of environmentally harmful materials disguised as sustainable options.

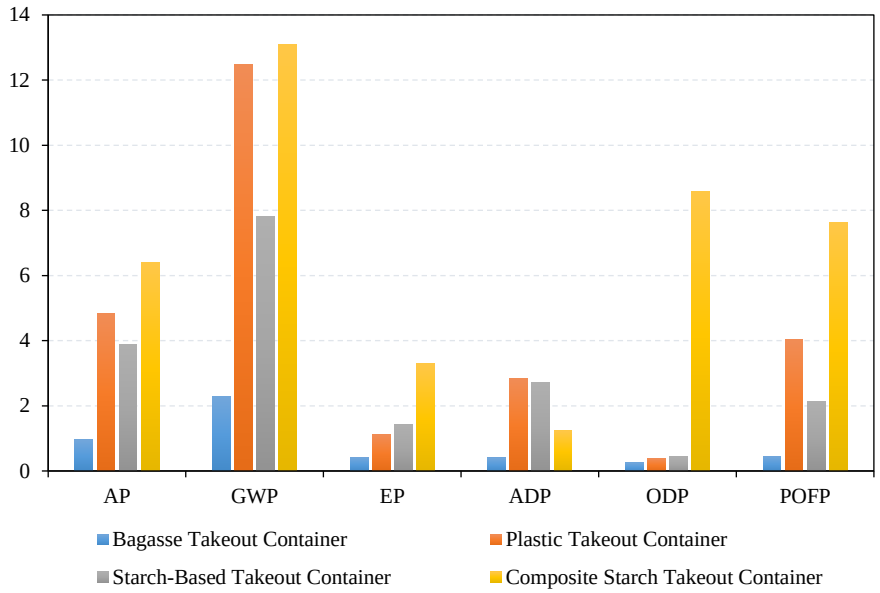

Figure 5. Characterization of environmental impacts for different container materials (Units: GWP (kg CO_2-eq), AP (kg SO_2-eq), EP (kg PO_4^{3-}-eq), ADP (kg Sb-eq $\times 10^{-3}$), ODP (kg CFC-11-eq $\times 10^{-5}$), POFP (kg ethene-eq $\times 10^{-1}$)).

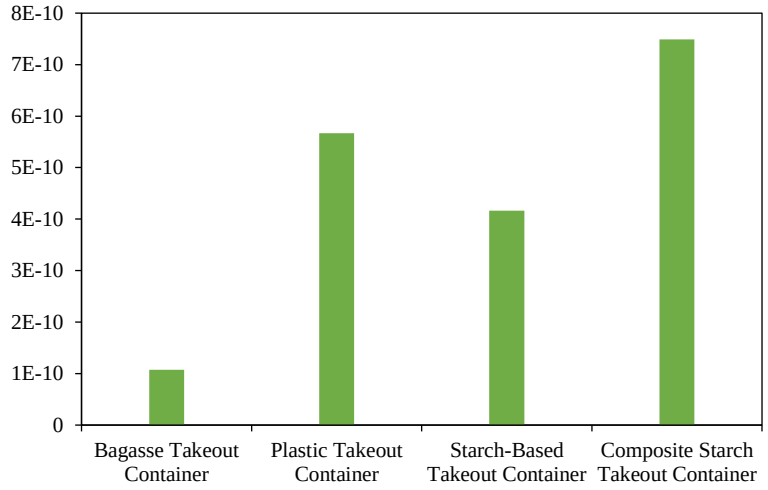

Figure 6. Comparative normalized and weighted environmental impacts of different container

4. DISCUSSION

The results of this life cycle assessment (LCA) highlight the superior environmental performance of sugarcane-bagasse takeout containers relative to conventional alternatives, particularly in reducing Global Warming Potential (GWP) and Abiotic Depletion Potential (ADP) by more than 70%. However, to validate these conclusions and enhance their practical relevance, it is necessary to examine real-world applications and policy implementations that demonstrate the feasibility and scalability of bagasse packaging. This section expands the policy implications by integrating empirical case studies, comparative LCA validations from analogous biomass-based systems, and strategic recommendations grounded in ongoing initiatives in China and Southeast Asia. By applying the LCA findings to these contexts, we confirm the robustness of the model and identify pathways for broader adoption within a circular-economy framework.

4.1. Application-based empirical validation and case studies

The LCA model in this study, based on a representative enterprise in Laibin, Guangxi, is consistent with broader empirical evidence regarding sugarcane bagasse in packaging and waste management. For example, in Southeast Asia, the SWITCH-Asia “Only One Planet” initiative reportedly replaced more than 4 million foam food boxes with

household-compostable sugarcane-based products in food service, significantly reducing non-biodegradable waste. This initiative corroborates the end-of-life benefits emphasized in our LCA: compared with plastic landfilling, incineration of bagasse containers contributes lower GWP; the project's waste-diversion efforts have led to measurable reductions in greenhouse-gas emissions and improved resource recovery within circular systems.

In China, analogous applications in food packaging support our findings on the integrated "sugar mill-pulp mill-container factory" model. Case studies by Bioleader Packaging show how bagasse tableware (including trays and containers) has been implemented in commercial settings, yielding benefits such as reduced waste and enhanced compostability. Practical performance tests for lidded bagasse trays—including strength evaluations and food-safety assessments—confirm the material's durability during production and use and its low environmental burden, aligning with our sensitivity analysis that identified bamboo pulp and additives as hotspots. These applications validate the model's prediction of >70% reduction in environmental burden, as independent comparative LCAs in related studies indicate that, when recovery is included, bagasse outperforms expanded polystyrene in categories such as eutrophication and acidification.

Moreover, global validations from LCAs of biomass-based packaging reinforce our conclusions. A systematic review of sugarcane-bagasse utilization—including packaging—highlights similar environmental effects, such as carbon-footprint reductions through valorization of agricultural residues, reflecting our cradle-to-grave boundary. Within food and beverage applications, LCAs show that biomass-derived materials like bagasse can reduce greenhouse-gas emissions by up to 25% relative to conventional plastics, providing quantitative support for our comparative results among plastic, starch, and composite-starch containers. These real-world validations address uncertainties identified in our sensitivity analysis for upstream processes (e.g., bamboo-pulp sourcing), as field implementations—such as low-energy pulping—have been shown to effectively mitigate these hotspots.

4.2 Policy implications and strategic recommendations

Building on these validations, policy efforts should prioritize coordinated actions along the value chain to enable large-scale adoption. In China, the 14th Five-Year Plan for Plastic Pollution Control provides a framework for promoting bagasse packaging. As demonstrated in Guangxi, implementation integrates agricultural residues into the circular economy. To strengthen source control, policies can mandate designated collection systems for resources such as bagasse, similar to centralized processing in ASEAN member states, which enhances feedstock stability and reduces waste. This approach validates our LCA's replicability across South China and Southeast Asia, where sugarcane hubs like Laibin can export the integrated model to regions with comparable agricultural profiles.

For process optimization, investment in clean pulping technologies and eco-friendly functional additives is essential. Case studies from sustainable-packaging alliances indicate that adopting bio-based substitutes reduces ODP and POFP impacts, consistent with our weighted analysis. Governments should incentivize R&D through subsidies and encourage firms to form synergies under the "sugar mill-pulp mill-container factory" model, which has demonstrated enhanced resource efficiency in real-world biofuel and packaging applications.

At end-of-life, establishing low-carbon logistics and recycling mechanisms is necessary. India's national circular-economy roadmap for reducing plastic waste offers parallel experience for Southeast Asia, emphasizing carbon labeling and green procurement to realize environmental value. In China, including bagasse containers in government procurement catalogues can accelerate market uptake, as studies show biodegradable alternatives can mitigate pollution from takeaway services. Promoting new-energy vehicles and centralized distribution—recommendations consistent with our optimization strategy—aligns with ASEAN's eco-friendly packaging ecosystems, in which such measures decrease transport-related ADP.

By applying the LCA conclusions to these validated applications, this study confirms the potential of bagasse packaging to drive green transitions. Future research should focus on longitudinal case studies to monitor long-term impacts and ensure that policies evolve with emerging data on biomass valorization. This integrated approach not only substantiates our findings but also positions sugarcane bagasse as a core sustainable material within the circular economy.

5. CONCLUSION

Using a representative manufacturing enterprise in Laibin, Guangxi, China, as a case study, this study employs life cycle assessment (LCA) to systematically evaluate the full life-cycle environmental impacts of sugarcane bagasse takeout containers. Using the CML 2001 framework, six key environmental indicators were assessed: Global Warming Potential (GWP), Acidification Potential (AP), Eutrophication Potential (EP), Abiotic Depletion Potential (ADP), Ozone Depletion Potential (ODP), and Photochemical Ozone Formation Potential (POFP). The results demonstrate that bagasse-based containers outperform conventional plastic, starch, and composite starch containers in all assessed categories. Notably, the advantages in GWP and ADP are particularly significant, with overall environmental burdens reduced by more than 70% compared to traditional materials. This confirms the feasibility of sugarcane bagasse packaging as a low-carbon, biodegradable, and resource-efficient alternative. However, environmental hotspots remain within the product life cycle, particularly in bamboo pulp production, biomass combustion, and incineration at the end-of-life stage. Sensitivity analysis further identifies bamboo pulp input, additive use, and boiler fuel as the key contributors to environmental impact. Therefore, future optimization efforts should focus on adopting cleaner pulping technologies, substituting green additives, improving biomass combustion efficiency, and developing low-carbon logistics systems.

Additionally, this study examines the regional scalability of bagasse packaging. As one of China's major sugarcane-producing areas, Laibin has implemented an integrated "sugar mill-pulp mill-container factory" model that improves resource efficiency and reduces environmental load. This model holds potential for replication across other agricultural regions in South China and Southeast Asia.

To promote the large-scale adoption of bagasse-based packaging, policy measures should focus on three coordinated areas: (1) Source control—ensuring stable supply of agricultural residues and promoting regional resource utilization; (2) Process optimization—enhancing investment in clean technologies, modular equipment, and industrial collaboration; (3) End-of-life management—developing green logistics and recycling systems, and establishing carbon labeling and green procurement standards. Overall, sugarcane bagasse packaging demonstrates strong potential for low-carbon innovation and is poised to play a key role in the green transformation of the packaging industry and the advancement of the circular economy. Looking ahead, continuous efforts in technological innovation, policy incentives, and regional cooperation will be essential to amplify its environmental and economic benefits, supporting the dual goals of sustainable materials development and green industry transition.

AUTHOR CONTRIBUTIONS

Conceptualization, Methodology, Investigation, Data Curation, Formal Analysis, and Writing-Original Draft: Meng Fan. Supervision and Writing-Review and Editing: Chokeanand Bussracumpakorn.

DECLARATION OF CONFLICT OF INTEREST

The authors disclosed no conflict of interest.

REFERENCES

Arfelli F, Roguszewska M, Torta G, Iurlo M, Cespi D, Ciacci L, et al. Environmental impacts of food packaging: Is it all a matter of raw materials? Sustainable Production and Consumption 2024;49:318-28.

Barasa Kabeyi M, Olanrewaju O. Sugarcane bagasse and cane trash as a fuel. In: Proceedings of the 4th Asia Pacific International Conference on Industrial Engineering and Operations Management. Ho Chi Minh City, Vietnam: IEOM Society International; 2023.

Cruz RMS, Krauter V, Krauter S, Agriopoulou S, Weinrich R, Herbes C, et al. Bioplastics for food packaging: Environmental impact, trends and regulatory aspects. Foods 2022; 11(19):Article No. 3087.

Debnath M, Sarder R, Pal L, Hubbe MA. Molded pulp products for sustainable packaging: Production rate challenges and product opportunities. BioResources 2022;17(2):3810-70.

El Haouat Z, Essalih S, Bennouna F, Amegouz D. Development of a global framework for an integrated life cycle assessment (LCA) model in quality, safety and environmental (QSE) management systems: Improving environmental, social and economic sustainability performance. Sustainability 2025; 17(8):Article No. 3521.

Fan M, Bussracumpakorn C. The influence path of industry collaboration network and policy support on the optimization of sugarcane bagasse packaging value chain: An empirical study based on structural equation modeling. International Journal of Sustainable Development and Planning 2025;20(6):2409-24.

Fürst K, Feng Y. China's regulatory respond to plastic pollution: Trends and trajectories. Frontiers in Marine Science 2022;9:Article No. 982546.

Grand View Research. Biodegradable Tableware Market (2024-2030). San Francisco (CA): Grand View Research, Inc.; 2024.

Hauschild M, Rosenbaum R, Olsen S. Life Cycle Assessment: Theory and Practice. Cham: Springer; 2018.

Heijungs R, Huijbregts M. A review of approaches to treat uncertainty in LCA. In: Proceedings of the 2nd International Congress on Environmental Modelling and Software; 2004 June 14-17; University of Osnabrück, Germany: 2004.

Hossam Y, Fahim IS. Towards a circular economy: Fabrication and characterization of biodegradable plates from sugarcane waste. Frontiers in Sustainable Food Systems 2023;7:Article No. 1220324

Janika AS, Afrrin M, Rahul R, Thirumoorthy S, Karthik P. Valorization of sugarcane bagasse in food packaging. In: Agro-wastes for Packaging Applications. 1st ed. Boca Raton: CRC Press; 2024.

Liu C, Luan P, Li Q, Cheng Z, Sun X, Cao D, et al. Biodegradable, hygienic, and compostable tableware from hybrid sugarcane and bamboo fibers as plastic alternative. Matter 2020;3(6):2066-79.

Liu J, Zheng L. Structure characteristics and development sustainability of municipal solid waste treatment in China. Ecological Indicators 2023;152:Article No. 110391.

Lu P, Zhou Y, Liu Q, Guan A, Yang Z. A high resolution gridded dataset for takeaway packaging waste in China. Scientific Data 2025;12(1):Article No. 600.

Pizzol M, Laurent A, Sala S, Weidema B, Verones F, Koffler C. Normalisation and weighting in life cycle assessment: Quo vadis? International Journal of Life Cycle Assessment 2017;22(6):853-66.

Semple KE, Zhou C, Rojas OJ, Nkeuwa WN, Dai C. Moulded pulp fibers for disposable food packaging: A state-of-the-art review. Food Packaging and Shelf Life 2022;33:Article No. 100908.

Singh RV, Sharma P, Sambyal K. Application of sugarcane bagasse in chemicals and food packaging industry: Potential and challenges. Circular Economy and Sustainability 2022;2(4):1479-500.

Stroescu M, Marc AR, Mureșan CC. A comprehensive review on sugarcane bagasse in food packaging: Properties, applications, and future prospects. Hop and Medicinal Plants 2024;32(1-2):169-84.

Thongsomboon W, Baimark Y, Srihanam P. Valorization of cellulose-based materials from agricultural waste: Comparison between sugarcane bagasse and rice straw. Polymers 2023;15(15):Article No. 3190.

Varghese SA, Pulikkalparambil H, Promhuad K, Srisa A, Laorenza Y, Jarupan L, et al. Renovation of agro-waste for sustainable food packaging: A review. Polymers 2023; 15(3):Article No. 648.

Zhang Y, Wen Z. Mapping the environmental impacts and policy effectiveness of takeaway food industry in China. Science of the Total Environment 2022;808:Article No. 152023.

Environment and Natural Resources Journal

Volume 24
Issue 2
2026

Catalytic Ozonation with ZnO Nanoparticles: A Novel Approach to Lignin Degradation in Synthetic Wastewater

Yupaporn Amnath and Chatchaval Aiyathiti*

Department of Environmental Engineering, Faculty of Engineering, Khon Kaen University, Khon Kaen 40002, Thailand

ARTICLE INFO

Received: 11 Jan 2025
Received in revised: 16 Oct 2025
Accepted: 21 Oct 2025
Published online: 24 Nov 2025
DOI: 10.32526/ennrj/24/20250017

Keywords:
Catalytic ozonation/ Lignin degradation/ Zinc Oxide

*** Corresponding author:**
E-mail: chapiy@kku.ac.th

ABSTRACT

The purpose of this study is to evaluate ZnO nanoparticle-catalyzed ozonation degradation lignin in synthetic wastewater. By applying response surface methodology (RSM) and central composite design (CCD), we analyzed the interaction between key factors and optimized their conditions. pH, ZnO dose, time, and lignin concentration were varied and encoded into a second-order model, with ANOVA confirming its significance (F-value=19.53). The model predicted a 99.99% lignin degradation efficiency under optimal conditions: pH 11, 1.0 g ZnO, 50 minutes, and 50 mg/L lignin. The high correlation (R^2=0.9480) validated the model, highlighting the effectiveness of ZnO nanoparticle-catalyzed ozonation for lignin removal.

HIGHTLIGHTS

This study used response surface methodology (RSM) with central composite design (CCD) to optimize key factors in the catalytic ozonation process with ZnO nanoparticles. The effects of pH, ZnO dosage, time, and lignin concentration on lignin decolorization were evaluated, with pH and catalyst dosage found to be the most influential factors.

1. INTRODUCTION

Ozone is increasingly used in wastewater treatment for organic contaminants, breaking bonds through two mechanisms: direct reaction with organic substances via electrophilic or cyclo-dipolar addition (direct ozone) and indirect reaction via free radicals like hydroxyl, superoxide, and hydrogen peroxyl radicals. These reactions reduce large polymer molecules or break double/triple bonds into single ones. The global pulp and paper sector generates more than fifty million tons of lignin each year, a thick black liquid that can't be directly released into water (Haqa et al., 2020; Kumar et al., 2021). Lignin is a complex polymer made of carbon-carbon bonds, with components like thiol, sulfide, and phenolic groups (hydroxyl, methoxy, carboxylic, and carbonyl). Derived from monolignols, lignin exhibits biological activities such as antioxidant and antimicrobial properties, which vary based on plant source.

Many researchers have developed advanced oxidation processes (AOPs) for lignin wastewater treatment to manage large organic compounds by breaking double bonds and reducing color (Zhou et al., 2023). AOPs, which generate hydroxyl radicals (˙OH), efficiently degrade pollutants by reacting with functional groups, double bonds, and aromatic carbons (Einaga et al., 2024; Nawrocki and Kasprzyk-Hordern, 2010). The catalytic ozone process (COP), an effective AOP for degrading organic matter and lignin, involves metal oxide catalysts reacting with ozone to produce superoxide radicals, which generate hydroxyl radicals (˙OH) that non-selectively degrade organic matter (Mao et al., 2025). COP enhances ozone efficiency, reduces by-products, and lowers treatment costs by accelerating oxidation and reducing contact time (Einaga et al., 2024). Common catalysts include TiO_2, MnO_2, Al_2O_3, CuO, MgO, and others, which boost radical generation and reaction rates (Li et al., 2023; Mohammadi et al., 2016).

The effectiveness of catalytic ozonation depends on several factors, including the pH of the solution, pollutant type, catalyst amount, ozone

Citation: Amnath Y, Aiyathiti C. Catalytic ozonation with ZnO nanoparticles: A novel approach to lignin degradation in synthetic wastewater. Environ. Nat. Resour. J. 2026;24(2):162-173. (https://doi.org/10.32526/ennrj/24/20250017)

exposure time, and pollutant concentration. Catalytic ozonation is divided into homogeneous and heterogeneous types, the heterogeneous ozonation being a new AOP that enhances ozone generation in the presence of effective hydroxyl radical scavenging catalysts. COP is an economical wastewater treatment method because of its catalyst recoverability and low secondary contamination. Its catalytic mechanisms enhance free radical generation, facilitate singlet oxygen release, and improve the adsorption of ozone and organic molecules on the catalyst surface.

Zinc oxide (ZnO) is a cost-effective, non-toxic, and ecologically benign heterogeneous catalyst capable of degrading diverse organic pollutants, frequently employed in wastewater treatment. A primary application is ozone decomposition, originally utilized for oxidizing various organic compounds in the liquid phase. The well-developed surface, a characteristic feature of nanomaterials, plays a significant role in advancing catalysis. The reduction in average particle size and the corresponding increase in specific surface area enhance the number of active sites available for reactions. A limited number of publications have explored the use of ZnO catalyst for ozone decomposition and the removal of organic pollutants. However, other authors have not studied the use of zinc oxide as a catalyst in combination with ozone for lignin degradation.

2. METHODOLOGY

2.1 Materials

Stock solution containing soda lignin (Lignin Alkaline, Molecular Formula $C_{30}H_{25}SO_4$) Cas. No. 8068-05-1 (Tokyo Chemical Industry Co., LTD) at 1,000 mg/L. ZnO powder particle size 25 nm (XRD analysis) obtained from the Agricultural Nano Research Center, King Mongkut's University of Technology Thonburi, sodium hydroxide (AR grade, Ajax Finechem, Australia) at 0.01 M adjusted for pH level each condition and nitric acid (AR grade, Ajax Finechem, Australia) at 0.01 M.

Catalyst preparation and characterization; zinc oxide (ZnO) nanopowder (25-50 nm) supplied by the Agricultural Nanotechnology Center, King Mongkut's Institute of Technology, Thailand, was used as the catalyst. ZnO was immobilized onto river gravel (1-3.5 mm diameter) by a sol-gel coating technique. Briefly, ZnO powder was suspended in a water-methanol mixture (1 g catalyst per 20 mL solution), and the pH was adjusted to 3.0±0.1 with 1 N nitric acid. Gravel substrates were immersed in the ZnO suspension for 1 min, air-dried at room temperature for 12 h, and subsequently calcined at 500°C for 2 h. After calcination, the coated gravel was cooled, rinsed with distilled water to remove loosely bound particles, dried at 104±1°C for 6 h, and stored in a desiccator prior to use.

The ZnO loading on the gravel support was determined according to Equation (1):

$$X_{Zn} = X_{S+Zn} - X_S \quad (1)$$

Where; X_{Zn} represents the net ZnO loading (g), X_S is the initial weight of the support (g), X_{S+Zn} is the total weight of ZnO and support after calcination (g).

The crystallographic structure of immobilized ZnO was analyzed using X-ray diffraction (XRD). Surface morphology and elemental composition were characterized by scanning electron microscopy (SEM) coupled with energy-dispersive X-ray spectroscopy (EDS). These analyses were performed to confirm the presence, distribution, and stability of ZnO on the gravel substrates for subsequent lignin decolorization experiments.

2.2 Experimental apparatus and procedure

Ozonation experiment included an oxygen gas generator, ozone generator (Biozone ozone generator 5 g/h, MMS Engineering Co. Ltd. Thailand) for production of ozone. The ozone flow rate was 7.0 L/min (ozone production was 23.4 mg O_3/min, Figure 1). The laboratory scale ozone batch reactor is borosilicate glass 1.0 L (inner diameter 0.16 m, height 0.50 m). The ozone gas concentration at the outlet was measured using an ozone trap reactor containing 50 mL of acidified 2.0% KI solution for determination of unreacted ozone. Table 1 presents the average characteristics of the influent wastewater. The concentration of ozone in the gas was measured by the iodometric titration method. The experimental setup utilized a 1.0 L bottle containing of 50, 100, and 150 ppm lignin synthetic solution. Each trial conducted in a batch setup over a 60-minute period. At the end of each trial, 30 mL of samples were collected through a tube with an installed valve at the bottom of the bottle, stored at 4°C, and analyzed on the same day as the treatment. The experiments were performed at room temperature (30±1°C) in 1.0 L of lignin synthetic wastewater solution under batch condition. The bottom of the reactor was equipped with gas diffusers to produce fine ozone bubbles. The parameters

influencing lignin degradation include solution pH, ZnO dosage, ozone exposure time, and initial lignin concentration. Samples were taken at specified reaction times to determine the residual lignin concentration. The lignin degradation rate was calculated by using Equation 2, where C_t is the lignin concentration at a given time (t), and C_0 is the initial lignin concentration.

$$\text{Degradation rate (\%)} = \frac{(C_0 - C_t) \times 100}{C_0} \quad (2)$$

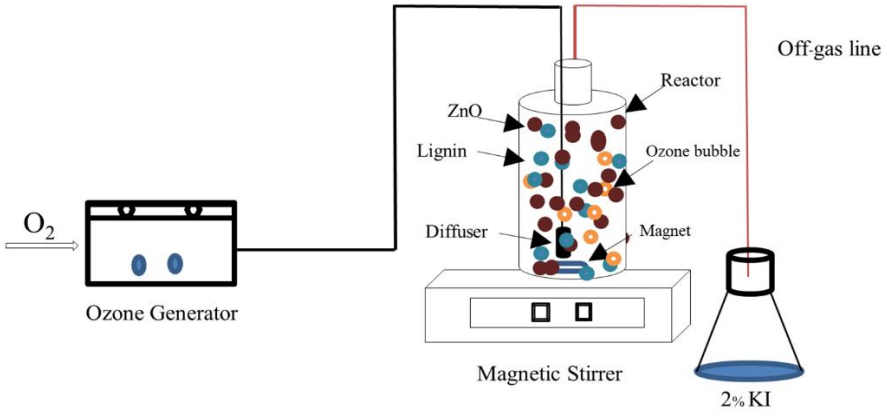

Figure 1. Schematic diagram of lignin degradation in a catalytic ozonation (ZnO) batch reactor

2.3 Analytical methods

Lignin degradation refers to the color concentration analyzed using a spectrophotometer (DR6000, Hach) following the ADMI method, and pH solution measured by Knick 761 pH-Meter Calimatic.

2.4 Experimental design

This study employed a factorial Central Composite Design (CCD) with four levels and a full CCD with three levels, guided by RSM (Hanapi et al., 2021). A total of thirty experimental evaluations were used, consisting of eight axis points, sixteen factorial points, and six center points. These experiments were designed to optimize key variables: pH, ZnO dosage, time, and initial lignin concentration. The experimental parameters and levels used CCD for this study were determined and shown in Table 1.

Optimization of the process involves calculating coefficients, predicting responses, and verifying the developed model. The response expressed using Equation 3:

$$Y=\beta_o+\sum_{i=1}^{n}\beta_i X_i+\sum_{j=1}^{n}\beta_{ii}X_i^2+\sum_{i=j}^{n-1}\sum_{i=j+1}^{n}\beta_{ij}X_iX_j+E \quad (3)$$

Where; Y is the response (removal efficiency, %); β_0 represents the regression coefficient; β_i, β_{ii}, and β_{ij} correspond to the linear, quadratic, and interaction coefficients; X_i and X_j correspond to the coded values independent process factors, and E is the experimental or residual error. Equation 3 shows the correlation between independent variables in coded values and predicted response based on Tables 1 and 2.

In addition, ANOVA analysis was used to assess the significance of the quadratic regression model using p-values at the 95% confidence level. Coefficient parameters were RSM analyzed using Minitab 19.

Table 1. Parameters, symbol, and coded values used in the CCD for lignin degradation using ZnO catalysis ozonation.

Parameters	Symbol	Actual and coded values		
		-1	0	+1
pH	A	5	8	11
ZnO dose (mg/L)	B	1	2	3
Ozonation time (min)	C	1	30	60
Lignin concentration (mg/L)	D	50	100	150

Table 2. Experimental design of lignin degradation experiment

Run	A	B	C	D	Efficiency (%)	
					Experiment	Predicted
1	8	2	0	100	0.10	22.42
2	8	4	27.5	100	83.15	74.81
3	8	2	27.5	0	99.99	93.59
4	8	2	72.5	100	72.00	91.88
5	8	2	27.5	100	69.30	71.17
6	8	2	27.5	100	72.00	71.17
7	2	2	27.5	100	50.00	31.29
8	8	2	27.5	200	69.00	72.27
9	8	0	27.5	100	45.80	51.00
10	14	2	27.5	100	7.72	23.30
11	8	2	27.5	100	67.30	71.17
12	5	1	5.0	150	5.41	18.54
13	8	2	27.5	100	73.00	71.17
14	8	2	27.5	100	72.80	71.17
15	5	3	50.0	50	90.50	93.18
16	5	3	5.0	50	20.27	31.18
17	5	1	5.0	50	8.98	21.45
18	11	3	5.0	150	25.00	32.54
19	11	1	5.0	150	15.40	9.25
20	11	3	5.0	50	23.00	30.69
21	11	1	5.0	50	10.00	10.65
22	5	3	50.0	150	65.00	73.25
23	5	3	5.0	150	24.00	31.52
24	11	1	50.0	50	94.64	83.65
25	11	3	50.0	50	98.70	94.47
26	5	1	50.0	50	91.30	92.66
27	11	1	50.0	150	64.00	61.99
28	5	1	50.0	150	80.64	69.49
29	8	2	27.5	100	70.30	71.17
30	11	3	50.0	150	90.00	76.06

3. RESULTS AND DISCUSSION

3.1 Catalyst characterization

Zinc oxide (ZnO) was successfully immobilized on gravel supports via a modified sol-gel method. The XRD pattern of the ZnO/gravel composite (Figure 2) confirmed the formation of ZnO crystals, consistent with earlier reports (Hayat et al., 2011; Zhao et al., 2025). No extraneous peaks were observed, indicating the high purity of the ZnO phase. The XRD analysis revealed that ZnO crystallized in the hexagonal wurtzite structure with a polycrystalline nature, while high-resolution transmission electron microscopy (HR-TEM) indicated a particle size distribution of 32-37 nm.

Morphological characteristics were examined using SEM (Figure 3). SEM images showed distinct ZnO coatings on the gravel surface prior to lignin degradation (Figure 3(a)). After 60 min of ozonation with lignin solution, morphological changes were evident on the ZnO-coated surface (Figure 3(b)), while uncoated gravel was used as a control (Figure 3(c)).

XRF spectroscopy was employed to confirm ZnO immobilization. The Zn content of the catalyst was 0.207% (equivalent to 0.257% ZnO) after impregnation, verifying the successful loading of ZnO onto the gravel support (Table 3).

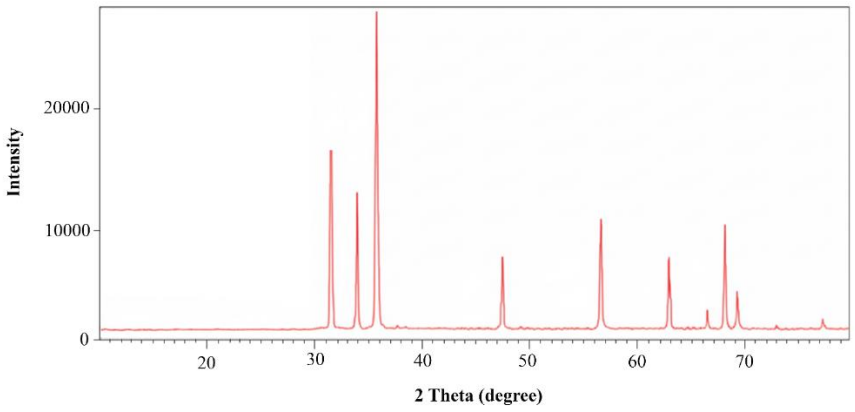

Figure 2. XRD pattern of ZnO catalysts prior to lignin degradation

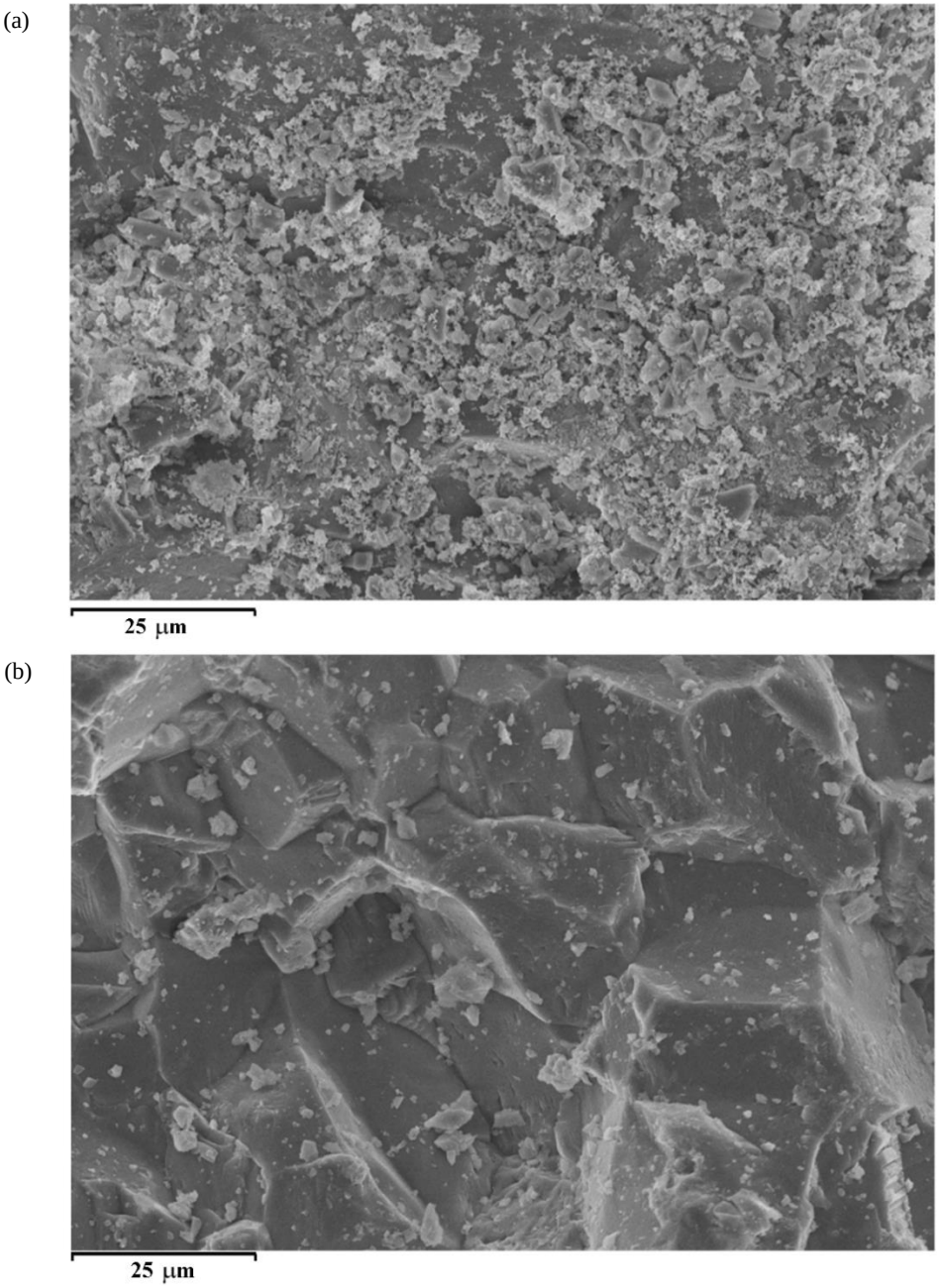

Figure 3. SEM micrographs: (a) ZnO/gravel before use, (b) ZnO/gravel after 60 min operation, and (c) gravel control

(c)

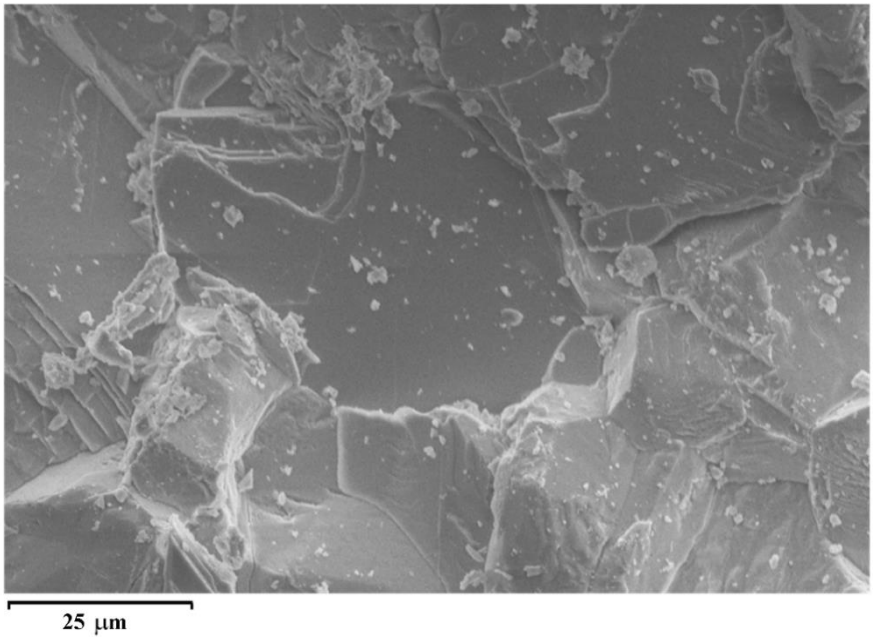

Figure 3. SEM micrographs: (a) ZnO/gravel before use, (b) ZnO/gravel after 60 min operation, and (c) gravel control (cont.)

Table 3. XRF analysis of pure gravel and ZnO/gravel catalysts

Formula	Mass (%)		Element	Mass (%)	
	pure	ZnO/Gravel		pure	ZnO/Gravel
CaO	99.26	97.370	Ca	70.94	69.592
ZnO	97.50	0.257	Zn	97.09	0.207
SiO_2		1.759	Si		0.822
Cr_2O_3		0.299	Cr		0.205
Br_2O		0.009	Br		0.009
PbO		0.302	Pb		0.281
			O		28.885
Norm.		100			100

3.2 Statistical analysis

3.2.1 CCD model fitting

The optimal conditions for lignin degradation in COP were identified using CCD within the framework of RSM and we are represented by the following Equation 4:

$$Y_{(\text{lignin degradation})} = -40.7 + 14.14A + 2.8B + 3.787C - 3.385D + 0.859AB + 0.0066AC + 0.0025AD - 0.102BC + 0.0163BD - 0.0045CD - 1.060A^2 - 0.64B^2 - 0.0305C^2 + 0.002D^2 \quad (4)$$

Where; A is pH, B is the amount of ZnO, C is the ozonation time, and D is the initial lignin concentration. The quality of the model is expressed as R^2. The acceptability of the RSM model was confirmed by using analysis of variance (ANOVA), a statistical method that serves as an exploratory tool to interpret observations and test hypotheses about the model parameters (shown in Table 4).

F value used to evaluate second-order regression. An F value of 18.62 for the quadratic model confirms its significance. Additionally, a "Prob>F" value less than 0.05 is statistically significant at the 95% confidence level. Larger F-values and smaller p-values highlight the significant effects of the corresponding coefficients. The results show that the regressions for lignin degradation are statistically significant, with p-values<0.05 and large F values. According to the ANOVA table for the catalytic ozonation process, linear model terms (pH, dose, time, and initial lignin concentration) and the interaction term (B*D) were significant ($p<0.05$), however the interaction terms are not significant. The experiment error because of using the lack of fit (LOF), with a p-value 0.004 confirmed

model significance. The LOF 0f F value 0.004 suggests that the result is significant compared to pure error, with a 68.13% chance this outcome occurred due to noise. A non-significant LOF indicates a good model fit. The closer the R^2 value is near one that the better to the fit, with the predicted R^2 value of 0.9456, in good agreement with the adjusted R^2 value (0.8948). The optimum signal to noise ratio from the study is 14.608 (Adeq Precision). Thus, the quadratic model can be used to optimize operational parameters. Figure 4 shows the model aligns with the ANOVA results, and residual plots indicate a standard distribution, supporting the significance of terms like pH, dose, ozonation time, initial lignin concentration, and BD. Non-significant terms include AB, AC, AD, BC, and CD. A normal probability plot close to a straight line confirms a good model fit, validating the regression models for calculating lignin degradation under the given conditions responding by Hanapi et al. (2021).

Table 4. Analysis of variance (ANOVA) for lignin degradation (%)

Source	Sum of squares	F-value	p-value Prob>F
Model	29,027.6	18.62	< 0.0001
A	95.7	0.86	0.369
B	849.7	7.63	0.015*
C	22,779.7	204.54	0.000*
D	681.8	6.12	0.026*
A*B	106.2	0.95	0.344
A*C	3.2	0.03	0.868
A*D	2.3	0.02	0.888
B*C	84.9	0.76	0.396
B*D	10.6	0.09	0.762
C*D	410.7	3.69	0.074
A^2	2,537.0	22.78	0.000*
B^2	11.3	0.10	0.755
C^2	4,104.4	36.85	0.000
D^2	532.0	4.78	0.045*
Lack of fit values=1,645.6; R^2=0.9456 (*p-Value indicates that model is significant)			

3.3 The effects of catalytic ozonation ZnO different parameters on lignin degradation

3.3.1 Effect of initial pH

The pH (A) and ZnO dosage (B) on lignin degradation use ZnO nanoparticle ozone catalysis, while ozone time (C) and lignin concentration (D) were constant at intermediate level (C=27.5 min, D=100 mg/L) and shown in Figure 4(a). When pH and ZnO content increased, the lignin degradation efficiency continued to increase. The initial pH was 8, and using more than 2 g of ZnO nanoparticles, the degradation efficiency >70% achieved, as shown in Figure 4(a). The lignin degradation rate increased with the simultaneous rise in pH and ozonation time. Specifically, when pH values exceeded 11, and ozonation time surpassed 40 min, further increases in each of these variables individually boosted removal efficiency. In alkaline conditions with ozone exposure time of 50 min, the lignin degradation efficiency was more than 80% as shown in Figure 4(b). Moreover, Figure 4(c) indicates that the maximum lignin degradation occurred at a high pH (pH=11), and the lowest lignin (10 mg/L) in fixed conditions achieved with an operating time of 27.5 min and a ZnO 3 g. In contrast, lignin degradation decreased as lignin concentration increased.

The pH solution influences the form in which lignin molecules exist, the decomposition of ozone and interactions with hydroxyl group on ZnO catalyst surface. It is well established that ozone resonance reacts preferentially with functional group complexes (OCH_3) and C=C bond of aromatic in acidic conditions through selective reactions. On the contrary, in alkaline conditions, ozone molecules decompose to produce hydroxyl radicals, superoxide radicals, and hydrogen superoxide radicals, which are substances whose oxidizing power reacts non-selectively with organic substances, thus, together with the catalyst, promoting the formation of more hydroxyl radicals, which are beneficial for the decomposition of conjugated double bonds, functional groups of organic substances with complex lignin structures (Amini et al., 2023; Norabadi et al., 2020).

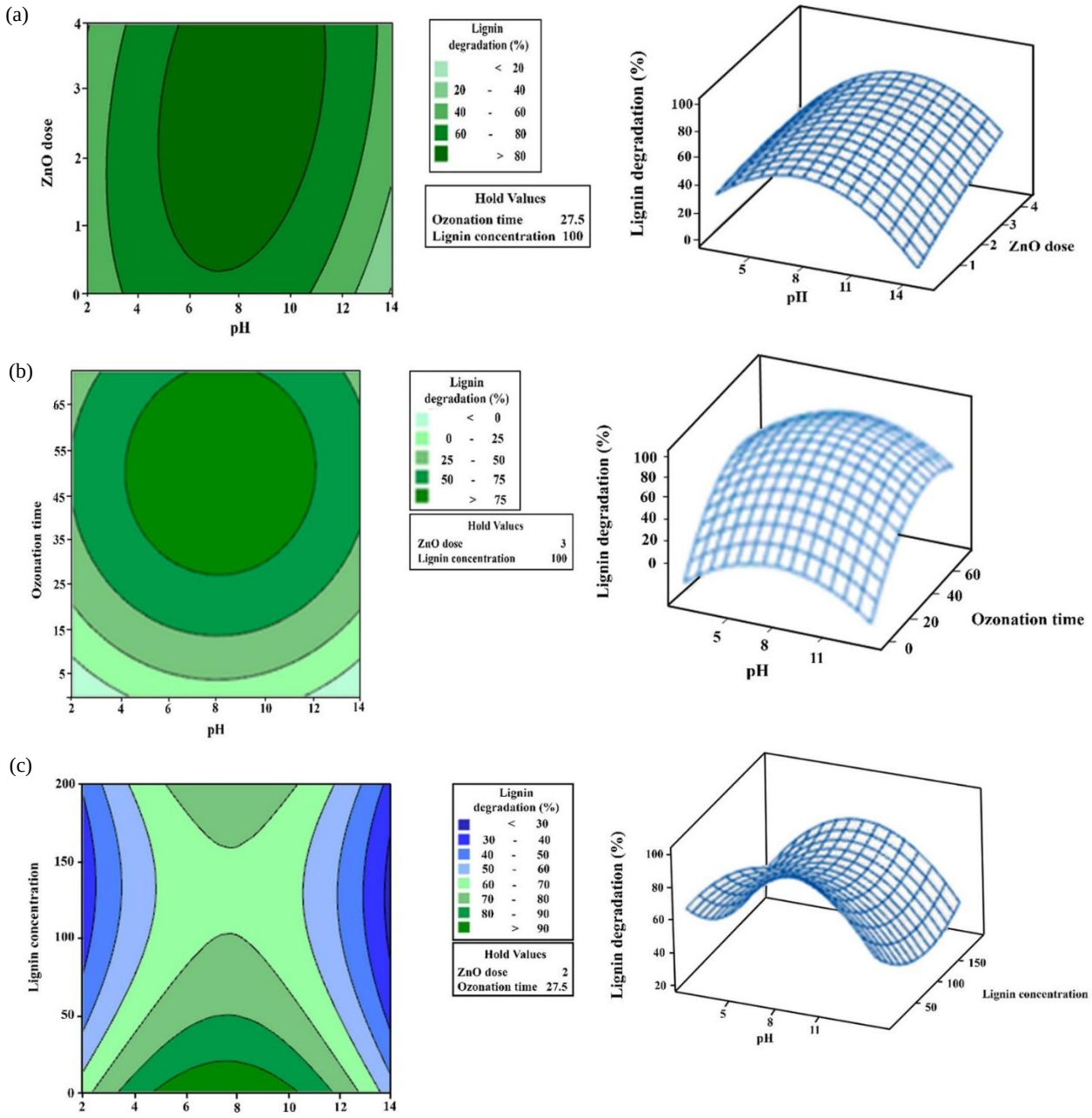

Figure 4. The effectiveness of pH solution on lignin degradation by ZnO COP, (a) ZnO dosage (g/L), (b) ozonation time (min) and (c) lignin concentration (mg/L)

The pH solution influences the form in which lignin molecules exist, the decomposition of ozone and interactions with hydroxyl group on ZnO catalyst surface. It is well established that ozone resonance reacts preferentially with functional group complexes (OCH_3) and C=C bond of aromatic in acidic conditions through selective reactions. On the contrary, in alkaline conditions, ozone molecules decompose to produce hydroxyl radicals, superoxide radicals, and hydrogen superoxide radicals, which are substances whose oxidizing power reacts non-selectively with organic substances, thus, together with the catalyst, promoting the formation of more hydroxyl radicals, which are beneficial for the decomposition of conjugated double bonds, functional groups of organic substances with complex lignin structures (Amini et al., 2023; Norabadi et al., 2020). Increasing the pH accelerates the rate of ozone decomposition through ZnO catalytic reactions. Due to the formation of highly reactive radicals (such as $HO\cdot$ and others like $OH\cdot$, $HO_2\cdot$, and $HO_3\cdot$), enhances the degradation rate of lignin. Based on Figures 4(a)-(c), it was found that the optimal pH for lignin degradation of ZnO catalytic ozonation process is 8. Moreover, the catalytic potential of ZnO in the ozonation process for lignin degradation confirmed.

The results of this study are consistent with Zhao et al. (2009) who used zinc catalyst to degrade nitrobenzene with an increase in pH value of 11. Phenols are one of the most important constituents in the structure of lignin that it removed by catalytic ozonation in pH solution of the neutral to weak alkaline range (pH 7-8). As stated by Li et al. (2018), in alkaline conditions, the metal oxide catalyst can capture ozone molecules and be in the state of a particle that breaks down to 1 oxygen molecule. Then, it will react with water to form metal oxides and hydroxyl radicals that can oxidize the double bonds or functional groups of the pollutants to be removed, promoting the formation of hydroxyl radicals and ZnO-hydroxyl radicals (oxidation radicals), thus increase the efficiency of the degradation of pollutants. The following mechanisms have been proposed for the formation of these hydroxyl and ZnO-hydroxyl radicals in Equation 5-7).

$$O_3 + ZnOs \rightarrow ZnOs\text{-}O_3 \quad (5)$$

$$ZnOs\text{-}O_3 \rightarrow ZnOs\text{-}O^{\bullet} + O_2 \quad (6)$$

$$ZnOs\text{-}O^{\bullet} + 2H_2O + O_3 \rightarrow ZnOs\text{-}{}^{\bullet}OH + 3{}^{\bullet}OH + O_2 \quad (7)$$

3.3.2 Effective of ZnO dosage

As shown in Figure 5(a), an increase in lignin degradation is observed with higher amounts of ZnO nanoparticles and longer ozonation times. At 100 mg/L lignin concentration and pH 8, when the operating time exceeded 40 min and the ZnO dosage exceeded 2 g, lignin degradation efficiency exceeded 80%. Figure 5(b) demonstrates the combined effect of ZnO dosage to lignin on the rate of lignin degradation. Under constant conditions, initial pH (8) and operating time of 27.5 min, an increase in lignin concentration can reduce degradation rate. Specifically, at lignin concentrations greater than 100 mg/L, the efficiency of the process decreased despite the increase in ZnO nanoparticles.

The lignin degradation ability by ZnO was low when the ozone exposure time was short. When the amount of ZnO was more than 2 g and the ozonation time increased to 30 min, the degradation efficiency was 80%. It shows that when the number of catalysts is higher, the surface area of the metal oxide catalyst is larger, the surface hydroxyl groups are increasingly reactive with ozone, resulting in the elimination of functional groups or conjugate bonds in the lignin structure, and lower color value for the decomposition of ozone molecules and the subsequent reactions. Like observed in previous studies, including those by Shao et al. (2009) on catalytic ozonation of nitrobenzene (with ZnO) removal through metal oxide catalytic ozonation. Additionally, as noted by Rosal et al. (2008), increasing catalyst concentration at a fixed ozone flow rate can enhance the transfer of ozone from the gas phase to the aqueous phase, thereby accelerating ozone molecule decomposition.

3.3.3 Ozonation time effective

The effectiveness of ozonation time (minutes) and lignin concentration (mg/L), while two variables (pH=8 and ZnO dose=2.0 g) were constant. As shown, the lignin removal increased with an extended ozonation operating time. ZnO catalytic efficiency increased from 69.30% to 99.6% as the ozonation time was increasing from 20 to 50 minutes. However, higher lignin concentration negatively affected lignin degradation shown in Figure 6.

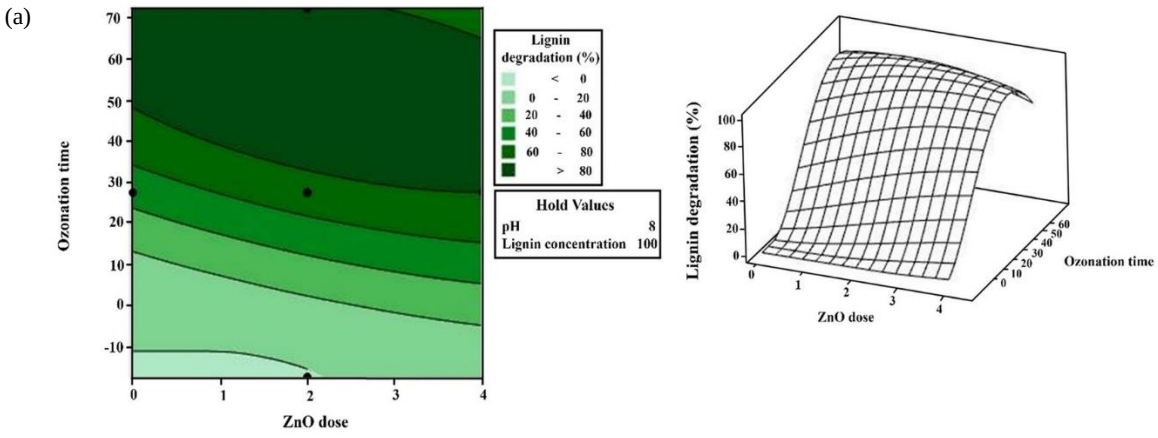

Figure 5. The effectiveness of ZnO dosage on lignin degradation by ZnO catalytic ozonation process, (a) ozonation time (min) and (b) initial lignin concentration (mg/L)

(b)

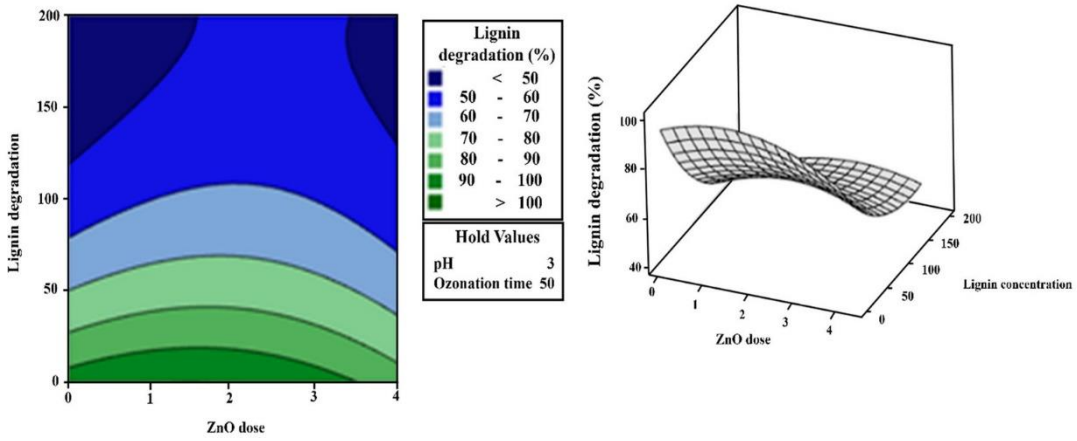

Figure 5. The effectiveness of ZnO dosage on lignin degradation by ZnO catalytic ozonation process, (a) ozonation time (min) and (b) initial lignin concentration (mg/L) (cont.)

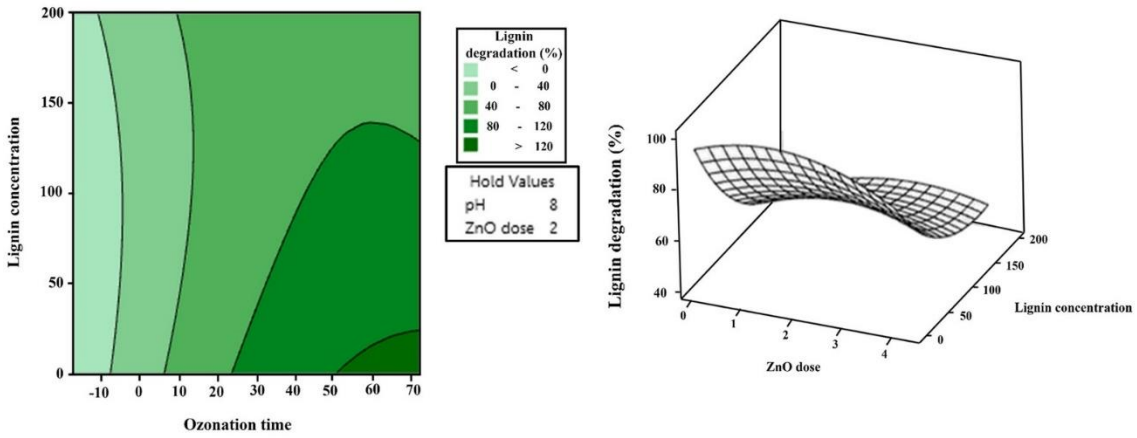

Figure 6. The effectiveness of ZnO catalytic ozonation with varying catalyst dosage by RSM

The effect of ozonation operating time is a crucial factor in achieving the desired purification objectives, as it plays a crucial role in the design and operation of the oxidation process. Ozonation operating time increased and lignin concentration decreased. Similar observations which were studied by Yaghmaeian et al. (2014) on amoxicillin antibiotic degradation and mineralization through catalytic ozonation (NH_4Cl). The catalytic activity of ZnO in lignin degradation attributed to hydroxyl group on surface which attract ozone ion to produce hydroxyl radical high oxidizing agent for the decomposition sulfonated soda lignin due to color reduction.

3.3.4 Equation fitting model test

Two runs of additional experiments evaluated to confirm the equation fitting model. Table 5 depicts lignin degradation efficiency as a function of the chosen conditions for ZnO dosage, the initial pH, the initial lignin concentration, and ozonation time. These two trials gave results close to the estimation, proving fitting model reliability. Figure 7 showed the lignin solution in each experiment.

Table 5. Confirmation experiments

Conditions	A	B (g/L)	C (mg/L)	D (min)	Lignin degradation (%)	
					Experimental	Predicted
1	8	2	50	60	80.53	81.1
2	8	3	50	60	89.92	79.23

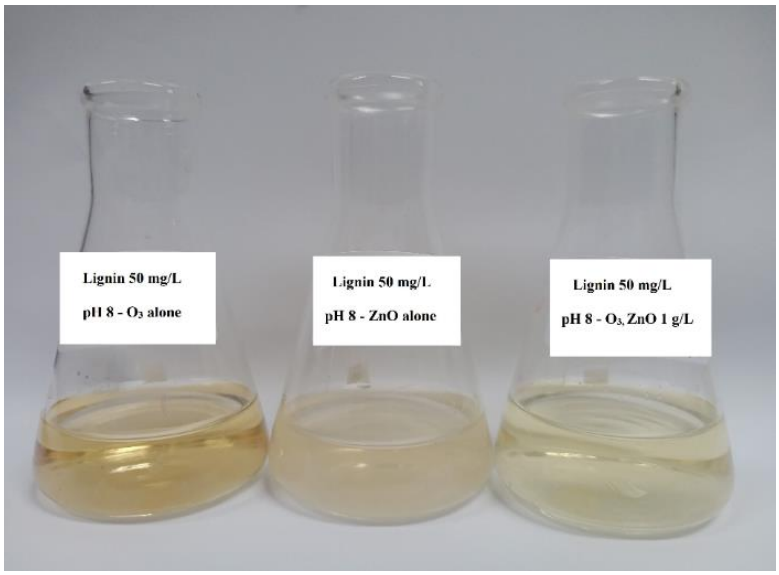

Figure 7. Lignin treatment by Catalytic ozonation ZnO nanoparticles on operating time 50 mins

4. CONCLUSION

In conclusion, the effectiveness of ZnO catalytic ozonation for lignin degradation in synthetic wastewater was investigated. A CCD combined and RSM was applied to model the relationships between key factors, including pH, ZnO dosage, ozonation time, and initial lignin concentration, to determine the optimal operational conditions. The experimental data revealed that lignin degradation increased with higher pH, ZnO dosage, and ozonation operating time. However, increased lignin concentration negatively impacted process efficiency. The predicted results suggested that optimal lignin degraded (99.6%) in pH 8, ZnO dose 1.0 g/L, ozonation operating time 50 minutes, and an initial lignin concentration 50 mg/L. Under these conditions, the experimental degradation rate reached 89.99%. Overall, the study concluded that ZnO nanoparticles are an effective catalyst for lignin degradation and mineralization in the catalytic ozonation process.

ACKNOWLEDGEMENTS

This research was financially supported by the Science, Research and Innovation Promotion Fund (Fundamental Fund, Fiscal Year 2023) through Khon Kaen University under research grant No. 179566, together with the Graduate Research Fund of Khon Kaen University for the academic year 2020.

AUTHOR CONTRIBUTIONS

Conceptualization, Aiyathiti C; Methodology, Aiyathiti C, Amnath Y; Validation, Aiyathiti C, Amnath Y; Formal Analysis, Amnath Y; Investigation, Aiyathiti C, Amnath Y; Resources, Aiyathiti C; Data Curation, Amnath Y; Writing-Original Draft Preparation, Amnath Y; Writing-Review and Editing, Aiyathiti C; Visualization, Amnath Y; Supervision, Aiyathiti C; Project Administration, Aiyathiti C; Funding Acquisition, Aiyathiti C.

DECLARATION OF CONFLICT OF INTEREST

The authors declare no conflict of interest.

REFERENCES

Amini M, Hosseini S, Chaibakhsh N. High-performance NiO@Fe_3O_4 magnetic core-shell nanocomposite for catalytic ozonation degradation of pharmaceutical pollution. Environmental Science and Pollution Research 2023; 30(43):98063-75.

Einaga H, Sano Y, Minakata D, Yamaguchi A. Fundamental insights and recent advances in catalytic ozonation. Applied Catalysis B: Environmental 2024;350:Article No. 123591.

Hanapi NHM, Abdullah SHYS, Ismail AB, Juahir H. Central composite design: A response surface methodology approach in biodegradation of textile dye wastewater. Journal Korean Society Environmental Engineering 2021;43(6):461-75.

Haqa I, Mazumderb P, Kalamdhad AS. Recent advances in removal of lignin from paper industry wastewater and its industrial applications: A review. Bioresource Technology 2020;312:Article No. 12363.

Hayat K, Gondal MA, Khaled MM, Ahmed S, Shemsi AM. Nano ZnO synthesis by modified sol gel method and its application in heterogeneous photocatalytic removal of phenol from water. Applied Catalysis A: General 2011;393(1-2):122-9.

Li J, Zhang M, Li J, Wang D. Corn stover pretreatment by metal oxides for improving lignin removal and reducing sugar degradation and water usage. Bioresource Technology 2018;263:232-41.

Li X, Liu J, Zhang Y, Chen G. Application of heterogeneous catalytic ozonation in wastewater treatment: An overview. Catalysts 2023;13(2):Article No. 342.

Kumar A, Srivastava NK, Gera P. Removal of color from pulp and paper mill wastewater-methods and techniques: A review.

Journal of Environmental Management 2021;298:Article No. 113527.

Mao H, Li J, Wang X, Zhang T. Co-Mn bimetallic oxide catalyzed continuously ozonation of lignin into aromatic aldehydes. Industrial Crops and Products 2025;220:Article No. 117615.

Mohammadi L, Bazrafshan E, Noroozifar M, Moghaddam AA. Application of heterogeneous catalytic ozonation process with magnesium oxide nanoparticles for toluene degradation in aqueous environments. Health Scope 2016;5(4):e40439.

Nawrocki J, Kasprzyk-Hordern B. The efficiency and mechanisms of catalytic ozonation. Applied Catalysis B: Environmental 2010;99(1-2):27-42.

Norabadi E, Panahi AH, Reza Ghanbari R, Meshkinian A, Kamani H, Ashrafi SD. Optimizing the parameters of amoxicillin removal in a photocatalysisozonation process using Box-Behnken response surface methodology. Desalination and Water Treatment 2020;192:234-40.

Rosal R, Rodríguez A, Perdigón-Melón JA, Mezcua M, Hernando MD, Letón P, et al. Removal of pharmaceuticals and kinetics of mineralization by O_3/H_2O_2 in a biotreated municipal wastewater. Water Research 2008;42(14):3719-28.

Zhao L, Sun Z, Ma J. Novel Relationship between hydroxyl radical initiation and surface group of ceramic honeycomb supported metals for the catalytic ozonation of nitrobenzene in aqueous solution. Environmental Science and Technology 2009; 43(11):1-11.

Zhao R, Zong S, Ma QQ, Xu Z, Yuan J. Investigating the electrocatalytic properties of ZnO-based composite membrane for dye removal. Scientific Reports 2025;15:Article No. 6306.

Zhou C, Liu S, Wang Q. Catalytic ozonation for pulp and paper mill wastewater treatment: COD reduction and organic matter degradation mechanism. Separations 2023;10(3):Article No. 148.

Yaghmaeian K, Moussavi G, Alahabadi M. Removal of amoxicillin from contaminated water using NH_4Cl-activated carbon: Continuous flow fixed-bed adsorption and catalytic ozonation regeneration. Chemical Engineering Journal 2014;236:538-44.

Environment and Natural Resources Journal

Volume 24
Issue 2
2026

Differential Protein and Morphological Responses of Mosses to Heavy Metal Exposure: Insights from SDS-PAGE Analysis and Microscopic Examination

Supatra Chunchob, Susana Giyasov, Chetsada Phaenark, and Weerachon Sawangproh*

Conservation Biology Program, School of Interdisciplinary Studies, Mahidol University (Kanchanaburi Campus), 199, Moo 9, Lumsum, Saiyok District, Kanchanaburi 71150, Thailand

ARTICLE INFO

Received: 25 Jul 2025
Received in revised: 16 Oct 2025
Accepted: 21 Oct 2025
Published online: 9 Dec 2025
DOI: 10.32526/ennrj/24/20250190

Keywords:
Biomarkers/ Adaptation strategies/ Stress responses/ Housekeeping proteins/ Protein profile

*** Corresponding author:**
E-mail:
weerachon.saw@mahidol.ac.th

ABSTRACT

Heavy-metal pollution poses significant risks to ecosystems and human health. We evaluated acute proteomic and cytological responses of two mosses, *Ectropothecium dealbatum* and *Hyophila involuta*, to cadmium (Cd), lead (Pb), and zinc (Zn). Gametophores were immersed for 72 h to single-metal solutions (10, 20, or 30 mg/L; controls in distilled water), ensuring observed effects reflected single-metal toxicity. Protein profiles were resolved by SDS-PAGE, and light microscopy quantified chloroplasts per lamina cell and the proportion of dead cells. Cd elicited the strongest responses in both species, with intensified high-molecular-weight bands (~90, ~100, ~121 kDa) and pronounced cytological injury; Pb produced qualitatively similar but weaker changes. In contrast, Zn primarily modulated band intensity without generating new bands and caused limited injury at the tested doses. Concordant shifts across methods—reduced chloroplast counts and elevated lamina cell death co-occurring with Cd/Pb-associated bands—support a molecular–physiological linkage of acute metal stress. However, these high-molecular-weight bands (including the ~121 kDa signal) are size-based, putative markers only; independent identification (e.g., LC-MS/MS or immunodetection) and functional validation are still required. Within this 72-h window and concentration range, sensitivity followed Cd > Pb ≫ Zn. The findings nominate candidate proteins for rapid discrimination of damaging (Cd, Pb) versus comparatively tolerated (Zn) exposures and motivate targeted protein identification plus longer, field-calibrated studies to establish biomonitoring thresholds.

HIGHLIGHTS

- SDS-PAGE and microscopy revealed rapid moss responses to heavy metals.
- Cd induced unique 90-121 kDa proteins and severe chloroplast degradation.
- Pb caused weaker but similar proteomic and cytological stress patterns.
- Zn altered band intensity only, showing minimal injury in both mosses
- Cd > Pb ≫ Zn defined toxicity; candidate bands may serve as stress markers.

1. INTRODUCTION

Heavy metal pollution poses a serious threat to environmental and human health. Due to their elemental nature, heavy metals cannot be chemically degraded; thus their detoxification in the environment primarily relies on stabilizing them in place or removing them entirely (Suman et al., 2018). Persistent pollutants such as cadmium (Cd), lead (Pb), and zinc (Zn) originate from both natural processes and various anthropogenic activities, including mining, industrial operations, and agricultural practices (Wuana and Okieimen, 2011). These metals tend to accumulate in soil, water, and organisms, leading to long-term contamination and adverse ecological consequences (Rehman et al., 2013).

The toxicity of heavy metals depends on multiple factors, including their concentration, the plant species involved, and environmental conditions (Cârdei

Citation: Chunchob S, Giyasov S, Phaenark C, Sawangproh W. Differential protein and morphological responses of mosses to heavy metal exposure: Insights from SDS-PAGE analysis and microscopic examination. Environ. Nat. Resour. J. 2026;24(2):174-185. (https://doi.org/10.32526/ennrj/24/20250190)

et al., 2021). Among them, cadmium and lead are particularly toxic to plants even at low concentrations (Shukla et al., 2007), as they disrupt essential physiological processes, reduce photosynthetic efficiency, stunt growth, and impair nutrient uptake (Rizvi et al., 2022). On the other hand, zinc toxicity is relatively less common, since zinc is an essential micronutrient required for numerous metabolic functions (Leon-Mediavilla et al., 2018). However, excessive zinc in soil can still be detrimental to plants, producing symptoms similar to those caused by cadmium or lead exposure (Kuziemska et al., 2022).

Bryophytes, including mosses, have increasingly been recognized as effective bioindicators of heavy-metal contamination due to their high surface-area-to-volume ratios (Sun et al., 2009), efficient capacity for metal uptake, and high sensitivity to environmental changes (Stanković et al., 2018), as well as their poikilohydry and widespread distribution across urban, industrial, and remote environments (Tremper et al., 2004; Elliott and Velasquez, 2024). As non-vascular plants that absorb water and nutrients directly from their surroundings, mosses are particularly vulnerable to heavy-metal uptake (Bellini et al., 2021). Understanding how mosses respond to heavy-metal exposure is therefore crucial for accurately assessing contamination levels and formulating effective mitigation strategies (Chaudhuri and Roy, 2024). Mosses serve as sentinel organisms (Świsłowski et al., 2021; Phaenark et al., 2024), reflecting the bioavailability, accumulation, and toxicity of metals in situ. By investigating the molecular mechanisms underlying moss responses, researchers can identify biomarkers of stress and clarify adaptive strategies to cope with metal toxicity (Sun et al., 2011). Acute exposures studies capture the early injury phase—oxidative bursts, rapid chloroplast disruption, and initial cell death—that often precede longer-term acclimation in bryophytes. We therefore profiled short-term (72 h) responses to delineate the immediate injury landscape for Pb, Cd, and Zn as a foundation for subsequent chronic, recovery, and field-relevant studies.

The aim of this study is to examine the physiological and biochemical responses of the moss species *Ectropothecium dealbatum* (Reinw. & Hornsch.) A. Jaeger and *Hyophila involuta* (Hook.) A. Jaeger under exposure to three heavy metals (Cd, Pb, and Zn). Specifically, we analyze protein patterns using sodium dodecyl sulfate-polyacrylamide gel electrophoresis (SDS-PAGE), identify potential biomarkers of heavy-metal exposure through analysis of protein expression patterns (Sardar et al., 2022), and quantify chloroplast numbers and lamina cell death across lamina zones to compare responses under different experimental conditions. Ultimately, this research seeks to inform targeted monitoring and risk assessment for heavy metals—particularly Pb and Cd—while providing mechanistic and phenotypic baselines for future, longer-duration, and field-validated studies.

2. METHODOLOGY

2.1 Plant materials and acclimation

The study involved two moss species: the pleurocarpous moss *E. dealbatum* and the acrocarpous moss *H. involuta*. These species are commonly found year-round in moist areas on the ground at Mahidol University's Kanchanaburi Campus, situated at an altitude of approximately 200 meters above sea level. Species identification was confirmed based on morphological characteristics using a dichotomous key developed by Eddy (1991) and verified by a local bryologist (Mr. Patsakorn Ajintaiyasil, pers. comm.) from Kasetsart University. Moss samples were collected from the university's nursery area adjacent to the campus basketball court (14.129636 N, 99.158747 E) between August and September 2023. During collection, both soil and fresh mosses were carefully gathered using a spatula and placed in multi-purpose zipper bags. We did not characterize soil's metal concentration at the moss collection sites; our study was designed to test acute, controlled exposures under laboratory conditions rather than to correlate moss responses with ambient field contamination. In the laboratory, the mosses were acclimated by transferring them to transparent plastic boxes equipped with ventilation holes and filled with the same soil initially collected with the mosses, which served as a substrate and growth medium. LED bulbs provided a 12-hour lighting source (06:00-18:00 h) on shelves within the chambers, while the air conditioner maintained an ambient temperature of 25±2ºC. Moss samples were watered once daily or as needed to maintain adequate humidity.

2.2 Preparation of metal aqueous solution

Working aqueous solutions (10, 20, and 30 mg/L as metal) of Cd, Pb, and Zn were prepared by diluting certified single-element standards (Merck) with deionized water. For reference, a 1,000 mg/L stock corresponds approximately to 0.009 M

$Cd(NO_3)_2$, 0.005 M $Pb(NO_3)_2$, and 0.015 M $Zn(NO_3)_2$. The pH of all working solutions was adjusted to 5.60±0.02 at 25°C using 6 M NaOH and 6 M HNO_3 as required.

2.3 Heavy metal treatment

Prior to experimentation, fresh gametophores (leafy, stalk-like structures of the gametophyte) with rhizoids removed were collected from the growth chambers, rinsed with tap water, and transferred to clean Petri dishes. Gametophores of *E. dealbatum* or *H. involuta* designated as controls were submerged in 20 mL of distilled water for three days. The remaining gametophores were submerged in 20 mL of heavy metal solutions at concentrations of 10, 20, and 30 mg/L. For each moss species, a total of 27 Petri dishes were prepared (3 metals × 3 concentrations × 3 replicates = 27 Petri dishes). Metal exposure was maintained for three days under LED lighting and controlled air conditioning at 25±2°C (06:00-18:00 hrs). The exposure was limited to three days (72 h) to resolve early, acute responses (protein expression changes, chloroplast loss, cell death) while minimizing potential interference from growth or developmental processes.

2.4 Protein extraction

After 3 days of exposure to metal solutions, 0.3 g of moss gametophores, including leaves and stems, were ground in a pre-chilled pestle and mortar using liquid nitrogen to disrupt cell walls and release proteins. Subsequently, 1,000 µL of lysis buffer containing detergents (1% SDS, 1 M Tris HCl pH 6.8, 2 mM EDTA, 20 mM DTT and 1 × protease inhibitor) for protein solubilization was added, followed by 1,000 µL of distilled water. Once thoroughly mixed, 1,000 µL of the lysate was transferred to a new microcentrifuge tube and centrifuged at 12,000 rpm for 5 min. Later, 600 µL of the lysate was transferred to another new microcentrifuge tube, to which 600 µL of 20% cold TCA was added, thoroughly mixed, and incubated on ice for 60 min for protein precipitation. Once the incubation was finished, the lysate-TCA mixture was centrifuged at 12,000 rpm for 5 min to pellet the precipitated proteins. The clear liquid was decanted, and cold 100% acetone was added to the protein pellet and centrifuged at 12,000 rpm for 5 min to remove contaminants. After decanting the supernatant and a brief air-drying to eliminate residual acetone, the dry pellet was resuspended in 1,000 µL of 80% acetone and centrifuged at 12,000 rpm for 5 min. The clear liquid was decanted once again, and the protein pellet was centrifuged at 12,000 rpm for 2 min. After decanting the clear liquid, the protein pellet was incubated at 55ºC in a water bath for 5 min or until the protein pellet became dry. Finally, the resulting protein pellet was resuspended by adding 70 µL of dissolving buffer (20 mM DTT, 7 M Urea, and 2 M Thiourea) and stored in a fridge at 4ºC for total protein quantification. These techniques were adapted from Barbara et al. (2007).

2.5 Total protein quantification

Total protein content was determined using the Bradford assay with bovine serum albumin (BSA) as the standard, prepared at concentrations ranging from 0 to 1 mg/mL (Bradford, 1976). For the assay, 5 µL of protein samples or BSA standards were pipetted into a 96-well plate, and 250 µL of Bradford reagent was added to each well. The mixtures were thoroughly mixed and incubated at room temperature for 10 minutes to allow dye binding. Absorbance was measured at 595 nm using a microplate spectrophotometer (BMG LabTech, SPECTROstar Nano), with a reagent-only blank as the reference. A standard curve was constructed from the absorbance values of the BSA standards (0.2, 0.4, 0.6, 0.8, 1.0, and 1.2 mg/mL), and protein concentrations of the samples were calculated using the linear regression equation (y=mx). The resulting concentrations (mg/mL) were used to normalize protein input, ensuring equal protein amounts were loaded into each lane for SDS-PAGE analysis.

2.6 Protein separation using SDS-PAGE

Protein separation using SDS-PAGE was conducted using discontinuous buffer systems in Mini PROTEAN® Tetra Cell system from Bio-Rad following a modified procedure (Laemmli, 1970). Initially, 15 µg of extracted proteins were loaded onto a 12% sodium dodecyl sulfate-polyacrylamide gel. The gel cassette was prepared with a 12% separating gel and a 4% stacking gel. The composition of the separating gel included 3.4 mL of distilled water, 2.5 mL of 1.5 M Tris-HCl (pH=8.8), 4 mL of 30% acrylamide, 100 µL of 10% (w/v) SDS, 50 µL of 10% (w/v) APS, and 20 µL of tetramethylene-diamine (TEMED). The stacking gel consisted of 3.1 mL of distilled water, 1.25 mL of 0.5 M Tris-HCl (pH 6.8), 0.65 mL of 30% acrylamide, 100 µL of 10% (w/v) SDS, 50 µL of 10% (w/v) APS, and 10 µL of tetramethylene-diamine (TEMED). The gels were run

in tris-glycine buffer (1 × working solution containing 25 mM Tris-Cl, 250 mM glycine, and 0.1% SDS) at 20 mA/gel for 1.5 hours to induce protein migration based on their molecular size and charge. A pre-stained protein ladder of molecular weight ranging from 10.5 to 175 kDa (Vivantis Technologies Sdn. Bhd.) was used as a standard marker. Following electrophoresis, the gel was stained overnight with Coomassie blue (G-250) protein dye and later de-stained until the background cleared, and protein bands became visible. Finally, the gel was carefully transferred onto a cellophane membrane previously submerged in running buffer. Another cellophane membrane, previously soaked in running buffer, was placed on top of the gel, and the gel was allowed to air dry for visualizing protein banding patterns.

2.7 Microscopic study of lamina cells of mosses

To examine changes in lamina cell structure, gametophore samples were randomly selected from each Petri dish, rinsed with distilled water, and fresh leaves (phyllids) from the middle section of three distinct shoots were chosen using forceps. These leaves were mounted on microscopic slides, covered with coverslips, and observed under a compound light microscope equipped with a digital camera (Nikon DS-Fi3). Following Phaenark et al. (2024), images of the lamina were captured from the basal, median, and apical regions of each leaf and analyzed using NIS-Elements Microscope Imaging Software. Quantitative assessments focused on two key cell characteristics: the number of chloroplasts per lamina cell and the proportion of dead cells, which were compared between heavy-metal-treated moss samples and controls to evaluate stress-induced structural responses.

Counting the chloroplasts in the lamina cells of gametophores in *E. dealbatum* was relatively straightforward because of the leaf lamina's single-cell layer, transparency, and the relatively large chloroplast size. However, counting chloroplasts in the lamina cells of *H. involuta* was challenging due to its papilose cell surface, which hindered clear visualization under the compound microscope. Consequently, only dead cells identified by their distinct brownish color and empty appearance were counted in this species.

2.8 Statistical analyses

The Petri dish was considered the experimental unit (n=3 dishes per species × metal × concentration). Within each metal and lamina zone, concentrations (0, 10, 20, 30 mg/L) were compared using one-way ANOVA when assumptions were met (Shapiro-Wilk on residuals; Levene's test for homogeneity), with Fisher's LSD for post hoc contrasts (α=0.05); when assumptions were violated, we used the Kruskal-Wallis test with Bonferroni-adjusted pairwise comparisons. All analyses were conducted in IBM SPSS Statistics, version 29.

3. RESULTS AND DISCUSSION

3.1 Protein profile based on SDS-PAGE analysis

For years, certain plant species including lower plants such as bryophytes have been suggested as appropriate indicators of pollution (Basile et al., 2013). The use of bryophytes as bioindicators stems from their capacity to accumulate toxic elements, as noted by many authors such as Oishi and Hiura (2017), Stanković et al. (2018), and Printarakul and Meeinkuirt (2022). Bryophytes are effective biomonitors of pollution due to their rapid absorption rate, their ability to absorb substances through their plant surfaces in the absence of roots, and their differential capacity to accumulate a broad spectrum of metals (Rachna and Vashistha, 2017). Previous studies have indicated a considerable sensitivity of certain species to pollution, alongside a notable tolerance in others, as documented by Basile et al. (2005), Esposito et al. (2007), and Esposito et al. (2012). Therefore, the results of our study extend these observations by demonstrating the effects of heavy metal pollution on other bryophyte species as evidenced in protein profile and morphological alteration in lamina cell contents.

The SDS-PAGE analysis of moss protein profiles following exposure to heavy metal exposure provides valuable insights into the adaptive responses of moss species to environmental stressors. The results indicate significant alterations in protein expression in both *E. dealbatum* and *H. involuta* under Cd and Pb treatments, while Zn treatments primarily affected expression levels rather than inducing changes in protein profiles (Figures 1 and 2). Sardar et al. (2022) confirmed that SDS-PAGE is an efficient technique used for enhancing the understanding of plant proteomic modulation under chromium (Cr) stress. Similarly, Gallo et al. (2022) investigated protein profiles in plants from the Brassicaceae family, including both non-metal hyperaccumulators and hyperaccumulators, exposed to nano and ionic forms of Cd and Zn. Their study used 2D SDS-PAGE to

compare protein modulation in response to heavy metals, highlighted differential responses of plant species to metal stress, which aligns with the findings in these moss species.

3.2 Protein expression in *E. dealbatum*

Across all metal treatments (Cd, Pb, Zn), *E. dealbatum* resolved ten SDS–PAGE bands: seven constitutive bands at ~14, 20, 24, 26, 29, 31, and 62 kDa—proteins the cell produces continuously for basic, ongoing functions—and they appeared in every treatment. Three high-molecular-weight bands (90, 100, 121 kDa) varied with metal type and concentration (Figure 1). Under Cd, the 90-, 100-, and 121-kDa bands were upregulated at 10-20 mg/L but declined sharply at 30 mg/L (Figure 1(a)), coinciding with chlorosis of gametophores after three days (Figure 3). This pattern is consistent with the genotoxic and cytotoxic effects of Cd reported for bryophytes (e.g., *Sphagnum palustre*; Sorrentino et al., 2017). With Pb, the same three bands were induced—most clearly at 20-30 mg/L (Figure 1(a))—and plants showed pale laminae (Figure 3), in line with Pb-related disruption of photosynthesis and chlorophyll degradation (Phaenark et al., 2022; Phaenark et al., 2024).

By contrast, Zn did not induce the 90-, 100-, or 121-kDa bands at any concentration (Figure 1(b)). Lamina cell morphology remained unchanged, and no necrosis was observed (Figure 3). Given the stability of the seven constitutive bands across all treatments and the absence of Zn-specific differential bands or visible damage, *E. dealbatum* appears more tolerant to Zn than to Cd or Pb, consistent with Zn's role as an essential plant micronutrient (Stanković et al., 2018).

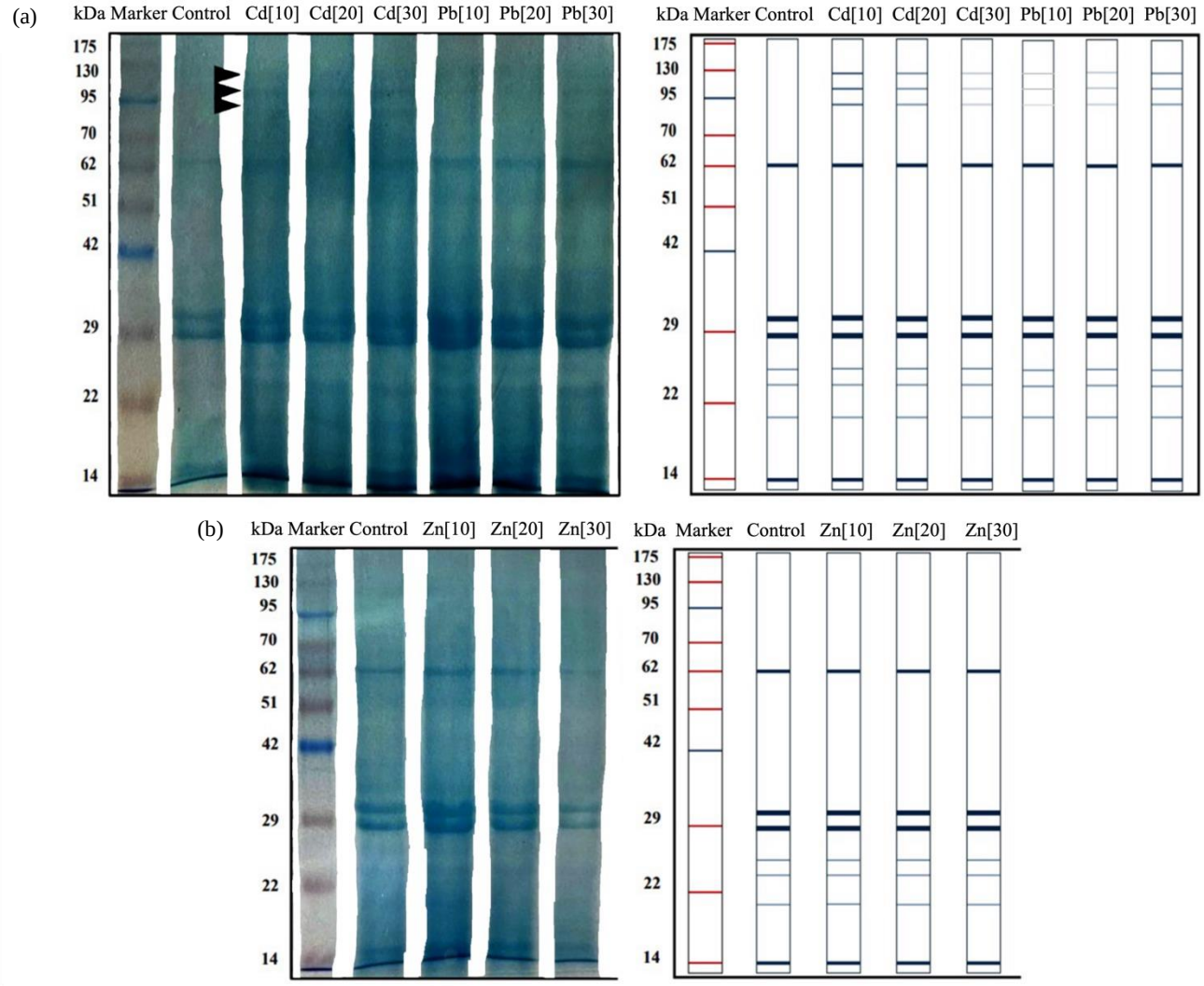

Figure 1. Three proteins, approximately 90, 100, and 121 kilodaltons (kDa) were consistently detected in *E. dealbatum* after the treatment of gametophore (leaves and stems) with Cd and Pb across all concentrations (10, 20, and 30 mg/L) (a). However, these proteins were absent when *E. dealbatum* was subjected to identical concentrations of Zn (b). The left panel displays SDS-PAGE bands, while the right panel illustrates the schematic diagram derived from the protein profile of SDS-PAGE.

3.3 Protein expression in *H. involuta*

We analyzed differential protein expression in *H. involuta* under Cd, Pb, and Zn exposure. Across the control and all metal treatments, *H. involuta* resolved nine SDS-PAGE bands: three high-molecular-weight proteins (~90, 100, and 121 kDa) and six low-molecular-weight proteins (14, 20, 22, 28, 31, and 62 kDa). The high-molecular-weight proteins were clearly up-regulated by Cd at 10-20 mg/L and by Pb at 10-30 mg/L (Figure 2(a)), indicating activation of a conserved heavy-metal stress response (Shafiq et al., 2019). These high-MW bands were not induced by Zn at any concentration (Figure 2(b)).

The six low-molecular-weight proteins were detected in every lane, including the untreated control and all Cd, Pb, and Zn treatments. Under Zn exposure, they exhibited a biphasic pattern—up-regulated at 10-20 mg/L but down-regulated at 30 mg/L relative to the control (Figure 2(b)). This threshold-type response is consistent with Zn's dual role as an essential micronutrient at low levels and a toxicant at high levels that impairs physiology and growth (Akram et al., 2022; Wei et al., 2022). Correspondingly, pronounced lamina alterations and cell death were observed at 30 mg/L Zn (Figure 4), aligning with reports of Zn-induced structural damage in plant tissues (Vijayarengan and Mahalakshmi, 2013).

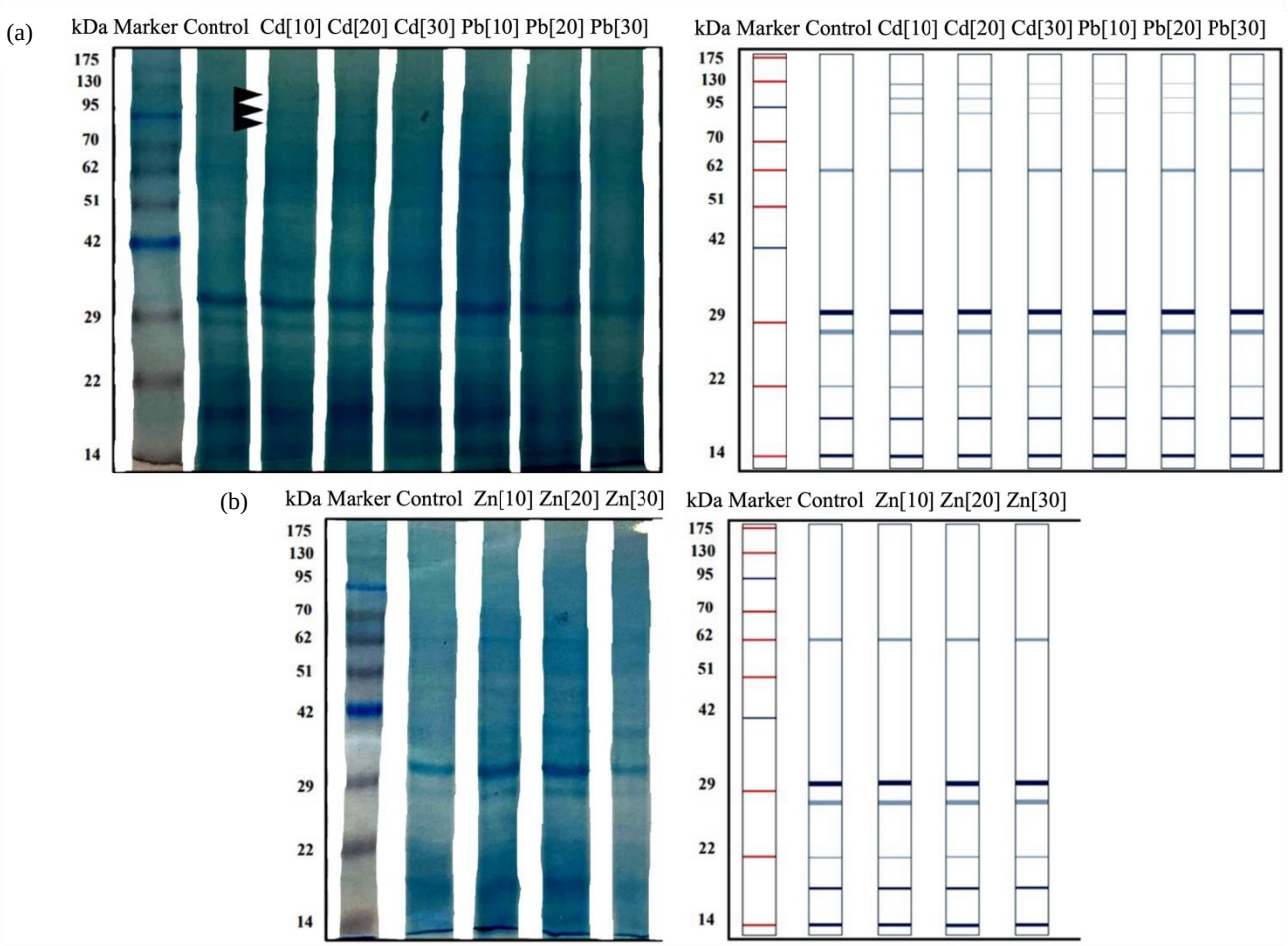

Figure 2. Three proteins, approximately 90, 100, and 121 kilodaltons (kDa) were consistently detected in *H. involuta* after the treatment of gametophore (leaves and stems) with Cd at concentrations of 10, 20, and 30 mg/L, and Pb at 10, 20, and 30 mg/L (a). However, in the lower diagram, these proteins were absent when *H. involuta* was subjected to identical concentrations of Zn (b). The left panel displays SDS-PAGE bands, while the right panel illustrates the schematic diagram derived from the protein profile of SDS-PAGE.

3.4 Stress protein expression in bryophytes under heavy metal exposure

In our study, heavy-metal exposure produced clear protein-expression shifts: bands in the ~90-121 kDa range intensified under Cd and, to a lesser extent, Pb, while Zn elicited little change at the tested doses—suggesting comparatively weaker activation of stress-response pathways. This pattern aligns with established bryophyte responses in which stress proteins commonly appear around ~70, ~90, and ~121 kDa. Heat-shock

proteins (HSP70 at ~70 kDa and HSP90 at ~90 kDa) function as molecular chaperones that stabilize nascent or denatured proteins and limit damage; Pb-exposed *Thuidium qataranse* shows elevated HSPs consistent with tolerance and detoxification (Usman et al., 2022). Because metal stress typically generates reactive oxygen species (ROS), which activate stress-responsive genes including HSPs (Shaheen, 2023), our Cd- and Pb-associated bands are consistent with HSP-mediated defenses. Similar proteomic trends have been reported in higher plants under heavy-metal exposure (Li et al., 2016) and in mosses exposed to Pb and Ni, with pronounced changes in the 70-90 kDa range (Sun et al., 2009).

The ~121 kDa band warrants caution. SDS-PAGE cannot identify proteins or assign them to pathways; migration near ~121 kDa could reflect a large chaperone class (e.g., HSP100-like proteins that cooperate with HSP70/90) or other high-molecular-weight factors associated with oxidative/metal stress (e.g., transport, trafficking, or detoxification proteins). We therefore refrain from assigning protein identities. To progress from patterns to mechanisms, independent techniques based on different principles are required: targeted immunoblotting for candidate chaperones and discovery proteomics (LC-MS/MS peptide mapping, MALDI-TOF profiling) to identify the ~90/~100/~121 kDa species, quantify their regulation across metals and doses, and evaluate post-translational modifications (e.g., phospho-/redox-proteomics) (Shlomi et al., 2006; Parrish et al., 2007).

Once protein identities and their regulatory patterns are validated, integration with network resources (e.g., KEGG, PathBank) and protein-protein interaction data can place these species within chaperone, antioxidant, chelation, and transporter modules, enabling a systems-level view of proteostasis under metal stress (Mlecnik et al., 2005; Nayar and Altman, 2024). At that stage, applied uses—such as developing candidate protein panels to discriminate damaging (Cd, Pb) from comparatively tolerated (Zn) exposures—may be explored, recognizing that any diagnostic thresholds would require calibration against field samples and independent datasets.

In sum, our SDS-PAGE results are consistent with a chaperone-linked stress response under Cd/Pb and a comparatively muted response under Zn; however, definitive protein identities and pathway assignments await targeted immunoblotting and mass-spectrometric confirmation.

3.5 Alteration in chloroplast numbers and lamina cell death

E. dealbatum Chloroplast numbers declined sharply in a dose-dependent manner under Cd across basal, median, and apical zones, with significant reductions beginning at 10 mg/L and the greatest losses at 30 mg/L (e.g., basal: 35±6 → 9±3; median: 29±6 → 8±3; apical: 26±5 → 7±4) (Table 1). Pb caused a milder decline, significant only at 30 mg/L in basal (35±6 → 21±3) and median (29±6 → 18±1) cells, while apical cells were unchanged. Zn produced no significant differences in any zone; means fluctuated but retained control superscripts. In controls (0 mg/L), chloroplast numbers followed basal > median > apical.

Lamina cell mortality increased steeply and dose-dependently under Cd, reaching 92.00% (basal), 88.76% (median), and 70.00% (apical) at 30 mg/L, with the overall mean rising from 0±0 to 83.59±11.88. Pb produced a weaker, zone-specific pattern—apical cells were most sensitive at 20-30 mg/L (56.00-72.88%), median cells rose mainly at 30 mg/L (65.71%), and basal cells changed modestly (~20%). Zn caused negligible mortality at all doses (Table 2). Observations under light microscopy were consistent with these trends (Figure 3).

Table 1. Numbers of chloroplasts in the lamina cells of *E. dealbatum* moss measured across the basal, median, and apical zones of gametophore leaves after exposure to Cd, Pb, and Zn at concentrations of 0, 10, 20, and 30 mg/L.

Concentration of heavy metals	Area of lamina cell		
	Basal cell	Median cell	Apical cell
Cd (mg/L)			
0	35±6^{a}	29±6^{a}	26±5^{a}
10	21±3^{b}	18±4^{b}	15±2^{b}
20	18±3^{b}	15±6^{bc}	11±2^{bc}
30	9±3^{c}	8±3^{c}	7±4^{c}

Table 1. Numbers of chloroplasts in the lamina cells of *E. dealbatum* moss measured across the basal, median, and apical zones of gametophore leaves after exposure to Cd, Pb, and Zn at concentrations of 0, 10, 20, and 30 mg/L (cont.).

Concentration of heavy metals	Area of lamina cell		
	Basal cell	Median cell	Apical cell
Pb (mg/L)			
0	35±6[a]	29±6[a]	26±5[a]
10	31±6[a]	29±3[a]	24±4[a]
20	29±1[a]	27±2[a]	21±3[a]
30	21±3[b]	18±1[b]	17±5[a]
Zn (mg/L)			
0	35±6[a]	29±6[a]	26±5[a]
10	30±7[a]	25±2[a]	28±7[a]
20	34±3[a]	20±1[a]	23±4[a]
30	39±5[a]	25±3[a]	26±5[a]

Remarks: Values represent the mean±standard deviation (SD) (n=3). Different superscript letters within the same column for each heavy metal indicate significant differences (ANOVA followed by Fisher's LSD post-hoc test, equal variance assumed).

Table 2. Percentage of dead lamina cells in *E. dealbatum* moss measured across the basal, median, and apical zones of gametophore leaves after exposure to Cd, Pb, and Zn at concentrations of 0, 10, 20, and 30 mg/L.

Concentration of heavy metals	Area of lamina cell			Overall mean of dead cells in the lamina cells
	Basal cell	Median cell	Apical cell	
Cd (mg/L)				
0	0.00	0.00	0.00	0.00±0.00[a]
10	22.78	8.62	19.00	16.80±7.33[ab]
20	34.29	27.78	22.47	28.18±5.92[ab]
30	92.00	88.76	70.00	83.59±11.88[b]
Pb (mg/L)				
0	0.00	0.00	0.00	0.00±0.00[a]
10	23.91	4.08	16.07	14.69±9.99[ab]
20	8.04	4.17	56.00	22.74±28.87[ab]
30	19.72	65.71	72.88	52.77±28.84[b]
Zn (mg/L)				
0	0.00	0.00	0.00	0.00±0.00[a]
10	0.00	0.00	1.49	0.50±0.86[a]
20	0.00	1.25	4.29	1.85±2.21[a]
30	0.00	0.00	8.24	2.75±4.76[a]

Remarks: Values represent the mean±standard deviation (SD) (n=3). Different superscript letters within each heavy metal treatment indicate significant differences (Kruskal-Wallis test) with Bonferroni-adjusted pairwise comparisons.

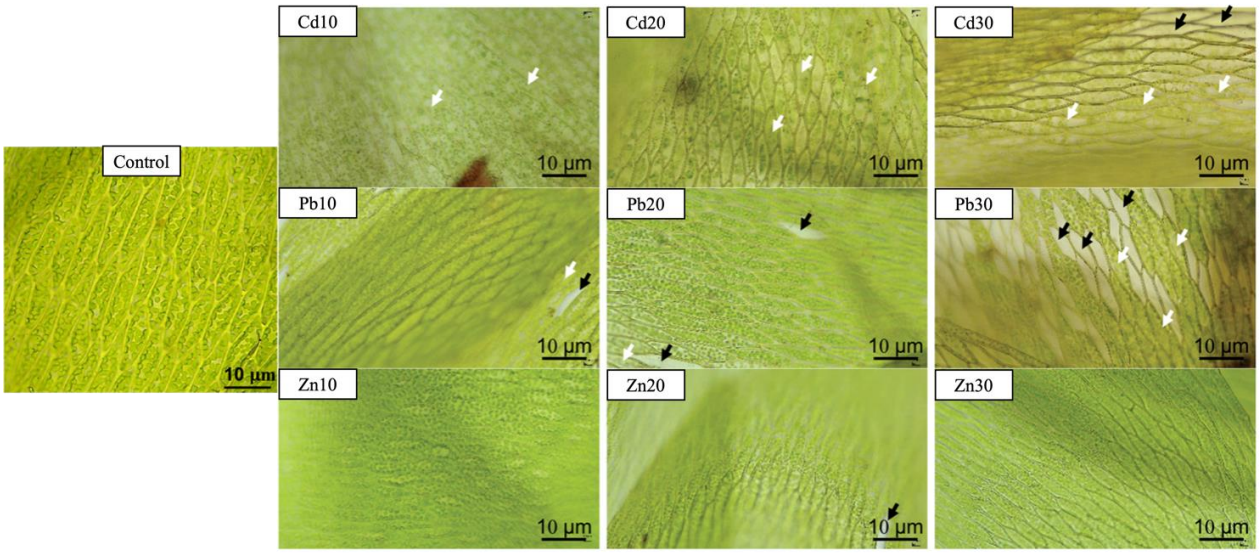

Figure 3. Median cells of the gametophore lamina from *E. dealbatum* were treated with Cd, Pb, and Zn solutions at concentrations of 10, 20, and 30 mg/L. Dead cells are indicated by empty spaces (black arrows) in the figure, while degenerating cells are marked with white arrows. Please note that basal and apical cells of the gametophore lamina were not included in the illustration.

H. involuta Chloroplast numbers could not be reliably quantified because papillose leaf cells obscured chloroplast visibility (Figure 4). Nevertheless, Cd elicited pronounced basal-zone vulnerability, with 100% cell death at 10-30 mg/L, whereas median and apical zones increased only slightly (≤17.05% and ≤3.33%). Pb and Zn had minimal effects across zones (overall means ≤10.21% and ≤2.51%, respectively), with no significant deviations from control (Table 3).

Table 3. Percentage of dead lamina cells in *H. involuta* moss measured across the basal, median, and apical zones of gametophore leaves after exposure to Cd, Pb, and Zn at concentrations of 0, 10, 20, and 30 mg/L.

Concentration of heavy metals	Area of lamina cell			Mean of dead cells in the lamina cells
	Basal cell	Median cell	Apical cell	
Cd (mg/L)				
0	0.00	0.00	0.00	0.00±0.00[a]
10	100.00	1.24	0.48	33.91±57.24[a]
20	100.00	3.13	2.34	35.16±56.16[a]
30	100.00	17.05	3.33	40.13±52.30[a]
Pb (mg/L)				
0	0.00	0.00	0.00	0.00±0.00[a]
10	3.79	0.19	3.57	2.52±2.02[a]
20	4.24	7.02	2.42	4.56±2.32[a]
30	20.42	6.97	3.25	10.21±9.03[a]
Zn (mg/L)				
0	0.00	0.00	0.00	0.00±0.00[a]
10	4.37	0.00	0.56	1.64±2.38[a]
20	0.00	0.00	1.11	0.37±0.64[a]
30	1.74	3.79	2.00	2.51±1.12[a]

Remarks: Values represent the mean±standard deviation (SD) (n=3). Different superscript letters within each heavy metal treatment indicate significant differences (Kruskal-Wallis test) with Bonferroni-adjusted pairwise comparisons.

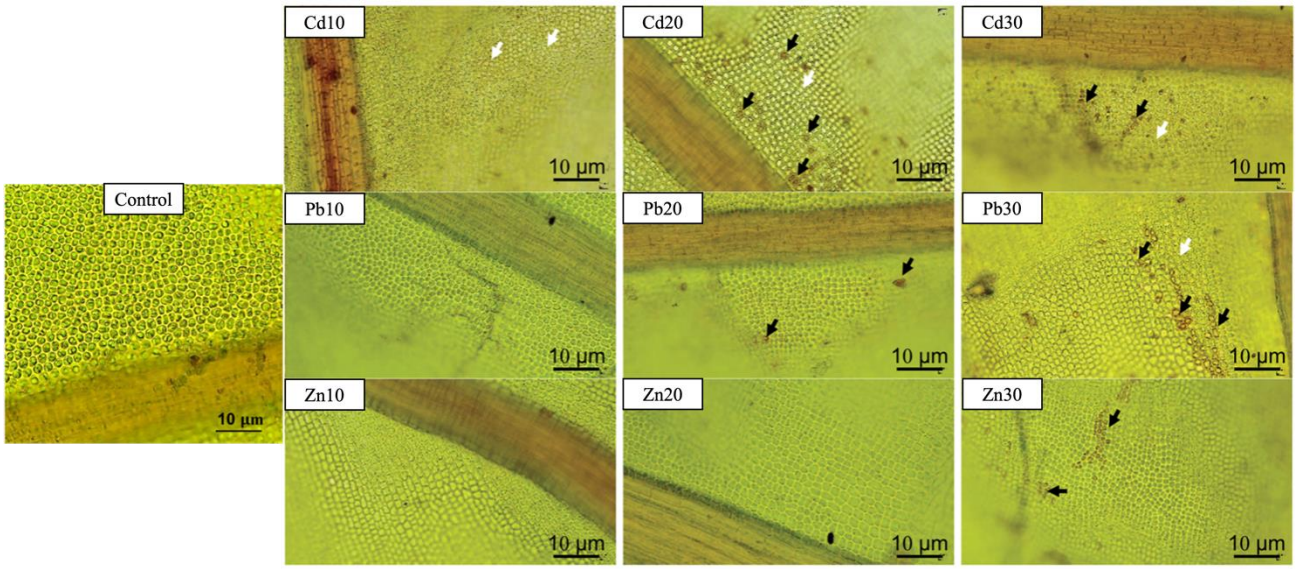

Figure 4. Median cells of gametophore lamina from *H. involuta* were treated with Cd, Pb, and Zn solutions at concentrations of 10, 20, and 30 mg/L. Dead cells are indicated by empty spaces (black arrows) in the figure, while degenerating cells are marked with white arrows. Please note that basal and apical cells of the gametophore lamina were not included in the illustration.

Overall, our findings show that Cd imposes the strongest stress on both mosses: in *E. dealbatum* through concordant losses in chloroplast numbers and large increases in lamina cell death, and in *H. involuta* through extreme basal-zone mortality. Such outcomes align with Cd's well-documented genotoxic and cytotoxic effects that compromise photosynthetic capacity and cellular integrity in other bryophytes (Sorrentino et al., 2017). Pb effects were weaker and zone-dependent, consistent with reports of

Pb-induced disruption of photosynthesis and chlorophyll stability that is often less acute than Cd (Phaenark et al., 2022; Phaenark et al., 2024). The observed species- and zone-specific patterns likely reflect anatomical and physiological differences; in *H. involuta*, basal-zone susceptibility to Cd may relate to local variation in uptake or sequestration pathways (Phaenark et al., 2022; Phaenark et al., 2024).

Zn was largely innocuous at the concentrations tested, producing no significant mortality and no notable changes in chloroplast counts. A slight, non-significant tendency toward higher chloroplast numbers in *E. dealbatum* under Zn is consistent with Zn's essential role and reports of Zn-stimulated pigment accumulation in some plants (Dang et al., 2024), while the broader literature cautions that excess Zn can still impair physiology depending on dose and context (Vijayarengan and Mahalakshmi, 2013; Akram et al., 2022; Wei et al., 2022). Because soils were not analyzed at collection sites, we cannot relate baseline field metal burdens to the laboratory responses. This is unlikely to confound our acute outcomes—the exposure solutions dominated metal availability over 72 h—but it does limit inference about how pre-exposure history might shape proteomic baselines. The absence of site-soil chemistry prevents us from assessing prior metal exposure or edaphic modifiers (pH, organic matter, texture) that can influence bioavailability. Future work should pair moss sampling with standardized soil digests (e.g., EPA 3051A/ISO 11466) and porewater extractions to calibrate biomarker bands against environmentally realistic concentrations. Together with microscopy (Figures 3 and 4), these results highlight Cd as the dominant driver of physiological damage, Pb as a moderate, zone-specific stressor, and Zn as largely non-damaging in this study, underscoring the value of mosses as bioindicators of heavy-metal pollution.

Consistent with the physiological outcomes, both moss species showed co-induction of ~90, ~100, and ~121 kDa bands under Cd (and to a lesser extent Pb), whereas Zn did not alter the overall banding pattern but only modulated band intensity. Under acute (72 h) exposure across 10-30 mg/L, this dose- and time-spanning concordance between high-molecular-weight band induction and chloroplast loss/lamina cell death supports these bands as candidate biomarkers of metal-induced damage. In contrast, the stability of constitutive bands (≈14-62 kDa) provides an internal reference for tolerance. Mechanistically, the ~90-121 kDa window plausibly includes stress-chaperone proteins (e.g., HSP90/HSP100) involved in proteostasis; their lack of induction under Zn aligns with the negligible cytological injury observed at the tested doses.

4. CONCLUSION

This study compared the short-term (72 h) responses of two common mosses, *E. dealbatum* and *H. involuta*, to Cd, Pb, and Zn under controlled laboratory conditions. Both species were more tolerant to Zn than to Pb or Cd, but the degree and pattern of sensitivity differed between species. In *E. dealbatum*, Cd caused a pronounced, dose-dependent loss of chloroplasts across lamina zones together with large increases in cell death, whereas Pb produced weaker, zone-specific effects. In *H. involuta*, chloroplast numbers could not be reliably quantified due to papillose cells, yet Cd still triggered severe basal-zone mortality, with only modest changes under Pb and minimal effects under Zn. Overall, the toxicity gradient followed Cd > Pb ≫ Zn, with species-specific manifestations (photosynthetic impairment and widespread mortality in *E. dealbatum* versus localized, basal-zone vulnerability in *H. involuta*). Proteomically, Cd and, to a lesser extent, Pb elicited high-molecular-weight SDS-PAGE bands (~90, ~100, ~121 kDa) that coincided with chloroplast loss and/or lamina cell death, whereas Zn primarily altered band intensity without changing overall patterns. These findings indicate an acute molecular–physiological association under Cd/Pb exposure rather than demonstrating long-term adaptation.

The present results suggest that these two mosses may have potential for targeted assessments of Cd and Pb under controlled conditions; however, we do not conclude that they are established bioindicators of metal pollution. Confirmation will require independent validation of the putative biomarker bands (e.g., immunoblotting, LC-MS/MS), longer and chronic exposures, environmentally realistic mixtures, and field calibration against measured metal levels. Because soils were not analyzed at collection sites, we cannot relate baseline field metal burdens to the observed laboratory responses; this limits inference about how prior exposure histories could shape proteomic baselines. Accordingly, future work should (i) expand to other metals/metalloids and mixtures, (ii) incorporate time-course dose-response designs over

longer durations, (iii) identify and verify differentially expressed proteins, and (iv) pair moss sampling with standardized soil digests and porewater extractions to derive field-relevant thresholds before any operational biomonitoring is proposed.

ACKNOWLEDGEMENTS

The authors would like to acknowledge the Science Laboratory for Education (SLE) at Mahidol University (Kanchanaburi Campus) for providing laboratory facilities.

AUTHOR CONTRIBUTIONS

Supatra Chunchob: Conceptualization, Methodology, Software, Validation, Formal analysis, Investigation, Resources, Data curation, Writing-original draft preparation, Writing-review and editing, Visualization, Supervision, Project administration. Susana Giyasov: Validation, Formal analysis, Investigation, Resources, Data curation. Chetsada Phaenark: Validation, Formal analysis, Investigation, Resources, Data curation, Writing-original draft preparation, Writing-review and editing. Weerachon Sawangproh: Conceptualization, Methodology, Validation, Investigation, Writing-original draft preparation, Writing-review and editing, Visualization, Supervision. All authors have read and agreed to the published version of the manuscript.

DECLARATION OF CONFLICT OF INTEREST

The authors declare that they have no known competing financial interests or personal relationships that could have appeared to influence the work reported in this paper.

REFERENCES

Akram MW, Sajid M, Ahmad A, Waqar M, Kusar S, Iqbal A, et al. Effect of foliar spray of ascorbic acid on nodulation, gas exchange attributes and mineral ion contents of *Pisum sativum* under zinc stress. Plant Protection 2022;6(2):101-11.

Barbara C, Braglia R, Basile A, Cobianchi RC, Forni C. Proteomics and bryophytes: A comparison between different methods of protein extraction to study protein synthesis in the aquatic moss *Leptodictyum riparium* (Hedw.). Caryologia 2007;60(1-2):102-5.

Basile A, di Nuzzo RA, Capasso C, Sorbo S, Capasso A, Carginale V. Effect of cadmium on gene expression in the liverwort *Lunularia cruciata*. Gene 2005;356:153-9.

Basile A, Sorbo S, Conte B, Cardi M, Esposito S. Ultrastructural changes and Heat Shock Proteins 70 induced by atmospheric pollution are similar to the effects observed under in vitro heavy metals stress in *Conocephalum conicum* (Marchantiales-Bryophyta). Environmental Pollution 2013; 182:209-16.

Bellini E, Betti C, Sanità di Toppi L. Responses to cadmium in early-diverging Streptophytes (Charophytes and Bryophytes): Current views and potential applications. Plants 2021; 10(4):Article No. 770.

Bradford MM. A rapid and sensitive method for the quantitation of microgram quantities of protein using the principle of protein dye binding. Analytical Biochemistry 1976;72(1-2):248-54.

Cârdei P, Tudora C, Vlăduț V, Pruteanu MA, Găgeanu I, Cujbescu D, et al. Mathematical model to simulate the transfer of heavy metals from soil to plant. Sustainability 2021;13(11):Article No. 6157.

Chaudhuri S, Roy M. Global ambient air quality monitoring: Can mosses help? A systematic meta-analysis of literature about passive moss biomonitoring. Environment, Development and Sustainability 2024;26:5735-73.

Dang K, Mu J, Tian H, Gao D, Zhou H, Guo L, et al. Zinc regulation of chlorophyll fluorescence and carbohydrate metabolism in saline-sodic stressed rice seedlings. BMC Plant Biology 2024;24(1):Article No. 464.

Eddy A. A Handbook of Malesian Mosses. Vol. 2 Leucobryaceae to Buxbaumiacea. London, UK: Natural History Museum Publications; 1991.

Elliott DD, Velasquez PM. Non-vascular plants [Internet]. 2024 [cited 2024 July 23]. Available from: https://bio.libretexts.org/Bookshelves/Botany/Botany_in_Hawaii_(Daniela_Dutra_Elliott_and_Paula_Mejia_Velasquez)/06%3A_Plant_evolution_and_non-vascular_plants/6.03%3A_Non-vascular_plants.

Esposito S, Cobianchi RC, Sorbo S, Conte B, Basile B. Ultrastructural alterations and HSP70 induction in *Elodea canadensis* Michx. exposed to heavy metals. Caryologia 2007;60(1-2):115-20.

Esposito S, Sorbo S, Conte B, Basile A. Effects of heavy metals on ultra- structure and HSP70s induction in the aquatic moss *Leptodictyum riparium* Hedw. International Journal of Phytoremediation 2012;14(4):1-13.

Gallo V, Serianni VM, Imperiale D, Zappettini A, Villani M, Marmiroli M, et al. Protein analysis of *A. halleri* and *N. caerulescens* hyperaccumulators when exposed to nano and ionic forms of Cd and Zn. Nanomaterials 2022;12(23):Article No. 4236.

Kuziemska B, Klej P, Wysokiński A, Jaremko D, Pakuła K. Yielding and bioaccumulation of zinc by cocksfoot under conditions of different doses of this metal and organic fertilization. Agronomy 2022;12(3):Article No. 686.

Laemmli UK. Cleavage of structural proteins during the assembly of the head of bacteriophage T4. Nature 1970;227:680-5.

Leon-Mediavilla J, Senovilla M, Montiel J, Gil-Diez P, Saez A, Kryvoruchko IS, et al. MtMTP2-facilitated zinc transport into intracellular compartments is essential for nodule development in *Medicago truncatula*. Frontiers in Plant Science 2018;9:Article No. 990.

Li GK, Gao J, Peng H, Shen Y, Ding H, Zhang ZM, et al. Proteomic changes in maize as a response to heavy metal (lead) stress revealed by iTRAQ quantitative proteomics. Genetics and Molecular Research 2016;15(1):1-14.

Mlecnik B, Scheideler M, Hackl H, Hartler J, Sánchez-Cabo F, Trajanoski Z. PathwayExplorer: web service for visualizing high-throughput expression data on biological pathways. Nucleic Acids Research 2005;33:633-7.

Nayar G, Altman R. Heterogeneous network approaches to protein pathway prediction. Compuational and Structural Biotechnology Journal 2024;23:2727-39.

Oishi Y, Hiura T. Bryophytes as bioindicators of the atmospheric environment in urban-forest landscapes. Landscape and Urban Planning 2017;167:348-55.

Parrish J, Yu J, Liu G, Hines J, Chan J, Mangiola B, et al. A proteome-wide protein interaction map for *Campylobacter jejuni*. Genome Biology 2007;8:Article No. R130.

Phaenark C, Niamsuthi A, Paejaroen P, Chunchob S, Cronberg N, Sawangproh W. Comparative toxicity of heavy metals Cd, Zn, and Pb to three acrocarpous moss species using chlorophyll contents. Trends in Sciences 2022;20(2):Article No. 4287.

Phaenark C, Seechanhoi P, Sawangproh W. Metal toxicity in *Bryum coronatum* Schwaegrichen: Impact on chlorophyll content, lamina cell structure, and metal accumulation. International Journal of Phytoremediation 2024;26(8): 1336-47.

Printarakul N, Meeinkuirt W. The bryophyte community as bioindicator of heavy metals in a waterfall outflow. Scientific Reports 2022;12(1):Article No. 6942.

Rachna P, Vashistha BD. Effects of heavy metals on protonemal growth and bud formation in the moss *Hydrogonium arcuatum*. Agricultural Science Digest 2017;37(2):117-21.

Rehman K, Ashraf S, Rashid U, Ibrahim M, Hina S, Iftikhar T, et al. Comparison of proximate and heavy metal contents of vegetables grown with fresh and wastewater. Pakistan Journal of Botany 2013;45(2):391-400.

Rizvi A, Ahmed B, Khan MS, Rajput VD, Umar S, Minkina T, et al. Maize associated bacterial microbiome linked mitigation of heavy metal stress: A multidimensional detoxification approach. Environmental and Experimental Botany 2022; 200:Article No. 104911.

Sardar R, Zulfiqar A, Ahmed S, Shah AA, Iqbal RK, Hussain S, et al. Proteomic changes in various plant tissues associated with chromium stress in sunflower. Saudi Journal of Biological Sciences 2022;29(4):2604-12.

Shafiq S, Zeb Q, Ali A, Sajjad Y, Nazir R, Widemann E, et al. Lead, cadmium and znc phytotoxicity alter DNA methylation levels to confer heavy metal tolerance in wheat. International Journal of Molecular Sciences 2019;20(19):Article No. 4676.

Shaheen S, Majeed Z, Mahmood Q. The assessment of metal resistance through the expression of hsp-70 and ho-1 proteins in giant reed. International Journal of Plant Biology 2023;14(3):687-700.

Shlomi T, Segal D, Ruppin E, Sharan R. QPath: A method for querying pathways in a protein-protein interaction network. BMC Bioinformatics 2006;7:Article No. 199.

Shukla SR, Rao RV, Sharma SK, Kumar P, Sudheendra R, Shashikala S. Physical and mechanical properties of plantation-grown *Acacia auriculiformis* of three different ages. Australian Forestry 2007;70(2):86-92.

Sorrentino MC, Capozzi F, Giordano S, Spagnuolo V. Genotoxic effect of Pb and Cd on in vitro cultures of *Sphagnum palustre*: An evaluation by ISSR markers. Chemosphere 2017;181: 208-15.

Stanković J, Sabovljević A, Sabovljević MS. Bryophytes and heavy metals: A review. Acta Botanica Croatica 2018; 77(2):109-18.

Suman J, Uhlik O, Viktorova J, Macek T. Phytoextraction of heavy metals: A promising tool for clean-up of polluted environment? Frontiers in Plant Science 2018;9:Article No. 1476.

Sun S-Q, He M, Cao T, Zhang Y-C, Han W. Response mechanisms of antioxidants in Bryophyte (*Hypnum plumaeforme*) under the stress of single or combined Pb and/or Ni. Environmental Monitoring and Assessment 2009;149(1-4):291-302.

Sun SQ, He M, Wang GX, Cao T. Heavy metal-induced physiological alterations and oxidative stress in the moss *Brachythecium piligerum* chad. Environmental Toxicology 2011;26(5):453-8.

Świsłowski P, Nowak A, Rajfur M. The influence of environmental conditions on the lifespan of mosses under long-term active biomonitoring. Atmospheric Pollution Research 2021;12(10):Article No. 101203.

Tremper AH, Agneta M, Burton S, Higgs DEB. Field and laboratory exposures of two moss species to low level metal pollution. Journal of Atmospheric Chemistry 2004;49:111-20.

Usman K, Souchelnytskyi S, Zouari N, Abu-Dieyeh MH. Proteomic analysis of *T. qataranse* exposed to lead (Pb) stress reveal new proteins with potential roles in Pb tolerance and detoxification mechanism. Frontiers in Plant Science 2022;13:Article No. 1009756.

Vijayarengan P, Mahalakshmi G. Zinc toxicity in tomato plants. World Applied Sciences Journal 2013;24(5):649-53.

Wei C, Jiao Q, Agathokleous E, Liu H, Li G, Zhang J, et al. Hormetic effects of zinc on growth and antioxidant defense system of wheat plants. Science of the Total Environment 2022;807(Part 2):Article No. 150992.

Wuana RA, Okieimen FE. Heavy metals in contaminated soils: A review of sources, chemistry, risks and best available strategies for remediation. International Scholarly Research Notices 2011;2011(1):Article No. 402647.

Environment and Natural Resources Journal

Volume 24
Issue 2
2026

Pollution Levels of Lead and Copper in the Areas Surrounding Diyala State Company, Iraq

Duha Abdulhakim Mohammed*, Munther Hamza Rathi, and Esam Hamid Hummadi

Department of Biology, College of Science, University of Diyala, Baqubah, Iraq

ARTICLE INFO

Received: 25 Jul 2025
Received in revised: 22 Oct 2025
Accepted: 29 Oct 2025
Published online: 16 Feb 2026
DOI: 10.32526/ennrj/24/20250191

Keywords:
Industrial pollution/ Diyala State Company/ Heavy metals/ Lead/ copper/ Phytoremediation/ Bioremediation

*** Corresponding author:**
E-mail:
duhaabdulhakim@uodiyala.edu.iq

ABSTRACT

Pollution by toxic metals represents a great environmental concern. Industrial activities release high levels of metals into the environment, adversely affecting human health. This study aimed to assess levels of lead and copper contamination in the areas surrounding Diyala State Company as well as to evaluate the efficiency of roadside plants in absorbing these metals from soil by their leaves, thereby exploring their role in reducing environmental pollution. Soil and leaf samples were collected from four directions surrounding the company and at distances in each direction (100, 500, 1,000, 2,000 meters). Leaf samples were collected from four plants: *Eucalyptus camaldulensis*, *Ricinus communis*, *Dodonaea viscosa*, and *Malva parviflora* between June and August 2024. The findings revealed high concentrations of lead and copper. The highest lead concentration was in the eastern part (3 mg/kg) in *E. camaldulensis* at site E3. The highest copper concentration was in the northern part (1.36 mg/kg) in *R. communis* at site N2, and *D. viscosa* was recorded with the highest lead concentration (2.43 mg/kg) in the northern part at site N4. *M. parviflora* showed higher lead concentration in the western part (1.58 mg/kg) at site W1. The maximum bioaccumulation coefficient for lead uptake was exhibited in *E. camaldulensis*, followed by *R. communis*, which also demonstrated the highest uptake of copper in most locations, particularly in the northern part. According to their efficiency in heavy metal uptake and accumulation, the plants were ranked as follows: *E. camaldulensis* > *R. communis* > *D. viscosa* > *M. parviflora*. It is clear that these plants have shown a high capacity for absorbing heavy metals, which positively impacts the environment and allows for their inclusion in bioremediation programs.

HIGHLIGHTS

- The ability of roadside plants to absorb lead and copper was evaluated around Diyala State Company.
- Shrubby and herbaceous plants were tested for their capacity to absorb heavy metals.
- The highest bioaccumulation coefficient for lead revealed in *E. camaldulensis* whilst *R. communis* had the higher capacity for copper uptake.
- The examined Plants exhibited promise for phytoremediation with potential efficiency ranking as *E. camaldulensis* > *R. communis* > *D. viscosa* > *M. parviflora*.

1. INTRODUCTION

Industrial enterprises emit a wide range of pollutants during production processes, such as heavy metals, solid and liquid particulate matter, harmful gases, and high waste heat (Zhao and Yin, 2024). Industrial pollution poses a growing threat to health and ecosystems and this is expected to continue increasing, requiring effective remedial approaches and monitoring programs to significantly reduce its impact on health and the environment (Ondrasek et al., 2025). Diyala State Company is an industrial corporation located in Baqubah City, Diyala Province, Iraq. The company specializes in manufacturing electrical appliances such as fans, irons, electrical meters, power and distribution transformers. These devices contain toxic materials, including lead, cadmium, nickel, iron and copper, and therefore can affect the environment and human health (Alkouh et al., 2023).

Many of these metal ions are released into the environment, causing serious pollution. Heavy metal ions also negatively affect the aquatic and terrestrial

Citation: Mohammed DA, Rathi MH, Hummadi EH. Pollution levels of lead and copper in the areas surrounding Diyala State Company, Iraq. Environ. Nat. Resour. J. 2026;24(2):186-198. (https://doi.org/10.32526/ennrj/24/20250191)

animals and plants. It is well known that heavy metal toxicity causes various types of cancer, kidney and liver damage, skin problems, among others, as a result of toxic exposure to heavy metals (Kumar and Singh, 2024). As a result of its various industrial, domestic, agricultural, medical and technological applications, it has become widely spread in the environment (Mohammed et al., 2023).

Lead can enter water and soil through electrical waste and distribution or plumbing lines. Plumbing parts that contain lead, such as solder, galvanized pipes, and brass fittings, which can contain up to 8% lead, can leach lead (Fawkes and Sansom, 2021). Current studies show that the non-biodegradability of lead and continuous use lead concentrations accumulate in the environment and cause various harmful effects, such as neurotoxicity and alteration in the psychological and behavioral development of various organisms (Kumar and Singh, 2024). Pollution by copper is becoming increasingly severe and seriously threatens human health and ecosystems. It was reported that copper concentrations in wastewater range from about 2.5 mg/L to 10,000 mg/L, one of the risks posed by untreated industrial wastewater is (Liu et al., 2023). Metals are among the most dangerous pollutants as they are not biodegradable and easy to accumulate in the food chain (Hussein et al., 2021). Therefore, its pollution must be mitigated and its spread in the environment limited by using some eco-techniques. Biological technologies such as phytoremediation, agricultural waste, fruit peels, and algae are considered safe, much cheaper, economical, eco-friendly, and almost free of adverse effects (Zahra et al., 2020). There are some plant species with high phytoremediation capacity due to their ability to absorb heavy metals and reduce pollution, especially in industrial and residential areas (Mocek-Płóciniak et al., 2023). Plants are categorized by their short life cycle, high capacity to tolerate and absorb metals, and accumulate it in their root system (Mazumdar and Das, 2015). Many plant species were used as bio-adsorbent agents, such as *Calotropis gigantea*, *Sida cordifolia*, *R. communis*, *Spartina alterniflora*, *Alternanthera philoxeroides*, *Eichhornia crassipes* (Wang et al., 2021) and *E. camaldulensis* (Madejon et al., 2017).

Local studies in Iraqi and regional countries have evaluated soil and plant contamination with heavy metals such as lead and copper. Several studies have been conducted in Iraq on heavy metal pollution and phytoremediation in different areas. However, the impact of pollution from the Diyala State Industrial Company on the surrounding areas has not yet been studied. This study is the first to evaluate some of the local plants found in these areas, which have not been previously studied, such as *M. Parviflora*, *R. communis*, *D. viscosa* in terms of their quantitative capacity to absorb lead and copper. This approach enables the identification of plants suitable for local phytoremediation programs, providing new insights not covered in previous studies in the region.

A study revealed levels of lead in soil and plants estimated by 3.57 mg/kg and 1.97 mg/kg, respectively (Mahmood and Rathi, 2024). In Baghdad Province, Amer and Abdulhussein (2022), showed that the lead levels in soil are similar to those in the current study (2.2 mg/kg). The concentrations of lead and copper in Kirkuk, north of Iraq, were elevated in soil samples and some local plants by 2.2 mg/kg and 67 mg/kg, and 55 mg/kg and in plants 11 mg/kg for copper, respectively (Khurshid et al., 2022). Mahmood and Rathi (2024) found that the lead concentrations exceeded the internationally permissible limit in soil of Basra, south of Iraq, by 37.32 mg/kg. They also found 24.13 mg/kg concentration in soil in Maysan Province. In leaf samples, lead levels reached 0.17 mg/kg and 0.13 mg/kg in Basra and Maysan, respectively (Mahdi et al., 2020). A study conducted in Riyadh City in Saudi Arabia on palm soil exhibited lead levels of 5.08 mg/kg and copper levels of 11.36 mg/kg, affecting soil fertility and the quality of agricultural production (Alarifi et al., 2022). In Isfahan Province in Iran, lead concentrations in soil of Tang-e Douzan mine/Isfahan were estimated at 2,500 mg/kg, and were 298 mg/kg in local plants (Hesami et al., 2018).

Diyala State Company is among the biggest and oldest industrial facilities in the area, and due to its diverse industrial processes, heavy metals (e.g., lead and copper) and toxins are released to the surrounding environment and transported and accumulate in the human body, affecting the health of the residents in the area. Due to the current expansion in residential population, buildings are becoming close to the company boundaries and negatively affecting health and quality of people life in these areas causing health problems such as respiratory or skin diseases due to this pollution, therefore, this study was designed to determine the extent of pollution by lead and copper in the areas surrounding the company and identify the ability of some plant species as eco-friendly way to absorb and accumulate these metals in order to reduce pollution levels. This study offers scientific data to

help decision-makers in the local governorate to deal with this pollution and promote future studies on the effects of heavy industries in Iraq on the environment and human health, and find eco-friendly solutions.

2. METHODOLOGY

2.1 Description of the study area

Diyala State Company is an Iraqi industrial company in Diyala Province, Baqubah District, located northeast of Baghdad Province. It is located southeast of Baqubah City between latitudes 33.7459° and longitudes 44.6390°. The area of Diyala State Company is estimated at 400,000 square meters. It is an industrial company that manufactures electrical appliances. It is an industrial area with no markets, and traffic is heavy and continuous. The population density is low. There are blacksmiths and car repair shops. The industrial density is very low and is considered a relatively distant area from the center of Baqubah city (Mahmood and Rathi, 2024), as shown in Figure 1.

2.2 Samples collection

The leaf samples were collected with the required measurements between June and August 2024 from four plants included *E. camaldulensis*, *D. viscosa*, *R. communis*, and *M. parviflora* located on the sides of roads in the areas surrounding Diyala State Company from four directions in Baqubah City (North, South, East, West) as shown in Table 1. The intact leaves were taken from bottom, middle, and top of the plants in clean bags labeled with the date and type of site and kept in the freezer until transported to the laboratory. The soil samples in which the plant grows were collected at depth of 10-15 cm from the surface in re-sealable plastic bags labeled with the date and site (Bibi et al., 2023; Jiang et al., 2023).

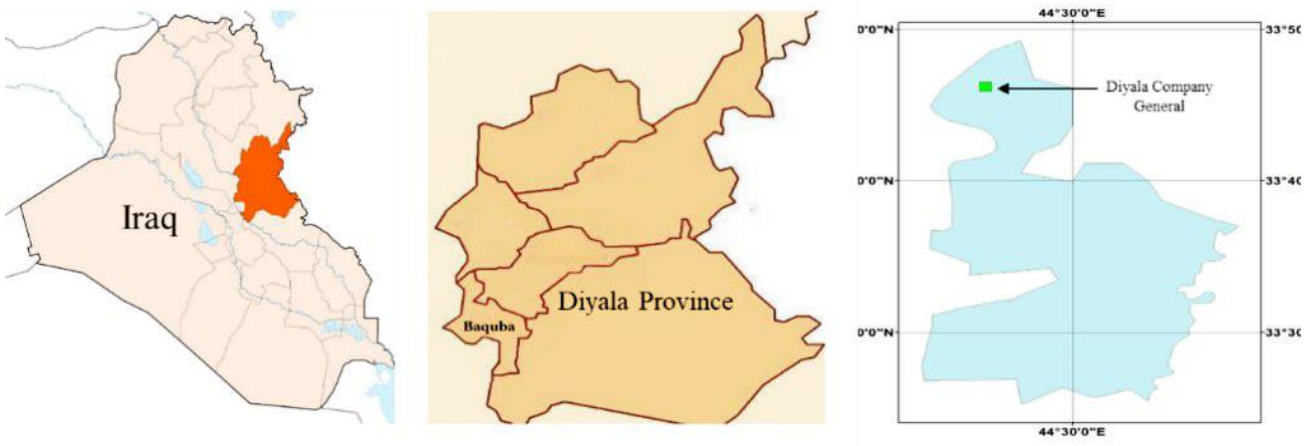

Figure 1. Sampling map of the study area surrounding Diyala Company State (Rasheed et al., 2024)

2.3 Estimating the concentrations of lead and copper in samples

The levels of lead and copper in leaves and soil were estimated via a flame atomic absorption spectrophotometer (FAAS) at Ibn Sina Center, Ministry of Industry and Minerals, Iraq according to Abdulhay and Rathi (2017).

2.4 Plant leaf samples analysis

The leaves were first washed with tap water to remove dust, then washed with distilled water to remove any contaminants. The samples were dried in an oven at 70°C. After that, they were ground using a coffee grinder to get fine powder and stored in airtight containers for chemical digestion. Half a gram of each plant powder sample was weighed and placed in a microwave digestion device with a mixture of nitric acid and hydrogen peroxide (HNO_3:H_2O_2) (5:1) until the solution became clear. The solution was left at 150°C for 25 min, then cooled to room temperature and shaken well before filtering. The volume of each sample was made up to 50 mL with deionized water to standardize the calculated elemental concentration. The recovery rate for both lead and copper was within the acceptable range (92-98%). A portion of the resulting solution was withdrawn and used for atomic absorption spectrometry analysis (Shi et al., 2023; Rawat et al., 2024).

Table 1. Sampling sites based on directions and distances

Sites	Directions	Distances (m)	Regions	Samples collection coordinates	
				N°	E°
N 1	North	100	Main Street of the Company	33.77056885003631	44.59013173172016
N2		500	Main Street of the Company	33.77280737955255	44.59007808754462
N3		1,000	Agriculture Floor	33.778586261010126	44.59031412199417
N4		2,000	Agriculture Floor	33.78755702369312	44.589917155166134
S1	South	100	Main Street of the Company	33.768722688111474	44.590206833570214
S2		500	Main Street of the Company	33.76506592139569	44.59018537589413
S3		1,000	Al-Rahma	33.76059731901732	44.590560885174455
S4		2,000	Al-Yarmouk	33.75169509745489	44.591322632494304
E1	East	100	Main Street of the Company	33.76961455874416	44.59126898826168
E2		500	Main Street of the Company	33.769623477404664	44.59560343805435
E3		1,000	Jerusalem Intersection	33.76955212809353	44.60104295793418
E4		2,000	Huwaider	33.76942726665334	44.61180398044811
W1	West	100	Main Street of the Company	33.76957888409708	44.58910176353766
W2		500	Main Street of the Company	33.76945402271635	44.58478877135697
W3		1,000	Jerusalem intersection	33.769445104035036	44.57934925160782
W4		2,000	Al-Hadid Village	33.76931132376585	44.56859895782609

2.5 Soil samples analysis

Soil samples were collected from the same sites where the plant samples were collected. The samples were first dried in an oven at 70°C to prevent evaporation of the elements and then passed through 2 mm sieve to remove large impurities and gravel. Finally, they were ground to a homogeneous consistency and were placed in clean, sealed containers. To perform the chemical digestion, 1 g of soil sample was digested in microwave using a mixture of HNO_3:HF:HCl (3:1:1) until a clear solution was obtained. The solution was then left at 150°C for 25 min and cooled to room temperature. The volume of each sample was made up to 50 mL with deionized water to standardize the calculated element concentration. The recoveries for both lead and copper were within the acceptable range (92-98%). A portion of the resulting solution was withdrawn and used for atomic absorption spectrometry analysis (Shi et al., 2023; Rawat et al., 2024).

2.6 Bioaccumulation factors (BAF)

The BAF was used to assess the ability of plants to absorb and remove heavy metals from soil and was calculated using equation (1) (Aladesanmi et al., 2019):

$$BAF = \frac{C\ plant}{C\ soil} \quad (1)$$

Where: C_{plant}=level of the metal element in the plant (mg/kg); C_{soil}=level of the same metal element in the plant soil (mg/kg).

2.7 Statistical analysis

MS Excel® was used to analyze the data statistically and find the mean and standard deviation of the samples using a completely random design known as complete random distribution.

3. RESULTS AND DISCUSSION

3.1 Level of lead and copper in plant leaves and soil in the northern part

In this experiment, we tested the levels of the heavy metals in the north site of the company. The results indicated a high levels of the metals in this area. Compared with the approved standard values (0.3 mg/kg), all leaf samples collected fromthis area showed variable levels of contamination with lead. The highest level of lead in N4 site ranged between 2.43 mg/kg in leaves of *D. viscosa*, and the lowest level in *M. parviflora* leaves reached up to 1.96 mg/kg in N1 site (Table 2). In plant soil, the highest level of lead was in *R. communis* (2.59 mg/kg) in site N2, followed by *M. parviflora* and *D. viscosa* (2.42 mg/L and 1.62 mg/kg) in sites N1 and N4, respectively. *E. camaldulensis* revealed the lowest concentration (1.26 mg/kg) at site N3. The result was statistically

significant ($p<0.05$), between the soil of *M. parviflora*, *E. camaldulensis*, and *D. viscosa*, and not statistically significant ($p\geq0.05$) in soil of *M. parviflora* and *R. communis*, and between soil of *E. camaldulensis* and *D. viscosa* compare with the natural abundance in Table 2.

As for copper, the highest concentration was in leaves of *R. communis* at site N2 (1.36 mg/kg), and the lowest level was in *M. parviflora* at site N1 (0.64 mg/kg). It was found that all the plant leaves were polluted with copper (0.2 mg/kg), with no significant differences between them and other plants. The highest concentration of copper in plant soil was in *D. viscosa* (6.90 mg/kg) at site N4, followed by *E. camaldulensis* and *R. communis* (5.22 mg/kg and 5.15 mg/kg) in sites N3 and N2, respectively. *M. parviflora* exhibited the lowest concentration (5.07 mg/kg) in site N1. No significant differences appeared between the soils of all plants and the concentrations obtained with the natural abundance of copper (23.13 mg/kg) (Abd Al-wahab, 2020).

The higher lead levels in the soil of the plant in the N1 and N2 sites may be attributed to the proximity of the two sites to the company, compared to N3 and N4, which are further away. Even if industries have relatively low levels of heavy metal emissions, they may contribute to the pollution of the surrounding agricultural soil through continuous emissions (Yao et al., 2024). The findings indicated that the sites with high copper pollution were the sites that were farthest from the company (N3 and N4) compared to the closer sites (N1 and N2). This could be explained by the transport of the pollutants to sites far from the manufacturing company by weather conditions (e.g., wind). Pollutants could accumulate by settling in soil or water in areas far from the pollution source and cause high pollution in those areas. In addition to the contaminants transported by the company, human activities in areas far from the manufacturing company may play a role in increasing pollution levels, such as agriculture or local manufacturing, because they are residential areas that are more exposed to pollution and have constant human traffic. In addition to the smoke emitted from cars resulting from the combustion of gasoline, to which tetramethyl lead or tetraethyl lead is added to improve the performance of the car engine (Kayiranga et al., 2023). These results are consistent with a survey conducted in Diyala Province by (Mahmood and Rathi (2024) in which lead reached its highest level in soil of the industrial area (2.34 mg/kg). The current study agreed with the study conducted in Morocco, Tadla Plain by Ennaji et al. (2020) which showed that the lead level exceeded the permissible limit in farm soil and reached 31.72 mg/kg. The findings of the current study conflicted with a survey conducted in Diyala Province by Abd Al-wahab (2020), in which the copper levels exceeded the average natural abundance, reaching 33.00 mg/kg. The reason for the consistency of our results with a study conducted in 2024 is that there was a decrease in element concentrations compared to another study conducted in 2022 in the same province. This could be attributed to a relative improvement in environmental conditions in recent years or the implementation of some measures to reduce pollution. Differences in climatic factors or the timing of sample collection, such as the season or the amount of rainfall, may also have played a role in this decrease, which helps in environmental restoration (Armiento et al., 2022).

Table 2. Lead and copper concentrations in soil and plant leaves at four sites in north of Diyala State Company

Site	Sample	Metals concentration (mg/kg) (mean±SD)			
		Lead	Natural abundance value	Copper	Natural abundance value
N1	*M. parviflora*	1.966±0.035355^{a}	0.3	0.6425±0.077075^{a}	0.2
	Soil	2.425±0.033941^{b}	1.08	5.074±0.060811^{c}	23.13
N2	*R. communis*	2.3225±0.006364^{b}	0.3	1.365±0.062225^{a}	0.2
	Soil	2.5995±0.023335^{b}	1.08	5.158±0.079903^{c}	23.13
N3	*E. camaldulensis*	2.413±0.008485^{b}	0.3	1.017±0.106066^{a}	0.2
	Soil	1.264±0.035355^{a}	1.08	5.226±0.078489^{c}	23.13
N4	*D. viscosa*	2.4335±0.062933^{b}	0.3	1.124±0.017678^{a}	0.2
	Soil	1.6285±0.053033^{a}	1.08	6.906±0.052326^{c}	23.13

* Different letters vertically mean statistically significant differences ($p<0.05$).

3.1.1 Bioaccumulation factor in north sites

The highest value of lead bioaccumulation (1.62) was in *E. camaldulensis* at site north 1000, followed by *D. viscosa* at site north 2000 by 1.10, then *R. communis* at site north 500 by 0.89, and *M. parviflora* with the lowest BAF value of 0.81 (Figure 2). The highest BAF value for copper was in *R. communis* at site north 500 (BAF=0.26), *E. camaldulensis* at site north 1000 (BAF=0.20), then *D. viscosa* at site north 2000 with BAF of 0.18, and *M. parviflora* at site north 100 (BAF=0.12).

The results indicate that *E. camaldulensis* was the best in removing lead from industrial areas, which is consistent with the study of Mahmood and Rathi (2024), a study conducted in Diyala Province, where the value of the bioaccumulation factor for lead in plant leaves was estimated at 0.89. A study by Kaur et al. (2021) demonstrated that *R. communis* was most efficient in eliminating copper. The findings of the current study showed that the bioaccumulation factor changes with the change in heavy element type and plant type. Also, the physiological and anatomical factors within the plant can affect the absorption of metals because they may not accumulate in their parts if the bioaccumulation factor is less than 1 (Satpathy et al., 2014). *Eucalyptus* can adapt to different conditions and therefore it is efficient in metals absorption,especially lead (Madejon et al., 2017). In addition, *R. communis* can tolerate high levels of heavy metals due to its strong root system and tissue characteristics (Yeboah et al., 2021). The ability of plants to absorb and accumulate heavy metals varies across species, which in turn affects the levels of these elements in the ecosystem. Heavy metals are continuously absorbed by plants throughout their growth and accumulate in plant tissues, so some plants are used to absorb and accumulate heavy metals from contaminated soil (Gani et al., 2024).

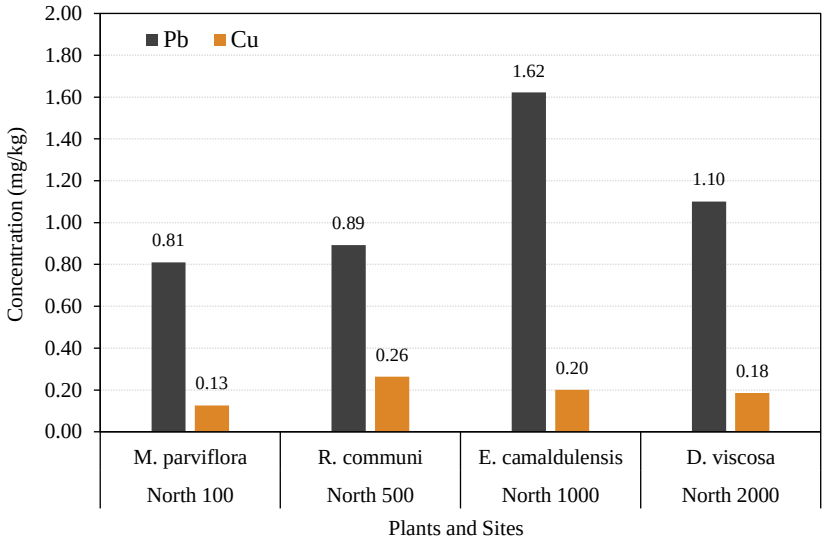

Figure 2. Plant BAF at four locations in north of Diyala State Company

3.2 Levels of lead and copper in plant leaves and soil in the southern part

The results showed that all soils and plant leaves were polluted with lead and copper in close proportions with the same plant, *E. camaldulensis*, present at three sites (S1, S3, and S4). In addition, *E. camaldulensis* tolerate high levels of heavy metals in soil and leaves than other species growing in the same environment (Madejon et al., 2017). The highest concentration of lead in the S4 region was 2.07 mg/kg in leaves of *E. camaldulensis*, and the lowest concentration (1.21 mg/kg) was revealed in *D. viscosa* leaves insite S2. Compared with the approved standard values, all leaves in the plants in all the studied areas were polluted with lead. The result was statistically significant ($p<0.05$) between *E. camaldulensis* and other plants. As for the plant soil, the highest concentration of lead was in *D. viscosa*, which was 2.73 mg/kg in site S2, followed by *E. camaldulensis* (2.68 mg/kg, 1.70 mg/kg) in sites S4 and S3, respectively. Also, *E. camaldulensis*, which had the lowest concentration (1.26 mg/kg) in site S1, with significant differences ($p<0.05$) between soil of *E. camaldulensis* and *D. viscosa*, in comparison with the natural abundance as shown in Table 3.

The highest concentration of copper was in the leaves of *E. camaldulensis* at site S4, at a concentration of 1.14 mg/kg, and the lowest level was in *E. camaldulensis* at site S3, at 0.90 mg/kg. It was found that all the leaves were polluted with copper. In plant soil, the highest concentration of copper was in *D. viscosa*, reaching 7.39 mg/kg at site S2, followed by *E. camaldulensis* (7.11, 6.40, 6.03 mg/kg) at sites S1, S4 and S3, respectively. The result was statistically significant ($p<0.05$) between soils of all plants, and the concentrations obtained with the natural abundance of the element indicate that it was not polluted with copper in large quantities compared to its natural abundance (Abd Al-wahab, 2020). Acidity and the ketone exchange capacity are the two most significant physical and chemical characteristics that may contribute to the buildup of heavy metals in soil and plants. These are the main elements influencing how metals migrate through the soil and how bioavailable they are. Elevated acidity makes these metals more soluble, which promotes their uptake by plants and soil. Element penetration into the soil is facilitated by poor exchange capacity, therefore, cation exchange capability is essential to stabilize these metals (Ikhajiagbe et al., 2019).

The findings of the study contradicted a study conducted by Jabara (2024) in Diyala, where the study showed that all soil in all studied areas was polluted with lead and copper, 61.2 and 22.1 mg/kg respectively. The results also conflicted with the results of a study conducted in Baghdad by Amer and Abdulhussein (2022), in which they showed that lead levels in the soil of an industrial area reached 19.50 mg/kg. Another study conducted in China by Yuan et al. (2021) conflicted with the current study, which had very high lead levels in soil, its level reached 30.74 mg/kg. The findings of the current study disagree with a study by Alberto et al. (2023), which showed that copper exceeded the permissible limit in agricultural soils up to 36 mg/kg. The results of previous studies show higher levels than those of the current study. This may be explained by the fact that the environment in this location is less polluted than other regions, especially big cities, such as the capital, due to the large number of industrial areas and the population movement. Rapid industrial growth and human activities all play a role in increasing pollution (Vuong et al., 2025).

Table 3. Levels of lead and copper concentrations of soil and leaves in south of Diyala State Company for four sites

Site	Sample	Metals concentration (mg/kg) (mean±SD)			
		Lead	Natural abundance value	Copper	Natural abundance value
S1	*E. camaldulensis*	1.5495±0.060104[a]	0.3	1.081±0.057276[a]	0.2
	Soil	1.26±0.049497[a]	1.08	7.1155±0.057983[c]	23.13
S2	*D. viscosa*	1.215±0.06364[a]	0.3	1.0825±0.044548[a]	0.2
	Soil	2.735±0.02192[b]	1.08	7.399±0.071418[c]	23.13
S3	*E. camaldulensis*	1.643±0.06364[a]	0.3	0.9005±0.006364[a]	0.2
	Soil	2.687±0.02687[b]	1.08	6.035±0.065054[c]	23.13
S4	*E. camaldulensis*	2.0765±0.062933[b]	0.3	1.1485±0.06364[a]	0.2
	Soil	1.702±0.049497[a]	1.08	6.403±0.072125[c]	23.13

* Different letters vertically mean statistically significant differences ($p<0.05$).

3.2.1 Bioaccumulation factor in south site

The highest value of lead bioaccumulation was in *E. camaldulensis* at site south 2000 with 2.07, followed by the sites south 1000 and south 100 with the same plant, where it reached 1.64 and 1.54 respectively, then *D. viscosa* at site south 500 by 0.44, which is the lowest value of the bioaccumulation factor (Figure 3). The highest BAF value for copper was recorded in *E. camaldulensis* at sites south 2000, south 1000, and south 100 by 0.179, 0.15, and 0.14, respectively, and the lowest BAF value was recorded in *D. viscosa* at site south 100. The findings in Figure 3 indicate that *E. camaldulensis* has the potential to remove lead and copper from the areas surrounding the company. These outcomes are similar to a study conducted in Basra in Al-Haritha by Azeez (2021), where the study showed that the BAF values for copper in plants were less than 1. It also aligns with another study conducted by Luo et al. (2016), which found that eucalyptus trees were efficient in removing lead and copper. Choosing the right plants is crucial in the phytoremediation process. The capacity of plants to absorb, withstand, and collect pollutants is taken into consideration when choosing them. The

solubility, transport, and subsequent uptake of metals are also significantly influenced by the region surrounding plant roots (rhizosphere) (Zhao and Wang, 2020).

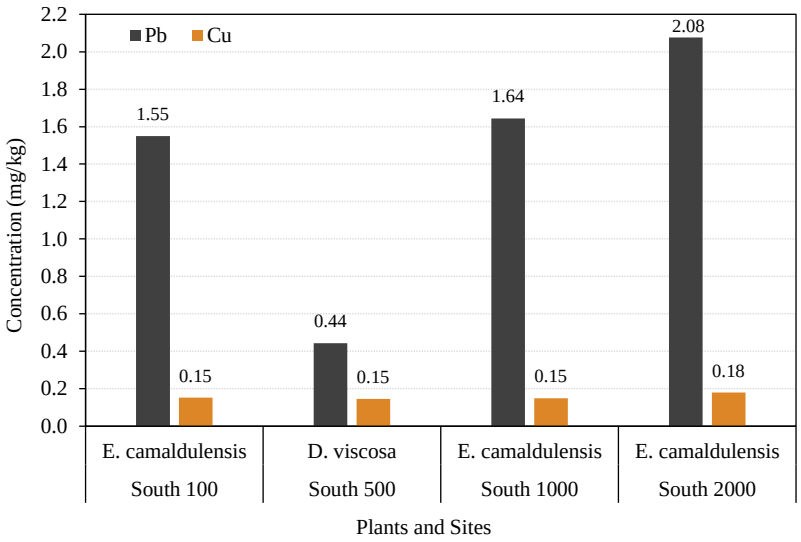

Figure 3. Plant BAF at four sites in south of Diyala State Company

3.3 Level of lead and copper in leaves and soil in the eastern part

In this study, heavy metal levels were measured at the company's eastern site. The highest lead concentration in site E3 reached 3.00 mg/kg in the leaves of *E. camaldulensis*, and the lowest concentration in the same plant reached 1.99 mg/kg in site E2. Compared with the approved standard value (0.3 mg/kg), all the leaves in plants in all areas were polluted with lead, with significant differences between *E. camaldulensis*, *D. viscosa*, and *R. communis* ($p<0.05$). As for the plant soil, the highest concentration of lead revealed in *E. camaldulensis* soil by 3.318 mg/kg in site E2 and 1.75 mg/kg in site E3, followed by *D. viscosa* by 1.46 mg/kg in site E4, and the lowest concentration was in *R. communis* in site E1 1.40 mg/kg The result was statistically significant ($p<0.05$) between soil of *E. camaldulensis*, *D. viscosa*, and *R. communis* compare with the natural abundance (Table 4).

Regarding copper, *D. viscosa* leaves at site E4 had the highest content (1.20 mg/kg), while *E. camaldulensis* leaves at site E3 had the lowest value (0.78 mg/kg). It was found that all the leaves were polluted with copper (0.2 mg/kg), with no significant differences between them and other samples. Regarding the soil for plants, the highest concentration of copper was in the soil of *E. camaldulensis* (7.09 mg/kg) in site E3, followed by *R. communis* in site E1 (6.91 mg/kg) and *E. camaldulensis* in site E2 (6.66 mg/kg). The lowest level in *D. viscosa* in site E4 reached up to 5.90 mg/kg. The result was not statistically significant ($p\geq0.05$) between soils of all plants, and the natural abundance of copper (Abd Al-wahab, 2020). By forming stable organic complexes, the amount of organic matter in the soil may help to decrease the mobility of these elements. The acidity of the soil can make heavy metals more bioavailable. Soil deterioration, a worldwide issue that presents a serious danger to environmental sustainability, can result from increased bioavailability of heavy metals in the soil-plant system (Núñez-Delgado et al., 2020).

The findings of the current study conflict with a study conducted in Kirkuk Province, Iraq, by Khurshid et al. (2022), in which they found a high level of lead and copper contamination in soil and some plants, with lead levels in soil and plants reaching 2.2 and 67 mg/kg, respectively. Copper levels in soil reached 55 mg/kg and in plants, 11 mg/kg. Another study conducted in Basra and Maysan Provinces by Mahdi et al. (2020) revealed concentrations of lead exceeding the internationally permissible limit in soil. Lead levels in Basra Province soil reached 37.32 mg/kg, and in Maysan Province, 24.13 mg/kg. This study conflict with a study conducted by Yang et al. (2022), which showed that copper exceeded the natural abundance by 33.43 mg/kg. However, the findings of this study are consistent with the outcomes of Briffa et al. (2020), which revealed the lead levels exceeded the normal background values and reached a level of 9.6 mg/kg.

Table 4. Lead and copper concentrations of soil and leaves for plants at four sites in east of Diyala State Company

Site	Sample	Metals concentration (mg/kg) (mean±SD)			
		Lead	Natural abundance value	Copper	Natural abundance
E1	*R. communis*	2.1105±0.00495[b]	0.3	1.1035±0.072832[a]	0.2
	Soil	1.4005±0.07566[a]	1.08	6.9155±0.057276[d]	23.13
E2	*E camaldulensis*	1.998±0.009899[a]	0.3	1.1605±0.068589[a]	0.2
	Soil	3.3185±0.052326[c]	1.08	6.6625±0.007778[d]	23.13
E3	*E. camaldulensis*	3.0045±0.00495[c]	0.3	0.789±0.039598[a]	0.2
	Soil	1.7505±0.049497[a]	1.08	7.0905±0.04879[d]	23.13
E4	*D. viscosa*	2.896±0.007071[b]	0.3	1.208±0.074953[a]	0.2
	Soil	1.462±0.072832[a]	1.08	5.9025±0.048083[d]	23.13

* Different letters vertically mean statistically significant differences ($p<0.05$).

3.3.1 Bioaccumulation factor in east sites

Figure 4 shows that the highest value of lead bioaccumulation was in *D. viscosa* at site east 2000, which amounted to 1.98, followed by *E. camaldulensis* at site east 1000 with 1.71, then *R. communis* at site east 100, which amounted to 1.50, and finally, *E. camaldulensis* at site east 500 with lowest value BAF by 0.60. The highest BAF value (0.20) for copper was recorded in *D. viscosa* at site east 2000, followed by *E. camaldulensis* at site east 500 with 0.17, then 0.15 for *R. communis* at site east 100. The lowest BAF value was recorded in *E. camaldulensis* at site east 1000. The findings represented in Figure (4) display that *D. viscosa* was the best in removing lead and copper from the areas surrounding the company. This may elucidate that *D. viscosa*, a perennial plant, is exposed to pollutants for a long period, accumulating pollution in its leaves and other parts (Goyal et al., 2020). The results of the current study conflict with a study conducted by Abed et al. (2022) in Diyala Province which exhibited that the BAF level reached 2.45 times higher than our outcomes. The findings show a decrease in pollution levels in this area over three years, which could be attributed to differences in plant species, climate change, or changes in soil properties (Chen et al., 2022).

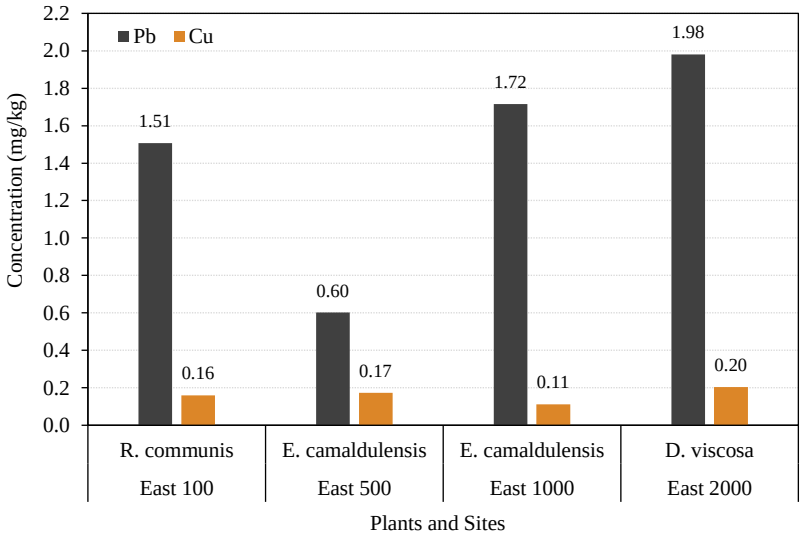

Figure 4. Plant BAF at four sites in east of Diyala State Company

3.4 Level of lead and copper in plant leaves and soil in the western part

The leaves of *R. communis* had the maximum concentration of lead in site W2, up to 1.79 mg/kg, as indicated in Table 5, while the leaves of *D. viscosa* had the lowest concentration, 1.39 mg/kg, in site W3. All plant leaves in every location under study had lead contamination when compared to the authorised standard values. The result was not statistically significant ($p\geq0.05$) for the plant soil, the highest concentration of lead was in *E. camaldulensis*, reaching 3.73 mg/kg at site W4, followed by

M. parviflora, 2.48 mg/kg at site W1, then *D. viscosa*, reaching 2.17 mg/kg at site W3, and the lowest concentration was in *R. communis*, site W2, 2.12 mg/kg, with statistically significant ($p<0.05$) between *M. parviflora* and *R. communis*, *D. viscosa*, *E. camaldulensis*, and not statistically significant ($p\geq0.05$) between *R. communis* and *D. viscosa* compared with the natural abundance.

The highest concentration of copper was noticed in the leaves of *R. communis* at site W2, at a concentration of 1.24 mg/kg, and the lowest level was in *E. camaldulensis* at site W4, at a concentration of 0.89 mg/kg. We found that all plant leaves were polluted with copper, with no significant differences between them and other plants. As for the plant soil, the highest concentration of copper was also in *E. camaldulensis*, where its level reached 8.521 mg/kg in site W4, followed by *D. viscosa* in site W3, 7.74 mg/kg, then *R. communis* in site W2 with concentration of 6.03 mg/kg, and the lowest level in *M. parviflora* in site W1 (5.96 mg/kg), with no significant differences ($p<0.05$) between soils of all plants. The concentrations obtained from the plant indicate that it was not polluted with copper in large quantities compared to its natural abundance (Abd Al-wahab, 2022). The results of the current study were consistent with a study conducted in Diyala Province by Mahmood and Rathi (2024), which showed high levels in lead in the earth's crust. It contradicted another study in Diyala conducted by Abd Al-wahab (2020), the concentration of lead ranged between 43.10-112.30 mg/kg and ranged between 21.40-58.60 mg/kg for copper. In Kurdistan province, lead and copper contamination levels in soil increased, with lead levels reaching 16.22 mg/kg and copper levels reaching 63.33 mg/kg (Hamad et al., 2019). And also consistent with another study conducted by Zhao et al. (2022) in China high level of copper 63.73 mg/kg was shown in farmland in Anxin County.

Table 5. Copper and lead concentrations in soil and plant leaves at four sites in west of Diyala State Company

Site	Sample	Metals concentration (mg/kg) (mean±SD)			
		Lead	Natural abundance value	Copper	Natural abundance value
W1	*M. parviflora*	1.585±0.003536[a]	0.3	1.2385±0.076368[a]	0.2
	Soil	2.4825±0.096167[a]	1.08	5.9635±0.091924[d]	23.13
W2	*R. communis*	1.7915±0.00495[a]	0.3	1.2465±0.061518[a]	0.2
	Soil	2.1235±0.044548[b]	1.08	6.032±0.054447[d]	23.13
W3	*D. viscosa*	1.399±0.008485[a]	0.3	1.0565±0.067175[a]	0.2
	Soil	2.179±0.094045[b]	1.08	7.7495±0.062933[d]	23.13
W4	*E. camaldulensis*	1.425±0.002828[a]	0.3	0.898±0.007071[a]	0.2
	Soil	3.736±0.064347[c]	1.08	8.521±0.046669[d]	23.13

* Different letters vertically mean statistically significant differences ($p<0.05$).

3.4.1 Bioaccumulation factor in west sites

Figure 5 shows *R. communis* at site west 500 had the greatest RAF value (0.84), followed by *D. viscosa* at site west 1000 (0.64) and *M. parviflora* at site west 100 (0.63). The BAF of *E. camaldulensis* at site west 2000 is (0.38), the lowest value in the western area of the company. Regarding copper, *M. parviflora* at site west 100 had the highest BAF value (0.20), followed by *R. communis* at site west 500 (0.20), *E. camaldulensis* at site west 2000 (0.27), and *D. viscosa* at site west 1000 (0.13). According to our findings, *M. parviflora* was the most effective in removing copper from the vicinity of the company, while *R. communis* was the greatest at removing lead. As mentioned previously, the castor plant can tolerate high levels of heavy metals due to its strong root system and their tissue characteristics. The baker's plant has been shown to have an average ability to absorb pollutants (Yeboah et al., 2021). In 2023, Hassan and Umer found BAF value of copper greater than the one in Dohuk soil which is conflicted with our study. The results are also in a disagreement with a study undertook by Azeez (2021) in Basra, where the BAF value for lead was less than one. The difference in findings between previous studies and the current study may be due to differences in soil properties, plant type, as they differ in their ability to absorb, or due to differences in climatic conditions (Vuong et al., 2025).

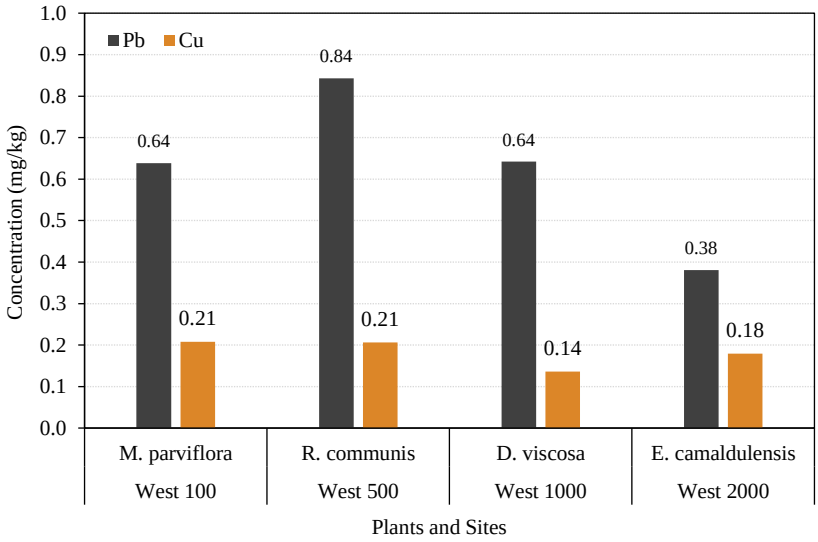

Figure 5. Plant BAF at four sites in west of Diyala State Company

4. CONCLUSION

The findings clearly showed environmental pollution with lead and copper in some areas surrounding the Diyala State Company. Lead concentrations were higher than those of copper, making lead the dominant pollutant in the studied areas. The highest concentration (3.00 mg/kg) was recorded in the eastern part of the company, at site E3. The selected plants demonstrated a high capacity to absorb and accumulate both lead and copper in their leaves. *E. camaldulensis* was highly efficient at absorbing lead, particularly at sites N3 and S4, while *R. communis* showed the highest capacity for absorbing copper at site N2. Based on the results, the studied plants can be ranked according to their ability to bioaccumulate lead and copper as follows: *E. camaldulensis* (highest accumulating capacity, especially for lead), *R. communis* (highest accumulating capacity for copper), *D. viscosa* and *M. parviflora* (lowest accumulating capacity). Therefore, these plants could be included in phytoremediation programs to reduce heavy metal pollution in the region. These results underscore the importance of incorporating the studied plant species into phytoremediation programs in contaminated industrial areas. *E. camaldulensis* can be recommended for treating lead pollution, and *R. communis* for treating copper pollution, especially in locations with high concentrations. By applying this strategy in areas surrounding factories, the accumulation of heavy metals in the soil will reduced and limit the risk of their transfer to plants, crops, and food chain. It is also an environmentally sustainable and less costly method compared to traditional chemical or physical methods for remediating pollution.

ACKNOWLEDGEMENTS

The authors would like to express their gratitude to the management of Diyala State Company for their support and providing the facilities needed to finish this research. The authors would like to thank Engineer Ahmed Tawfeeq Abduljabbar from the Company for his support and cooperation in facilitating the sample collection and providing the necessary data about the company.

AUTHOR CONTRIBUTIONS

The research idea was conceived by Rathi MH and Hummadi EH. The methodology, data collection, and analysis of the results were implemented by Mohammed DA. Mohammed DA wrote the first draft of the research. Rathi MH and Hummadi EH reviewed, edited and corrected the final draft. Rathi MH and Hummadi EH supervised the project.

DECLARATION OF CONFLICT OF INTEREST

The authors declare no conflict of interest.

REFERENCES

Abd Al-Wahab SK. The Investigation of Some Heavy Metals in the Agricultural Soil of Diyala Province and Treating them with Different Types of Plants [dissertation]. Diyala (Iraq): University of Diyala, College of Education for Pure Science; 2020. p. 107.

Abdulhay HS, Rathi MH. Lead, cadmium and nickel contamination of roadside soils and plant leaves in Baghdad City. Journal of Chemical and Pharmaceutical Research 2017;9(8):47-51.

Abed SH, Rathi MH, Khalil GI, Taha ME. *Nerium oleander* L. as a phytoremediation of heavy metals in Diyala Governorate-

Iraq. Journal of Environment and Earth Science 2022;12(9):32-9.

Aladesanmi OT, Oroboade JG, Osisiogu CP, Osewole AO. Bioaccumulation factor of selected heavy metals in Zea mays. Journal of Health and Pollution 2019;9(24):Article No. 191207.

Alarifi SS, El-Sorogy AS, Al-Kahtany K, Alotaibi M. Contamination and environmental risk assessment of potentially toxic elements in soils of palm farms in northwest Riyadh, Saudi Arabia. Sustainability 2022;14(22):Article No. 15402.

Alberto Then NM, Delanoy R, Rodríguez Alberto D, Méndez Henández R, Díaz Rizo O, Bello L. Heavy metal pollution assessment in the agricultural soils of Bonao, Dominican Republic. Sustainability 2023;15(23):Article No. 16510.

Alkouh A, Keddar KA, Alatefi S. Remanufacturing of industrial electronics: A case study from the GCC region. Electronics 2023;12(9):Article No. 1960.

Amer M, Abdulhussein FM. Assessment of the contamination of Baghdad soils with lead element. Iraqi Geological Journal 2022;55(1F):166-77.

Armiento G, Barsanti M, Caprioli R, Chiavarini S, Conte F, Crovato C, et al. Heavy metal background levels and pollution temporal trend assessment within the marine sediments facing a brownfield area (Gulf of Pozzuoli, Southern Italy). Environmental Monitoring and Assessment 2022;194(11): Article No. 814.

Azeez NM. Bioaccumulation and phytoremediation of some heavy metals (Mn, Cu, Zn, and Pb) by bladderwort and duckweed. Biodiversitas Journal of Biological Diversity 2021;22(5): 2993-8.

Bibi D, Tőzsér D, Sipos B, Tóthmérész B, Simon E. Heavy metal pollution of soil in Vienna, Austria. Water Air Soil Pollution 2023;234(4):Article No. 232.

Briffa J, Sinagra E, Blundell R. Heavy metal pollution in the environment and their toxicological effects on humans. Heliyon 2020;6(9):e04691.

Chen D, Ye X, Jiang Y, Xiao W, Zhang Q, Zhao S, et al. Continuously applying compost for three years alleviated soil acidity and heavy metal bioavailability in a soil-asparagus lettuce system. Frontiers in Plant Science 2022;3:Article No. 972789.

Ennaji W, Barakat A, El Baghdadi M, Rais J. Heavy metal contamination in agricultural soil and ecological risk assessment in the northeast area of Tadla plain, Morocco. Journal of Sedimentary Environments 2020;5(3):307-20.

Fawkes L, Sansom G. Preliminary study of lead-contaminated drinking water in public parks—an assessment of equity and exposure risks in two texas communities. International Journal of Environmental Research and Public Health 2021;18(12):Article No. 6443.

Gani A, Hussain A, Pathak S, Banerjee A. An empirical investigation on the elimination of heavy metals using bioremediation method for selected plant species. Physics and Chemistry of the Earth Parts A/B/C 2024;134:Article No. 103568.

Goyal D, Yadav A, Prasad M, Singh TB, Shrivastav P, Ali A, et al. Effect of heavy metals on plant growth: An overview. In: Naeem M, Ansari AA, Gill SS, editors. Contaminants in Agriculture: Sources, Impacts and Management. Cham: Springer Nature Switzerland AG; 2020. p. 79-101.

Hamad R, Balzter H, Kolo K. Assessment of heavy metal release into the soil after mine clearing in Halgurd-Sakran National Park, Kurdistan, Iraq. Environmental Science and Pollution Research 2019;26(2):1517-36.

Hassan NE, Umer MI. Potential of local plants as phytoremediator of polluted soil in Kwashe industrial area, Duhok Province, Kurdistan Region, Iraq. Journal of Jilin University (Engineering and Technology Edition) 2023;42(1):97-111.

Hesami R, Salimi A, Ghaderian SM. Lead, zinc, and cadmium uptake, accumulation, and phytoremediation by plants growing around Tang-e Douzan lead-zinc mine, Iran. Environmental Science and Pollution Research 2018; 25(9):8701-14.

Hussein SA, Rathi MH, Kadhim TJ. Determination of the levels of lead and cadmium in canned fish and meat, imported to the local markets of Diyala Province, Iraq. IOP Conference Series Earth and Environmental Science 2021;79(1):Article No. 012043.

Ikhajiagbe B, Musa SI, Okeme JO. Effect of changes in soil cation exchange capacity on the reclamation of lead by *Eleusine indica* (L.) Gaertn. FUDMA Journal Science 2019;3(4):176-82.

Jabara AWAR. Environmental Risk Assessment of Heavy Metals in Dust and Their Impact on Roadside Plants Due to Traffic Activity in Diyala Governorate, Iraq. Wasit Journal for Pure sciences 2024;3(4):273-80.

Jiang H, Li X, Guo C, Zhang Y, Zhou R, Hai C, et al. Evaluation of soil quality in Inner Mongolia desert steppe—A case study of Siziwang Banner. PLoS One 2023;18(8):e0290301.

Kaur J, Bhatti SS, Bhat SA, Nagpal AK, Kaur V, Katnoria JK. Evaluating potential ecological risks of heavy metals of textile effluents and soil samples in vicinity of textile industries. Soil Systems 2021;5(4):Article No. 63.

Kayiranga A, Li Z, Isabwe A, Ke X, Simbi CH, Ifon BE, et al. The effects of heavy metal pollution on collembola in urban soils and associated recovery using biochar remediation: A review. International Journal of Environmental Research and Public Health 2023;20(4):Article No. 3077.

Khurshid CA, Mahdi K, Ahmed OI, Osman R, Rahman M, Ritsema C. Assessment of potentially toxic elements in the urban soil and plants of Kirkuk City in Iraq. Sustainability 2022;14(9):Article No. 5655.

Kumar K, Singh D. Toxicity and bioremediation of the lead: A critical review. International Journal of Environmental Research 2024;34(4):1879-909.

Liu Y, Wang H, Cui Y, Chen N. Removal of copper ions from wastewater: A review. International Journal of Environmental Research and Public Health 2023;20(5):Article No. 3885.

Luo J, Qi S, Peng L, Wang J. Phytoremediation efficiency of Cd by *Eucalyptus globulus* transplanted from polluted and unpolluted sites. International Journal of Phytoremediation 2016;18(4):308-14.

Madejon P, Maranon T, Navarro-Fernandez CM, Dominguez MT, Alegre JM, Robinson B, et al. Potential of *Eucalyptus camaldulensis* for phytostabilization and biomonitoring of trace-element contaminated soils. PLoS One 2017;12(6):e0180240.

Mahdi QH, Abass MH, Matrood AA. Heavy metals pollution of wheat fields (soil and leaves) sampled from Basrah and Maysan Provinces. Periodico Tche Quimica 2020;17(35):315-26.

Mahmood SS, Rathi MH. Efficiency of some plant grown on roadsides of Baqubah City in the phytoremediation of lead and cadmium. Environment and Ecology Research 2024;12(3):299-307.

Mazumdar K, Das S. Phytoremediation of Pb, Zn, Fe, and Mg with 25 wetland plant species from a paper mill contaminated site in North East India. Environmental Science and Pollution Research 2015;22:701-10.

Mocek-Płóciniak A, Mencel J, Zakrzewski W, Roszkowski S. Phytoremediation as an effective remedy for removing trace elements from ecosystems. Plants 2023;12(8):Article No. 1653.

Mohammed DA, Rathi MH, Kadhim TJ. The effect of living place and smoking on blood level of lead, cadmium and mercury: As a model of pollutants in human blood. International Journal of Drug Delivery Technology 2023;13(2):610-9.

Núñez-Delgado A, Zhou Y, Anastopoulos I, Shaaban M. New research on soil degradation and restoration. Journal of Environmental Management 2020;269:Article No. 110851.

Ondrasek G, Shepherd J, Rathod S, Dharavath R, Rashid MI, Brtnicky M, et al. Metal contamination–a global environmental issue: Sources, implications and advances in mitigation. RSC Advances 2025;15(5):3904-27.

Rasheed MM, Saeed IO, Ibrahim OM. Study of pollution by some heavy metals in the water of the Tigris River in some areas of Salah Al-Din Governorate. Egyptian Journal of Aquatic Biology and Fisheries 2024;28(2):317-26.

Rawat H, Bhat SA, Dhanjal DS, Singh R, Gandhi Y, Mishra SK, et al. Emerging techniques for the trace elemental analysis of plants and food-based extracts: A comprehensive review. Talanta Open 2024;10:Article No. 100341.

Satpathy D, ReddV, Dhal SP. Risk assessment of heavy metals contamination in paddy soil, plants, and grains (*Oryza sativa* L.) at the East Coast of India. Biomed Research International 2014;2014:Article No. 545473.

Shi J, Qian W, Jin Z, Zhou Z, Wang X, Yang X. Evaluation of soil heavy metals pollution and the phytoremediation potential of copper-nickel mine tailings ponds. PLoS One 2023;18(3):e0277159.

Vuong TX, Nguyen DP, Nguyen VHN, Pham TTH, Nguyen TTT. Immobilization of lead and zinc in contaminated soil using taro stem-derived biochar and apatite amendments: A comparative study of application ratios and pyrolysis temperatures. RSC Advances 2025;15:11975-2000.

Wang Y, Chen Y, Wang Y, Li Q. Combination effects of heavy metal and inter-specific competition on the invasiveness of *Alternanthera philoxeroides*. Environmental and Experimental Botany 2021;189:Article No. 10453.

Yang J, Sun Y, Wang Z, Gong J, Gao J, Tang S, et al. Heavy metal pollution in agricultural soils of a typical volcanic area: Risk assessment and source appointment. Chemosphere 2022;304:Article No. 135340.

Yao C, Yang Y, Li C, Shen Z, Li J, Mei N, et al. Heavy metal pollution in agricultural soils from surrounding industries with low emissions: Assessing contamination levels and sources. Science of the Total Environment 2024;917:Article No. 170610.

Yeboah A, Lu J, Gu S, Liu H, Shi Y, Amoanimaa-Dede H, et al. Evaluation of two wild castor (*Ricinus communis* L.) accessions for cadmium tolerance in relation to antioxidant systems and lipid peroxidation. Environmental Science and Pollution Research 2021;28(39):55634-42.

Yuan X, Xue N, Han Z. A meta-analysis of heavy metals pollution in farmland and urban soils in China over the past 20 years. Journal of Environmental Sciences. 2021;101:217-26.

Zahra Z, Habib Z, Chung S, Badshah MA. Exposure route of TiO_2 NPs from industrial applications to wastewater treatment and their impacts on the agro-environment. Nanomaterials 2020;10(8):Article No. 1469.

Zhao FJ, Wang P. Arsenic and cadmium accumulation in rice and mitigation strategies. Plant and Soil 2020;446:1-21.

Zhao G, Ma Y, Liu Y, Cheng J, Wang X. Source analysis and ecological risk assessment of heavy metals in farmland soils around heavy metal industry in Anxin County. Scientific Reports 2022;12(1):Article No. 10562.

Zhao X, Yin Y. Hazards of pollutants and ventilation control strategy in industrial workshops: Current state and future trend. Building and Environment 2024;251:Article No. 111229.

Environment and Natural Resources Journal

Volume 24
Issue 2
2026

Biochemical Assessment of Oxidative Stress Markers in Rats Following Exposure to Spray and Scented Candle Air Fresheners

Mariam Abdulsalam S. Al-Maliki* and Nada Abdulrahman F. Al-Easawi

Department of Biology, College of Science, University of Baghdad, Baghdad, Iraq

ARTICLE INFO

Received: 22 Jul 2025
Received in revised: 28 Oct 2025
Accepted: 8 Nov 2025
Published online: 8 Dec 2025
DOI: 10.32526/ennrj/24/20250186

Keywords:
Air fresheners/ Scented candles/ Indoor air quality/ Oxidative stress

*** Corresponding author:**
E-mail:
mariam.saad1202@sc.uobaghdad.edu.iq

ABSTRACT

Air freshener and scented candles are widely used to improve indoor air quality or eliminate unpleasant odors, but these consumer products release volatile organic compound (VOCs), particulate matter, and other chemicals that can adversely affect public health. This study evaluated the effects of air freshener spray and scented candle using a locally manufactured inhalation exposure chamber in Baghdad. Effects in rats were assessed with particular focus on the oxidative stress. A total of (40) healthy Wistar male rats, weighing between (180-200) gm, were randomly divided into 4 groups, each group containing 10 rats. The first group was exposed to air freshener spray, the second group exposed to scented candles, the third group exposed to mixture of air freshener spray and scented candle and the fourth group exposed to fresh air only. The inhalation exposure periods were (10, 20, 30) days for each group. The total exposure time was one hour daily, while the exposure time to the substance itself was estimated to be 15 minutes. Blood samples were collected from each rat, and serum was separated for biochemical analysis. Oxidative stress biomarkers (SOD, GPX, and LPO) were measured using ELISA kits, while GSH was determined manually using the Ellman method. The results demonstrated that exposure to the air freshener led to significant increase in GPX levels, while GSH concentrations were notably reduced. Additionally, the activities of antioxidant enzymes SOD and LPO were elevated compared to the control group. These findings indicate that such emissions can disrupt redox balance and may have toxic effects.

HIGHLIGHTS

A local inhalation chamber was designed to simulate real indoor exposure. VOC emitting sprays and candles altered oxidative stress biomarkers in rats. GPX and LPO levels increased, while GSH significantly decreased after exposure. Air fresheners disrupted redox balance, indicating potential toxic effects.

1. INTRODUCTION

People are generally aware that polluted outdoor air can harm human health, but many fail to overlook the fact that indoor air pollution can be equally, if not more, detrimental. The Environmental Protection Agency (EPA) monitors and regulates air quality both outdoors and indoors. According to the EPA, the concentration of indoor air pollutants can be up to 100 times higher than that outdoor air pollutants. This makes indoor air quality a critical concern for public health, especially considering that individuals spend nearly 90% of their time within enclosed environments (Seguel et al., 2017). Common indoor pollutants, such as carbon monoxide (CO), ozone (O_3), particulate matter (PM), and volatile organic compounds (VOCs) are often found at concentrations significantly higher than those measured outdoors, posing substantial risks to human health (Cheek et al., 2021). Numerous studies have highlighted the hazardous nature of VOCs emphasizing their capacity to induce adverse health effects and contribute to indoor air pollution (Hammod et al., 2020). Indoor exposure to VOCs has been associated with non-carcinogenic and carcinogenic health risks. Recent investigations in small scale workplaces have shown significant occupational exposure to compounds such as benzene, ethylbenzene and other compounds exhibiting potential carcinogenic effects. Moreover,

Citation: Al-Maliki MAS, Al-Easawi NAF. Biochemical assessment of oxidative stress markers in rats following exposure to spray and scented candle air fresheners. Environ. Nat. Resour. J. 2026;24(2):199-208. (https://doi.org/10.32526/ennrj/24/20250186)

long term occupational exposure to VOCs particularly formaldehyde and acetaldehyde has been reported to exceed acceptable hazard thresholds posing both non carcinogenic and carcinogenic risks (Seo et al., 2025; Choi et al., 2023). Indoor environments contain a complex mixture of pollutants originating from both outdoor and indoor sources. Outdoor contaminants primarily derive from vehicular traffic and industrial emissions that can infiltrate through natural or mechanical ventilation systems. In addition, numerous indoor sources contribute to pollutant levels, including the combustion of fuels, coal, tobacco products, and candles, as well as emissions from building materials, and household cleaning products, and occupant behaviors such as smoking (Cincinelli and Martellini, 2017).

Air fresheners are extensively used across various indoor settings within modern society. All forms of air fresheners (such as gels, sprays, oils, solids, and diffusers), including those marketed as "green" or "organic" products, have been found to release VOCs that may pose health risks. Among these, one major compound, d-limonene has been reported at an average concentration of 6.78 µg/m^3 in area using air fresheners compared to 0.84 µg/m^3 in non-using areas with reduction up to 96% after discontinuation (Goodman et al., 2020). The increasing popularity of scented candles has prompted scientific interest due to concerns over their contribution to indoor air pollution resulting emissions. These products emit a complex mixture of aromatic and non-aromatic substances, including volatile organic compounds (VOCs and SVOCs), as well as particulate matter. For example, Yun et al. (2025) reported that PM levels increased by 1.52 times during candle burning (Yun et al., 2025; Adamowicz et al., 2019). Prolonged or repeated inhalation of these substances, especially volatile organic compounds (VOCs), has been associated with irritation of the eyes, nose, and throat, as well as symptoms such as nausea, difficulty in breathing, and potential damage to the central nervous system and other organs (Singh et al., 2023).

Oxygen plays a crucial role in aerobic metabolism due to its high reactivity; however, this same property also contributes to the generation of free radicals that oxidize biological molecules. These reactive species can also serve as part of the body's defense mechanisms against invading pathogens. To limit potential cellular damage, organisms maintain tight regulation over the production of reactive oxygen species (ROS). Antioxidants can act as key molecular defense systems, and variations in their levels are often used as biomarkers to assess of environmental stress (Hellou et al., 2012; Alfahdawi et al., 2023). In fact, pollutants such as particulate matter, ozone, nitrogen oxides, and transition metals are either strong oxidants themselves or capable of generating reactive oxygen species. The resulting oxidative stress can activate redox-sensitive signaling pathways, which, in turn initiate biological processes including inflammation and programmed cell death (Lodovici and Bigagli, 2011).

Endogenous antioxidant enzymes, such as glutathione and superoxide dismutase. Play essential roles in protecting humans from oxidative damage; however, variations in antioxidant defense systems exist across species. Oxidative stress arises from an imbalance between the production of ROS, metal ion homeostasis, and the body's antioxidant defenses systems (Banks and Rhea, 2021). Recent studies have shown that the activities of key antioxidant enzymes—glutathione peroxidase, superoxide dismutase, and catalase—in the blood are strongly but inversely associated with an increased risk of developing coronary artery disease. Moreover, elevated levels of oxidized DNA in blood cells have been linked to pollution exposure in several cross-sectional studies (Khalid and Rabee, 2025).

Superoxide dismutase is a vital antioxidant enzyme that helps protect the body against the harmful effects of oxidative stress (Fakhri and Al-Ani, 2025). Glutathione peroxidase is also commonly measured in epidemiological studies to assess oxidative stress levels. Although numerous studies have attempted to determine the link between exposure to ambient particulate air pollution respiratory diseases and other health outcomes, the relationship between ambient particulate matter and major oxidative stress biomarkers remains inconclusive (Li et al., 2020).

This study was conducted to assess the effects of indoor air pollution associated with spray air fresheners and scented candles on some biological parameters in rats. To highlight the possible health hazards linked to such exposure within indoor settings.

2. METHODOLOGY

2.1 Collection of air freshener and scented candle samples

For this study, two (2) samples, non-combustible and combustible samples were conveniently selected at random from the air freshener sections of various stores representing different

manufacturers and sellers in Baghdad City. Both products are commercially available and can be used by consumers. However, the same brands and product types are widely distributed throughout Iraq and in internationally markets. The types of air fresheners sampled were one spray air freshener and one scented candle. All air fresheners were kept in their original containers and maintained at ambient temperature until analysis. The key features of the investigated sample are summarized in Table 1. Sample were collected from October 2023 to December 2023.

Table 1. Principal features of the investigated air freshener

Samples	Container	Status fragrance	Origin	Weight
Air freshener spray	Plastic spray can	Clean	Turkiye	500 mL
Scented candle	Glass beaker	Twisted Peppermint (Cool Peppermint, Sugared Snow, Vanilla Butter cream)	USA (including US and non-US parts)	411 g

The study was conducted with the assistance of the animal house unit at the Biotechnology Research Center, University of AL-Nahrain, from January 2024 to June 2024.

2.2 The inhalation exposure unit

The inhalation exposure unit is dynamic system, whole-body chamber commonly used in studies involving prolonged exposure and large numbers of laboratory animals. Designed according to the WHO specifications as described by (Al-Easawi, 2015; WHO, 1978).

2.2.1 The inhalation unit manufacturing

The laboratory unit used in this study consists of the following components as shown in Figure 1 below:

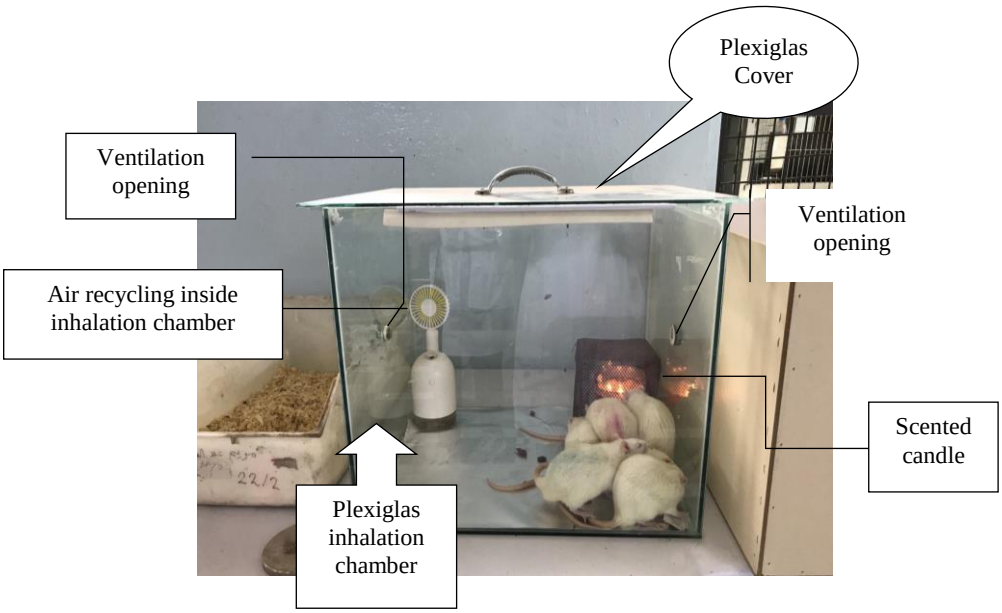

Figure 1. The locally manufactured inhalation exposure unit and its components

The features and design of the inhalation exposure chamber followed the description by Al-Easawi (2015): a 5 mm transparent Plexiglas chamber, manufactured locally with the following dimensions (50 cm length × 40 cm width × 40 cm height) of 80 Lt. Capacity (1) The chamber contained three openings: input, output and ventilation. The input and output openings were located on both sides of the chamber, while ventilation opening is a narrow strip along the top cover of the chamber. To ensure homogeneous distribution of the emitted vapors inside the exposure chamber, a small internal fan was installed to circulate the air during exposure sessions, promoting even mixing of emissions from both the air freshener and scented candle (Figure 1). To minimize carryover effects between different exposure types (spray, candle, and mixed), the chamber was thoroughly cleaned and ventilated with fresh air after each exposure session, and the next exposure was initiated only after confirming that baseline air conditions were restored. The chamber was equipped with a thermometer to monitor temperature during the

inhalation exposure experiments. Animal wastes fell onto removable aluminum foil covering the chamber floor, facilitating cleaning after each daily exposure.

2.3 Experimental animal groups

Forty (40) male Wistar rats, weighing between 180-200 g, were used in this study. They were acclimated to laboratory conditions for seven days before the experiment. They were purchased from the National Center for Drug Control and Research. After acclimatization period, the rats were weighed and the data recorded then divided into four groups; each ten rats in each group, including exposed and control groups. The rats were kept in a polypropylene cages (30 cm × 15 cm × 15 cm diameter) covered with wire grid lids and maintained at a temperature range of 27-29°C. Cages were kept under standard animal house conditions. Cages were kept under standard animal house conditions where the humidity ranged between 56-58% and 12±2 h (light/day). Rodent diet and drinking water were available *ad libitum*, except during inhalation exposure.

All experimental procedures were carried out in compliance with ethical standards for animal research. Approval from the ethics committee was obtained prior to conducting the study (Baghdad University/College of Science/Department of Biology/Ref.: CSEC/1123/0123 on November 26, 2023).

2.4 Experiment design

Forty (40) rats were randomly divided into four groups (30 exposed and 10 controls) according to LT50, with each group containing ten animals as follows:

Group (A): 10 rats were exposed to inhaled air freshener spray (2.5 mL). Exposure lasted 60 minutes daily, beginning 15 minutes after opening the freshener.

Group (B): 10 rats were exposed to inhaled scented candle. Exposure lasted 60 minutes daily, beginning 15 minutes after lighting the candle.

Group (C): 10 rats were exposed to fresh air only (control group).

Group (D): 10 rats were exposed to a mixture of air freshener spray (2.5 mL) and scented candle at the same time. Exposure lasted 60 minutes daily, beginning 15 minutes after opening the air freshener and lighting the candle.

For each exposure session 2.5 mL of the air freshener product was placed in an electric diffuser positioned inside the inhalation chamber. After introducing the rats the diffuser was turned on to actively emit the product and the chamber was sealed for 15 minutes to maintain a stable exposure atmosphere. The chamber was then kept closed for the remainder of the 60 minutes exposure period to ensure consistent inhalation conditions.

Each group was further divided into three subgroups based on exposure duration: three rats for 10 days, three rats for 20 days, and four rats for 30 days.

2.5 Animal's blood test

The rats in their various groups were exposed for 10, 20, and 30 days, and three rats from each group were sacrificed at the end of their respective exposure periods. Blood samples were collected for biochemical analysis of oxidative stress markers.

Blood samples were obtained via cardiac puncture using 1 mL Syringes and placed into Gel tubes, to determine the following: glutathione peroxidase (GPX), lipid peroxidase (LPO), superoxide dismutase (SOD) and reduced glutathione (GSH). The blood samples were placed in gel tubes and left to coagulate at room temperature for 10-20 minutes. Serum was then separated by centrifugation for 20 minutes at 2,000-3,000 rounds per minute (rpm). The supernatant without sediment was collected in the eppendorf tube, and stored at -20°C until assayed (Abu Ghazal et al., 2023).

2.6 Oxidative stress parameters

2.6.1 Determination of Serum GSH concentration

The serum concentration of GSH was assessed using the Ellman method (Ellman, 1959; Al-Badry et al., 2023).

To prepare the reagents required for GSH estimation, phosphate buffer solutions were first prepared.

(A) Phosphate (H_2NaPO_4) was prepared at a concentration of 0.2 M by dissolving 0.2 g of the salt in 100 mL of distilled water.

(B) Disodium phosphate (HNa_2PO_4) was prepared at a concentration of 0.2 M by dissolving 0.2 g of the salt in 100 mL of distilled water.

Reagent A: (Phosphate buffer 0.2 M; pH=7) was prepared by mixing 41 mL of B with 9 mL of solution A and adjusting the volume to 100 mL using distilled water, and pH was corrected before and after dilution.

Reagent B: (Phosphate buffer 0.2 M; pH=8) was formed by combining 5 mL of solution A with 45 mL

of solution B, adjusted to 100 mL with distilled water, and pH was corrected before and after dilution.

Reagent C (DTNB reagent): was prepared by dissolving 39.6 mg of DTNB in 10 mL of reagent A, with a small amount of Na_2CO_3 added.

For the assay, 20 µL of serum was diluted with 1,000 µL of distilled water, followed by the addition of 1,000 µL of reagent B and mixed well. From this mixture, 1,500 µL was transferred into new tube and mixed with 200 µL of reagent C. The reaction mixture was incubated at 37°C for 60 minutes. A blank sample was prepared similarly, replacing serum with distilled water. Absorbance was read at λ=42 nm. The concentration of GSH was calculated according to the following formula Equation 1:

$$\text{GSH con. inserum}\ \frac{\mu mol}{L} = (T - B) \times \frac{df}{\varepsilon} \times 10 \qquad (1)$$

Where; T: test absorbance; ε: extinction coefficient=13,600 $M^{-1}.cm^{-1}$; B: blank absorbance =0.030 in this test; df: dilution factor=102.

2.6.2 Determination of serum SOD, LPO and GPX concentration

Serum levels of superoxide dismutase (SOD), lipid peroxidation (LPO), and glutathione peroxidase (GP_X) were measured using ELISA Kit: SOD: BT LAB, China, Catalog No. E0168Ra, LPO: BT LAB, China, Catalog No. E0285Ra, and GPX: BT LAB, China, Catalog No. E1242Ra. All procedures were performed according to the manufacturer's instructions (Ahmed and Yenzeel, 2017).

2.7 Statistical analysis

The statistical packages for the social sciences (SPSS) (2019) program was used to analyze the effect of different groups and factors on the study parameters. The least significant difference (LSD) test was used to compare means between groups, with significance considered at $p<0.05$.

3. RESULTS AND DISCUSSION

3.1 Biomarkers of oxidative stress

3.1.1 Glutathione peroxidase (GPX)

The highest mean value (1745.48±53.99 pg/mL) was recorded in rats exposed to the spray air freshener after 30 days, while the minimum mean value (833.67±35.09 pg/mL) was observed in the control group after 10 days; (Table 2). Statistically, analysis showed no significant differences over time within each group, as GPX levels remained relatively stable from day 10 to day 30. However, significant differences were observed between the groups on each day, with the exposed groups showing much higher GPX levels than control. This is confirmed by the LSD values and ($p\leq0.05$).

Table 2. Mean value±SE of GPX levels pg/mL in experimental animals exposed to air freshener spray, scented candle, mixed, and control group after10, 20, and 30 days

Group	Mean±SE of GPX pg/mL			L.S.D.
	10 day	20 day	30 day	
Air fresheners (A)	1,717.91±253.73 A a	1,720.69±304.92 A a	1,745.48±53.99 A a	64.39 NS
Scented candle (B)	1,558.77±82.58 B a	1,611.55±203.31 AB a	1,671.04±94.75 A a	123.67 NS
Mix (D)	1,665.05±33.40 AB a	1,556.63±124.81 B a	1,656.85±94.82 A a	133.84 NS
Control (C)	833.67±35.09 C a	971.04±98.39 C a	955.64±106.36 B a	139.02 NS
L.S.D.	147.47 *	163.58 *	141.66 *	---

Different capital letters in column and small letters in row indicate significant differences * ($p\leq0.05$). NS: Non-significant.

The present study showed a significant increase in serum GPX levels in rats exposed to air fresheners and scented candles compared to the control group. The observed elevation in GPX levels may reflect a physiological adjustment by the antioxidant defense system in response to ongoing oxidative stress caused by VOCs exposure. These findings are consistent with the observation of Airaodion et al. (2020a), who reported a significant increase in GPX levels after 28 days of daily exposure to sunlight air freshener in rats, suggesting a compensatory antioxidant response to oxidative challenge. The similarity may be attributed to comparable exposure duration and inhalation route. However, the current study differs from that of

Gabriel-Brisibe et al. (2020), who reported a decrease in GPX levels after up to 28 days of exposure. Although the reduction was not statistically significant, it was interpreted as an early depletion of antioxidant capacity under acute oxidative stress conditions. This contrast may be explained by differences in the type of air freshener used and variations in ELISA kits. It is worth nothing that while some studies measured GPX enzymatic activity (U/mg protein), the present study assessed its concentration in pg/mL, which might also explain the observed discrepancy.

Afighor et al. (2019) demonstrated that VOCs present in air fresheners rapidly react with O_3 to generate more harmful oxidant molecules and related by-products. Moreover, oxidative stress has been linked to neuroinflammation, which is associated with the degeneration of neuronal pathways involved in learning and memory. In this context, the effects of long-term air freshener exposure have gained growing scientific attention. These changes are likely associated with the oxidative stress caused by VOCs exposure.

3.1.2 Lipid peroxidase (LPO)

Table 3 shows that LPO levels were highest in the mixed exposure group across all days, especially on day 10 (23.81±1.15 nmoL/mL). The air freshener and scented candle groups also showed elevated LPO levels, with slight variations over days. In contrast, the control group consistentently had the lowest LPO values throughout the experiment during 10, 20, and 30 days (10.4±2.33 nmoL/mL; 8.38±0.64 nmoL/mL; 11.17±1.28 nmoL/mL) respectively. Statistical rows analysis showed no significant differences in LPO levels over time within each group analysis between days 10, 20, and 30. This suggests that LPO levels remained stable within each group throughout the exposure period. In contrast, comparison between groups (columns) revealed significant differences ($p \leq 0.05$).

Table 3. Mean value±SE of LPO nmoL\mL in experimental animals exposed to air freshener spray, scented candle, mixed and control group after10, 20, and 30 days

Group	Mean±SE of LPO nmoL/mL			L.S.D.
	10 day	20 day	30 day	
Air fresheners (A)	18.83±0.63 B a	21.29±1.57 A a	22.60±0.59 A a	4.01 NS
Scented candle (B)	20.07±1.22 AB a	19.44±2.10 A a	19.67±2.43 A a	2.69 NS
Mix (D)	23.81±1.15 A a	21.92±1.12 A a	22.94±1.27 A a	2.94 NS
Control (C)	10.45±2.33 C a	8.38±0.64 B a	11.17±1.28 B a	3.02 NS
L.S.D.	4.51 *	5.06 *	4.72 *	---

Different capital letters in column and small letters in row indicate significant differences * ($p \leq 0.05$). NS: Non-significant.

In the present study, LPO levels, measured in nmoL/mL, showed a clear increasing trend in rats exposed to air freshener, scented candle and their combination, compared to the control. This suggests that exposure to airborne chemical compounds induces oxidative stress, as evidenced by elevated serum LPO levels. Although hepatic enzymes were not assessed in the present study, the observed elevation in serum LPO levels following air freshener exposure may serve as an early indicator of oxidative stress potentially affecting hepatic tissues. This aligns with Airaodion et al. (2020b), who reported that air fresheners induce oxidative stress through increasing reactive oxygen species and LPO contributing to hepatotoxicity, particularly in association with formaldehyde exposure.

According to Yakasai and Mohammed (2022), air fresheners are made from hydrocarbons, along with other ingredients. Inhaling these hydrocarbons has been found to be toxic to the liver, as their metabolism generates free radicals that react with macromolecules in the liver, ultimately causing lipid peroxidation. The formation of active metabolites, together with accompanying LPO, appears to be among the primary mechanisms by which air fresheners may damage liver cells. These finding are consistent with the current study, which reported a significant increase in serum LPO levels following exposure to both air freshener and scented candles. This similarity supports the

notion that the oxidative stress by volatile compounds emitted from these products may represent a common underlying mechanism.

Airaodion et al. (2020c) reported that exposure to air fresheners resulted in increased malondialdehyde levels in rats, accompanied by increased antioxidant enzyme activity compared to the control group. This increase may indicate potential disruption of the body's antioxidant defense mechanisms, which is consistent with the findings of the present study. In additional, widespread tissue damage caused by free radicals-driven LPO may compromise the integrity of cell membranes, ultimate leading to decreased membrane fluidity (Oyenihi et al., 2016). Previous studies have also shown that prolonged exposure to air fresheners can increase malondialdehyde levels while reducing endogenous antioxidant molecules in the brains of mice (Afighor et al., 2019).

3.1.3 Superoxide dismutase (SOD)

The highest serum SOD level was observed in the air freshener group (5.54±0.17 ng/mL), while the lowest value was recorded in the control group across 10, 20, and 30 days. Statistical analysis showed no significant differences over time within each group (row analysis). However, comparison between groups (columns analysis) revealed significant differences only on day 10 ($p \leq 0.05$) (Table 4).

Table 4. Mean value±SE of SOD levels ng/mL in experimental animals exposed to air freshener spray, scented candle, mixed exposure, and control group after 10, 20, and 30 days

Group	Mean±SE of SOD ng/mL			L.S.D.
	10 day	20 day	30 day	
Air fresheners (A)	5.53±0.54 A a	5.11±0.67 A a	5.54±0.17 A a	1.02 NS
Scented candle (B)	5.38±0.26 A a	5.18±0.03 A a	4.49±0.51 A a	1.37 NS
Mix (D)	5.35±0.50 A a	4.12±0.39 A a	5.24±0.29 A a	1.31 NS
Control (C)	3.16±0.47 B a	3.57±0.34 A a	3.76±0.23 A a	1.27 NS
L.S.D.	1.42*	2.031 NS	2.178 NS	---

Different capital letters in column and small letters in row indicate significant differences * ($p \leq 0.05$). NS: Non-significant.

Supporting our results, Kim et al. (2021) found that air freshener exposure increased the expression of oxidative stress- related proteins, such as SOD, in mice with NAFLD. This suggests that air freshener can trigger an antioxidant response under oxidative stress conditions. While their study measured SOD in liver tissue of diseased mice, and ours assessed serum levels in healthy rats. Despite these differences, both observed elevated SOD after exposure. The difference in sample type and health status may explain why the increase in our study was not statistically significant.

Air freshener exposure led to a marked increase in antioxidant enzyme activity compared to the control group. SOD plays a role in mitigating the harmful effects of free radical attacks, as it is the only enzymatic system capable of converting (O_2^-) into oxygen and hydrogen peroxide (H_2O_2). This function is essential for protecting cells against oxidative stress. These radicals are known to damage polyunsaturated fatty acids and proteins (Airaodion et al., 2020a).

3.1.4 Reduced glutathione (GSH)

The control group consistently showed the highest mean of GSH levels (191.00±11.00 µmol/L; 183.00±1.00 µmol/L; 192.00±2.00 µmol/L) across days 10, 20, and 30 respectively. In contrast, the lowest GSH level in the treated group, especially the scented candle group (71.25±48.75 µmol/L) on day 10 and the mixed exposure group (69.75±32.25 µmol/L) on day 30, suggesting that exposure to air freshener and scented candle products may reduce GSH levels over time. Statistically, rows, no significant differences (NS) were observed within each group over days, indicating that GSH levels remained relatively stable within each treatment across the study period. In contrast, comparison between groups (columns analysis) showed statically significant differences ($p \leq 0.05$) at each day (Table 5).

Table 5. Mean value±SE of GSH levels µmol/L in experimental animals exposed to air freshener spray, scented candle, mixed exposure and control group after10, 20, and 30 days

Group	Mean±SE of GSH µmol/L			L.S.D.
	10 day	20 day	30 day	
Air fresheners (A)	86.25±26.25 B a	93.50±3.50 B a	81.50±61.00 B a	33.61 NS
Scented candle (B)	71.25±48.75 B a	88.25±5.75 B a	88.75±8.75 B a	28.55 NS
Mix (D)	82.50±30.00 B a	83.75±43.75 B a	69.75±32.25 B a	28.06 NS
Control (C)	191.00±11.00 A a	183.00±1.00 A a	192.00±2.00 A a	37.21 NS
L.S.D.	27.34 *	31.08 *	26.95 *	---

Different capital letters in column and small letters in row indicate significant differences * ($p \leq 0.05$). NS: Non-significant.

The findings of the present study are consistent with those reported by Airaodion et al. (2020a), who assessed the impact of air freshener exposure on oxidative stress and immune function in male Wistar rats. Both studies demonstrated a notable reduction in serum GSH levels in the exposed groups compared to the control group. These observed similarities supports the hypothesis that prolonged inhalation of air fresheners impairs redox homoeostasis by exhausting GSH reserves.

Glutathione functions by detoxifying hydrogen peroxide and lipid peroxide through electrons donation, converting these reactive species into harmless byproducts such as water and oxygen. This process plays a critical role in shielding cellular components including lipids from oxidative degradation. The observed decrease in GSH levels among rats exposed to air freshener for 28 days may be attributed to oxidative stress induced by air pollutions, as well as the direct binding of GSH with reactive intermediates formed during pollutant oxidation (Airaodion et al., 2020d). These findings are consistent with the results of the present study.

The reduction in blood antioxidant levels observed after air freshener exposure is likely due to the presence of VOCs, which alters the equilibrium between ROS and the body's defense mechanisms, leading to oxidative stress as a result of excessive ROS generation (Yang et al., 2007). Disruption of the antioxidant defense system increases the body's susceptibility to various diseases (Wang et al., 2013). Chronic exposure to air pollutants, particularly elevated concentrations of particulate matter, has been linked to cancer development through mechanisms involving cellular oxidative stress (Cocârţă et al., 2021). Previous studies have reported that air fresheners induce oxidative stress by increasing ROS generation. The adverse effect of air freshener on male sex hormones could also result from increased free radicals production and oxidative stress induction by these products (Airaodion et al., 2020e).

4. CONCLUSION

The findings of this study reveal that exposure to air freshener and scented candle induced a clear state of oxidative stress in the treated rats, as evidenced by significant biochemical alterations. GSH levels decreased markedly in all treated groups compared to control, reaching the lowest value of 69.75 µmol/L in the 30 day mixed exposure group, versus 191.00 µmol/L in controls. Conversely, LPO levels increased across all exposure duration, with the highest value of 22.94 nmol/mL recorded in the mixed exposure group after 30 days. SOD levels progressively rose, reaching 5.54 ng/mL in the 30 days spray group compared to 3.16 ng/mL in controls. GPX levels also increased, with highest level of 1,745.48 pg/mL in 30 day spray group. Collectively, these results demonstrate that exposure disrupted redox balance and caused cellular injury, highlighting the pro-oxidant and potentially toxic nature of air freshener sprays and scented candles.

ACKNOWLEDGEMENTS

Our sincere gratitude is extended to the staff of the Animal House Unit at Biotechnology Research Center, University of Al-Nahrain, for their valuable support and assistance throughout the experimental procedures.

AUTHOR CONTRIBUTIONS

Conceptualization, Al-Maliki MAS; Methodology, Al-Maliki MAS; Investigation, Al-Maliki MAS; Formal analysis, Al-Maliki MAS; Data curation, Al-Maliki MAS; Writing original draft, Al-Maliki MAS; Writing review and

editing, Al-Maliki MAS; Visualization, Al-Maliki MAS; Supervision, Al-Easawi NAF; Project administration, Al-Maliki MAS, Al-Easawi NAF.

DECLARATION OF CONFLICT OF INTEREST

The authors declare that this study was conducted without any conflicts of interest.

REFERENCES

Abu Ghazal TS, Subih HS, Obeidat BS, Awawdeh MS. Hemp seed oil effects on female rats fed a high-fat diet and modulating adiponectin, leptin, and lipid profile. Agriculture 2023;13(2):1-9.

Adamowicz J, Juszczak K, Poletajew S, Van Breda SV, Pokrywczynska M, Drewa T. Scented candles as an unrecognized factor that increases the risk of bladder cancer; is there enough evidence to raise a red flag? Cancer Prevention Research 2019;12(10):645-52.

Afighor M, Ben-Azu B, Ajayi AM, Umukoro S. Role of cytochrome C and tumor necrosis factor-alpha in memory deficit induced by high doses of a commercial solid air freshener in mice. Journal of Chemical Health Risks 2019; 9(4):263-74.

Ahmed AK, Yenzeel JH. Determination of some oxidative stress parameters and antioxidants in sample of Iraqi beta thalassemia major patients. Iraqi Journal of Science 2017;58(1A):1-3.

Airaodion AI, Alabi OJ, Ogbuagu EO, Atiba FA, Olawoyin DS. Nephro and hepatotoxic effect of air-freshener in Wistar rats. Asian Journal of Research in Nephrology 2020b;3(2):1-9.

Airaodion AI, Ngwogu AC, Ekenjoku JA, Ngwogu KO. Hepatoprotective potency of ethanolic extract of *Garcinia kola* (Heckel) seed against acute ethanol-induced oxidative stress in Wistar rats. International Research Journal of Gastroenterology and Hepatology 2020c;3(1):42-51.

Airaodion AI, Ngwogu KO, Ngwogu AC. Common household insecticides used in Nigeria induced oxidative stress in Wistar rats. Asian Pacific Journal of Allergy and Immunology 2020d;3(1):84-90.

Airaodion AI, Ogbuagu EO, Atiba FA, Olawoyin DS, Alabi OJ. Frequent exposure to air-freshener reduces male fertility. Asian Research Journal of Gynaecology and Obstetrics 2020e;3(3):19-31.

Airaodion AI, Olawoyin DS, Alabi OJ, Atiba FA, Ogbuagu EO. Air freshener induced oxidative stress and its adverse effects on immunity. International Journal of Health, Safety and Environment 2020a;6(05):579-87.

Al-Badry SH, Ibrahim NG, AlMashhadani HA, Kadhim MM. The role of oxidative stress in patients with chronic kidney disease. Wiadomosci Lekarskie Medical Advances 2023;76(5 p. 1):951-5.

Al-Easawi NA. The Effect of Exposure to Shisha Smoke and Cigarette in Some Vital Organs of Male Mice [dissertation]. Baghdad: Collage of Science, University of Baghdad; 2015.

Alfahdawi OA, Alfahdawi AA, Mohammed IM. Effects of aqueous extract of cumin seed (*Cuminum cyminum*) on the structure and function of albino rat kidneys treated with dibutyl phthalate. Iraqi Journal of Science 2023;64(5):2168-77.

Banks WA, Rhea EM. The blood-brain barrier, oxidative stress, and insulin resistance. Antioxidants 2021;10(11):1-14.

Cheek E, Guercio V, Shrubsole C, Dimitroulopoulou S. Portable air purification: Review of impacts on indoor air quality and health. Science of the Total Environment 2021;766:Article No. 142585.

Choi YH, Kim HJ, Sohn JR, Seo JH. Occupational exposure to VOCs and carbonyl compounds in beauty salons and associated health risks in South Korea. Ecotoxicology and Environmental Safety 2023;256:Article No. 114873.

Cincinelli A, Martellini T. Indoor air quality and health. International Journal of Environmental Research and Public Health 2017;14(11):1-5.

Cocârţă DM, Prodana M, Demetrescu I, Lungu PE, Didilescu AC. Indoor air pollution with fine particles and implications for workers' health in dental offices: A brief review. Sustainability 2021;13(2):1-17.

Ellman GL. Tissue sulfhydryl groups. Archives of Biochemistry and Biophysics 1959;82(1):70-7.

Fakhri YA, Al-Ani AW. Association of superoxide dismutase with ticagrelor treatment in patients with peripheral arterial disease. Iraqi Journal of Science 2025;66(5);1812-23.

Gabriel-Brisibe CU, Odinga T, Wokocha PG, Agara HN, Adinde TC. Exposure to air freshner and its distresses on the antioxidant biomarkers of male Wistar rats. Journal of Toxicology and Environmental Health Sciences 2020; 12(3):22-6.

Goodman N, Nematollahi N, Agosti G, Steinemann A. Evaluating air quality with and without air fresheners. Air Quality, Atmosphere and Health 2020;13(1):1-4.

Hammod NM, Al-Janabi KWS, Hasan SA. Determination of some volatile organic compounds in the water produced at Al-Ahdab oilfield using headspace SPE-GC-FID. Indian Journal of Forensic Medicine and Toxicology 2020;14(1):994-9.

Hellou J, Ross NW, Moon TW. Glutathione, glutathione S-transferase, and glutathione conjugates, complementary markers of oxidative stress in aquatic biota. Environmental Science and Pollution Research 2012;19(6):2007-23.

Khalid FK, Rabee AM. Association of traffic-related air pollution with DNA damage and some other biological parameters among minibuses drivers in Baghdad City. Iraqi Journal of Science 2025;66(4):1478-85.

Kim S, Lee AY, Cho MH. Inhaled exposure to air fresheners aggravated liver injury in a murine model of nonalcoholic fatty acid liver disease. Heliyon 2021;7(3):1-7.

Li Z, Liu Q, Xu Z, Guo X, Wu S. Association between short-term exposure to ambient particulate air pollution and biomarkers of oxidative stress: A meta-analysis. Environmental Research 2020;191:Article No. 110105.

Lodovici M, Bigagli E. Oxidative stress and air pollution exposure. Journal of Toxicology 2011;2011(1):1-9.

Oyenihi OR, Afolabi BA, Oyenihi AB, Ogunmokun OJ, Oguntibeju OO. Hepato-and neuro-protective effects of watermelon juice on acute ethanol-induced oxidative stress in rats. Toxicology Reports 2016;3:288-94.

Seguel JM, Merrill R, Seguel D, Campagna AC. Indoor air quality. American Journal of Lifestyle Medicine 2017;11(4):284-95.

Seo JH, Kim PG, Choi YH, Shin W, Sochichiu S, Khoshakhlagh AH, et al. Evaluation of personal exposure to volatile organic chemicals (VOCs) in small-scale dry-cleaning facilities using passive sampling. Atmospheric Environment 2025;353: Article No. 121235.

Singh A, Kumari A, Fatima L. Beyond aromatherapy: Illuminating the underappreciated risks associated with scented candle

exposure. Environmental Science and Technology 2023;57(41):15299-300.

Statistical Packages for the Social Sciences (SPSS). SPSS/IBM Statistics, Version 26 Step by Step. 16th ed. SPSS; 2019.

Wang F, Li C, Liu W, Jin Y. Oxidative damage and genotoxic effect in mice caused by sub-chronic exposure to low-dose volatile organic compounds. Inhalation Toxicology 2013; 25(5):235-42.

World Health Organization (WHO). Principles and Methods of Evaluating the Toxicity of Chemicals. Part 1. Environmental Health Criteria 6. Geneva: World Health Organization; 1978.

Yakasai AU, Mohammed B. Biochemical effects of gel and liquid air fresheners sold in Kano on Swiss albino rats (*Rattus norvegicus*). Bayero Journal of Pure and Applied Sciences 2022;13(1):554-9.

Yang W, Li J, Hekimi S. A measurable increase in oxidative damage due to reduction in superoxide detoxification fails to shorten the life span of long-lived mitochondrial mutants of Caenorhabditis elegans. Genetics 2007;177(4):2063-74.

Yun H, Seo JH, Kim YG, Yang J. Impact of scented candle use on indoor air quality and airborne microbiome. Scientific Reports 2025;15(1):1-10.

Environment and Natural Resources Journal

Volume 24
Issue 2
2026

Forest Cover and Landslide Susceptibility Assessment Using a Machine Learning Approach in Northern Midland and Mountainous Region of Vietnam

Thuong Tran[1], Hoa Trieu[2*], and Nathaniel Bantayan[3]

[1]*International School - Thai Nguyen University, Vietnam*
[2]*Thai Nguyen University of Agriculture and Forestry, Vietnam*
[3]*University of the Philippines Los Baños, Philippines*

ARTICLE INFO

Received: 16 Jun 2025
Received in revised: 11 Nov 2025
Accepted: 13 Nov 2025
Published online: 15 Jan 2026
DOI: 10.32526/ennrj/24/20250178

Keywords:
Forest/ Landslides susceptibility/ ML/ KNN/ RF/ MLP/ Cau River Watershed

*** Corresponding author:**
E-mail:
xuanhoatrieu@tuaf.edu.vn

ABSTRACT

Landslides are a major geo-environmental hazard in Vietnam's midland and mountainous regions, further intensified by land-use pressures and climate change. This study investigated the influence of forest cover on landslide susceptibility in Cau River Watershed. A forest status map was constructed using inventory and field data by the K-Nearest Neighbors (KNN) algorithm, while landslide susceptibility was modeled using historical events and nine conditioning factors through a hybrid machine learning approach integrating Random Forest (RF), Multilayer Perceptron (MLP) and KNN. The proposed hybrid model achieved an overall accuracy of 85.33%, demonstrating its robustness in susceptibility prediction. Results indicated that natural and native-species forests significantly reduce landslide density and susceptibility relative to non-forested areas and exotic plantations. These findings highlight the critical role of forest structure and species composition in stabilizing slopes. The study provides evidence-based insights to guide adaptive land management, forest policy, and regional strategies for climate resilience and sustainable development.

HIGHLIGHTS

A hybrid KNN-RF-MLP framework was developed for landslide susceptibility mapping. The hybrid model achieved 85.33% accuracy, outperforming the standard RF model. Forest cover maps were enhanced using KNN imputation for incomplete field data. Native forests and species-rich stands greatly reduced landslide susceptibility. Findings guide sustainable reforestation and climate-resilient land management.

1. INTRODUCTION

Understanding the link between landslide susceptibility and climate-induced hazards is increasingly critical, particularly in Southeast Asia, where climate variability is intensifying. Northern Vietnam is characterized by steep terrain, high rainfall, and rapid land-use changes. In such regions, assessing landslide susceptibility is vital for climate resilience. It enables the identification of high-risk zones and supports sustainable land-use planning (Chen and Pan, 2019).

Forests and vegetation cover are essential in mitigating the impacts of natural hazards, particularly landslides (WB, 2019). Forest ecosystems provide essential services such as slope stabilization, erosion control, water regulation, and biodiversity conservation. Tree roots reinforce soil structure and improve infiltration, while canopy cover reduces the erosive impact of rainfall (FAO, 2013). These functions make intact and biodiverse forests key to reducing landslide severity and protecting human settlements and infrastructure.

In Vietnam, recent government initiatives have emphasized reforestation and early zoning of landslide-prone areas as part of national adaptation strategies to natural disasters (VNDMA, 2023b). The importance of forest-based resilience is also supported by regional studies. According to FAO's report (2013), Asia remains one of the most landslide-prone continents, where increasing rainfall extremes and

Citation: Tran T, Trieu H, Bantayan N. Forest cover and landslide susceptibility assessment using a machine learning approach in northern midland and mountainous region of Vietnam. Environ. Nat. Resour. J. 2026;24(2):209-221. (https://doi.org/10.32526/ennrj/24/20250178)

ongoing land degradation continue to exacerbate disaster risks. In mountainous provinces of northern Vietnam, catastrophic landslides in recent years have resulted in significant loss of life and damage to both agricultural and forested land (VNDMA, 2023b).

To improve hazard prediction and environmental planning, machine learning (ML) techniques are increasingly used in landslide susceptibility modeling. These data-driven approaches can integrate diverse environmental variables to generate highly accurate susceptibility maps, even in regions with limited or incomplete field data. Such maps are essential tools for identifying zones exposed to both environmental and meteorological risks. They provide spatially explicit information that facilitates early warning systems, risk communication, and adaptive land-use planning.

In northern Vietnam, heavy rainfall is widely recognized as the dominant triggering factor of landslides (Le and Kaneko, 2017). However, forest cover is a critical variable that can be directly managed to mitigate slope instability. With its relatively high forest cover, Cau River Watershed offers an ideal setting to examine how forest classifications influence landslide susceptibility. Therefore, this study aims to: (i) assess the spatial distribution of forest cover and landslide susceptibility in Cau River Watershed; (ii) develop and validate a hybrid machine learning framework (KNN-RF-MLP) for improving landslide susceptibility prediction; and (iii) evaluate the effects of different forest types on landslide occurrence.

2. METHODOLOGY

2.1 Study area

This study focuses on Cau River Watershed located in Thai Nguyen Province (CRWTN), as illustrated in Figure 1. The watershed spans from latitude 21°26′8″N to 22°2′54″N and longitude 105°28′36″E to 106°7′41″E, covering approximately (3,527 km², equivalent to 79.6%) of the total land area of Thai Nguyen Province (as of June 2025). Of this area, around 1,876 km² is classified as forest land (VNGSO, 2024).

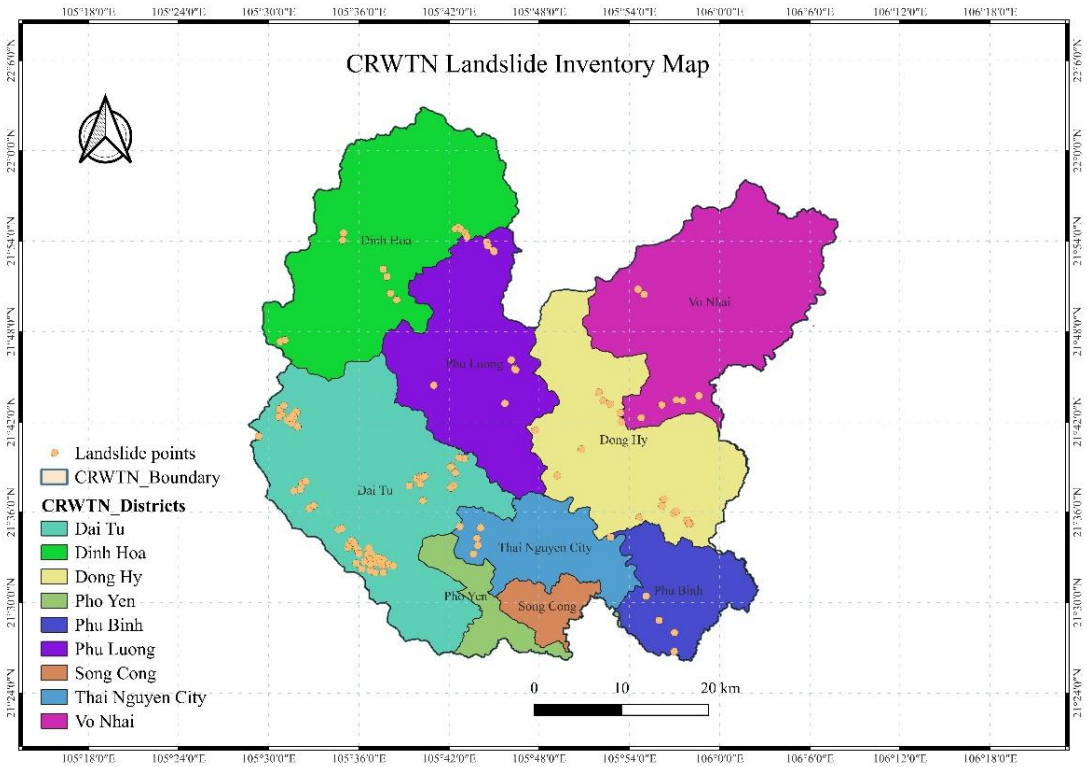

Figure 1. Landslide inventory map of CRWTN

The study area is characterized by typical natural features of a mountainous province in northern Vietnam, situated within a tropical monsoon climate zone. The topography is predominantly composed of hills and mountains, which define the region's dominant terrain. Most of the area lies below 300 meters in elevation, although approximately two-thirds of the province's total land area consists of hilly and

mountainous terrain exceeding 100 meters in elevation (Le and Kaneko, 2017). The region experiences a tropical monsoon climate with a distinctly cold winter. Annual precipitation is high, with a prolonged rainy season extending from May to October. The most intense rainfall typically occurs between June and August, during which maximum daily rainfall events range from approximately 208 mm to 496 mm. This contributes to an annual rainfall total ranging from 1,360 to 2,572 mm. According to annual forest reports by the Vietnam Administration of Forestry (VAF, 2024), the forested area in Thai Nguyen Province has shown a general increasing trend from 2010 to 2023. As of 2023, forest cover in Cau River Watershed exceeded 1,575 km^2, representing 56.1% of the total study area (TNFPD, 2024). Situated at the heart of the Northern Midland and Mountainous Region - one of Vietnam's most landslide-prone areas (Bui, 2017), (Le and Kaneko, 2017) - the study area has experienced significant landslide events. Over the past two decades, Thai Nguyen Province has suffered extensive damage from landslides, resulting in 110 fatalities and widespread destruction of residential structures (VNDMA, 2023a).

2.2 Data and methods

The methodological framework of this study consisted of: (i) data collection and preprocessing, (ii) forest status and landslide susceptibility mapping, and (iii) empirical analysis of the relationships between forest and landslides (Figure 2).

2.2.1 Data collection and processing

The mapping component involved the delineation of forest types and the spatial distribution of areas susceptible to landslides. For forest status mapping, data were collected from the Thai Nguyen Forest Protection Department, including official forest inventory records. Additional field data were obtained from the sample plots.

For landslide susceptibility modeling, the input dataset included a landslide inventory map (Figure 1) that was developed using historical landslide events from previous research projects, field observations, and entries from the NASA Global Landslide Catalog (updated in 2019), as well as various landslide conditioning factors (LCFs) as in Figure 3. These nine LCFs were selected to represent the topographic, geological, vegetation, land cover, and climatic characteristics of the study area (Table 1).

Table 1. Landslide conditioning factors

Factor(s)	Category	Source/Resolution	Period
Slope, Elevation, Drainage Density, Relief Degree of Land Surface (RDLS)	Topographic	DEM (SRTM 30 m, USGS)	2020
Lithology	Geological	Thai Nguyen Department of Science and Technology	2015
Soil type	Pedological	National Pedology Map (Open Development Mekong)	2015
NDVI	Vegetation	Landsat 8 (30 m, USGS)	2023
LULC	Land cover	JAXA Northern Vietnam LULC Map	2020
Precipitation	Climatic	Hydrometeorological stations, Thai Nguyen	2010-2023

These factors have been widely recognized in previous studies as key variables influencing slope stability and landslide occurrence.

2.2.2 Forest status and landslide susceptibility mapping

a) Forest status mapping

To establish a forest status map, data from the Forest Inventory provided by the local Forest Protection Department were integrated with field survey records. A significant challenge encountered during this process was the presence of numerous locations with incomplete or missing data. To address this limitation, the K-Nearest Neighbors (KNN) algorithm was applied to validate existing entries and impute the missing values, thereby enhancing the completeness and reliability of the dataset.

KNN algorithm is a widely used, straightforward, and effective supervised machine learning technique. It classifies new data points based on the majority class among the K closest instances in the training dataset, using a distance metric such as Euclidean distance (Harrison, 2018).

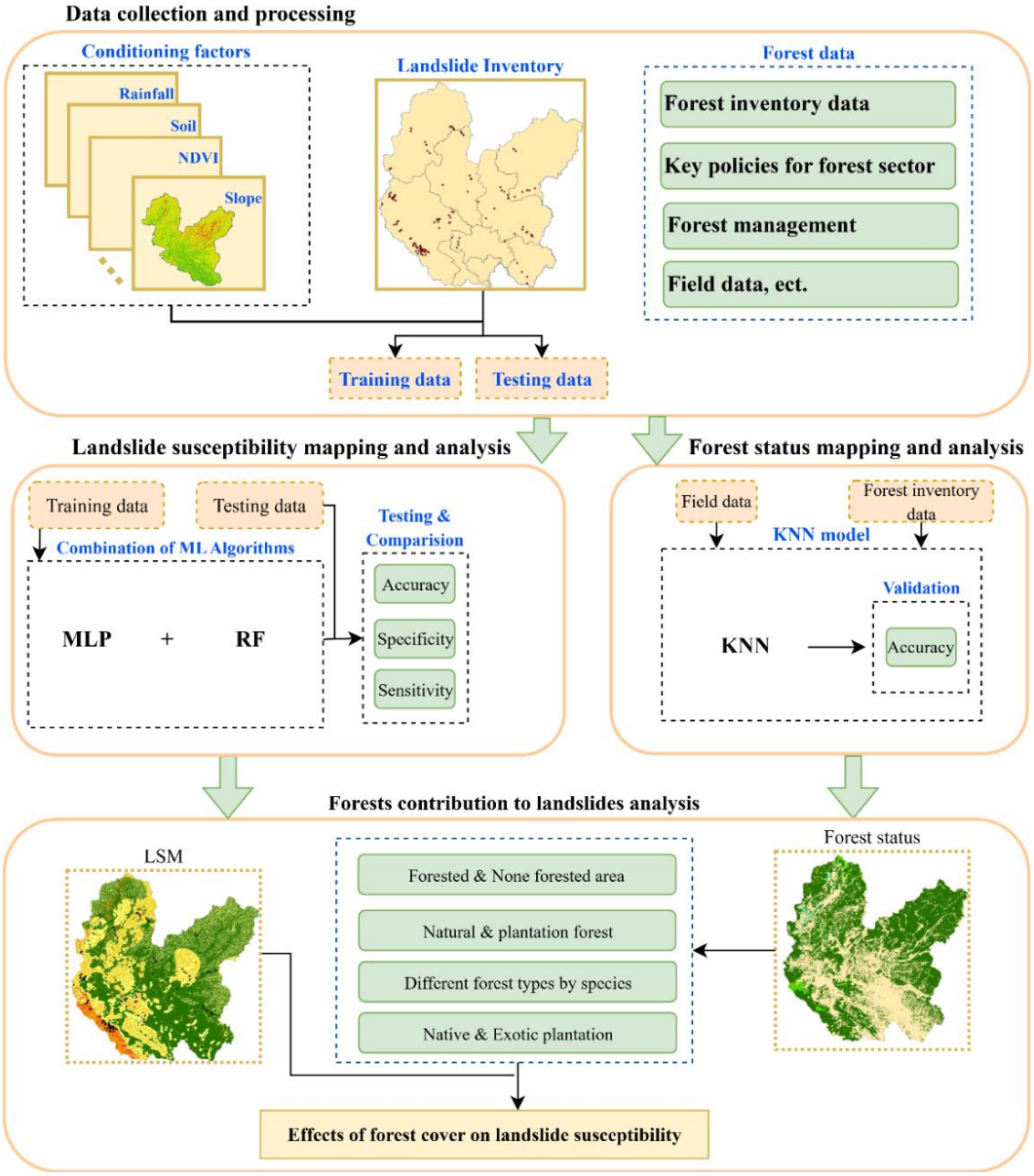

Figure 2. Framework for Forest Cover and Landslide Susceptibility Assessment

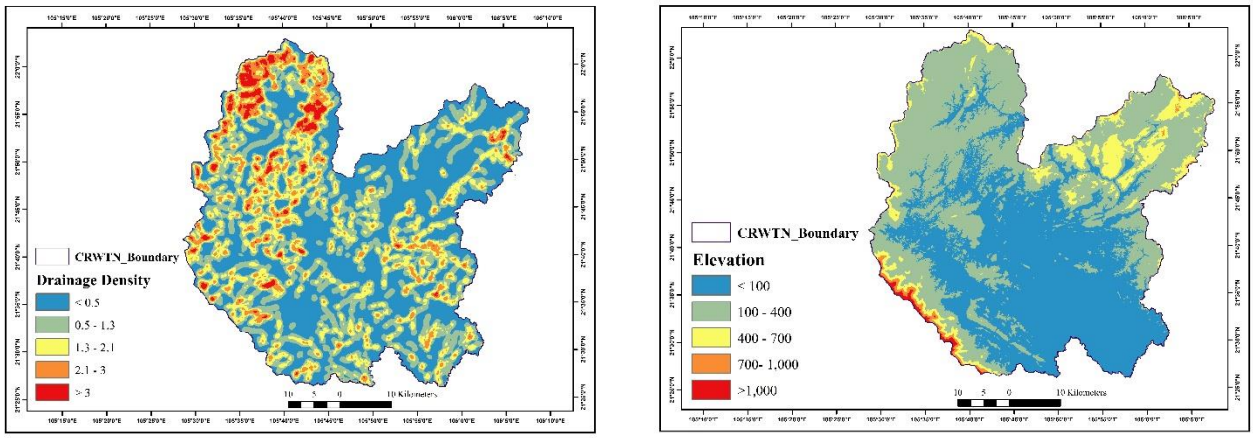

Figure 3. Landslide conditioning factors (LCFs)

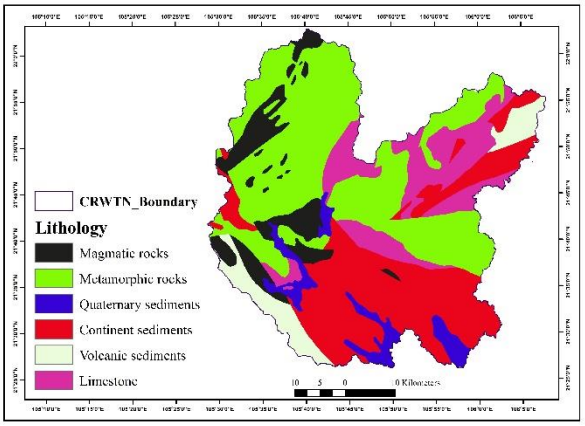

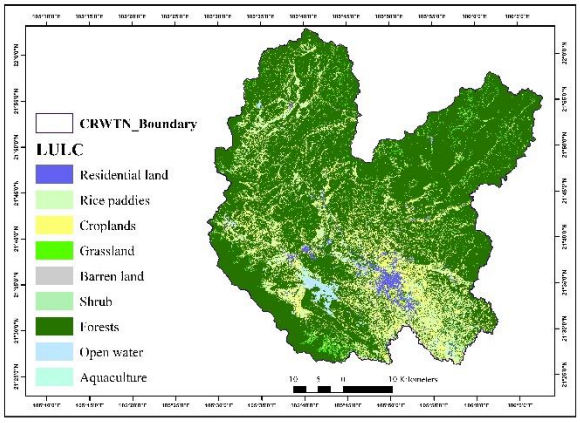

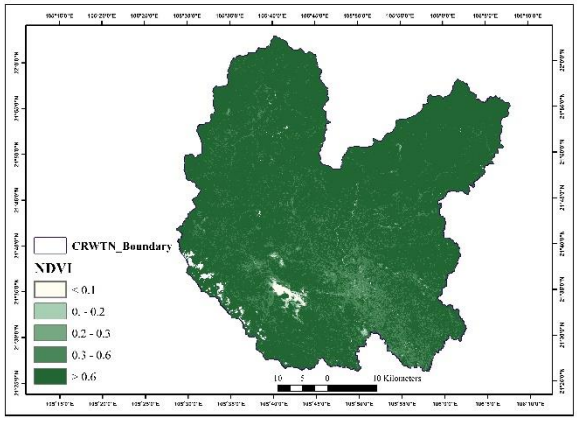

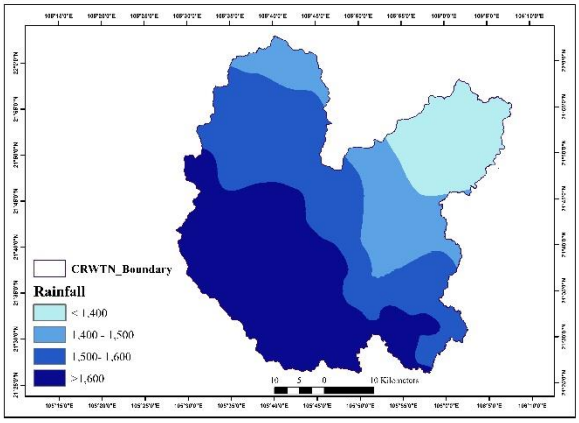

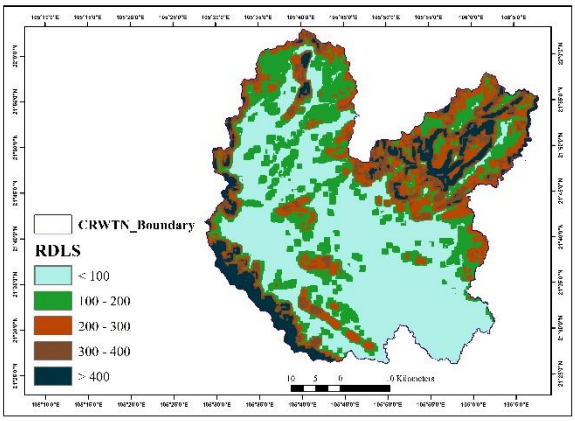

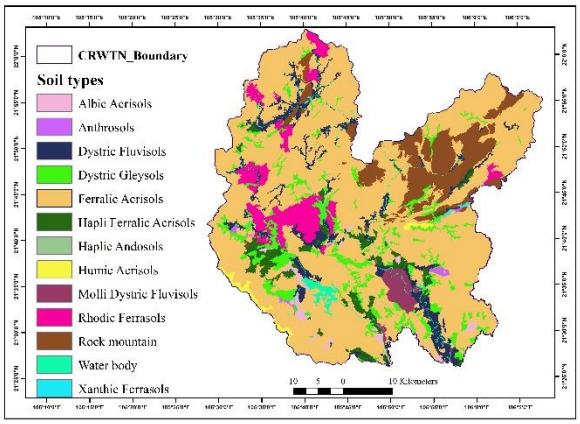

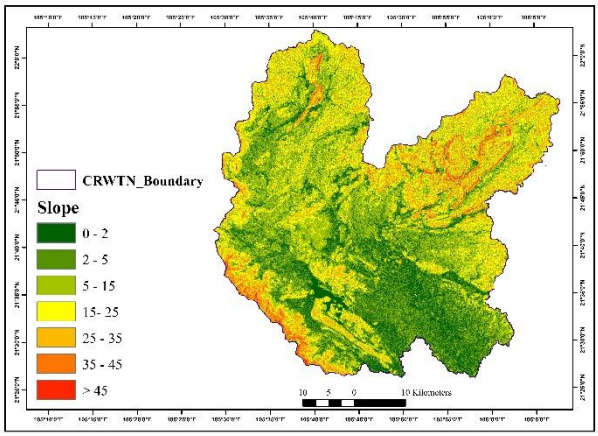

Figure 3. Landslide conditioning factors (LCFs) (cont.)

Basic steps of how the KNN works are depicted as below:

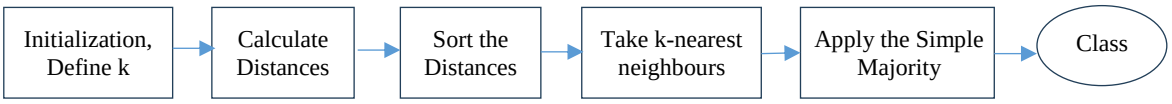

The performance of the KNN model has been evaluated using the accuracy criteria, as it provides a straightforward and comprehensive measure of overall classification correctness. Given that the dataset was relatively balanced and KNN was applied primarily for imputation rather than predictive modeling, accuracy (ACC) was considered sufficient for assessing model quality. This quality criterion refers to the closeness of a measurement to the true or accepted value (James, 2013).

$$ACC = \frac{TP+TN}{TP+FP+TN+FN}$$

The model's output has been imported into a GIS tool. Subsequently, a forest status map for the study area was generated by integrating these processed data.

b) Landslide susceptibility mapping

Step 1: Landslide susceptibility model construction

For landslide susceptibility modeling, the input dataset contained a landslide inventory map documenting 125 landslide events and nine LCFs (Figure 3). All grid cells in the dataset referring to landslides were assigned a value of 1. An equal number of grid cells referring to non-landslide was randomly sampled from the landslide-free regions and assigned a value of 0. Corresponding LCF values were extracted to form labeled datasets indicating the presence or absence of landslides, including all LCF attributes. The dataset was randomly divided into training and testing subsets using a 70/30 split. To ensure robust classification performance, a fivefold cross-validation procedure was employed. The dataset was partitioned into five subsets, with the model trained on four and tested on the remaining one. This process was repeated five times to provide a reliable estimate of model performance.

A two-phase training strategy (Tran et al., 2024) was used for model construction. In Phase 1, a ML model was trained on the original training dataset. The resulting outputs were then integrated with the original data to create an augmented dataset. In Phase 2, the model was retrained using this enhanced input, and its predictive performance was assessed. This strategy effectively leveraged the Phase 1 model to enrich the training data, while the Phase 2 model performed the final landslide susceptibility prediction. In this study, a hybrid approach combining Random Forest and Multilayer Perceptron was developed and applied for landslide susceptibility mapping. Additionally, the KNN algorithm was applied to verify and impute missing data before executing the two main phases (Figure 4).

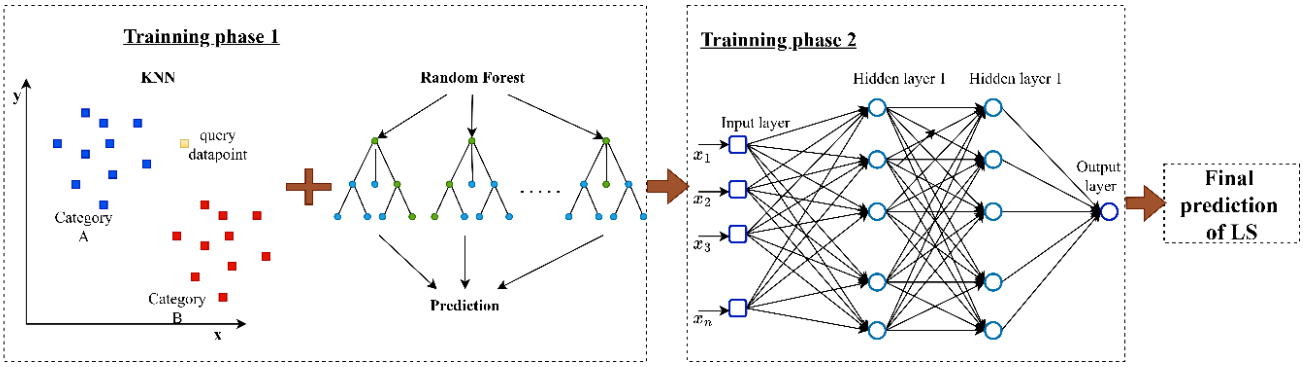

Figure 4. Architecture of the hybrid ML model for landslide susceptibility prediction

- Random forest algorithm

RF algorithm employs an ensemble of decision trees to enhance the accuracy and robustness of predictions (Breiman, 2001). Each tree in the ensemble is trained on a randomly selected subset of the training data and a random subset of input features, which helps reduce the inter-tree correlation and improves the model's generalization capability. In this work, to further optimize the performance of the RF model, hyperparameter tuning was performed using

the grid search technique. Hyperparameters are defined as user-set parameters that influence the learning process but are not learned directly from the data. Grid search systematically explored a predefined range of hyperparameter values to identify the combination that yielded the best performance on a validation set. Key hyperparameters that were tuned in RF models include: (i) the number of decision trees in the ensemble; (ii) the maximum depth of each tree; and (iii) the maximum number of features considered when splitting a node.

- *Multilayer perceptron*

MLP is a type of feedforward artificial neural network that consists of three main components: an input layer, one or more hidden layers, and an output layer. The input layer receives variables representing the features of the dataset. Each neuron (or node) in a hidden or output layer computes a weighted sum of the inputs it receives from the previous layer, adds a bias term, and applies a nonlinear activation function, such as the rectified linear unit used in this study, to introduce non-linearity into the model.

During training, MLP learns by adjusting the weights and biases of the network through the backpropagation algorithm, in conjunction with an optimization technique such as stochastic gradient descent in this work. The training objective is to minimize a loss function - commonly mean squared error for regression or cross-entropy for classification - by computing gradients of the loss with respect to each weight and bias and updating them iteratively. The architecture of MLP network used in this study is illustrated in Figure 4 (phase 2).

Step 2: Model validation

Several statistical metrics-namely Accuracy (ACC), Sensitivity (SEN), and Specificity (SPE) - were employed to evaluate the performance of the predictive models. Accuracy represents the overall correctness of the model by measuring the percentage of total predictions (both positive and negative) that are correct. It indicates how closely the model's predictions match with the actual outcomes. Sensitivity, also known as the true positive rate or recall, measures the model's ability to correctly identify positive instances (e.g., actual landslides). Specificity evaluates the model's ability to correctly classify negative instances (e.g., non-landslide areas). These evaluation metrics were calculated using the following formulas:

$$\mathrm{ACC} = \frac{\mathrm{TP+TN}}{\mathrm{TP+FP+\ TN+FN}};\quad \mathrm{SEN} = \frac{\mathrm{TP}}{\mathrm{TP+FN}};\quad \mathrm{SPE} = \frac{\mathrm{TN}}{\mathrm{TN+FP}}$$

Where: TP (True Positive): the percentage of actual landslide cases correctly classified as landslides; FP (False Positive): the percentage of non-landslide cases incorrectly classified as landslides; TN (True Negative): the percentage of non-landslide cases correctly classified as non-landslides; FN (False Negative): the percentage of actual landslide cases incorrectly classified as non-landslides.

Step 3: Map establishment: The output of the model was imported into a GIS tool to create a landslide susceptibility map.

2.2.3 Effect of forest cover on landslides assessment

Using the forest status map and the landslide susceptibility map generated in the previous sections, the relationship between forest cover and landslide occurrence was evaluated. The analysis considered the distribution and susceptibility of landslides across the following categories: (i) forested versus non-forested areas; (ii) broad forest classifications, including natural forests and planted forests (based on original classification criteria); (iii) forest types distinguished by species composition, such as woody forests, mixed-species forests, palm and coconut plantations, and bamboo forests; (iv) subcategories of planted forests, specifically native versus exotic plantations.

Tools: Python's scikit-learn, Google Earth Engine, ArcGIS 10.5.

3. RESULTS

3.1 Forest status mapping and analysis in CRWTN

A KNN model was developed to generate the forest status map of CRWTN, utilizing data from the Local Forest Protection Department's forest inventory and supplementary field observations. Missing values in the dataset were imputed using predictions generated by the trained model. The model's performance was tested over an area of 2,423.85 km² in Van Yen commune, accounting for 32.37% of the total area with initially missing data, and achieved an accuracy of 86.26%. As a result, in Van Yen commune, forested land covers 86.41% of the total area, with a total forest area of 2,097 hectares. This includes 1,059.66 hectares of natural forests and 1,037.34 hectares of planted forests. Based on species classification, the commune contains 1,833.66

hectares of woody forests, 5.13 hectares of bamboo forests, and 258.21 hectares of mixed forests. After validation, the model was applied to the entire study area to produce the final forest status map of CRWTN (Figure 5).

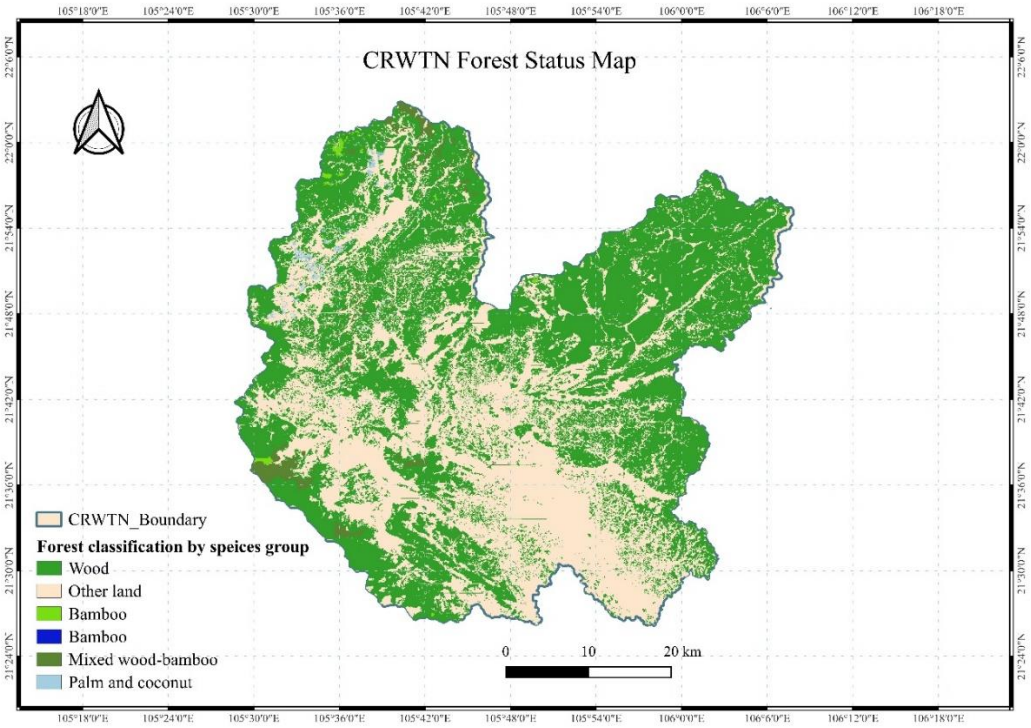

Figure 5. Forest status map in terms of species

Regarding forest origin, among the total 158,515.59 hectares of forested land in the study area, natural forests account for 40.8%, while planted forests represent 59.2%. Based on species classification, four main forest types are identified: woody forests (151,708.7 ha), bamboo forests (807.66 ha), mixed forests (4,467.06 ha), and palm and coconut plantations (1,234.19 ha). Woody forests are the most dominant, covering 95.89% of the total forest area in the watershed. In addition to native tree species, exotic species are also widely used in planted forests throughout CRWTN, primarily for the timber production and other economic purposes.

Similar to other forest-dominated regions in Vietnam, forests in CRWTN play a vital role in the local environment, society, and economy. They provide essential ecosystem services such as water supply, soil protection, flood control, air purification, and biodiversity conservation. Forests also support key industries including timber, agriculture, tourism, and food processing. Valuable species like pine, oak, and rosewood are used for wood products, while fruit trees and medicinal plants support local livelihoods. Therefore, effective forest protection and management are crucial for the sustainable development of CRWTN and the well-being of its communities.

3.2 Landslide susceptibility mapping and analysis in CRWTN

The two-phase training approach was used to develop a hybrid model integrating KNN, RF, and MLP. To evaluate the effectiveness of the proposed hybrid model, its performance was compared with the conventional RF model using three common classification metrics: ACC, SEN, and SPE. These metrics provide a comprehensive assessment of the model's ability to correctly classify landslide-prone and non-prone areas. As shown in Table 2, the hybrid model outperformed the single RF model across all evaluation criteria.

Table 2. The performance of models

Model	ACC	SEN	SPE
RF	76%	76%	76%
Hybrid	85.33%	85.71%	83.33%

Based on its superior classification performance, the hybrid model was applied to generate the landslide susceptibility map for CRWTN. The resulting map provides a spatial representation of landslide risk levels across the region and was divided into five susceptibility categories (Bui, 2017), (Chen and Pan, 2019): very low, low, moderate, high, and very high (Figure 6). This classification scheme enabled more effective interpretation of risk zones and supports the development of targeted mitigation and land-use planning strategies.

The spatial distribution of landslide susceptibility in CRWTN showed a predominance of low-risk zones. Areas classified as very low susceptibility covered approximately 154,129 hectares, accounting for 54.88% of the total area. Low susceptibility zones represented 48,334 hectares (17.21%), while moderate susceptibility areas spanned 22,159 hectares (7.89%). In contrast, regions of high and very high susceptibility were more limited in extent, comprising 14,258 hectares (5.08%) and 41,973 hectares (14.94%), respectively. These results indicate that approximately 20% of the area was classified as having high to very high susceptibility, emphasizing the need for detailed monitoring and proactive risk management in those zones.

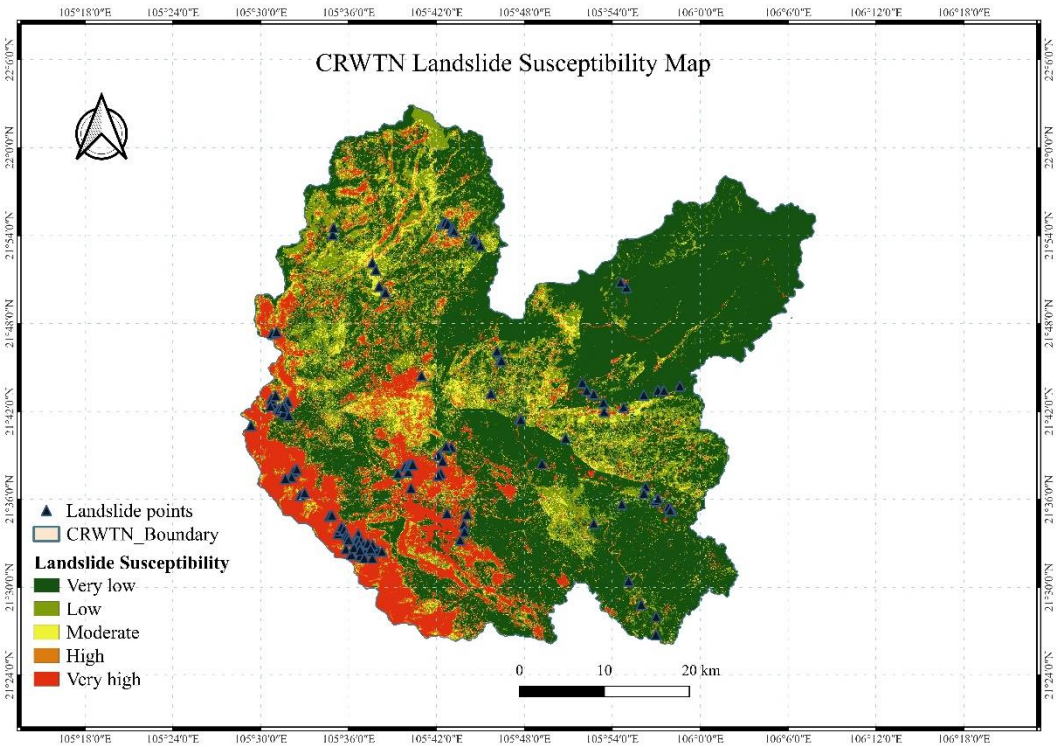

Figure 6. Landslide susceptibility map produced by the hybrid model

3.3 Effects of forest cover on landslide occurrences in CRWTN

The multi-dimensional assessment employed in this study enabled a deeper understanding of whether forest cover contributes to reducing landslide occurrence or, conversely, is associated with heightened landslide susceptibility in the study area. Using the forest status map and the landslide susceptibility map generated in previous sections, the relationship between forest cover and landslide occurrence was first assessed through the calculation of landslide density across various land cover categories. This assessment considered both forested and non-forested areas, as well as different forest classifications. These classifications included: (i) origin-based categories, such as natural forests and planted forests; (ii) species-based types, including woody forests, mixed forests, palm and coconut plantations, and bamboo forests; and (iii) planted forest types, distinguishing between native and exotic plantations (Figure 7). In this context, landslide density is defined as the number of landslides occurring per square kilometer within a specific land cover type. This metric was employed to evaluate the spatial variation in landslide occurrence across the identified forest categories and to provide insights into the potential mitigating effects of different forest types on landslide susceptibility.

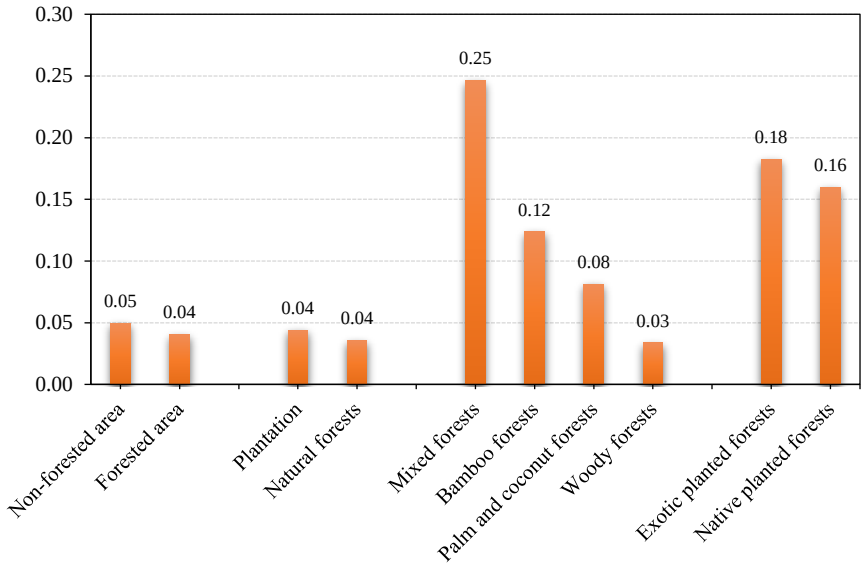

Figure 7. Landslide density across forest types

Furthermore, landslide susceptibility was analyzed and compared across multiple forest classifications, including forested versus non-forested areas, natural versus planted forests, four forest species groups, and native versus exotic plantations (Figures 8 and 9). In this context, landslide susceptibility refers to the quantitative or qualitative assessment of the likelihood and spatial distribution of either existing or potential landslide occurrences.

The analysis revealed that landslide density and susceptibility were both higher in non-forested areas than forested ones. As shown in Figure 8, non-forested land had 0.37% more area classified as high susceptibility and 3.65% more area classified as very high susceptibility compared to forested land. This demonstrates that forests play an important role in mitigating landslide risk, particularly by reducing the likelihood of landslides in high- and very high-susceptibility zones. These findings are consistent with previous studies highlighting the protective function of forests in slope stabilization (Schmaltz et al., 2017), (Chen and Shen, 2023), (Murgia et al., 2024), etc. Forested areas, through tree root systems and vegetation cover, contribute to soil stabilization and reduce surface runoff, whereas non-forested areas - especially those altered by human activities like deforestation or construction - are more vulnerable due to exposed and destabilized soils.

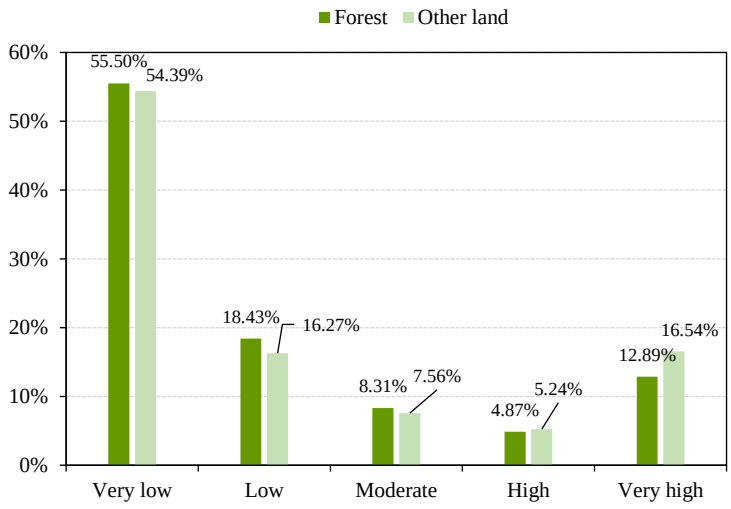

Figure 8. Landslide susceptibility on forest and non-forest areas

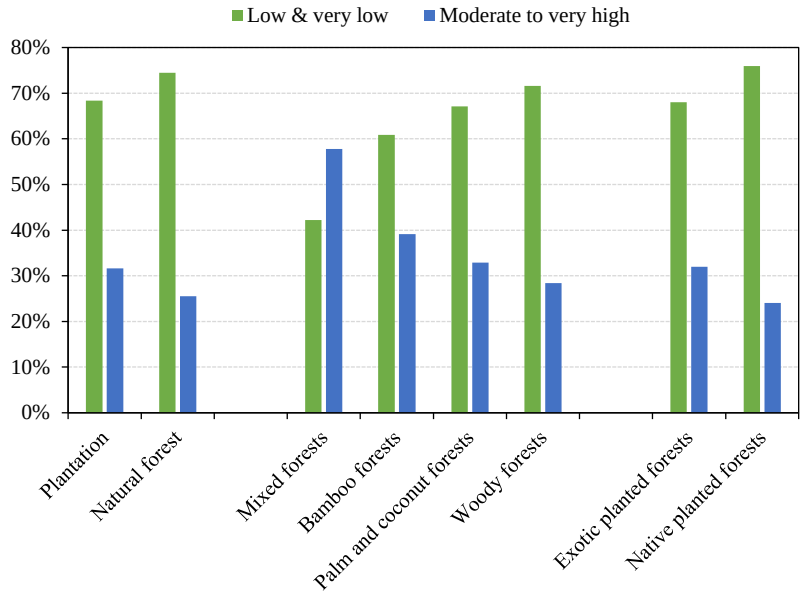

Figure 9. Landslide susceptibility over different forest types

Among forest types, natural forests exhibited lower landslide density and susceptibility than planted forests, likely due to their complex root structures, greater biodiversity, and higher organic matter content. In contrast, planted forests- often monocultures - tend to have simpler root systems and less stable soils. However, the impact of planted forests varied: native plantations demonstrated lower landslide density and higher proportions of very low to low susceptibility, suggesting better adaptation to local conditions and stronger soil-binding roots. Exotic plantations, on the other hand, were more prone to landslides, potentially due to shallow root systems and their influence on soil properties.

In the study area, native plantations are primarily composed of species such as *Manglietia conifera*, *Michelia mediocris*, and *Chukrasia tabularis*. These species are well adapted to local soil and climatic conditions and develop deep, fibrous root systems that contribute to slope stability. By contrast, exotic plantations are dominated by fast-growing species such as *Acacia mangium*, *Acacia auriculiformis*, and *Eucalyptus camaldulensis*, which are valued for timber and pulp production but typically form shallow root systems, providing limited reinforcement against slope failure (Bui, 2017; FAO, 2013).

When classified by species groups, woody forests had the lowest landslide occurrence and susceptibility, while mixed forests, bamboo forests, and palm and coconut plantations showed higher values. The shallow root systems common in these types likely provide less effective soil stabilization.

These findings confirmed the critical role of forest cover in reducing landslide risk in CRWTN. The effectiveness of forests depends on both forest types and species composition. In particular, well-managed forests - especially natural and native-species forests - can significantly contribute to landslide mitigation.

4. DISCUSSION

The integration of machine learning techniques in this study has proven valuable for analyzing the complex interactions between environmental variables and landslide susceptibility. The hybrid model addressed data gaps, improved classification accuracy, and enabled spatially explicit predictions of landslide-prone areas. This approach offers a replicable methodology for other regions. Given appropriate landslide inventory and conditioning data, it can be adapted and applied to other landslide-prone regions with similar environmental and data conditions, thereby extending its utility beyond CRWTN.

Previous studies have demonstrated the effectiveness of hybrid machine learning models in landslide susceptibility assessment, such as the Naïve Bayes-Random Subspace hybrid (Pham et al., 2021), the RF-MLP ensemble with Rotation Forest (Bui et al., 2022), and recurrent neural network frameworks (Wang et al., 2022). Beyond hybrid ML techniques, other studies examined the role of forests in slope stability: the spatio-temporal analysis showed that forest cover reduces shallow landslides in Switzerland

(Schmaltz et al., 2017); RF proved effective in forest-covered areas of Lin'an, China (Chen and Shen, 2023); and land-cover change simulations demonstrated that forest loss increases shallow landslide susceptibility in Central Italy (Murgia et al., 2024). Collectively, these studies reinforce the validity of our proposed KNN-RF-MLP framework and highlight the novelty of linking hybrid ML modeling with forest cover types to assess landslide susceptibility.

Beyond the core findings on forest effects, this discussion has extended to broader implications for land-use planning and disaster risk management. The study underscores the importance of not only preserving forest cover but also considering forest composition and management practices. While forest extent is important, the type of vegetation and its ecological characteristics play a critical role in influencing slope stability. These insights are relevant to Vietnam's reforestation programs. Such programs often favor fast-growing exotic species for economic purposes, but this can compromise long-term slope stability and resilience.

Nevertheless, the study had some limitations. Anthropogenic activities such as road construction, quarrying, and unplanned settlements substantially increase slope instability by altering drainage patterns, removing vegetation, and disturbing soil and rock structures. These factors can amplify landslide risk and, in some cases, override the stabilizing effects of forest cover—for example, slope undercutting along roads or excavation for quarrying often triggers failures even in forested areas. Because such activities were not explicitly included in the model, the results may underestimate their impact. Moreover, temporal changes in forest cover and landslide dynamics were not captured, emphasizing the need for long-term monitoring. Incorporating high-resolution temporal data, hydrological modeling, and socio-economic drivers in future research would provide a more comprehensive understanding of landslide processes and forest-landscape interactions.

Despite these limitations, the application of the hybrid machine learning framework has proven effective in capturing the multifaceted relationships between biophysical variables and landslide risk. The combined use of KNN for data imputation and RF-MLP for susceptibility modeling delivers robust performance and improves predictive accuracy.

5. CONCLUSION

This study developed a hybrid machine learning framework to assess landslide susceptibility in Cau River Watershed by integrating forest status mapping with spatial analysis of environmental conditions. The findings have demonstrated the added value of combining KNN, RF, and MLP algorithms for imputing missing data and improving the accuracy of susceptibility prediction. By linking forest classifications with landslide occurrence, the research provides practical insights to support evidence-based forest and land-use management. The results advocate for the prioritization of natural forests and native-species plantations in reforestation and conservation strategies, given their stronger slope-stabilizing functions. For policymakers, planners, and environmental managers, this work reinforces the importance of integrating ecological considerations into spatial planning and disaster risk reduction frameworks.

AUTHOR CONTRIBUTIONS

Data Collection and Experimental Run, Thuong Tran and Hoa Trieu; Methodology, Validation, Supervision and Original Draft Writing, Thuong Tran, Hoa Trieu and Nathaniel Bantayan; Formal Analysis, Thuong Tran; Data Curation, Visualization, and Reviewing and Editing of the manuscript, Thuong Tran and Hoa Trieu and Nathaniel Bantayan.

DECLARATION OF CONFLICT OF INTEREST

The authors declare that they have no conflicts of interest.

REFERENCES

Breiman L. Random forests. Machine Learning 2001;45:5-32.

Bui DT. Spatial prediction of rainfall-induced landslides for the Lao Cai Area (Vietnam) using a hybrid intelligent approach of least squares support vector machines inference model and artificial bee colony optimization. Landslides 2017;14:447-58.

Bui DT, Shirzadi A, Shahabi H, Pham BT, Singh SK, Chapi K, et al. A novel integrated approach of random forest-multilayer perceptron with rotation forest for landslide susceptibility assessment. Environmental Earth Sciences 2022;81:Article No. 215.

Chen C, Shen Z. Modeling landslide susceptibility in forest-covered areas in Lin'an, China, using logistic regression, decision tree, and random forest. Remote Sensing 2023;15(18):Article No. 4378.

Chen WP, Pan L. Applying population-based evolutionary algorithms and a neuro-fuzzy system for modeling landslide susceptibility. Catena 2019;172:212-31.

Food and Agriculture Organization of the United Nations (FAO). Forests and Landslides: The Role of Trees and Forests in the Prevention of Landslides and Rehabilitation of Landslide-Affected Areas in Asia. Rome: FAO; 2013.

Harrison O. Machine learning basics with the K-nearest neighbors algorithm [Internet]. 2018 [cited 2025 Jul 15]. Available from: https://towardsdatascience.com/machine-learning-basics-with-the-k-nearest-neighbors-algorithm-6a6e71d01761.

James G, Witten D, Hastie T, Tibshirani R. An Introduction to Statistical Learning. Vol. 112. New York: Springer; 2013. p. 18.

Le TT, Kaneko S. Landslide detection analysis in north Vietnam based on satellite images and digital geographical information: Landsat 8 satellite and historical data approaches. Japan Society of Civil Engineering 2017;73(5):239-49.

Murgia I, Vitali A, Giadrossich F, Tonelli E, Baglioni L, Cohen D, et al. Effects of land cover changes on shallow landslide susceptibility using SlideforMAP software (Mt Nerone, Central Italy). Land 2024;13(10):Article No. 1575.

Pham BT, Jaafari A, Prakash I, Bui DT. Naïve bayes-random subspace hybrid model for landslide susceptibility mapping. Geoscience Frontiers 2021;12(1):101-12.

Schmaltz EM, Steger S, Glade T. The influence of forest cover on landslide occurrence explored with spatio-temporal information. Geomorphology 2017;285:250-64.

Thai Nguyen Forest Protection Department (TNFPD). Forest Inventory Data 2023. Thai Nguyen, Vietnam: TNFPD; 2024.

Tran T, Trieu H, Bantayan N. GIS-based hybrid machine learning for landslide susceptibility assessment in Thai Nguyen Province, Vietnam. Proceedings of the 2024 Geoinformatics for Spatial-Infrastructure Development in Earth and Allied Sciences (GIS-IDEAS) Conference IEEE Special Track; 2024 Dec 11-13; Grand Vista Hotel, Chiang Rai: Thailand; 2024.

Vietnam Administration of Forestry (VAF). Vietnam Annual Forest Data. Hanoi: VAF; 2024.

Vietnam Disaster Management Authority (VNDMA). Vietnam 20-year Floods and Landslides Handbook. Hanoi: VNDMA; 2023a.

Vietnam Disaster Management Authority (VNDMA). Disaster Management Report. Hanoi: VNDMA; 2023b.

Vietnam General Statistics Office (VNGSO). Statistical Yearbook of Vietnam 2023. Hanoi: Statistical Publishing House; 2024.

Wang Y, Yin K, Zhang N, Zhang L. Landslide susceptibility mapping using recurrent neural network frameworks. Landslides 2022;19:437-52.

World Bank (WB). Country Forest Note: Vietnam. Washington, DC: WB; 2019.

Environment and Natural Resources Journal

Volume 24
Issue 2
2026

Soil Temperature and Evaporation Dynamics under Water Stress in Varying Soil Textures and Amendments

Kamelia Dwi Jayanti[1,2], Ongko Cahyono[3], Komariah[3*], and Mujiyo[3]

[1]Doctoral Program of Agricultural Science, Faculty of Agriculture, Universitas Sebelas Maret, Jl. Ir. Sutami 36A, Surakarta, Indonesia
[2]Department of Agrotechnology, Faculty of Agriculture, Universitas Sintuwu Maroso, Jl. Pulau Timor No. 1, Poso, Indonesia
[3]Department of Soil Science, Faculty of Agriculture, Universitas Sebelas Maret, Jl. Ir. Sutami 36A, Surakarta, Indonesia

ARTICLE INFO

Received: 8 Aug 2025
Received in revised: 2 Nov 2025
Accepted: 11 Nov 2025
Published online: 19 Dec 2025
DOI: 10.32526/ennrj/24/20250209

Keywords:
Water stress/ Soil texture/ Soil amendment/ Soil temperature dynamics/ Evaporation

*** Corresponding author:**
E-mail: komariah@staff.uns.ac.id

ABSTRACT

This study aimed to assess the effects of various textures and types of soil amendments on soil temperature dynamics and evaporation rates. The experiment was performed using Factorial Randomized Complete Block Design with two independent factors. The first factor was soil textures comprising sand, sandy loam, loam, silt loam, and clay, while the second was the type of soil amendments, including control, guano, and rice husk. Each soil type, amended and unamended, was placed in polybags, saturated with water to field capacity, and subjected to water stress conditions (without additional irrigation) for approximately 34 days. The magnitude of soil temperature fluctuations increased under water stress relative to pre-stress conditions. The highest soil temperature during the day was produced by sandy textures, while at night, the temperature was slightly greater in silt loam and clay. Generally, higher sand fraction correlates with greater temperature during the day and lower at night. The application of soil amendments to all soil textures can produce lower soil temperature during the day and retain heat at night, making soil temperature warmer than the control. Based on the experiment, the highest cumulative evaporation was observed in silt loam soil and samples without the addition of soil amendments. Moreover, extended water stress led to a smaller loss of water by evaporation. To help manage water stress, future studies need to assess the effects of soil amendments on moisture thresholds and the applications in irrigation management.

HIGHTLIGHTS

- Combined soil textures and organic amendments under water stress conditions.
- Guano and rice husk reduced daytime heat and maintained warmth at night.
- Sandy soils heated fastest; clay and silt loam retained heat for longer periods.
- Amendments lowered evaporation and improved soil thermal stability.
- Results support climate adaptation and sustainable soil management efforts.

1. INTRODUCTION

Drought and water stress are still a significant issue globally. According to the Intergovernmental Panel on Climate Change (IPCC) (2023), the high water scarcity in arid lands is caused by global warming. In regions with limited water availability, weather changes can lead to unpredictable or prolonged droughts and affect groundwater availability (Costa de Oliveira et al., 2014). Prolonged water stress adversely affects soil properties (Siebert et al., 2019; Deng et al., 2021; Quintana et al., 2023; Reinsch et al., 2024), plant growth, development, and yield (Silva et al., 2013; Seleiman et al., 2021; Sansan et al., 2024).

The occurrence of water stress is attributed to the lack of sufficient moisture in soil, which affects heat storage and conduction. Differences in this moisture content will affect the thermal properties (Abu-Hamdeh, 2003), particularly temperature dynamics (Zhang et al., 2022). Soil temperature is influenced by changes in moisture content and related properties (Melo-Aguilar et al., 2022), including textures (Akter et al., 2016). Soil textures influence the sensitivity of temperature to moisture (Zhang et al.,

Citation: Jayanti KD, Cahyono O, Komariah, Mujiyo. Soil temperature and evaporation dynamics under water stress in varying soil textures and amendments. Environ. Nat. Resour. J. 2026;24(2):222-235. (https://doi.org/10.32526/ennrj/24/20250209)

2022). Therefore, water stress occurring in different soil textures can impact the storage and release of heat from soil (Ali et al., 2024).

Evapotranspiration, comprising transpiration and evaporation, is mainly driven by temperature and influenced by soil moisture (Seneviratne et al., 2010). Evaporation rates are influenced by the amount of available energy and the soil's capacity to store and transmit moisture to the surface (Lehmann et al., 2018). However, the lack of water on arid soil will prevent evaporation from increasing (United Nations Educational Scientific and Cultural Organization (UNESCO), 2020).

Sandy soil has low water-holding capacity (Suzuki et al., 2007), while soil with higher loam, silt, or clay content show moderate to high water-holding capacity (Çakir and Cangir, 2019; Wang et al., 2020). Soil with higher moisture content maintain more stable temperature (Gałęzewski et al., 2022) due to slow heating and gradual cooling (Badía et al., 2017). However, extended periods of warmer temperature can alter microbial activity and affect plant root development (Heinze et al., 2017).

As water stress worsens, soil moisture levels steadily decrease. This low moisture content can lead to a significant rise in soil temperature that is harmful to plant growth and development (Zhang et al., 2022). Therefore, it is crucial to increase initial soil moisture to ensure enough water is available during drought and to prevent extreme temperature spikes.

Soil moisture availability is influenced by soil texture and organic matter. According to previous studies, adding organic matter can increase water-holding capacity (Abukari, 2019; Rehman et al., 2020). This also indirectly impacts soil temperature, in addition to moisture retention (Tuntiwaranuruk et al., 2006; Zhang et al., 2020).

Organic materials can be used as soil amendments to improve water availability, stabilize temperature, and promote healthy plant growth. In the Poso District, guano and rice husks are two locally available organic materials, but remain underutilized. Moreover, Poso is vulnerable to drought as a result of severely limited water resources, particularly for agricultural purposes. Guano (bat excrement) is widely used as a fertilizer (Ajuzieogu et al., 2024; Możdżer, 2024) and rice husks are often applied as compost, biochar, or mulch (Lim et al., 2012; Tan et al., 2024; Budhirani et al., 2025); however, their effects on soil temperature and evaporation under water stress are still poorly understood. Understanding this can provide valuable insights for promoting sustainable soil management in drought-prone areas. Therefore, this study aims to assess the effects on temperature and evaporation when added to different soil textures under water stress.

2. METHODOLOGY

2.1 Study location

This study was conducted in Kawua Village, Poso District, Central Sulawesi (1°25'00"S 120°44'56"E) (Figure 1). Kawua is located at an elevation of 16 meters above sea level, with minimum air temperature ranging from 19.2°C to 23.0°C, maximum temperature 32.8°C to 35.2°C, and average relative humidity between 70.7% and 86.4% (Statistics of Poso Regency, 2024).

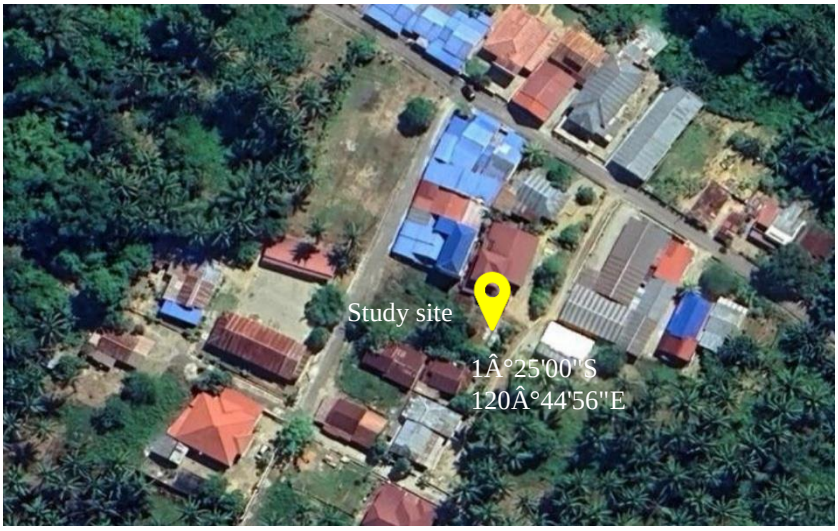

Figure 1. Study site location in Kawua Village, Poso District, Central Sulawesi

2.2 Soil and soil amendments

This study used five soil textures, namely sand, sandy loam, loam, silt loam, and clay, which were classified according to the USDA Soil Taxonomy. Soil amendments used in this study were guano and rice husks, as shown in Figure 2. The guano used consisted of naturally fermented bat feces collected from various cave environments in the Poso District. Rice husks used were raw and obtained directly from a local rice mill. The composition of textures and soil amendments is presented in Table 1.

Figure 2. Guano and rice husk

Table 1. Soil and soil amendments characteristics

Classes of soil textures	Characteristics					
	%Sand	%Silt	%Clay	Bulk density (g/cm^3)	Particle density (g/cm^3)	Porosity (%)
Sand	90	4	6	1.51	2.46	38.4
Sandy loam	59	27	14	1.23	2.20	44.2
Loam	36	41	24	1.32	2.24	41.2
Silt loam	34	51	15	1.10	2.29	52.1
Clay	3	39	58	1.15	1.94	40.8
Soil amendments	Characteristics					
	pH H_2O	C/N	Nitrogen	Phosphorus	Potassium	Bulk density (g/cm^3)
				%		
Guano	4.58	12	1.65	1.58	1.74	0.37
Rice husk	7.12	11	1.55	0.29	2.5	0.11

Sand, silt, and clay fractions were quantified for textures determination using the pipette method (Jackson and Saeger, 1935). Soil particle density was measured by the immersion method with a volumetric flask (Santos et al., 2022), Ethanol was replaced with pre-boiled distilled water (Agus and Marwanto, 2022). Furthermore, bulk density was determined using the core or cylinder method (Food and Agriculture Organization of the United Nations (FAO), 2023). Porosity was determined by subtracting the result of dividing bulk density by particle density from one (Agus and Marwanto, 2022).

Soil amendments pH analyses were conducted by measuring the electrical potential with a glass calomel electrode connected to a pH/millivolt meter at a controlled temperature of 25°C, using soil-to-water suspension ratio of 1:2.5 (m:v) (Food and Agriculture Organization of the United Nations (FAO), 2021b). Organic carbon content was determined using the Walkley-Black method (Food and Agriculture Organization of the United Nations (FAO), 2019). Total nitrogen was measured through the Kjeldahl method (Food and Agriculture Organization of the United Nations (FAO), 2021a). Available phosphorus was analyzed using the Olsen method (Olsen et al., 1954). Potassium was determined using a 1 M ammonium acetate (NH_4OAc) solution at pH 7 (Nel et al., 2023), followed by quantification of individual

elements through atomic absorption spectrophotometry (AAS) (Food and Agriculture Organization of the United Nations (FAO), 2022).

2.3 Experiment preparation

The experiment was conducted using topsoil obtained from a depth of 0-30 cm. The samples were sun-dried for approximately 4-7 days, depending on weather conditions. Subsequently, soil was ground and sieved using a 2 mm diameter sieve. Guano and rice husks were air-dried for one day and sieved to remove any adhering or attached dirt. The experiment used polybags with a diameter of 20 cm and a height of 30 cm. An air temperature and humidity measuring instrument (Model TL-303, aiqiua, China) was placed in the screen house to monitor temperature and humidity conditions every 3 h.

2.4 Experiment design and implementation

The experiment used a factorial randomized complete block design with two single factors. The first factor was soil textures, namely sand (T1), sandy loam (T2), loam (T3), silt loam (T4), and clay (T5). The second factor was the type of soil amendments applied, including a control treatment (A0), guano (A1), and rice husks (A2). These two factors were combined, leading to 15 treatment combinations, as shown in Table 2. Every treatment combination was repeated 3 times.

Table 2. Combination treatment of soil textures and soil amendments

Code	Description
T1A0	Sandy soil without amendment
T1A1	Sandy soil with guano
T1A2	Sandy soil with rice husks
T2A0	Sandy loam without amendment
T2A1	Sandy loam with guano
T2A2	Sandy loam with rice husks
T3A0	Loam without amendment
T3A1	Loam with guano
T3A2	Loam with rice husks
T4A0	Silt loam without amendment
T4A1	Silt loam with guano
T4A2	Silt loam with rice husks
T5A0	Clay without amendment
T5A1	Clay with guano
T5A2	Clay with rice husks

The sieved soil was mixed with soil amendments according to the treatment combination and placed into a polybag of equal volume. Guano was applied at 150 g/polybag, while rice husks were added at 100 g/polybag. The soil was maintained under moist conditions for 34 days (an estimated 6-day incubation period for the soil amendments followed by a 28-day vegetative period for shallots). During this time, the soil was saturated with water and maintained in consistently moist conditions. After this period, the soil was subjected to water stress for 34 days (the soil moisture content fell below 10%).

Soil temperature was measured every 3 h daily using soil thermometer (4-in-1 Soil Survey Instrument (Soil Test Meter), Shenzhen Handsome Technology Co., Ltd/Walcom International Industry Ltd., China). Evaporation was estimated by weighing soil-filled polybags every 3 days. The difference between successive weights represented the amount of water lost to evaporation during each interval. Evaporation can be measured using equation 1:

$$E = W1 - W2 \quad (1)$$

Where; E=evaporation loss during the interval (g), W1=weight of soil-filled polybag at the beginning of the interval (g), W2=weight of soil-filled polybag at the end of the interval (g).

2.5 Statistical analyses

The data obtained were tested for normality using the Shapiro-Wilk test. Data that followed a normal distribution were analyzed using analysis of variance (ANOVA) to determine the effect of treatment factors on each observation parameter. Treatment factors that showed significant or highly significant effects were further evaluated using Duncan's Multiple Range Test (DMRT) at a 95% confidence level (α=0.05) to compare treatment means. Normality testing, ANOVA, and post hoc analyses were performed using SPSS Statistics version 27.

3. RESULTS

3.1 Weather conditions in site study

The intensity of rainfall and the relative sunshine duration are shown in Figure 3. The monthly rainfall during the study period ranged from 254.0 to 364.0 mm, with the number of rainy days ranging from 15 to 19. The average relative sunshine duration ranged from 55% to 65%.

The fluctuations in air temperature are presented in Figure 4. The highest average air temperature, 36.11°C, was recorded at noon, while the

lowest of 27.48°C, was recorded at 6:00 am. The average air temperature increased from 6:00 am and reached the highest at noon subsequently, the average air temperature significantly decreased from noon (36.11°C) to 9:00 pm (28.32°C). Temperature decreased between 9:00 pm and 6:00 am, with an average decline of 0.84°C.

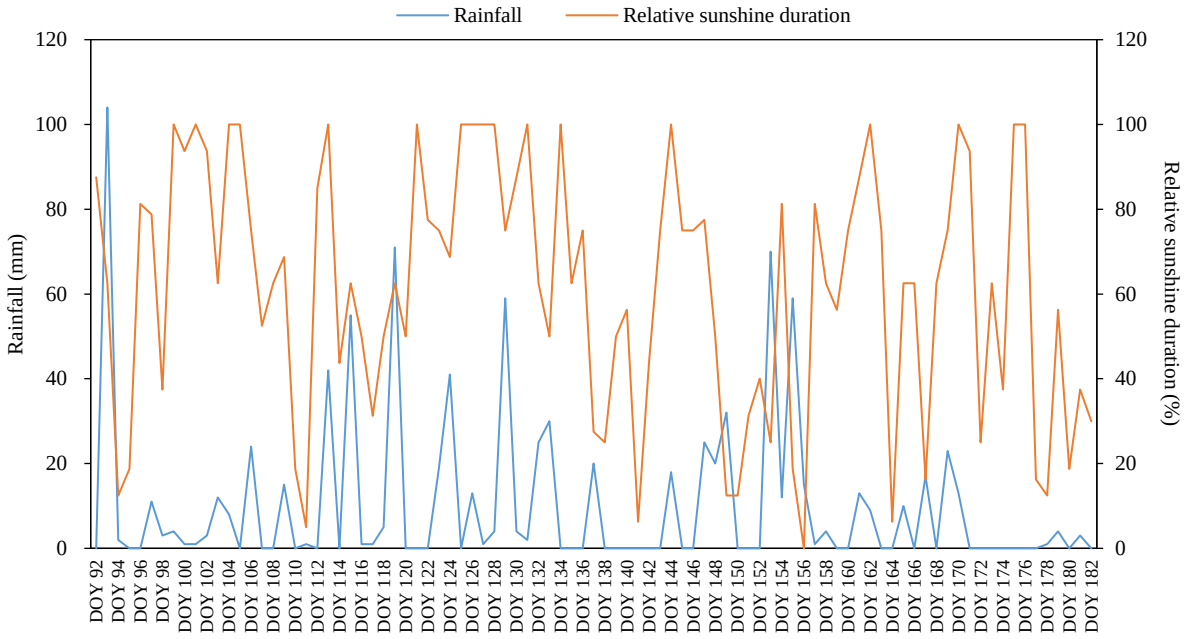

Figure 3. Rainfall intensity and relative sunshine duration during the study

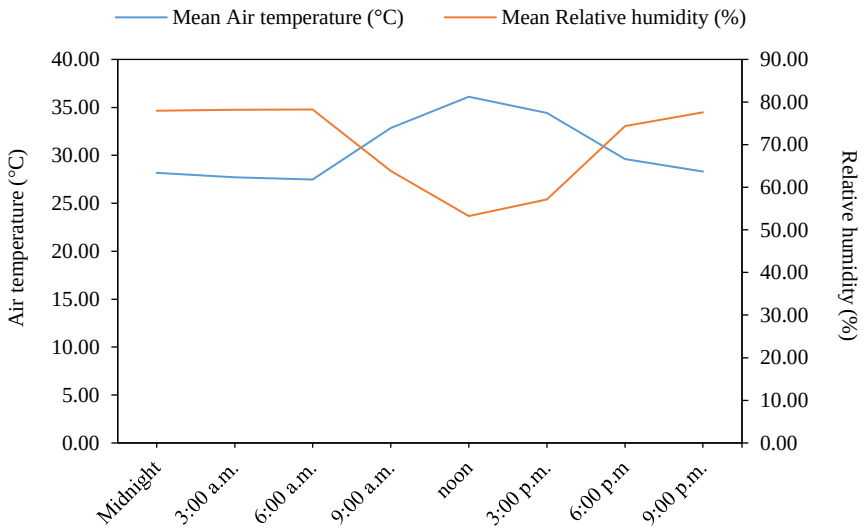

Figure 4. Average air temperature and relative humidity every 3 hours during the study

The dynamics of air humidity are shown in Figure 4. Air humidity was inversely proportional to air temperature. The lowest average air humidity was recorded at noon, at 53.24%, while the highest was at 6:00 am (78.25%). The average air humidity decreased significantly from 6:00 am to noon, and slightly increased by 3:00 pm (57.17%). The most significant increase in air humidity occurred between 3:00 pm and 6:00 pm, when the average was 74.33%. This was followed by a gradual increase until 6:00 am, although the rise was minimal and remained approximately constant.

3.2 Soil temperature dynamics

The dynamics of soil temperature before and after stress on different soil textures and soil

amendments are shown in Tables 3 and 4. Based on the results, soil temperature fluctuations for all treatment combinations followed the same pattern before and after water stress. Generally, the lowest soil temperature was recorded at 6:00 am, while the highest was at noon from 6:00 am to noon, a gradual increase in temperature was observed. At 3:00 pm, temperature slightly increased or decreased, but the changes were minimal. Soil temperature decreased significantly from 3:00 pm to 6:00 pm and continued to decline until 6:00 am the following day. As shown in Tables 3 and 4, temperature recorded between 9:00 pm and 6:00 am did not vary substantially, indicating a slight decrease.

3.2.1 Soil temperature before water stress

Table 3 showed that soil textures affected temperature at all observation times. In comparison, adding soil amendments significantly affected soil temperature at midnight, 3:00 am, noon, 6:00 pm, and 9:00 pm. The interaction effect of the two factors was observed only at 3:00 pm.

Soil temperature varied significantly with soil texture (Table 3), with sand showing the highest daytime peak (38.20±0.31°C) and clay and silt loam remaining cooler (35.83±0.58°C and 35.90±0.40°C, respectively; $p<0.01$). Nighttime temperatures were more uniform, ranging from 26.55±0.05°C in sand to 27.17±0.07°C in clay and silt loam, with differences not statistically significant. Among the amendments, guano and rice husk slightly moderated daytime peaks (reductions of ~0.20-0.23°C) and slightly increased nighttime temperatures (~0.05-0.11°C); these effects were statistically significant at peak daytime hours ($p<0.05$) but not at night. The interaction between soil texture and amendment was not significant, indicating that soil type is the main driver of diurnal temperature variation, while amendments contributed only minor, observed adjustments. Detailed measurements and statistical comparisons are provided in the Table 3.

3.2.2 Soil temperature after water stress

Table 4 showed that soil textures affected temperature after water stress at all observation times. In comparison, adding soil amendments significantly affected soil temperature from 9.00 am to 9:00 pm. There was no interaction effect between textures and soil amendments on soil temperature after stress. Soil textures affected the average temperature at all observation times, while the impact of soil amendments on average soil temperature was only shown during observations from 9:00 am to 9:00 pm.

Soil temperature varied primarily with soil texture, and these differences were statistically significant at all time points ($p<0.01$). Sand heated most rapidly, reaching the highest temperatures around midday (~39°C at noon), whereas finer-textured soils such as clay and silt loam remained cooler (~36-37°C), reflecting their greater water-holding capacity. Amendments showed minor effects: peak daytime temperatures were slightly lower with rice husk or guano, with reductions of ~0.3-0.5°C in clay. These differences were statistically significant at 9:00 am, noon, and 3:00 pm ($p<0.05$), whereas nighttime temperatures (~26-27°C) were unaffected ($p>0.05$). The interaction between soil texture and amendment was not significant at any time, indicating that soil type is the main driver of diurnal temperature variation, while observed differences among amendments were relatively small. Soil temperature patterns after stress resembled pre-stress trends, but with higher values.

3.3 Cumulative evaporation

Cumulative evaporation was strongly influenced by soil texture. Sand had the lowest evaporation (31.29±1.34 mm), reflecting its low water-holding capacity, while silt loam was highest (62.23±17.33 mm). Loam (57.49±2.37 mm), sandy loam (56.63±7.75 mm), and clay (55.06±13.44 mm) showed intermediate values, indicating a balance between water retention and loss. Soil amendments significantly reduced evaporation; guano (51.60±31.64 mm) and rice husk (50.77±31.87 mm) lowered cumulative water loss by 3-8 mm compared with the control (55.25±37.59 mm). The soil texture and amendment interaction was also significant ($p<0.05$), with rice husk reducing evaporation by ~15 mm in clay soils (from 57.40±1.23 mm to 48.79±1.23 mm), while amendments had minimal effect in sand (31-32 mm). These results indicate that although soil texture is the primary determinant of evaporation, organic amendments, particularly rice husk, can substantially enhance water retention in fine-textured soils under prolonged stress.

Table 3. Effect of treatment combinations, textures, and soil amendments on average soil temperature before water stress

Treatment	Soil temperature (°C) by time point							
	Midnight	3.00 am	6.00 am	9.00 am	Noon	3.00 pm	6.00 pm	9.00 pm
Soil textures								
Sand	27.20±0.09 a	26.55±0.05 a	25.86±0.00 a	31.58±0.19 d	38.20±0.31 d	37.70±0.29 d	31.41±0.37 a	28.37±0.18 a
Sandy loam	27.75±0.06 b	26.93±0.08 c	26.13±0.12 b	30.68±0.10 c	36.49±0.19 c	36.63±0.30 c	32.06±0.11 b	29.17±0.24 b
Loam	27.82±0.06 c	26.89±0.07 b	26.16±0.07 b	30.42±0.07 b	36.31±0.11 b	36.51±0.19 bc	32.15±0.16 b	29.23±0.20 bc
Silt loam	27.86±0.09 c	27.17±0.07 d	26.27±0.07 c	30.35±0.14 b	35.90±0.40 a	36.42±0.22 b	32.34±0.26 c	29.32±0.26 c
Clay	27.99±0.24 d	27.17±0.07 d	26.40±0.17 d	30.23±0.43 a	35.83±0.58 a	36.11±0.53 a	32.48±0.19 c	29.56±0.25 d
Sig.	**	**	**	**	**	**	**	**
Amendment								
Control	27.69±0.80 a	26.92±0.67 a	26.15±0.48	30.72±1.45	36.69±2.53 b	36.73±1.66	32.00±1.16 a	29.07±0.19 a
Guano	27.76±0.83 b	26.97±0.69 b	26.18±0.58	30.64±1.37	36.49±2.50 a	36.64±1.50	32.15±1.02 b	29.14±0.29 ab
Rice husk	27.72±0.085 ab	26.94±0.71 ab	26.15±0.58	30.60±1.58	36.46±2.74 a	36.65±1.78	32.10±1.17 ab	29.18±0.19 b
Sig.	*	*	ns	ns	**	ns	*	*
Interaction of soil textures and soil amendments								
T1A0	27.17±0.06	26.54±0.00	25.86±0.08	31.65±0.10	38.33±0.04	37.80±0.09 e	31.27±0.14	28.32±0.08
T1A1	27.24±0.03	26.57±0.00	25.86±0.00	31.50±0.18	38.08±0.20	37.57±0.09 e	31.57±0.11	28.33±0.06
T1A2	27.20±0.03	26.55±0.06	25.86±0.16	31.58±0.10	38.18±0.11	37.74±0.32 e	31.38±0.19	28.45±0.07
T2A0	27.74±0.04	26.90±0.02	26.15±0.02	30.73±0.12	36.57±0.21	36.76±0.29 d	32.04±0.15	29.06±0.07
T2A1	27.77±0.09	26.96±0.00	26.15±0.03	30.68±0.08	36.42±0.07	36.60±0.06 cd	32.02±0.07	29.23±0.06
T2A2	27.73±0.06	26.92±0.03	26.07±0.03	30.64±0.11	36.49±0.02	36.52±0.14 cd	32.11±0.03	29.24±0.19
T3A0	27.85±0.04	26.89±0.03	26.18±0.03	30.45±0.11	36.36±0.16	36.43±0.12 c	32.08±0.24	29.32±0.09
T3A1	27.82±0.05	26.92±0.02	26.18±0.03	30.43±0.03	36.29±0.12	36.51±0.06 cd	32.21±0.03	29.23±0.08
T3A2	27.80±0.04	26.86±0.03	26.13±0.02	30.39±0.03	36.27±0.14	36.58±0.16 cd	32.14±0.20	29.15±0.07
T4A0	27.83±0.02	27.14±0.00	26.25±0.00	30.37±0.15	36.07±0.03	36.33±0.07 bc	32.21±0.12	29.21±0.09
T4A1	27.90±0.08	27.20±0.02	26.25±0.03	30.39±0.05	35.88±0.04	36.43±0.09 c	32.38±0.06	29.29±0.07
T4A2	27.85±0.02	27.17±0.02	26.30±0.02	30.29±0.21	35.75±0.28	36.51±0.07 cd	32.42±0.17	29.45±0.13
T5A0	27.88±0.04	27.14±0.00	26.32±0.00	30.42±0.14	36.10±0.13	36.35±0.11 bc	32.40±0.21	29.44±0.08
T5A1	28.05±0.04	27.19±0.02	26.45±0.02	30.19±0.09	35.77±0.11	36.07±0.28 ab	32.56±0.15	29.62±0.20
T5A2	28.05±0.06	27.19±0.02	26.42±0.02	30.07±0.08	35.63±0.07	35.92±0.07 a	32.48±0.04	29.62±0.07
Sig.	ns	ns	ns	ns	ns	*	ns	ns

Note: The numbers followed by the same letter in the same factor and column are not significantly different at α=0.05. ns: not significant at α=0.05. T1: sand, T2: sandy loam, T3: loam, T4: silt loam, T5: clay, A0: unamended (control), A1: guano, A2: rice husk

Table 4. Effect of treatment combinations, soil textures, and soil amendments on average soil temperature after water stress

Treatment	Soil temperature (°C) by time point							
	Midnight	3.00 am	6.00 am	9.00 am	Noon	3.00 pm	6.00 pm	9.00 pm
Soil textures								
Sand	27.35±0.05 a	26.52±0.04 a	25.66±0.02 a	32.21±0.42 d	38.98±0.45 e	38.02±0.17 d	31.59±0.26 a	28.53±0.11 a
Sandy loam	27.75±0.05 b	26.82±0.04 b	25.96±0.09 b	31.23±0.20 c	37.33±0.33 d	37.00±0.33 c	32.18±0.09 b	29.29±0.13 b
Loam	27.79±0.07 b	26.82±0.05 b	25.99±0.11 bc	31.05±0.19 b	37.10±0.31 c	36.86±0.15 bc	32.33±0.12 c	29.31±0.18 b
Silt loam	27.94±0.09 c	27.05±0.04 c	26.02±0.05 cd	30.99±0.31 b	36.83±0.31 b	36.74±0.20 b	32.31±0.25 c	29.31±0.26 b
Clay	27.96±0.08 c	27.06±0.05 c	26.05±0.04 d	30.70±0.22 a	36.47±0.38 a	36.39±0.31 a	32.43±0.19 c	29.69±0.37 c
Sig.	**	**	**	**	**	**	**	**
Amendment								
Control	27.74±0.65	26.85±0.59	25.94±0.43	31.35±1.65 b	37.50±2.67 b	37.10±1.58 b	32.10±0.92 a	29.17±1.08 a
Guano	27.78±0.67	26.86±0.59	25.94±0.41	31.19±1.51 a	37.26±2.54 a	36.92±1.65 a	32.24±0.84 b	29.24±1.15 ab
Rice husk	27.75±0.67	26.86±0.60	25.92±0.42	31.16±1.50 a	37.26±2.61 a	36.98±1.71 a	32.16±0.92 ab	29.27±1.22 b
Sig.	ns	ns	ns	**	**	**	*	*
Interaction of soil textures and soil amendments								
T1A0	27.33±0.03	26.51±0.03	25.66±0.02	32.40±0.24	39.20±0.20	38.08±0.23	31.50±0.15	28.49±0.07
T1A1	27.37±0.03	26.52±0.02	25.67±0.02	32.15±0.29	38.86±0.16	37.95±0.16	31.71±0.14	28.53±0.09
T1A2	27.34±0.07	26.54±0.01	25.65±0.02	32.08±0.21	38.89±0.09	38.04±0.28	31.57±0.20	28.58±0.11
T2A0	27.74±0.04	26.81±0.01	25.97±0.02	31.31±0.09	37.49±0.17	37.13±0.21	32.14±0.04	29.24±0.05
T2A1	27.78±0.06	26.84±0.00	25.99±0.02	31.15±0.15	37.25±0.06	36.87±0.17	32.21±0.05	29.34±0.03
T2A2	27.75±0.04	26.82±0.02	25.92±0.00	31.24±0.15	37.25±0.07	36.99±0.14	32.18±0.03	29.28±0.12
T3A0	27.82±0.04	26.82±0.03	26.01±0.01	31.13±0.18	37.23±0.11	36.93±0.20	32.28±0.16	29.38±0.09
T3A1	27.78±0.05	26.83±0.01	26.01±0.02	30.99±0.10	36.98±0.15	36.82±0.07	32.38±0.01	29.31±0.03
T3A2	27.76±0.05	26.80±0.03	25.94±0.03	31.01±0.07	37.09±0.04	36.83±0.10	32.32±0.13	29.23±0.01
T4A0	27.90±0.03	27.03±0.00	26.00±0.01	31.12±0.13	36.96±0.08	36.83±0.10	32.19±0.09	29.19±0.05
T4A1	27.97±0.02	27.06±0.01	26.01±0.02	31.00±0.04	36.83±0.05	36.68±0.11	32.37±0.01	29.32±0.08
T4A2	27.94±0.02	27.06±0.01	26.04±0.04	30.87±0.18	36.71±0.12	36.70±0.16	32.37±0.17	29.41±0.09
T5A0	27.93±0.02	27.06±0.02	26.06±0.05	30.80±0.14	36.65±0.03	36.53±0.12	32.37±0.09	29.54±0.09
T5A1	28.00±0.02	27.05±0.01	26.04±0.04	30.68±0.14	36.40±0.09	36.29±0.16	32.52±0.04	29.69±0.16
T5A2	27.96±0.01	27.09±0.02	26.03±0.04	30.63±0.12	36.36±0.08	36.35±0.08	32.39±0.05	29.85±0.09
Sig.	ns	ns	ns	ns	ns	ns	ns	ns

Note: The numbers followed by the same letter in the same factor and column are not significantly different at α=0.05. ns: not significant at α=0.05. T1: sand, T2: sandy loam, T3: loam, T4: silt loam, T5: clay, A0: unamended (control), A1: guano, A2: rice husk

3.4 Soil moisture volume during water stress

All soils exhibited a steady decline in moisture over 34 days following water stress, with the rate of loss influenced by soil texture and amendments (Figure 5). In unamended soils, sand lost moisture most rapidly, dropping from ~850 mL to near 0 mL, whereas sandy loam and loam decreased from ~1,750 mL to 250-400 mL. Silt loam and clay retained more water, ending around 400 mL and 750 mL, respectively, with a slower decline after ~20 days, indicating resistance to further evaporation.

Amendments slowed moisture loss across all textures. With guano, sand still lost water rapidly, decreasing from ~1,050 mL to ~150 mL, while sandy loam and loam retained slightly more moisture, declining from ~1,700 mL to 400-500 mL. Silt loam and clay ended near 550 mL and 900 mL, indicating improved buffering against prolonged stress. Rice husk further enhanced water retention: sand approached 0 mL more slowly than the control, sandy loam and loam finished around 400-450 mL, and silt loam and clay retained the highest moisture, ending near 750 mL and 1,150 mL (Figure 5).

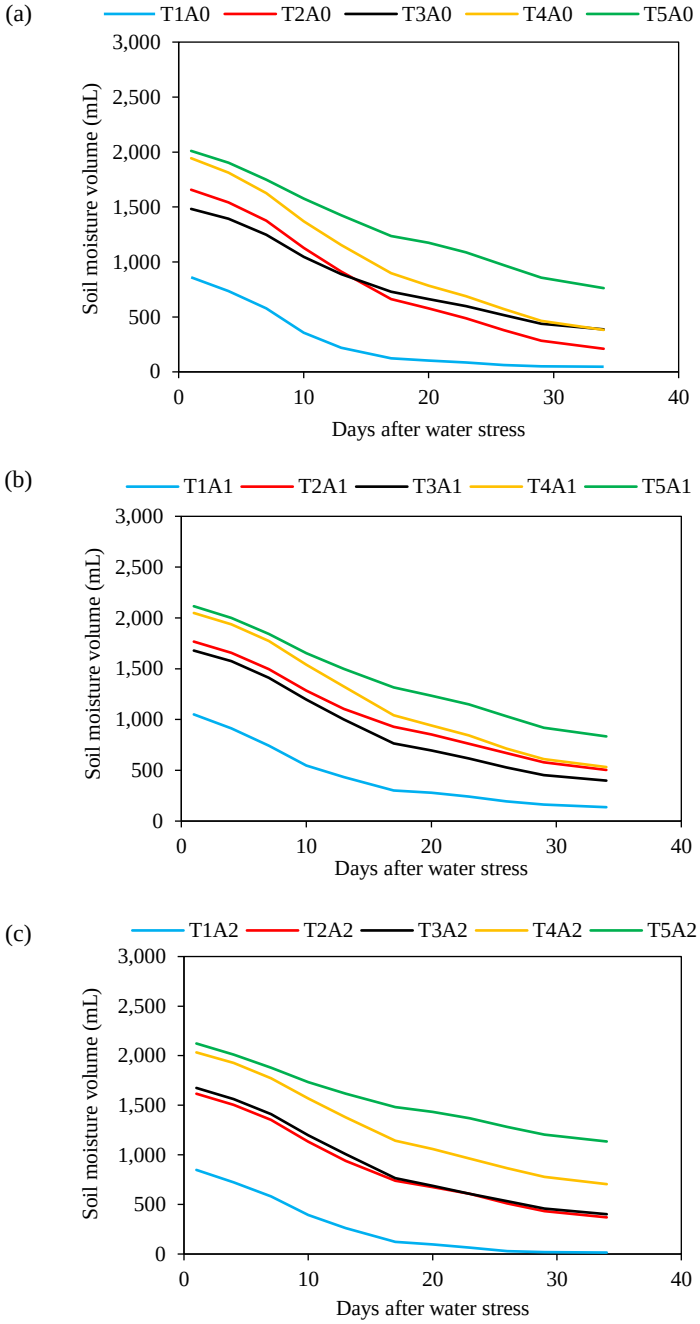

Figure 5. Effects of water stress on water volume across soil textures: unamended (a), guano-amended (b), and rice husk-amended soil (c). Note: T1: sand, T2: sandy loam, T3: loam, T4: silt loam, T5: clay, A0: unamended (control), A1: guano, A2: rice husk.

4. DISCUSSION

Water stress significantly increased soil temperature across all textures, although the overall temperature trends remained similar to pre-stress conditions. Akter et al. (2016) also reported comparable soil surface temperature patterns under both moist and dry conditions. Soil temperature was lowest at 6:00 a.m. and gradually rose until noon. A slight decrease occurred at 3:00 pm, particularly in sandy soil without amendments. In contrast, sandy loam, loam, silt loam, and clay soils showed no significant temperature drop between noon and 3:00 pm, reflecting higher thermal inertia due to finer particle distribution and greater water retention. By 6:00 pm, a substantial temperature reduction was observed, especially in sandy soil, with an average drop of approximately 7°C, likely caused by its low heat capacity and rapid radiative cooling. Temperatures stabilized between 3:00 am and 6:00 am, following a pattern similar to air temperature, indicating that soil temperature rises and falls alongside ambient conditions. Solar radiation also strongly influenced both soil and air temperature (Yolcubal et al., 2004; Onwuka and Mang, 2018; Khamidov et al., 2023).

During water stress, soil temperature is higher than under moist or wet conditions. This difference arises because moist soil cools more effectively through evaporation, which consumes energy as latent heat (Szilagyi et al., 2024). When soil moisture declines under stress, less energy is used for evaporation, causing the soil to heat more rapidly (Lozano-Parra et al., 2018). Soil moisture thus acts as a buffer, moderating temperature fluctuations (Zhang et al., 2022; Greiser et al., 2024). Wet soils warm more slowly due to water's high specific heat, which requires more energy to raise temperature (Howe and Smith, 2021). In contrast, under water stress, solar energy is absorbed directly by the soil, resulting in higher temperature increases (García-García et al., 2023).

Temperature changes were more pronounced in sandy soil. Between 6:00 am (25.66±0.02°C) and noon (38.98±0.45°C), soil temperature rose by approximately 13°C, reflecting sandy soil's low water-holding capacity and high thermal conductivity. By 6:00 pm, temperature decreased by 7°C to 31.59±0.26°C. These fluctuations were slightly smaller than those observed before water stress (Table 3). Water stress also increased the diurnal temperature range (Zhang et al., 2020). For example, sandy loam and loam soils experienced a ~10°C drop from noon to midnight, compared to ~8°C under non-stress conditions. These results highlight that soil moisture is critical for stabilizing soil temperature (Al-Kayssi et al., 1990).

Sandy soil heated more quickly during the day but cooled faster at night, while clay soil remained warmer at night. This indicates that higher sand content amplifies diurnal temperature swings due to lower specific heat and volumetric heat capacity (Abu-Hamdeh, 2003; Akter et al., 2016). Differences in soil texture also influence water retention, which in turn affects temperature dynamics (dos Santos et al., 2021; Stumpe et al., 2023). Soil temperature, surface moisture, and thermal properties are closely interconnected (Melo-Aguilar et al., 2022).

Soil amendments mitigated temperature increases during the day and maintained warmth at night (Table 3). This thermal buffering results from higher moisture retention and improved heat storage. Amendments increase porosity and water content (Liberalesso et al., 2021; Bhanwaria et al., 2022), which cools the soil through evaporation during the day and releases heat gradually at night (Tuffour et al., 2014; Jandaghian and Colombo, 2024). Enhanced porosity also improves aeration, supporting overall soil health (Abuarab et al., 2019).

Rice husk and guano affected soil temperature and evaporation through distinct yet complementary mechanisms. The lighter color and fibrous texture of rice husk likely increased soil albedo, reflecting a greater portion of incoming radiation and thereby reducing net heat absorption. In contrast, guano, with its high organic matter content, enhanced soil aggregation and porosity, which decreased bulk density and thermal conductivity, ultimately slowing heat transfer within the soil profile. Both amendments also improved water retention, increasing the soil's specific heat capacity and promoting evaporative cooling that further stabilized surface temperature. As a result, rice husk primarily influenced the soil's radiative energy balance, while guano modified subsurface thermal properties. Together, these effects contributed to the observed reductions in temperature peaks and evaporation rates.

Water stress affected cumulative evaporation differently across soil textures. Silt loam showed the highest cumulative evaporation, while sandy soil had the lowest (Table 5), reflecting differences in water retention capacity (Lehmann et al., 2018). Clay soil retained more water but had minimal evaporation, likely due to its high moisture retention (Song et al.,

2016). Soil amendments reduced evaporation by increasing moisture retention, limiting daytime heating, and improving microporosity and aggregate stability (Das et al., 2023; Feng et al., 2023; Wang et al., 2024). Higher soil moisture also raises specific heat capacity, reducing susceptibility to solar heating and minimizing additional moisture loss through evaporation (Liu et al., 2020; Zhang et al., 2020). Soil with low moisture content tended to produce less evaporation that could be converted into vapor (Baalousha et al., 2022; Priyanka et al., 2024).

Table 5. Cumulative evaporation from different soil textures, amendments, and the combination of textures and soil amendments

Treatment	Cumulative evaporation (mm)
Soil textures	
Sand	31.29±1.34 a
Sandy loam	56.63±7.75 b
Loam	57.49±2.37 b
Silt loam	62.23±17.33 c
Clay	55.06±13.44 b
Sig.	**
Amendment	
Control	55.25±37.59 b
Guano	51.60±31.64 a
Rice husk	50.77±31.87 a
Sig.	*
Interaction of soil textures and soil amendments	
T1A0	31.89±2.98 a
T1A1	30.83±2.77 a
T1A2	31.15±1.24 a
T2A0	60.17±7.21 c
T2A1	54.08±4.02 bc
T2A2	55.65±4.52 bc
T3A0	57.15±2.13 c
T3A1	58.58±2.15 c
T3A2	56.73±3.02 c
T4A0	69.63±3.78 d
T4A1	55.53±1.90 bc
T4A2	61.53±4.19 c
T5A0	57.40±1.23 c
T5A1	58.98±3.63 c
T5A2	48.79±1.23 b
Sig.	*

Note: The numbers followed by the same letter in the same factor and column are not significantly different at α=0.05. ns: not significant at α=0.05. T1: sand, T2: sandy loam, T3: loam, T4: silt loam, T5: clay, A0: unamended (control), A1: guano, A2: rice husk

The availability of soil moisture strongly influenced evaporation rates during stress. At the onset of stress, moisture declined sharply, consistent with the observation that initial water content drives evaporation rate (An et al., 2018). Over time, evaporation slowed as water availability decreased and remaining water became tightly bound within the soil matrix (Han and Zhou, 2013; Whalley et al., 2013; Qing et al., 2023; Nachum, 2025).

These findings show that soil thermal responses under moisture deficits are strongly influenced by both texture and amendments. In field-scale shallot cultivation, sandy soils, which dry rapidly and heat quickly, require closer monitoring and more frequent irrigation to avoid yield losses. Conversely, finer-textured soils like clay and silt loam retain heat and moderate temperature swings, allowing longer intervals between irrigation. Adding organic amendments such as guano or rice husks further stabilizes temperature, improves water retention, and enhances irrigation efficiency during drought. Maintaining favorable thermal and moisture conditions through amendments and texture-specific management can reduce irrigation frequency, optimize water use, improve crop resilience, and strengthen climate adaptation in agricultural systems.

5. CONCLUSION

This study demonstrates that water stress elevates soil temperatures, with sandy soils experiencing the highest daytime heat, while clay and silt loam retain more warmth overnight. The application of soil amendments across all textures effectively buffers temperature fluctuations and maintains higher nighttime temperatures. It also reduces cumulative evaporation, which is influenced by both soil texture and moisture availability. These findings provide novel insights into the interactions among soil texture, temperature dynamics, and water stress.

Further studies are recommended to assess the effects of soil amendments on critical soil moisture thresholds and to refine irrigation management strategies for mitigating the impacts of water stress. Such investigations will provide essential insights for optimizing soil and water management under changing climatic conditions.

ACKNOWLEDGEMENTS

The author is grateful to the dissertation promotor team, the Indonesian Education Scholarship (BPI) of the Ministry of Higher Education, Science, and Technology, the Center for Higher Education Funding and Assessment (PPAPT), and the Indonesian Endowment Funds for Education (LPDP), which provided funding for this study. The scholarship recipient's identification number is FR202312000754.

FUNDING

The Indonesian Education Scholarship (BPI) of the Ministry of Higher Education, Science, and Technology, the Center for Higher Education Funding and Assessment (PPAPT), and the Indonesian Endowment Funds for Education (LPDP).

AUTHOR CONTRIBUTIONS

Author KDJ collected and curated data, performed data analysis, wrote the original draft, edited, and finalized the manuscript. OC, K, and M conceived the idea and designed the study, providing supervision or mentorship. All authors read and agree to the submission of the manuscript to the journal.

DECLARATION OF CONFLICT OF INTEREST

The authors declare that there is no conflict of interest in the publication.

REFERENCES

Abu-Hamdeh NH. Thermal properties of soils as affected by density and water content. Biosystems Engineering 2003;86(1):97-102.

Abuarab ME, El-Mogy MM, Hassan AM, Abdeldaym EA, Abdelkader NH, El-Sawy MBI. The effects of root aeration and different soil conditioners on the nutritional values, yield, and water productivity of potato in clay loam soil. Agronomy 2019;9(8):Article No. 418.

Abukari A. Influence of rice husk biochar on water holding capacity of soil in the Savannah Ecological Zone of Ghana. Turkish Journal of Agriculture - Food Science and Technology 2019;7(6):888-91.

Agus F, Marwanto S. Determination of soil particle density. In: Physical Properties of Soil and Methods of Analysis. Bogor: Soil Research Institute; 2022. p. 1-322 (in Indonesia).

Ajuzieogu CA, Nwankwo UG, Ikedianya N. Impact of bat guano fertilizer on soil bacteria community structure and antibiogram of associated bacteria: An alert to food insecurity. Asian Journal of Research in Biosciences 2024;6(2):157-71.

Akter M, Miah M, Hassan M, Mobin M, Baten M. Textural influence on surface and subsurface soil temperatures under various conditions. Journal of Environmental Science and Natural Resources 2016;8(2):147-51.

Al-Kayssi AW, Al-Karaghouli AA, Hasson AM, Beker SA. Influence of soil moisture content on soil temperature and heat storage under greenhouse conditions. Journal of Agricultural Engineering Research 1990;45(C):241-52.

Ali MH, Kurjak Z, Beke J. Estimating the impact of the thermo-physical properties of the multilayer soil on earth-air heat exchanger system performance. International Journal of Thermofluids 2024;23:Article No. 100722.

An N, Tang CS, Xu SK, Gong XP, Shi B, Inyang HI. Effects of soil characteristics on moisture evaporation. Engineering Geology 2018;239:126-35.

Baalousha HM, Ramasomanana F, Fahs M, Seers TD. Measuring and validating the actual evaporation and soil moisture dynamic in arid regions under unirrigated land using smart field lysimeters and numerical modeling. Water 2022;14(18):Article No. 2787.

Badía D, López-García S, Martí C, Ortíz-Perpiñá O, Girona-García A, Casanova-Gascón J. Burn effects on soil properties associated to heat transfer under contrasting moisture content. Science of the Total Environment 2017;601-602:1119-28.

Bhanwaria R, Singh B, Musarella CM. Effect of organic manure and moisture regimes on soil physiochemical properties, microbial biomass Cmic:Nmic:Pmic turnover and yield of mustard grains in arid climate. Plants 2022;11(6):Article No. 722.

Budhirani L, Devi KM, Singh LR, Thoudam O, Maibam D. Effect of rice husk mulching on growth and yield of Chickpea (*Cicer arietinum* L.). International Journal of Plant and Soil Science 2025;37(1):40-5.

Çakir R, Cangir C. Water holding properties and soil water types in fine textured vertisol soils of thrace region in turkey. Polish Journal of Soil Science 2019;52(2):247-58.

Costa de Oliveira A, Marini N, Farias DR. Climate change: New breeding pressures and goals. In: Alfen NK Van, editor. Encyclopedia of Agriculture and Food Systems. Elsevier; 2014. p. 284-93.

Das S, Liptzin D, Maharjan B. Long-term manure application improves soil health and stabilizes carbon in continuous maize production system. Geoderma 2023;430:Article No. 116338.

Deng L, Peng C, Kim DG, Li J, Liu Y, Hai X, et al. Drought effects on soil carbon and nitrogen dynamics in global natural ecosystems. Earth-Science Reviews 2021;214:Article No. 103501.

Feng W, Wang T, Yang F, Cen R, Liao H, Qu Z. Effects of biochar on soil evaporation and moisture content and the associated mechanisms. Environmental Sciences Europe 2023;35:Article No. 66.

Food and Agriculture Organization of the United Nations (FAO). Standard Operating Procedure for Soil Organic Carbon Walkley-Black Method Titration and Colorimetric Method. Rome: FAO; 2019. p. 1-25.

Food and Agriculture Organization of the United Nations (FAO). Standard Operating Procedure for Soil Nitrogen Kjeldahl Method. Rome: FAO; 2021a. p. 1-21.

Food and Agriculture Organization of the United Nations (FAO). Standard Operating Procedure for Soil pH Determination. Rome: FAO; 2021b. p. 1-19.

Food and Agriculture Organization of the United Nations (FAO). Standard Operating Procedure for Cation Exchange Capacity and Exchangeable Bases: 1N Ammonium Acetate, pH 7.0 Method. Rome: FAO; 2022. p. 1-21.

Food and Agriculture Organization of the United Nations (FAO). Standard Operating Procedure for Soil Bulk Density Cylinder Method. Rome: FAO; 2023. p. 1-17.

Gałęzewski L, Jaskulska I, Kotwica K, Lewandowski Ł. The dynamics of soil moisture and temperature—strip-till vs. plowing: A case study. Agronomy 2022;13(1):Article No. 83.

García-García A, Cuesta-Valero FJ, Miralles DG, Mahecha MD, Quaas J, Reichstein M, et al. Soil heat extremes can outpace air temperature extremes. Nature Climate Change. 2023;13(11):1237-41.

Greiser C, Hederová L, Vico G, Wild J, Macek M, Kopecký M. Higher soil moisture increases microclimate temperature buffering in temperate broadleaf forests. Agricultural and Forest Meteorology 2024;345:Article No. 109828.

Han J, Zhou Z. Dynamics of soil water evaporation during soil drying: Laboratory experiment and numerical analysis. The Scientific World Journal 2013;2013:Article No. 240280.

Heinze J, Gensch S, Weber E, Joshi J. Soil temperature modifies effects of soil biota on plant growth. Journal of Plant Ecology. 2017;10(5):808-21.

Howe JA, Smith AP. The soil habitat. In: Gentry TJ, Fuhrmann JJ, Zuberer DA, editors. Principles and Applications of Soil Microbiology, 3rd ed. Elsevier; 2021. p. 23-55.

Intergovernmental Panel on Climate Change (IPCC). Climate Change 2023: Synthesis Report. Contribution of Working Groups I, II and III to the Sixth Assessment Report of the Intergovernmental Panel on Climate Change. Geneva, Switzerland: Intergovernmental Panel on Climate Change; 2023. p. 35-115.

Jackson CE, Saeger CM. Use of the pipette method in the fineness test of molding sand. Part of Journal of Research of the National Bureau of Standards 1935;14:59-65.

Jandaghian Z, Colombo A. The role of water bodies in climate regulation: Insights from recent studies on urban heat island mitigation. Buildings 2024;14(9):Article No. 2945.

Khamidov M, Ishchanov J, Hamidov A, Shermatov E, Gafurov Z. Impact of soil surface temperature on changes in the groundwater level. Water 2023;15(21):Article No. 3865.

Lehmann P, Merlin O, Gentine P, Or D. Soil texture effects on surface resistance to bare-soil evaporation. Geophysical Research Letters 2018;45(19):10398-405.

Liberalesso T, Tassi R, Ceconi DE, Allasia DG, Arboit NKS. Effect of rice husk addition on the physicochemical and hydrological properties on green roof substrates under subtropical climate conditions. Journal of Cleaner Production 2021;315:Article No. 128133.

Lim SL, Wu TY, Sim EYS, Lim PN, Clarke C. Biotransformation of rice husk into organic fertilizer through vermicomposting. Ecological Engineering 2012;41:60-4.

Liu P, Xia Y, Shang M. A bench-scale assessment of the effect of soil temperature on bare soil evaporation in winter. Hydrology Research 2020;51(6):1349-57.

Lozano-Parra J, Pulido M, Lozano-Fondón C, Schnabel S. How do soil moisture and vegetation covers influence soil temperature in drylands of mediterranean regions? Water 2018; 10(12):Article No. 1747.

Melo-Aguilar C, González-Rouco F, Steinert NJ, Beltrami H, Cuesta-Valero FJ, García-García A, et al. Near-surface soil thermal regime and land-air temperature coupling: A case study over Spain. International Journal of Climatology 2022;42(15):7516-34.

Możdżer E. Effect of guano fertilisation on yield and some quality traits of perennial ryegrass biomass. Journal of Ecological Engineering 2024;25(3):212-22.

Nachum S. Soil water potential in geosciences: An overview. Geosciences 2025;15(4):Article No. 123.

Nel T, Bruneel Y, Smolders E. Comparison of five methods to determine the cation exchange capacity of soil. Journal of Plant Nutrition and Soil Science 2023;186(3):311-20

Olsen SR, Cole CV, Watanabe FS. Estimation of Available Phosphorus in Soils by Extraction with Sodium Bicarbonate. Washington DC.: United States Department of Agriculture; 1954.

Onwuka B, Mang B. Effects of soil temperature on some soil properties and plant growth. Advances in Plants and Agriculture Research 2018;8(1):34-7.

Priyanka P, Kumar P, Panda S, Thakur T, Uday KV, Dutt V. Can machine learning models predict soil moisture evaporation rates? An investigation via novel feature selection techniques and model comparisons. Frontiers in Earth Science 2024;12:Article No. 1344690.

Qing Y, Wang S, Yang ZL, Gentine P, Zhang B, Alexander J. Accelerated soil drying linked to increasing evaporative demand in wet regions. Climate and Atmospheric Science 2023;6(1):1-10.

Quintana JR, Martín-Sanz JP, Valverde-Asenjo I, Molina JA. Drought differently destabilizes soil structure in a chronosequence of abandoned agricultural lands. Catena 2023;222:Article No. 106871.

Rehman A, Nawaz S, Alghamdi HA, Alrumman S, Yan W, Nawaz MZ. Effects of manure-based biochar on uptake of nutrients and water holding capacity of different types of soils. Case Studies in Chemical and Environmental Engineering 2020;2:Article No. 100036.

Reinsch S, Robinson DA, van Soest MAJ, Keith AM, Parry S, Tye AM. Temperate soils exposed to drought—key processes, impacts, indicators, and unknowns. Land 2024;13(11):Article No. 1759.

Sansan OC, Ezin V, Ayenan MAT, Chabi IB, Adoukonou-Sagbadja H, Saïdou A, et al. Onion (*Allium cepa* L.) and drought: Current situation and perspectives. Scientifica 2024;2024:Article No. 6853932.

dos Santos AKB, Popin GV, Gmach MR, Cherubin MR, Neto MS, Cerri CEP. Changes in soil temperature and moisture due to sugarcane straw removal in central-southern Brazil. Scientia Agricola 2021;79(6):e20200309.

Santos CF, Ribeiro ICA, Pelegrino MHP, Carneiro JP, Silva BM. A simple gravimetric methodology to determine soil particle density. Communications in Soil Science and Plant Analysis 2022;53(13):1623-9.

Seleiman MF, Al-Suhaibani N, Ali N, Akmal M, Alotaibi M, Refay Y, et al. Drought stress impacts on plants and different approaches to alleviate its adverse effects. Plants 2021; 10(2):Article No. 259.

Seneviratne SI, Corti T, Davin EL, Hirschi M, Jaeger EB, Lehner I, et al. Investigating soil moisture-climate interactions in a changing climate: A review. Earth-Science Reviews 2010;99(3-4):125-61.

Siebert J, Sünnemann M, Auge H, Berger S, Cesarz S, Ciobanu M, et al. The effects of drought and nutrient addition on soil organisms vary across taxonomic groups, but are constant across seasons. Scientific Reports 2019;9:Article No. 639.

Silva EC da, Albuquerque MB de, Neto AD de A, Junior CD da S, Silva EC da, Albuquerque MB de, et al. Drought and its consequences to plants – from individual to ecosystem. In: Akıncı S, editor. Responses of Organisms to Water Stress. IntechOpen; 2013.

Song WK, Cui YJ, Tang AM, Ding WQ, Wang Q. Experimental study on water evaporation from compacted clay using environmental chamber. Canadian Geotechnical Journal 2016;53(8):1293-304.

Statistics of Poso Regency. Poso Regency In Figures 2024. Poso: Statistics of Poso Regency; 2024. p. 1-255 (in Indonesia).

Stumpe B, Bechtel B, Heil J, Jörges C, Jostmeier A, Kalks F, et al. Soil texture mediates the surface cooling effect of urban and peri-urban green spaces during a drought period in the city area of Hamburg (Germany). Science of the Total Environment 2023;897:Article No. 165228.

Suzuki S, Noble AD, Ruaysoongnern S, Chinabut N. Improvement in water-holding capacity and structural stability of a sandy

soil in Northeast Thailand. Arid Land Research and Management 2007;21(1):37-49.

Szilagyi J, Zhang Y, Ma N, Crago RD, Qualls RJ, Jozsa J. Diminishing control of evaporation on rising land surface temperature of the Earth. Communications Earth and Environment 2024;5:Article No. 613.

Tan T, Xu Y, Liao X, Yi Z, Xue S. Formulating new types of rice husk biochar-based fertilizers for the simultaneous slow-release of nutrients and immobilization of cadmium. GCB Bioenergy 2024;16(6):e13142.

Tuffour HO, Bonsu M, Atakora WK, Abubakari A. Evaporative cooling of wet soil surface under different agricultural land use systems. International Journal of Scientific Research in Environmental Sciences 2014;2(9):323-31.

Tuntiwaranuruk U, Thepa S, Tia S, Bhumiratana S. Modeling of soil temperature and moisture with and without rice husks in an agriculture greenhouse. Renewable Energy 2006; 31(12):1934-49.

United Nations Educational Scientific and Cultural Organization (UNESCO). United Nations World Water Development Report 2020: Water and Climate Change. Paris: the United Nations Educational, Scientific and Cultural Organization; 2020. p. 1-235.

Wang P, Yu A, Wang F, Wang Y, Lyu H, Shang Y, et al. Nitrogen reduction by 20% with green manure retention reduces soil evaporation, promotes maize transpiration and improves water productivity in arid areas. Field Crops Research 2024;315:Article No. 109488.

Wang X, Zhao Y, Liu H, Xiao W, Chen S. Evaluating the water holding capacity of multilayer soil profiles using hydrus-1D and multi-criteria decision analysis. Water 2020;12(3):Article No. 773.

Whalley WR, Ober ES, Jenkins M. Measurement of the matric potential of soil water in the rhizosphere. Journal of Experimental Botany 2013;64(13):3951-63.

Yolcubal I, Brusseau ML, Artiola JF, Wierenga PJ, Wilson LG. Environmental physical properties and processes. In: Artiola JF, Pepper IL, Brusseau ML, editors. Environmental Monitoring and Characterization. Elsevier Inc.; 2004. p. 207-39.

Zhang Y, Hou W, Chi M, Sun Y, An J, Yu N, et al. Simulating the effects of soil temperature and soil moisture on CO_2 and CH_4 emissions in rice straw-enriched paddy soil. Catena 2020;194:Article No. 104677.

Zhang Z, Chen X, Pan Z, Zhao P, Zhang J, Jiang K, et al. Quantitative estimation of the effects of soil moisture on temperature using a soil water and heat coupling model. Agriculture 2022;12(9):Article No. 1371.

Environment and Natural Resources Journal

Volume 24
Issue 2
2026

Synergistic Effect of Microorganisms and Charcoal on the Removal of BTEX and TPH from Crude Oil Contaminated Soil

Ogu Chinedu[1,2*], Kariuki David[2], Wanjohi John[2], and Owhoeke Elechi[3]

[1]*Faculty of Science, University of Nairobi, Nairobi Kenya*
[2]*Department of Chemistry, Faculty of Science, University of Nairobi, Nairobi Kenya*
[3]*Department of Industrial and Petrochemical Science, Faculty of Science, University of Port-Harcourt, Rivers State, Nigeria*

ARTICLE INFO

Received: 3 Mar 2025
Received in revised: 19 Nov 2025
Accepted: 21 Nov 2025
Published online: 5 Feb 2026
DOI: 10.32526/ennrj/24/20250055

Keywords:
Charcoal/ Crude oil/ Microorganisms/ Organic contaminants/ Remediation

*** Corresponding author:**
E-mail:
cogu@students.uonbi.ac.ke

ABSTRACT

This study investigates the synergistic effect of microbial consortia and activated charcoal on the remediation of crude oil-contaminated soil in the Niger Delta region of Nigeria. Soil samples were treated over nine weeks using *Aspergillus niger*, *Pseudomonas aeruginosa*, *Sargassum filipendula*, activated charcoal, and their combinations. Key physicochemical parameters including pH, temperature, organic matter (OM), and total organic carbon (TOC) were monitored. The combined treatment of microorganisms and charcoal (S6) achieved the highest total petroleum hydrocarbon (TPH) removal efficiency (91.45%), outperforming individual treatments. BTEX compounds (benzene, toluene, ethylbenzene, and xylene isomers) showed substantial removal, with final degradation efficiencies ranging from 95.5% to 100% based on preliminary spectrophotometric data. However, due to limitations in the analytical method used (UV-Vis at 600 nm), these BTEX results are considered indicative and require validation through standard chromatographic techniques. The findings suggest that activated charcoal enhances microbial degradation by adsorbing toxic intermediates and providing a surface for microbial colonization. This integrated approach offers a cost-effective, scalable, and environmentally sustainable strategy for remediating oil-polluted soils, particularly in ecologically vulnerable regions such as the Niger Delta.

HIGHLIGHTS

- Synergy of microbes and charcoal boosted soil pollutant removal.
- Achieved 91.45% TPH removal, outperforming single treatments.
- Near-neutral pH supported microbial growth and remediation efficiency.
- Eco-friendly, low-cost method offers scalable soil recovery solutions.

1. INTRODUCTION

Crude oil is a complex mixture of several hydrocarbons, consisting of both low and high molecular weights. This mixture includes fully saturated hydrocarbons, branching hydrocarbons, unsaturated hydrocarbons, cyclic hydrocarbons (composed of carbon atoms only and with other atoms), and aromatic compounds (Kuppusamy et al., 2020; El Sabagh et al., 2019). Petrol-derived components such as total petroleum hydrocarbons (TPH), are among the most common environmental pollutants, along with benzene, toluene, ethylbenzene, and three isomers of xylene (ortho-, meta-, and para-) (collectively known as BTEX).

Crude oil and its derivatives commonly contain mono-aromatic hydrocarbons like benzene, toluene, ethylbenzene, and various isomers of xylene, all of which are major soil and groundwater contaminants. Accidental spills of diesel fuel or gasoline during transportation, as well as leaks from underground storage tanks and pipelines, release BTEX compounds into the environment (Khodaei et al., 2017). BTEX compounds are volatile aromatic hydrocarbons known to cause health problems such as irritation, headaches,

Citation: Chinedu O, David K, John W, Elechi O. Synergistic effect of microorganisms and charcoal on the removal of BTEX and TPH from crude oil contaminated soil. Environ. Nat. Resour. J. 2026;24(2):236-249. (https://doi.org/10.32526/ennrj/24/20250055)

liver and kidney damage, as well as cancer (Gunasinghe et al., 2021).

The Niger Delta region of Nigeria has suffered extensive environmental degradation due to oil pollution and gas flaring, affecting both terrestrial and aquatic ecosystems. The consequences include a decline in the soil productivity, which negatively impacts both biodiversity and the economic well-being of local communities. This degradation contributes to high rates of poverty and unemployment (Akpan et al., 2015; Ikhumetse et al., 2022). In Nigeria, oil spill incidents often experience delayed responses and limited remediation efforts, particularly in the Niger Delta region, where logistical, regulatory, and infrastructural challenges hinder timely environmental restoration.

Bioremediation refers to the use of biological mechanisms to degrade, decompose, convert, or effectively eliminate pollutants or substances that reduce the quality of soil and water (Nnaemeka and Iyiegbu, 2015). Bioremediation involves the application of microorganisms or their products (bioaugmentation), nutrients (biostimulation), and plants (phytoremediation) to restore environments contaminated with crude oil (Nnaemeka and Iyiegbu, 2015). The use of organic waste materials is increasingly replacing the utilization of chemical fertilizer due to its inherent advantages. Although numerous methods have been proposed for remediating petroleum contaminated soils, there remains a need for cost-effective and environmentally sustainable techniques that utilize locally available hydrocarbon-degrading agents. Bioremediation (a biological treatment) has proven to be both eco-friendly and economically viable (El Sabagh et al., 2019), compared to physical and chemical methods such as solidification/stabilization, thermal desorption, and burning. The novelty of this study lies in its examination of the synergetic effect achieved by the combination of microorganisms with activated charcoal for the bioremediation of crude oil pollution in soil. While previous studies have focused on either microbial treatments or the adsorptive capacity of charcoal individually, this study uniquely integrates both strategies to enhance the recovery of TPH and BTEX components. This synergy is expected because activated charcoal can adsorb toxic intermediates that inhibit microbial activity and simultaneously provide a porous surface that enhances microbial colonization and biofilm formation, thereby accelerating hydrocarbon degradation. This innovative approach offers a low-cost, eco-friendly and scalable solution for the remediation of oil polluted soils, particularly regions like the Niger-Delta. The study also presents new data on the microbial activity and adsorption processes, promoting the use of bioremediation.

2. METHODOLOGY

2.1 Chemicals and media

Chemicals: The BTEX hydrocarbons used in this work comprised of a mixture of benzene (99.9% purity, M & B, England), toluene (99.5% purity, BDH, England), ethylbenzene (99% purity, JHD, China) and xylene isomers (99% purity, JHD, China). The extraction solvent, dichloromethane (DCM) is a product of Merck and 98% purity. It was further distilled to obtain higher purity (99.9%) meeting analytical standards. BTEX degradation was assessed using microbial isolates obtained from treated soil samples. The isolates were cultured in liquid media supplemented with BTEX compounds, and degradation was quantified via UV spectrophotometry. This assay was conducted to assess the intrinsic BTEX-degrading capacity of microbes enriched in each soil treatment.

2.2 Sampling site

The site chosen for the experiment was located at the Port Harcourt Refinery Depot area in Alesa-Eleme, Rivers State, Nigeria (Figure 1). Situated within the Niger Delta region, this area has been heavily impacted by oil-related activities, including extraction, refining, and transportation, leading to frequent occurrences of oil spills. These spillages have caused substantial environmental degradation in the Alesa-Eleme area. Soil samples were collected in the vicinity of the Port Harcourt Refining Company Limited (PHRC), a subsidiary of the Nigerian National Petroleum Corporation (NNPC) Port Harcourt (Lat: 4°49'.0012" N and Long: 7°2'0.9996" E). The sample areas were selected because of their proximity to where crude oil products are refined, stored, and dispensed into tanker trucks for distribution.

2.3 Collection of microbes

In the Microbiology Laboratory at the University of Port Harcourt, concentrated suspension of three different microorganisms—fungi (*Aspergillus niger*), bacteria (*Pseudomonas aeruginosa*), and algae (*Sargassum filipendula*)—were prepared. Each strain was propagated under optimal growth conditions and prepared as a concentrated suspension with the following specifications: Bacteria and fungi: 1.0×10^{8}

colony-forming units per milliliter (CFU/mL) Algae: 1.0×10^{6} cells/mL (estimated via hemocytometer count). For each treatment, 0.5 mL of the respective suspension was applied to 250 g of contaminated soil, resulting in an effective dose of 5.0×10^{7} CFU for *P. aeruginosa*, *A. niger* and 5.0×10^{5} cells for *S. filipendula*. To preserve the viability and integrity of the microorganisms for future use, the bottles were promptly stored at 4°C. Refrigeration serves as a preservation method to ensure the stability and longevity of the microorganisms by slowing down their metabolic activities and preventing their proliferation before they are utilized for specific laboratory experiments, studies, or other scientific investigations. This controlled storage condition ensured the stability and characteristics properties of the microorganisms until they were required for further research or analysis in the laboratory setting.

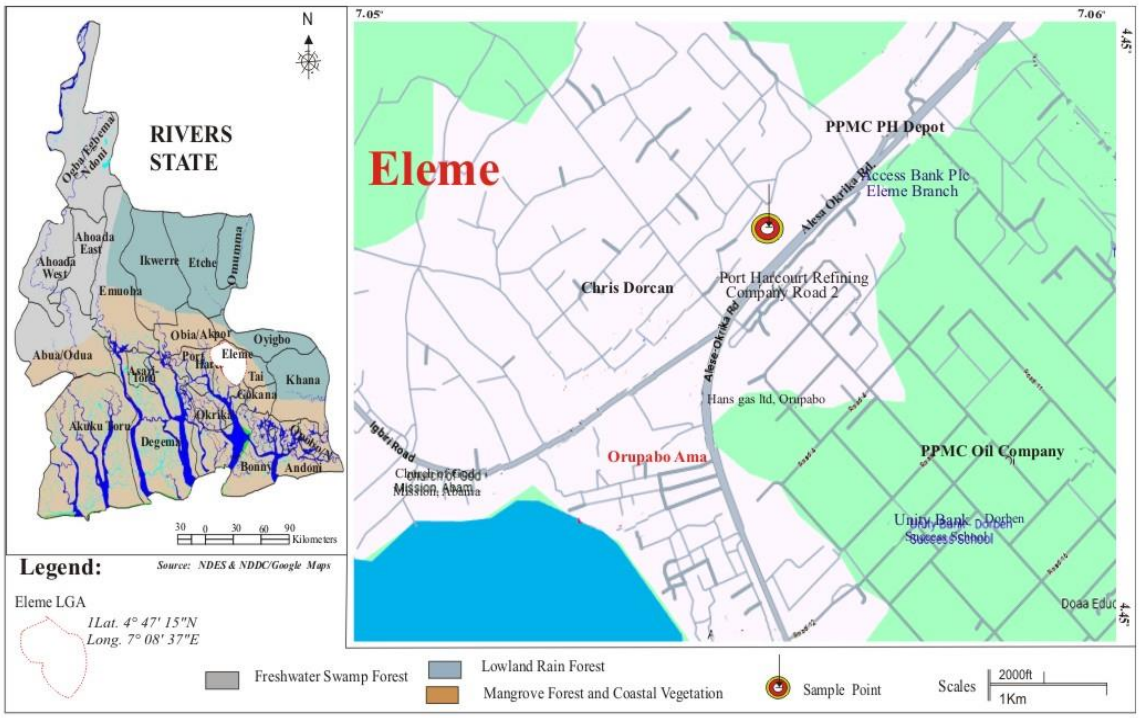

Figure 1. Map of sampling site

2.4 Sample collection and preparation

A stratified sampling approach was used in this study. The sampling field was divided into quadrants, and a total of fifteen (15) samples were taken by the proportionality rule, meaning that more samples were gathered from regions that contained a high concentration of contaminants. A composite sampling technique, which involves the blending of sampling units to generate a single sample, was utilized in conjunction with the stratified sampling approach. Oil-contaminated soil samples were collected using a sterile spatula, and the top two centimeters of each soil core were taken for analysis. To prevent cross-contamination, all samples were stored in clean, appropriate PVC bags, which were then sealed inside tin cans and sampling bottles. The experimental setup and corresponding samples groups are shown in Table 1.

2.5 Experimental design

The contaminated soil samples, contaminated with pollutants, were treated by combining them with specific biodegrading agents outlined in Table 1. This treatment aimed to facilitate the breakdown and remediation of pollutants present in the soil. To enhance aeration within the field cell environment, the soil samples were intermittently mixed by tilling. This process improved oxygen circulation, aiding the activities of microorganisms responsible for breaking down the contaminants in the soil. The experimental setup was allowed to settle for five-day intervals, after which samples were systematically collected for analysis. The primary focus of the analysis was to measure the remaining levels of both the TPH and BTEX within the treated soil samples. All experiments were conducted in triplicate, ensuring the reliability and consistency of the results. Furthermore, a control

sample was maintained at each stage of the experiment, providing a baseline for comparison with the treated samples. This approach enabled a comprehensive assessment of the efficacy of the biodegrading agents in reducing the levels of hydrocarbon contaminants in the soil. The structured experimental design enabled a comprehensive evaluation of the effectiveness of the biodegrading agents in reducing hydrocarbon contaminant levels in the soil. The systematic sampling and analysis at regular intervals, in triplicate, ensured a thorough and reliable assessment of the remediation process.

Table 1. Experimental sample set

Experimental set	Test experiment
S1	Polluted soil sample (250 g) + bacteria culture (0.5 mL)
S2	Polluted soil sample (250 g) + fungal culture (0.5 mL)
S3	Polluted soil sample (250 g) + algae culture (0.5 mL)
S4	Polluted soil sample (250 g) + charcoal (2.5 g)
S5	Polluted soil sample (250 g) + microbial consortium (0.5 mL)
S6	Polluted soil sample (250 g) + charcoal (2.5 g) + microbial consortium (0.5 mL) microbes (0.5 mL)
C1 (Control)	Unpolluted soil sample (250 g), no amendment

2.6 Soil pH

Fifty milliliters (50 mL) of distilled water was added to 20 g soil samples in a clean beaker. The mixture was stirred for 10 min, left to settle and stirred again for 2 min. The pH of the supernatant solution was measured using an Orion Research pH meter model 407 A.

2.7 Determination of temperature

The soil sample was prepared in the soil-to-water ratio mix of 1:1 by combining soil and distilled water. The mixture was allowed to settle before pH measurement using a calibrated pH meter. The temperature of the sample was measured using liquid in glass thermometer.

2.8 Electrical conductivity

The electrical conductivity of the soil was determined by measuring the conductivity of the filtrate obtained from the water extract, using the conductivity meter. The water extract was obtained from the soil sample through filtration, separating the liquid portion from the solid components. The conductivity meter, designed to measure for aqueous solutions, was then used to assess the ability of the filtrate to conduct electricity, and the measured value was recorded.

2.9 Determination of total petroleum hydrocarbon (TPH)

The testing for this analysis followed the ASTM D3921 standard method .Soil samples weighing 10 g each were carefully measured and prepared for analysis. These samples were then placed into a specialized apparatus known as a Soxhlet extractor, which facilitates the extraction of target compounds from solid samples. Within the Soxhlet extractor, the soil samples were combined with anhydrous sodium sulfate. This addition served the purpose of absorbing any moisture present in the samples, ensuring a dry environment for the extraction process. The elimination of moisture is critical for achieving optimal extraction efficiency. For the extraction of total crude oil hydrocarbons, a solvent known as methylene chloride, also referred to as dichloromethane, was employed. A volume of 200 mL of methylene chloride was used due to its strong solvating ability and selectivity for hydrocarbon compounds. During extraction process, the solvent continuously circulated through the soil sample in the Soxhlet apparatus, dissolving and extracting hydrocarbons from the soil matrix. This process was maintained for a sufficient duration to ensure thorough extraction and concentration of the target compounds. After the extraction process, the resulting solvent extract containing the hydrocarbons was collected and prepared for further analysis, as per the specified ASTM method. This method provides a consistent and reliable procedure for the quantitative recovery and analysis of total petroleum hydrocarbons (TPH) from soil samples, ensuring accuracy and reproducibility of results.

2.10 BTEX degradation experiment by microorganisms

For the microbial degradation of BTEX, the pH was adjusted to pH 6 and supplemented with 1% v/v

BTEX as the sole carbon source. An aliquot (1.0 mL) of 96 h prepared spore suspensions (1.0×10^6 cell/mL) was inoculated into each treatment flask. The control was left uninoculated and sterilized to account for abiotic losses such as volatilization. Experiments were carried out in triplicates at room temperature on a rotary shaker (Griffin Mechanical Shaker-Gallenkamp, England) (180 rpm) for 25 days (Kamal et al., 2017). An aliquot (5 mL) samples were taken aseptically at 5-day intervals. The residual BTEX compounds were extracted using 5 mL dichloromethane (DCM) and centrifuged (Griffin-Gallenkamp, England) (5,000 rpm) for 5 min. In this study, the BTEX degradation experiment was designed to access the microbial breakdown of benzene, toluene, ethylbenzene and xylene isomers using absorbance measurements at 600 nm. However, 600 nm is not suitable for the quantitative determination of BTEX compounds, which typically exhibit absorbance maxima in the ultraviolet (UV) range of 254-260 nm. Therefore, the use of UVis reading were used only to monitor the microbial response to BTEX exposure, rather than to quantify residual hydrocarbon concentrations. Accordingly, all BTEX data presented in this study are preliminary and indicative of microbial activity rather than chemical quantification. Further studies will adopt Gas chromatography coupled with Flame Ionization Detection (GC-FID) or Mass Chromatography to accurately measure individual BTEX compound and validate degradation efficiency.

3. RESULTS AND DISCUSSION

3.1 Remediation techniques and physical properties of contaminated soil

The physicochemical properties of polluted soil treated or remediated with bacteria (S1), fungi (S2), algae (S3), charcoal (S4), a mixture of micro-organisms (fungi, bacteria, and algae) (S5), and a combination of the microbial consortium with charcoal (S6) are shown in Table 2. The physic-chemical properties considered were soil pH, temperature, organic matter content and total organic carbon (TOC). These parameters serve as important indicators of soil health and microbial activity during the bioremediation process.

Table 2. Effect of remediation techniques on physical properties of contaminated soil

	S1		S2		S3		S4		S5		S6	
	WK1	WK9	WK1	WK9	WK1	WK9	WK1	WK9	WK1	WK9	WK1	WK9
pH	8.09	6.23	8.17	6.11	5.77	6.11	8.23	6.08	5.76	5.99	5.72	5.77
T ^oC	29.4	22.05	29.3	26.01	26.5	23.05	29.3	26.01	26.5	23.05	26.5	26.98
%OM	3.63	6.57	4.370	6.67	6.52	5.60	6.52	5.55	11.83	6.99	13.38	8.81
TOC	2.11	3.81	2.54	3.87	3.78	3.25	3.78	3.22	6.86	4.06	7.76	5.11

The pH of the contaminated soil after treatment with S1-S6 techniques was estimated at the range of 5.72-8.09, showing slight reductions in the value of the pH compared to the initial values. The pH values of soils treated with the mixture of microorganisms (*Aspergillus niger*, *Pseudomonas aeruginosa*, and *Sargassum filipendula*), and with the synergistic combination of microorganisms and charcoal were within the range of 5.76-5.99, indicating a slightly acidic condition when compared to soils treated with single microorganism. Neina (2019) reported that the pH within the proximity of neutrality aids the survival of bacteria, fungi, and algae, and as well supports the performance in remediating contaminated soil samples. The temperatures of the treated crude oil polluted soils ranged between 22.05^{o}C and 24.40^{o}C. For each of the techniques used, the temperature at week 1 was higher than that of the week 9. This temperature range also implies that the microorganisms used as remediation agents remained active and effective under the experimental conditions (Iranzo et al., 2001).

For the S1 and S2 techniques, the organic matter content increased progressively with time, indicating that both the *Aspergillus niger* and *Pseudomonas aeruginosa* were capable of decomposing the crude oil hydrocarbons. This biodegradation activity contributed to the accumulation of organic matter in the treated soils, as the microorganisms converted complex petroleum compounds into simpler organic substance (Hamdi et al., 2007; Jabeen et al., 2009).

The organic matter of the contaminated soil treated with S3, S4, S5, and S6 techniques contributed to a decrease in organic matter in the crude oil-polluted soil. The presence of algae and charcoal in the S3 and S4 likely contributed to the reduction in organic

matter, as these agents can decompose or adsorb organic compounds in crude oil-polluted soil. This also implies that the synergistic combinations of microorganisms with algae and charcoal (S5 and S6) may have enhanced the degradation or adsorption processes, leading to a further decline in organic matter. Similarly, Masciandaro et al. (2013) also observed a reduction in organic matter via a synergic approach, which involves organic matter, microorganisms, and plants in soil bioremediation. Macci et al. (2012) investigated the bioremediation of polluted soil using a combination of plants, earthworms, and organic matter and found a reduction in organic matter. Figure 2 illustrates the variation of organic matter for wk1 and wk9 using various treatment methods.

The total organic carbon (TOC) of the crude oil-polluted soil treated with different remediation techniques was recorded as S1 (2.11% and 3.81%), S2 (2.54% and 3.87%), S3 (3.78% and 3.25%), and S4 (3.78% and 3.22%) for week 1 and week 9. The S5 synergic approach showed a TOC reduction from 6.86% and 4.06% for week1 and week9, respectively, while the S6 technique treated soil with an estimated TOC removal of 7.76% and 5.11% for week1 and week 9, respectively (Figure 3).

The total organic carbon (TOC) showed a notable increase in S1 and S2 treatments by the end of the experiment. These findings are consistent with the results of Tanee and Kinako (2008) and Tanee and Abert (2011), who demonstrated that microbial activity can facilitate the decomposition of hydrocarbons, resulting in an elevation of organic carbon content in the soil. This phenomenon can be attributed to the inherently high carbon content present in crude oil, as documented by Speight (2014).

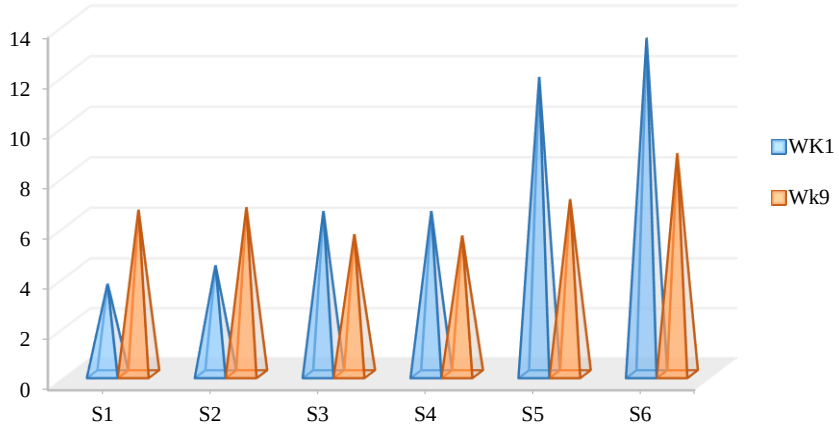

Figure 2. Variation of (a) organic matter for wk1 and wk9 at various techniques

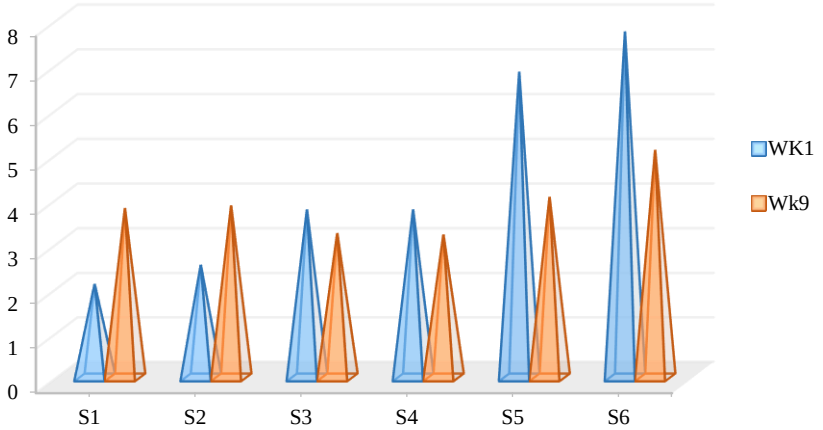

Figure 3. Variation of TOC for wk1 and wk9 at various techniques

In Contrast, when comparing week 1 to week 9, the S3, S4, S5, and S6 techniques helped to lower the TOC value of the crude oil-polluted soil. The algae and charcoal used in the S3 and S4 treatments, respectively, decreased the TOC in the crude oil soil. The observed decrease in TOC under the mixed microbial consortium (S5) contrasts with the increases recorded in the individual bacterial (S1) and fungal (S2) treatments. This may be attributed to synergistic microbial interactions that enhance the breakdown of complex hydrocarbons and accelerate mineralization of organic matter into CO_2. In mixed cultures, cooperative enzymatic activity and complementary metabolic pathways promote more complete degradation, thereby reducing residual organic carbon. Conversely, single-species treatments may promote microbial proliferation and partial transformation of hydrocarbons, contributing to TOC accumulation. Similar patterns have been reported in co-culture bioremediation systems where enhanced degradation correlates with reduced TOC levels (Li et al., 2021). Microorganisms may have converted the hydrocarbon in crude oil into other products, or charcoal may have adsorbed it. It also means that the algae and charcoal used in synergic techniques (S5 and S6) might be what lowers the TOC in soil that has been polluted by crude oil (Tanee and Kinako, 2008; Adams et al., 2017). The decrease in the TOC property for the synergy-treated soil was high when compared with the S3 and S4 techniques, which could also be linked to the interactive effects of the remediating agents on the polluted soil (Hamdi et al., 2007; Owhoeke et al., 2023; Agarry, 2018).

3.2 Analysis of TPH in polluted soil treated with different remediating techniques

The percentage removal of TPH from crude oil contaminated soil treated with S1-6 techniques is shown in Table 3.

Table 3. Percentage removal of TPH from contaminated soil

Periods	S1	S2	S3	S4	S5	S6
WK1	15.75	15.32	15.37	12.21	13.07	8.29
WK2	23.79	25.42	16.00	15.03	16.59	12.22
WK3	30.87	29.58	32.15	15.53	32.31	25.00
WK4	41.60	37.65	32.53	17.09	39.63	35.58
WK5	48.00	45.21	39.15	20.66	50.93	50.11
WK6	47.79	53.35	46.09	31.39	56.98	60.56
WK7	83.96	65.61	56.39	37.32	59.71	72.64
WK8	83.96	72.08	61.84	47.19	67.77	82.90
WK9	88.92	84.94	67.09	56.84	79.86	91.45

The percentage removal of TPH from the contaminated soil from week 1 to week. 9, using the different remediation techniques were S1 (15.75% and 88.92%), S2 (15.32% and 84.94%), S3 (15.37% and 67.09%), and S4 (12.22% and 54.84%), S5 (13.07% and 79.86%) and S6 (8.29% and 91.45%). The S4 technique which involved the use of charcoal had the lowest percentage of TPH removed, while S6 technique which combined the microorganisms and charcoal had the highest percentage of TPH removed at week 9 of the experiment.

The percentage removal of TPH increased from week 1 to week 9 which implies the ability of the microorganisms to metabolize the hydrocarbons in the polluted soil. Previous studies have demonstrated the effectiveness of charcoal in removing TPH from contaminated soil owing to its adsorptive properties (Semenyuk et al., 2014; Arroyo et al., 2019; Adebayo et al., 2023). Similarly, research involving microbial remediation has shown significant TPH removal efficiencies. For instance, Suja et al. (2014) documented a 79% reduction in TPH levels in crude oil contaminated soil using microorganisms, while Almansoory et al. (2019) highlighted the hydrocarbon-degrading potential of specific bacterial strains.

The mixture of microorganisms and the combination of charcoal with microorganisms both resulted in an increased percentage of TPH removal from crude oil-polluted soil. By week 9, the charcoal and microorganism amendment showed a higher percentage of TPH removal than the microorganism mixture. This findings suggests that the synergistic interaction between microorganisms and charcoal was more effective than microbial activity alone in

degrading hydrocarbons (Tanee and Kinako, 2008; Orie et al., 2015; Rong et al., 2021). Parhamfar et al. (2020) also reported a high percentage TPH removal through the synergistic use of indigenous bacteria isolates. Likewise, the results align with Zuzolo et al. (2021), who reported an 89% TPH reduction using a plant-bacteria-mycorrhiza synergy.

Figure 4 illustrates the variation of TPH for week 1 and week 9 at different techniques of remediation.

3.3 Analysis of BTEX in crude oil polluted soil treated with Remediation techniques

The analysis of BTEX compounds in crude oil polluted soil treated with different remediating techniques, such as bacteria(S1), fungi (S2), algae(S3), Charcoal (S4), mixture of microorganism (fungi, bacterial, and algae) (S5), and the mixture of microorganism with charcoal (S6) culture are shown in Table 4.

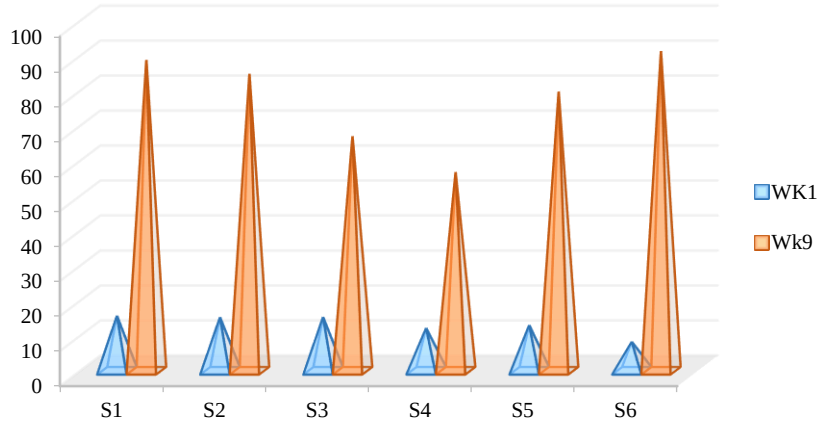

Figure 4. Variation of TPH for wk1 and wk9 at various techniques

Table 4. Percentage removal of BTEX from contaminated soil for week1 and week 9

	S1		S2		S3		S4		S5		S6	
Weeks	WK1	W9	WK1	WK9	WK1	WK9	WK1	WK9	WK1	WK9	WK1	WK9
Benzene	45.93	100	97.37	100	61.72	97.37	87.56	99.98	68.18	100	41.15	100
Toluene	18.07	100	86.48	100	82.90	100	86.48	100	100	100	83.88	100
Ethylbenzene	60.59	87.90	3.38	100	41.09	98.18	77.50	98.44	70.09	100	72.56	100
O-xylene	79.05	100	25.34	99.29	1.42	100	20.17	100	72.33	99.68	80.61	100
M-xylene	65.43	100	70.71	100	79.44	98.42	72.49	98.77	8.58	100	0.59	99.99
P-xylene	53.16	99.96	3.68	99.99	1.04	95.54	4.76	77.62	74.16	95.63	79.48	99.52

The percentage removal of benzene from soil treated with S1-S6 remediation techniques at week 1 and week 9 is presented in Table 4. The estimated benzene removal efficiencies for week 1 and week 9 were as follows: S1 (45.93% and 100%), S2 (97.37% and 100%), S3 (61.72% and 97.37%), and S4 (87.56% and 100%). The synergistic treatments also demonstrated notable benzene removal, with S5 (61.18% and 100%) and S6 (41.15% and 100%) showing complete degradation by the week 9.

There were notable increases in the percentage of benzene removal across the different remediation techniques applied on the contaminated soil. Complete benzene removal from the crude oil polluted soil was observed using the following treatments S1 (week 8), S2 (week 7), S5 (week 8) and S6 (week9). For S3 and S4 the benzene removal efficiencies reached 97.37% and 99.98% by the week 9.

The findings of Aburto-Medina and Ball (2015) are consistent with the present study, as they documented the impact of microorganisms on the anaerobic degradation of benzene. Similarly, in a study conducted by Soares et al. (2010), benzene was successful eliminated from the polluted soil through the combined application of soil vapor extraction and bioremediation techniques. The research findings were further supported by Wolicka et al. (2009), who demonstrated the effective removal of benzene at high concentrations from petroleum-contaminated soil

contaminated through the application of aerobic microorganism's bioremediation.

The chart for weekly analysis of benzene removal is illustrated in Figure 5.

The estimated toluene removal percentages at weeks 1 and week 9 were as follows: S1 (18.07% and 100%), S2 (86.48% and 100%), S3 (82.90% and100%), and S4 (86.48% and 100%) (see Table 4). The synergistic treatments showed the following removal efficiencies; S5 (10% and 100%) and S6 (83.88% and 100%) at weeks 1 and 9, respectively.

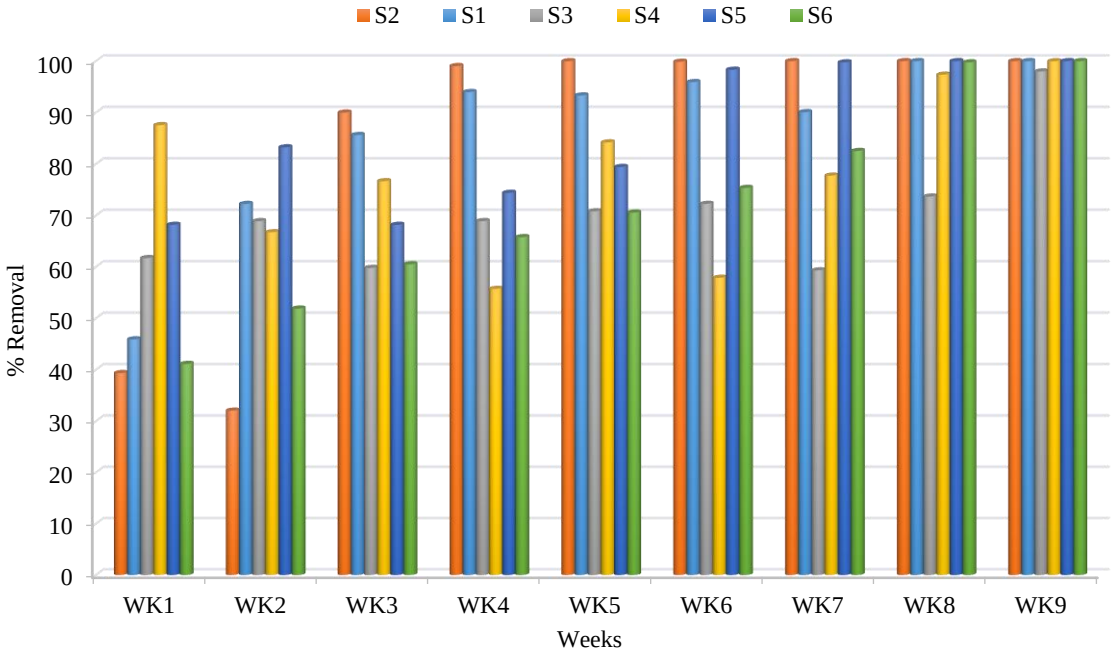

Figure 5. Benzene removal from week 1 to week 9 at various techniques

An overall increase in the toluene removal was observed across all remediation techniques from week 1 to week 9. During week 7, the removal of toluene was achieved by S1, S3, and S6. Complete toluene removal was achieved by week 7 for S1, S3, and S6; by week 6 for S4 and S5; and by week 5 for S2, demonstrating the varying efficiency and kinetics of the different treatments (Figure 6).

The complete removal of toluene observed within a few weeks suggests that the polluted soil did not contain substantial amounts of toluene, thereby indicating the efficacy of the treatment measures employed (Genovese et al., 2008). The work conducted by Moe et al. (2018) also confirmed the effective removal of toluene in contaminated soil through microbially mediated processes. Furthermore, Wolicka et al. (2009) supported these research findings by showcasing the effective elimination of toluene at high concentrations from petroleum-contaminated soil using the bioremediation potential of aerobic microorganisms.

The estimated ethylbenzene values for week 1 and week 9 were as follows: S1 (60.59% and 87.90), S2 (3.38% and 100%), S3 (41.09% and 100%), and S4 (77.50% and 98.44%) (Table 4). The synergistic treatment of ethylbenzene was observed with the following percentages; S5 (70% and 100%) and S6 (72.56% and 100%) during weeks 1 and 9, respectively (Table 4) (Figure 7).

The data from week 1 to week 9 demonstrate a progressive increase in the percentage of toluene removal from contaminated soil while utilizing different remediation procedures. Both S2 and S5 achieved a complete elimination of ethylbenzene (Wolicka et al., 2009; Soares et al., 2010). Additional results also indicated 100% removal efficiency for S6, as depicted in Figure 6. The results of Aburto-Medina and Ball (2015) support the current investigation, since they recorded the influence of microorganisms on the anaerobic breakdown of ethylbenzene.

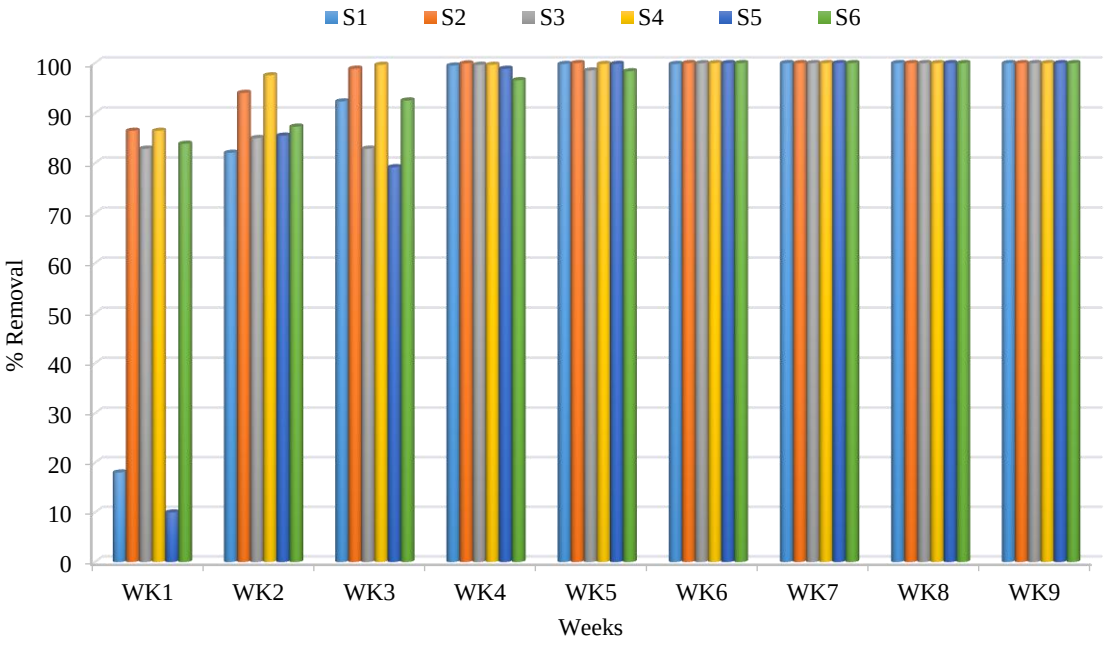

Figure 6. Toluene removal from week 1 to week 9 at various techniques

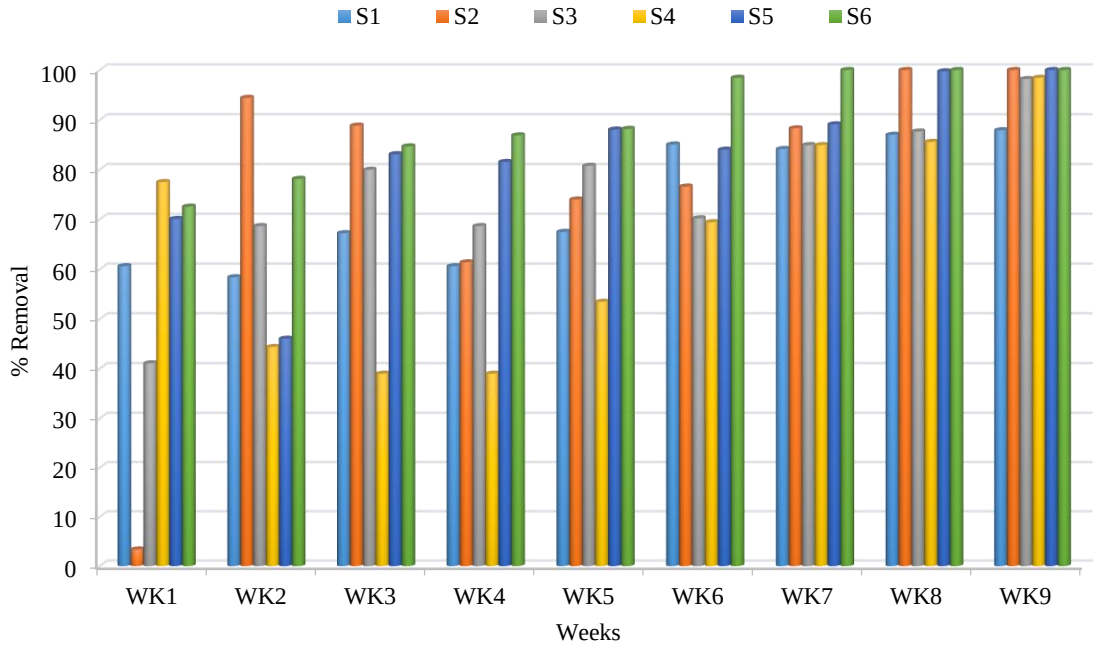

Figure 7. Ethylbenzene removal from week 1 to week 9 at various techniques

The estimated o-xylene values were as follows: S1 (79.05% and 100%), S2 (25.34% and 100%), S3 (1.42% and 100%), and S4 (20.17% and 100%). The synergistic treatment showed o-xylene removal percentages: S5 (72.33% and 99.68%) and S6 (80.61% and 100%) at the weeks 1 and 9, respectively. The data from weeks 1 and 9 show that the use of different remediation methods increased the efficiency of o-xylene removal from contaminated soil. At the seventh week, the rate of o-xylene removal in the S1 treatment was no longer detectable, indicating that the S1 technique achieved complete 100% of o-xylene from polluted soil. By week 9, the S2 and S5 techniques recorded 99.29% and 99.74% of o-xylene, removal respectively. Similarly, at week 9, complete removal of o-xylene was observed for the S3, S4, and S6 techniques (Figure 8). These results highlight the high sensitivity and efficiency of the remediation techniques in removing o-xylene from contaminated soil. The results of this study were in agreement with the findings of Singh and Fulekar's (2009), who reported the successful removal of o-xylene using a

microbial consortium derived from cow dung. Similarly, Wu et al. (2018) investigated o-xylene removal using one- and two-phase partitioning bio-trickling filters, focusing on the steady- and transient-state performance as well as the microbial community dynamics involved in the process. In another study, Taki et al. (2007) observed study where they successfully detected and characterized a significant reduction in o-xylene levels in polluted soil with o-xylene concentrations in contaminated soil through the activity of *Rhodococcus* spp. Additionally, Thakur and Balomajumder (2012) reported the biodegradation of o-xylene by *Azotobacter chroococcum*.

The estimated removal percentages of m-xylene values from crude oil-contaminated soil were as follows: S1 (65.43% and 100%), S2 (70.71% and 100%), S3 (79.44% and 98.42%), and S4 (72.49% and 98.77%) (Table 4). Synergistic treatments m-xylene removal efficiencies of S5 (8.58% and 100%) and S6 (0.59% and 99.99%) during weeks 1 and 9, respectively.

Additionally, the percentage of m-xylene removal increased when microorganisms were applied, and the combined use of charcoal and microorganisms proved effective in treating the crude oil-polluted soil. Complete 100% removal of m-xylene was achieved at week 9 using the S1, S2, and S5 techniques. At week 9, the S3, S4, and S6 techniques recorded 98.42%, 98.77%, and 99.99%, respectively. These results indicate that the microorganism, both independently and in combination with charcoal, are capable of decomposing m-xylene from crude oil-polluted soil.

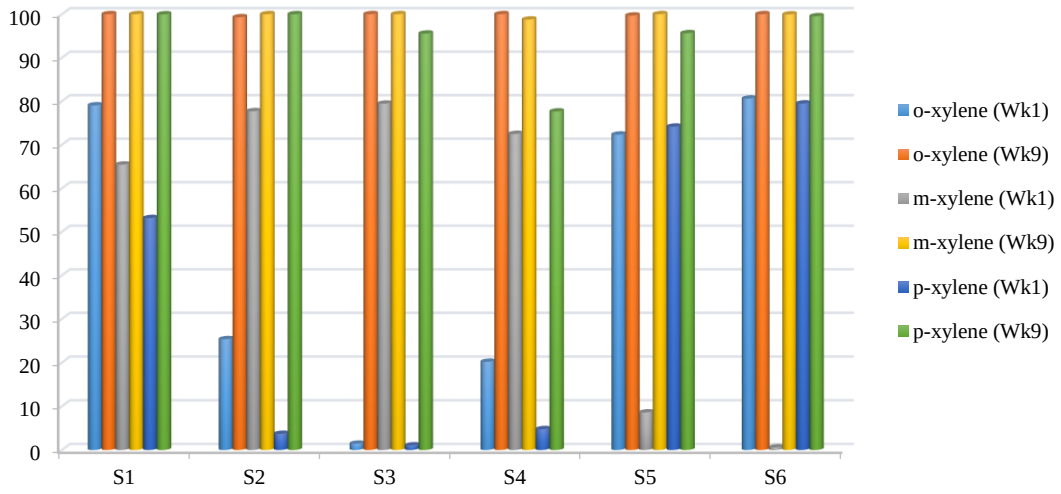

Figure 8. Xylene for week 1 and week 9 at various techniques

The findings of the present study are consistent with those conducted by Hess et al. (1997), which identified a significant concentration of m-xylene in a laboratory aquifer column contaminated with diesel fuel. Their research further demonstrated a marked reduction in m-xylene levels through the activity of degrading bacteria. Similarly, Yao et al. (2022) reported an efficient biodegradation of m-xylene using microorganisms. The results of this study also align with the findings of Ortega-González et al. (2013), who observed that a bacteria group from the rhizosphere soil of *Cyperus* sp. was capable of degrading up to 88% of m-xylene isomers.

The estimated percentages of p-xylene removed from crude oil-contaminated soil were as follows: S1 (53.16% and 99.96%), S2 (30.68% and 99.99%), S3 (1.04% and 95.54%), and S4 (4.76% and 77.62%) (Table 4). The synergistic treatments for p-xylene were recorded as S5 (74.16% and 95.63%) and S6 (83.88% and 100%) during weeks 1 and 9, respectively (Figure 8).

The use of microorganisms enhanced the removal efficiency of p-xylene. Additionally, a combining charcoal with microorganisms proved effective in treating crude oil contaminated soil. At week 9, the S1 and S2 treatments achieved 99.96% removal, while the S3, S4, S5, and S6 reached 95.54%, 77.62%, 95.63%, and 99.52%, respectively. This suggests that the microorganism, either individually or in combination with charcoal, can effectively degrade p-xylene in contaminated soil with crude oil (Yao et al., 2022). The results of this study align with the findings of Sui et al. (2005), who documented a significant reduction in p-xylene through microbial remediation. Similarly, Jeong et al. (2006) demonstrated the use of *Pseudomonas* sp. for p-xylene

removal. These results are also consistent with Prenafeta-Boldú et al. (2012), who achieved substantial removal of both ethylbenzene and p-xylene. Interactions between fungi and bacteria occur during the process of biodegrading TEX hydrocarbons. Miri et al. (2022) further investigated p-xylene biodegradation using three psychrophilic *Pseudomonas* strains, emphasizing gene expression analysis.

4. CONCLUSION

This study demonstrated that the combined application of microbial consortia and activated charcoal significantly enhanced the removal of total petroleum hydrocarbons (TPH) from crude oil-contaminated soil in the Niger Delta. Treatments involving both charcoal and microorganisms (S6) showed the highest TPH reduction and improved restoration of soil physicochemical properties, including pH, total organic carbon, and moisture content.

While preliminary observations suggested notable reductions in BTEX compounds, these results were derived from spectrophotometric measurements at 600 nm, a method not suitable for accurate quantification of volatile mono-aromatic hydrocarbons. Therefore, all BTEX-related findings should be interpreted as indicative of microbial activity rather than validated chemical degradation. Future studies will employ gas chromatography (GC-FID or GC-MS) to confirm BTEX removal and elucidate compound-specific degradation pathways.

Overall, the synergistic use of charcoal and microbial agents presents a promising strategy for soil remediation, particularly in resource-constrained settings. However, further validation using robust analytical techniques and expanded statistical analysis is essential to confirm the efficacy and reproducibility of this approach.

ACKNOWLEDGEMENTS

We thank the staff of the University of Port-Harcourt Laboratory for providing the facilities and technical support used for sample analysis.

AUTHOR CONTRIBUTIONS

Ogu Chinedu: Writing-original draft, investigation, formal analyses, data curation. David Kariuki: Writing-review and editing, supervision, methodology, validation. John Wanjohi: Writing-review and editing, supervision. Elechi Owhoeke: Validation, conceptualization.

DECLARATION OF CONFLICT OF INTEREST

The authors declare that they have no competing interests.

REFERENCES

Aburto-Medina A, Ball AS. Microorganisms involved in anaerobic benzene degradation. Annals of Microbiology 2015;65:1201-13.

Adams FV, Niyomugabo A, Sylvester OP. Bioremediation of crude oil contaminated soil using agricultural wastes. Procedia Manufacturing 2017;7:459-64.

Adebayo K, Engbonye JS, Musa A, George M, Oluwasanmi IO. Effect of charcoal and active carbon as filter media on electrokinetic remediated crude oil contaminated soil. Archives of Advanced Engineering Science 2023;3(2):1-7.

Agarry SE. Evaluation of the effects of inorganic and organic fertilizers and activated carbon on bioremediation of soil contaminated with weathered crude oil. Journal of Applied Sciences and Environmental Management 2018;22(4):587-95.

Akpan AE, Ebong ED, Emeka CN. Exploratory assessment of groundwater vulnerability to pollution in Abi, southeastern Nigeria, using geophysical and geological techniques. Environmental Monitoring and Assessment 2015;187:Article No. 244.

Almansoory AF, Hasan HA, Abdullah SRS, Idris M, Anuar N, Al-Adiwish WM. Biosurfactant produced by the hydrocarbon-degrading bacteria: Characterization, activity and applications in removing TPH from contaminated soil. Environmental Technology and Innovation 2019;14:Article No. 100347.

Arroyo S, Rosano-Ortega G, Martinez-Gallegos S, Perez-Armendariz B. Hydrocarbon removal from diesel-contaminated soil through reused activated carbon adsorption. Environmental Engineering and Management Journal 2019;18(9):1963-70.

El-Sabagh A, Hossain A, Barutcular C, Gormus O, Ahmad Z, Hussain S. Effects of drought stress on the quality of major oilseed crops: Implications and possible mitigation strategies: A review. Applied Ecology and Environmental Research 2019;17(2):4019-50.

Genovese M, Denaro R, Cappello S, Di Marco G, La Spada G, Giuliano L. Bioremediation of benzene, toluene, ethylbenzene, xylenes-contaminated soil: A biopile pilot experiment. Journal of Applied Microbiology 2008;105(5):1694-702.

Gunasinghe YHKIS, Rathnayake IVN, Deeyamulla MP. Plant and plant associated microflora: Potential bioremediation option of indoor air pollutants. Nepal Journal of Biotechnology 2021;9(1):63-74.

Hamdi H, Benzarti S, Manusadžianas L, Aoyama I, Jedidi N. Bioaugmentation and biostimulation effects on PAH dissipation and soil ecotoxicity under controlled conditions. Soil Biology and Biochemistry 2007;39(8):1926-35.

Hess A, Zarda B, Hahn D, Häner A, Stax D, Höhener P, et al. In situ analysis of denitrifying toluene- and m-xylene-degrading bacteria in a diesel fuel-contaminated laboratory aquifer column. Applied and Environmental Microbiology 1997; 63(6):2136-41.

Ikhumetse AA, Abioye OP, Ijah UJJ, Bankole MT. A critical review of oil spills in the Niger Delta aquatic environment: Causes, impacts, and bioremediation assessment. Environmental Monitoring and Assessment 2022;194(11): Article No. 816.

Iranzo M, Sainz-Pardo I, Boluda R, Sanchez J, Mormeneo S. The use of microorganisms in environmental remediation. Annals of Microbiology 2001;51(2):135-44.

Jabeen R, Ahmad A, Iqbal M. Phytoremediation of heavy metals: Physiological and molecular mechanisms. The Botanical Review 2009;75(4):339-64.

Jeong E, Hirai M, Shoda M. Removal of p-xylene with *Pseudomonas* sp. NBM21 in biofilter. Journal of Bioscience and Bioengineering 2006;102(4):281-7.

Kamal MS, Adewunmi AA, Sultan AS, Al-Hamad MF, Mehmood U. Recent advances in nanoparticles enhanced oil recovery: Rheology, interfacial tension, oil recovery, and wettability alteration. Journal of Nanomaterials 2017;2017:Article No. 2473175.

Khodaei K, Nassery HR, Asadi MM, Mohammadzadeh H, Mahmoodlu MG. BTEX biodegradation in contaminated groundwater using a novel strain (*Pseudomonas* sp. BTEX-30). International Biodeterioration and Biodegradation 2017;116:234-42.

Kuppusamy S, Maddela NR, Megharaj M, Venkateswarlu K. An overview of total petroleum hydrocarbons. In: Total Petroleum Hydrocarbons: Environmental Fate, Toxicity, and Remediation. Springer; 2020. p. 1-27.

Li X, Wu S, Dong Y, Fan H, Bai Z, Zhuang X. Engineering microbial consortia towards bioremediation. Water 2021;13(20):Article No. 2928.

Macci C, Doni S, Peruzzi E, Ceccanti B, Masciandaro G. Bioremediation of polluted soil through the combined application of plants, earthworms and organic matter. Journal of Environmental Monitoring 2012;14(10):2710-7.

Masciandaro G, Macci C, Peruzzi E, Ceccanti B, Doni S. Organic matter-microorganism-plant in soil bioremediation: A synergic approach. Reviews in Environmental Science and Bio/Technology 2013;12(4):399-419.

Miri S, Rasooli A, Brar SK, Rouissi T, Martel R. Biodegradation of p-xylene—A comparison of three psychrophilic *Pseudomonas* strains through the lens of gene expression. Environmental Science and Pollution Research 2022;29: 21465-79.

Moe WM, Reynolds SJ, Griffin MA, McReynolds JB. Bioremediation strategies aimed at stimulating chlorinated solvent dehalogenation can lead to microbially-mediated toluene biogenesis. Environmental Science and Technology 2018;52(16):9311-9.

Neina D. The role of soil pH in plant nutrition and soil remediation. Applied and Environmental Soil Science 2019;2019:Article No. 5794869.

Nnaemeka O, Iyiegbu H. Oil spill bioremediation using soil blending technique, over a bionutrient: A Niger Delta case. International Journal of Innovative Science, Engineering and Technology 2015;2(6):161-80.

Orie KJ, James AO, Akaranta O. The corrosion inhibition of mild steel in 0.5 M phosphoric acid and crown cork in water by folic acid. International Journal of Science and Research 2015;4(9):Article No. 1380.

Ortega-González DK, Zaragoza D, Aguirre-Garrido J, Ramírez-Saad H, Hernández-Rodríguez C, Jan-Roblero J. Degradation of benzene, toluene, and xylene isomers by a bacterial consortium obtained from rhizosphere soil of *Cyperus* sp. grown in a petroleum-contaminated area. Folia Microbiologica 2013;58:569-77.

Owhoeke E, Ali A, Nnaemeka OJ, Orie KJ, Ehiwario JN, Rashid A. Index model equation analysis: A case study of the risk and source of inorganic contaminants in roadside uncontaminated soil of the Egi oil producing area, Niger Delta. International Journal of Sediment Research 2023;38(6):891-900.

Parhamfar M, Abtahi H, Godini K, Saeedi R, Sartaj M, Villaseñor J, et al. Biodegradation of heavy oily sludge by a two-step inoculation composting process using synergistic effect of indigenous isolated bacteria. Process Biochemistry 2020;91:223-30.

Prenafeta-Boldú FX, Guivernau M, Gallastegui G, Viñas M, de Hoog GS, Elías A. Fungal/bacterial interactions during the biodegradation of TEX hydrocarbons (toluene, ethylbenzene and p-xylene) in gas biofilters operated under xerophilic conditions. FEMS Microbiology Ecology 2012;80(3):722-34.

Rong L, Zheng X, Oba BT, Shen C, Wang X, Wang H, et al. Activating soil microbial community using *Bacillus* and rhamnolipid to remediate TPH contaminated soil. Chemosphere 2021;275:Article No. 130062.

Semenyuk NN, Yatsenko VS, Strijakova ER, Filonov AE, Petrikov KV, Zavgorodnyaya YA, et al. Effect of activated charcoal on bioremediation of diesel fuel-contaminated soil. Microbiology 2014;83:589-98.

Singh D, Fulekar MH. Bioremediation of benzene, toluene and o-xylene by cow dung microbial consortium. Journal of Applied Biosciences 2009;14:788-95.

Soares AA, Albergaria JT, Domingues VF, Maria da Conceição M, Delerue-Matos C. Remediation of soils combining soil vapor extraction and bioremediation: Benzene. Chemosphere 2010;80(8):823-8.

Speight JG. The Chemistry and Technology of Petroleum. 5th ed. Boca Raton: CRC Press; 2014.

Sui H, Li XG, Jiang B. Benzene, toluene and p-xylene interactions and the role of microbial communities in remediation using bioventing. The Canadian Journal of Chemical Engineering 2005;83(2):310-5.

Suja F, Rahim F, Taha MR, Hambali N, Razali MR, Khalid A, et al. Effects of local microbial bioaugmentation and biostimulation on the bioremediation of total petroleum hydrocarbons (TPH) in crude oil contaminated soil based on laboratory and field observations. International Biodeterioration and Biodegradation 2014;90:115-22.

Taki H, Syutsubo K, Mattison RG, Harayama S. Identification and characterization of o-xylene-degrading *Rhodococcus* spp. which were dominant species in the remediation of o-xylene-contaminated soils. Biodegradation 2007;18:17-26.

Tanee FBG, Albert E. Biostimulation potential of sawdust on soil parameters and cassava (*Manihot esculenta*; Crantz) yields in crude oil polluted tropical soil. Advances in Environmental Biology 2011;5(5):938-45.

Tanee FBG, Kinako PDS. Comparative studies of biostimulation and phytoremediation in the mitigation of crude oil toxicity in tropical soil. Journal of Applied Sciences and Environmental Management 2008;12(2):143-7.

Thakur PB, Balomajumder C. Biodegradation of o-xylene by *Azotobacter chroococcum*. International Journal of Advanced Biotechnology and Research 2012;3(1):502-8.

Wolicka D, Suszek A, Borkowski A, Bielecka A. Application of aerobic microorganisms in bioremediation in situ of soil contaminated by petroleum products. Bioresource Technology 2009;100(13):3221-7.

Wu C, Xu P, Xu B, Li W, Li S, Wang X. O-xylene removal using one- and two-phase partitioning biotrickling filters: Steady/transient-state performance and microbial community. Environmental Technology 2018;39(1):109-19.

Yao X, Shi Y, Wang K, Wang C, He L, Li C, et al. Highly efficientdegradation of hydrogen sulfide, styrene, and m-xylene in a bio-trickling filter. Science of the Total Environment 2022;808:Article No. 152130.

Zuzolo D, Guarino C, Tartaglia M, Sciarrillo R. Plant-soil-microbiota combination for the removal of total petroleum hydrocarbons (TPH): An in-field experiment. Frontiers in Microbiology 2021;11:Article No. 621581.

Environment and Natural Resources Journal

Volume 24
Issue 2
2026

Circular Economy Pathway: Valorization of Cotton Stalk into Biochar for Textile Wastewater Treatment

Vishwa Vraj Shah[1] and N. M. Patel[2*]

[1]*Research Scholar, Environmental Engineering, Gujarat Technological University, Ahmedabad, India*
[2]*Chemical Engineering Department, Government Engineering College Valsad-3960001, Gujarat, India*

ARTICLE INFO

Received: 14 Oct 2025
Received in revised: 10 Dec 2025
Accepted: 19 Dec 2025
Published online: 28 Jan 2026
DOI: 10.32526/ennrj/24/20250255

Keywords:
Circular economy/ Phosphate modified cotton stalk biochar/ Multicomponent synthetic textile wastewater/ COD removal/ Adsorption kinetics/ Langmuir isotherm

*** Corresponding author:**
E-mail: prof.nmpatel@gmail.com

ABSTRACT

Agricultural residues, often burned openly pose environmental challenges but offers opportunities for valorization into functional materials. Converting such residues into biochar supports circular economy principles. Here, cotton stalk (CS) was converted into phosphate-modified biochar (PMCS) via pyrolysis at 350, 550, and 800°C. Response Surface Methodology (RSM) was applied to the adsorption process, treating pyrolysis temperature as a categorical factor in a rotatable CCD. PMCS was characterized by Brunauer-Emmett-Teller (BET), Scanning Electron Microscopy (SEM), and Fourier Transform Infrared Spectroscopy (FTIR), Point of Zero Charge while adsorption was evaluated through isotherm and kinetic modeling for synthetic textile wastewater containing Eriochrome Black T (EBT), starch, and salts. PCS800 exhibited a BET analysis of 750 m² per gram of biochar and achieved nearly 77% COD reduction at 33 min and 6.43 g/L for synthetic wastewater, while 60% with complete decolorization for real effluent. The optimum removal followed Langmuir behaviour (q_{max}=90.2 mg/g, K_L= 0.049 L/mg) with pseudo-second-order kinetics, reflecting micropore filling by starch. Overall, this study establishes a circular economy pathway by valorizing CS into an efficient adsorbent, mitigating residue burning while offering scalable potential for textile wastewater treatment.

HIGHLIGHTS

- Cotton stalk was valorized into phosphate-modified biochar via pyrolysis.
- Adsorption shifted from Freundlich multilayer to Langmuir monolayer at 800°C.
- PCS800 achieved 77% COD reduction for multicomponent synthetic water and 60% removal for real textile effluent.
- PCS550 provided balanced adsorption of both small and large organic molecules.
- Study supports circular economy by converting residues into functional adsorbents.

1. INTRODUCTION

Water is increasingly recognized not only as a vital resource but also as a reservoir of recoverable materials, a perspective central to the circular economy in wastewater management. Wastewater is no longer viewed solely as waste but as a source of nutrients, energy, and reusable materials (Tzanakakis et al., 2023; Agyemang et al., 2024). Within this framework, valorizing agricultural residues into functional materials offers a sustainable pathway for resource recovery. Biochar, produced through thermal conversion of biomass, exemplifies this approach: its porous structure and reactive surface chemistry enable efficient adsorption of dyes, heavy metals, and organics (He et al., 2022), while simultaneously recycling biomass that would otherwise drive environmental degradation (Xiang et al., 2022). Thus, biochar use in wastewater treatment unites pollution control with resource recovery, advancing circular economy principles (Colmenares et al., 2016).

Each year, India generates nearly 87.0 million tonnes of agro residues and their open field burning remaining the dominant disposal method that contributed to air pollution surpassing levels reported in other Asian countries. Where, India is also the second-largest contributor to carbon aerosol emissions, releasing approximately 84 teragram per year (Bhuvaneshwari et al., 2019; Grover and

Citation: Shah VV, Patel NM. Circular economy pathway: Valorization of cotton stalk into biochar for textile wastewater treatment. Environ. Nat. Resour. J. 2026;24(2):250-267. (https://doi.org/10.32526/ennrj/24/20250255)

Chaudhry, 2019; Dhanya, 2022). Among these, cotton stalk (CS) is a major agro-residue (Deshpande et al., 2023). This study establishes a closed-loop framework where CS residues from the textile sector are valorized into phosphate-modified biochar to mitigate the very pollution burden generated by that sector Figure 1.

The textile sector that is considered as a key pillar of the Indian economy, generate approximately 140-200 L of wastewater per kilogram of fabric with high organic load (Arous et al., 2024). The World Bank identifies it as a major environmental challenge, with dyeing and finishing alone contributing 17%-20% of industrial effluents (Okafor et al., 2021). These effluents contain dyes, chromium, alkalis, and acids (Sathya et al., 2022), among which persistent azo dyes e.g., benzene diazonium chloride derivatives, Naphthoic acid derivatives, Reactive Green 19, Eriochrome Black T are particularly concerning due to their transformation into mutagenic and carcinogenic aromatic amines (Sadeghi et al., 2021; Ali et al., 2022). Beyond dyes, textile wastewater also carries additives such as starch and salts, which significantly contribute to the Chemical Oxygen Demand (COD), a critical parameter in environmental management.

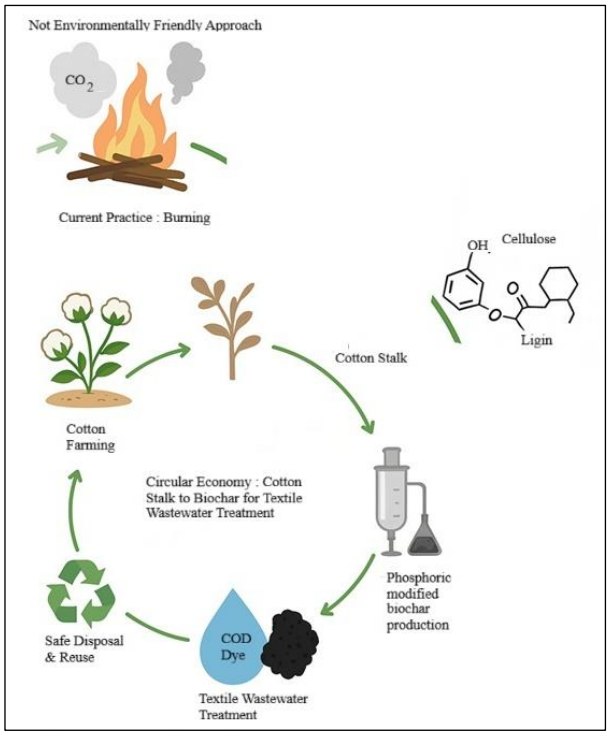

Figure 1. Circular economy approach for cotton stalk biochar

Conventional treatment technologies often prove inadequate for such complex pollution. Biochar offers a circular economy based solution, enabling effective contaminant removal and resource recovery while addressing biomass waste challenges (Wu and Wu, 2019; Kwarciak-Kozłowska and Fijałkowski, 2021). CS is a rich in cellulose, hemicellulose, and lignin, decomposes thermally into a stable aromatic matrix with micropores suitable for adsorption (Zhao et al., 2022; Zhu et al., 2022; Cui et al., 2024). Till date thermally prepared CS biochar preliminary utilized for heavy metal removal form water, achieving removal efficiencies of >80% (Cr^{+6}), 80.90 µg/g (As) and 146.78 mg/g for Pb^{+2} for pyrolysis temperature between 400-550°C (Hussain et al., 2020; Gao et al., 2021; Ahmad et al., 2022; Khalid and Inam, 2024). In contrast, Shah et al. (2022) reported a relatively lower adsorption capacity of 30-40 mg/g for Malachite green dye at 100 mg/L by unmodified CS. However, modified CS with H_3PO_4 acid enhanced dye removal capacity of 144.36 mg/g for RhB dye with >99.5% removal (Venkatesan et al., 2025). Similar improvements have been observed for agro waste derived biochar treated with H_3PO_4 such as coconut shell [95.4% MB removal, (Xu et al., 2023)], sugarcane bagasse [357.14 mg/g, (Zhou et al., 2022)], and corn straw [251.08 mg/g, (Liu et al., 2024)]. Recent advances therefore emphasize heteroatom modification particularly with phosphorus incorporation which substantially alters physicochemical properties, introducing unique surface functionalities (Tan et al., 2022; Xu et al., 2024; Zafar et al., 2024). Phosphorus modification restructures functional groups, increases graphite defect density, and enhances adsorption of diverse pollutants (Ou et al., 2023; Li et al., 2024b; Li et al., 2024a; Zeng et al., 2024). It also introduces acidic sites, improves stability, and markedly increases affinity for metal ions and alkaline organics (Arampatzidou et al., 2017; Liu et al., 2021; Shao et al., 2024; Du et al., 2025).

This study addresses a key research gap in textile wastewater treatment by developing a circular economy pathway for valorizing cotton stalk into phosphate-modified biochar (PMCS) under multi-component wastewater conditions. PMCS produced at 350, 550, and 800°C was characterized by Brunauer-Emmett-Teller (BET), Scanning Electron Microscopy (SEM), and Fourier Transform Infrared Spectroscopy (FTIR), Point of Zero Charge and evaluated for COD removal using a novel Response surface Methodology (RSM) framework that treats pyrolysis temperature as a categorical factor in a rotatable central composite design (CCD). Inclusion of RSM in adsorption process enables the development of statistically reliable

quadratic models while capturing curvature and interaction effects in the response surface. RSM provides a resource efficient alternative to traditional experimental approaches because it identifies optimal operating conditions using fewer experimental runs and simultaneously evaluates both main and interaction effects (Susaimanickam et al., 2023).

The adsorption efficiency is influenced by several interacting parameters, including pH, adsorbent dose, mixing time, temperature, and initial contaminant concentration (Yaseen and Scholz, 2019). Conventional one-variable-at-a-time (OVAT) methods fail to capture such interactions, are labour intensive, and provide limited insight into overall process behaviour in traditional RSM frame work (Dowlatshah et al., 2025). Hence, use of RSM in present study offers advantage to maximize the pollutant reduction by optimizing the operating parameters. Till date, limited studies have successfully employed RSM (CCD/BBD) to optimize adsorption parameters for COD and BOD removal processes using biosorbents and activated materials (Oyekanmi et al., 2019; Manzar et al., 2021; Roy et al., 2022).

By contrast, the RSM-CCD approach extends the conventional RSM framework by combining continuous and categorical inputs, enabling detailed assessment of how structural and functional biochar properties interact with process parameters. Furthermore, kinetic and isotherm modeling were employed to elucidate the governing adsorption mechanisms As highlighted by (Srivastav et al., 2024) such multi-pollutant evaluation is critical for scale-up. Hence, the study shows that phosphorus modification and pyrolysis markedly enhance adsorption efficiency and explain the mechanisms involved in multicomponent system. Moreover, this work provides a viable pathway for converting biomass into effective materials for feasible wastewater treatment in real world. Therefore, this approach offers a practical and cost-effective means for biomass utilization and cleaner wastewater management leads to circular economy concept in textile sector.

2. METHODOLOGY

2.1 Multi component synthetic textile wastewater

A synthetic wastewater representative of textile effluent was prepared to simulate partially treated effluent. Eriochrome Black-T (EBT, 30 mg/L) was obtained from a textile unit in Ahmedabad, while starch (250 mg/L), Na_2CO_3 (100 mg/L), $NaHCO_3$ (100 mg/L), NaCl (150 mg/L), NaOH (50 mg/L), and H_2SO_4 (30 mg/L) were laboratory grade reagents (Merck, India; >90% purity). Constituents were sequentially dissolved in distilled water under stirring (200 rpm, 30 min) to obtain a homogeneous dark-blue solution of neutral pH, consistent with actual effluent. The COD was 220±10 mg/L and BOD of 50±5 mg/L, having BOD:COD ratio of 0.23 which is <0.3 considered as non-biodegradable in nature (Muhammad et al., 2008). Fresh synthetic wastewater was prepared for each experiment to maintain reproducibility.

2.2 Synthesis of phosphate modified cotton stalk biochar (PMCS)

About 100 kg of cotton stalk (CS) was collected from farms near Himmantnagar, Gujarat, cut into 2-3 cm pieces, rinsed thoroughly with distilled water (DW) and subsequently dried for 4 h under sunlight. A 100 g batch was chemically activated by adding in 85% Phosphoric acid solution at a 0.5:1 ratio (CS:acid, w/w) under stirring for 1 h, then oven-dried at 110°C for 48 h. The precursor was subjected to thermal treatment in a muffle furnace at 350, 550, and 800°C for 2 h (heating rate 10°C/min, limited oxygen). Once cooled the biochar rinsed repeatedly with hot DW and neutralized with NaOH till pH of the rinse water pH reached 7, followed by drying in an oven at 105°C for 12 h. The dried product less than 0.5 mm kept in seal container. The synthesized samples were denoted PCS350, PCS550, and PCS800. A synthesis pathway is shown in schematic form in Figure 2.

2.3 Characterization of Phosphate Modified Cotton Stalk Biochar (PMCS)

Biochar PCS350, PCS550, and PCS800 were characterized to assess changes in surface morphology, functional groups, and pore structure across pyrolysis temperatures. The BET analysis, point of zero charge, SEM, and FTIR analyses were performed to evaluate surface area, charge, morphology, and functionalities, respectively. BET was measured using a Surface Area Analyzer (Test method: IKC/ACC/INS09/BET) at the Advanced Characterization Centre, Ashapura Mine Chem, Gujarat. Point of zero charge was determined by the pH drift method. SEM was conducted at the Central Instrumentation Facility, Central University of Gujarat (Model: EVO 18, Carl Zeiss), and FTIR spectra (400-4,000 cm^{-1}) recorded with a Perkin Elmer SP-65 using KBr pellets. Optimized biochar showing maximum

COD removal was further analyze with advanced SEM and FTIR for validation.

2.4 Optimization study for COD reduction using RSM.

RSM was adopted to enhance COD removal efficiency by analyzing the effects of adsorbent dose and mixing time, while treating pyrolysis temperature (350, 550, 800°C) as a categorical factor. This approach extends the conventional RSM framework by combining continuous and categorical inputs, enabling detailed assessment of how structural and functional biochar properties interact with process parameters. Experiments were conducted at pH 7 and 400 rpm under ambient conditions. A Face-Cantered Central Composite Design (CCD) was adopted with two continuous factors (dose, time) and one categorical factor (temperature). The factor ranges are summarized in Table 1.

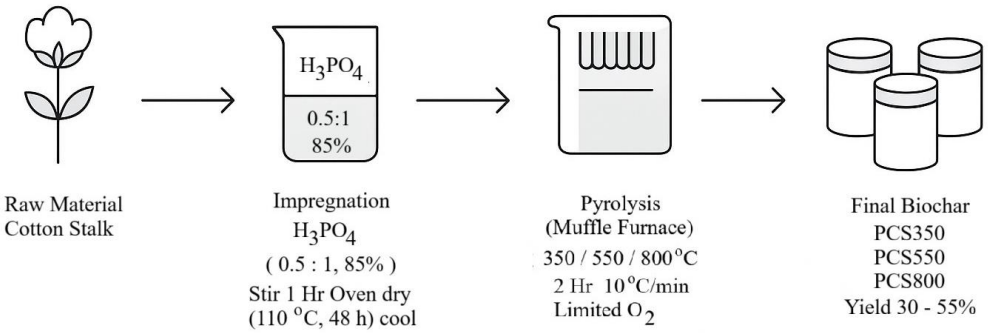

Figure 2. Phosphate modified CS biochar synthesis process

Table 1. RSM-CCD framework for optimization

Independent variables	Factor	Unit	Low	Centre	High
Adsorbent dose (PCS350, PCS550, and PCS800)	A	g/L	0.1	5.25	10
Mixing time	B	min	5	27.5	50
Pyrolysis temperature	L1, L2, L3	°C	350	550	800

The general formula for CCD is as (Equation 1). Where, k=number of continuous variables (here k=2), 2^k=no. of factorial points, 2k=star points, n_c=number of centre points (with replicates) and L=number of categoric levels.

$$N = (2^k + 2k + n_c) \times L \quad (1)$$

Hence, The CCD has developed 33 runs in Design of Experiment (DoE) covering factorial points, axial points, and replicated centre points, distributed across the three pyrolysis temperatures (350, 550, and 800°C) as categoric level. The datasets were analyzed and expressed through a second-order polynomial Equation 2):

$$Y = \beta_0 + \beta_1X_1 + \beta_2X_2 + \beta_3D_1 + \beta_4D_2 + \beta_{11}X_{12} + \beta_{22}X_{22} + \beta_{12}X_1X_2 + \beta_{13}X_1D_1 + \beta_{14}X_1D_2 + \beta_{23}X_2D_1 + \beta_{24}X_2D_2 \quad (2)$$

Where; Y is % COD reduction, X1 and X2 are dose and time, and D1, D2 are dummy variables for temperature. Model adequacy was assessed by ANOVA, and regression effects were visualized through 3D response surfaces. Design-Expert® software (v23.1.6, Stat-Ease Inc., USA) was implemented for optimization.

2.5 Isotherm study

Equilibrium adsorption of COD by phosphate-modified cotton stalk (PMCS) biochar was evaluated at the optimized mixing time and initial COD from the RSM study. Different adsorbent doses were tested, once equilibrium was attained COD_f was analyze to determine the uptake capacity q_e (in mg/g) using (Equation 3);

$$q_e = \frac{(Ci - Ce) * V}{W} \quad (3)$$

Where; C_i (initial) and C_e (equilibrium) concentration of COD (in mg/L), V is volume (in L), and W (adsorbent mass, in g).

To interpret the adsorption process, the data were modelled with Langmuir and Freundlich adsorption isotherm equations. According to the Langmuir model, adsorption is restricted to single monolayer, which is represented as (Equation 4) and Freundlich Model describe heterogenous adsorption and is represented as (Equation 5).

Langmuir Model:

$$\frac{1}{qe} = \frac{1}{qm} + \frac{1}{qmb} \times \frac{1}{Ce} \quad (4)$$

Freundlich Model:

$$\ln (qe) = \ln (k_f) + \frac{1}{n} \ln (Ce) \quad (5)$$

The adsorption constants (a, b, K_f, n) were determined from the respective linear plots, the degree of fit for each model was evaluated with R^2.

2.6 Kinetic study

Adsorption kinetics of COD on PMCS biochar (PCS350, PCS550, PCS800) were studied at optimized dose and initial COD. Batch tests were run at 400 rpm with contact times of 5-180 min. COD was measured at each interval, and the adsorption capacity at given time q_t (mg/g) was determined as per (Equation 6).

$$q_t = \frac{(Ci - Ct) \times V}{W} \quad (6)$$

Where; C_i (initial) and C_t (t, time) COD concentration where, V (in L) is the solution volume, and W (in g) is the mass of biochar. The kinetic data were modelled using pseudo first order (Equation 7) and pseudo-second-order (Equation 8) equations;

Pseudo-1st-Order (PFO) Model:

$$\ln (qe - qt) = \ln qe - k_1 \times (t) \quad (7)$$

Here, q_e (in mg/g) corresponds to adsorption capacity at equilibrium, q_t (in mg/g) indicates adsorption time (t), while k_1 (min^{-1}) is defined well by the pseudo-first-order rate constant.

Pseudo-2nd-Order Model:

$$\frac{t}{qt} = \frac{1}{k2 \times qe^2} + \frac{t}{qe} \quad (8)$$

Where; k_2 (g/mg·min) is the pseudo-second-order rate constant.

3. RESULTS AND DISCUSSION

3.1 BET and SEM analysis results at varied temperature

The available surface per unit mass and morphology of PMCS biochar were greatly influenced by pyrolysis temperature because of structural transition. Values increased from 180 (m^2/g, PCS350) to 450 (m^2/g, PCS550) and 750 (m^2/g, PCS800) due to increase in pore size and volume (Table 2). This enhancement results from devolatilization, where volatile loss leaves a porous carbon skeleton (Díaz et al., 2024). Similar correlations between temperature and pore development have been reported for cotton stalk (300-700°C) and wheat straw (700°C, 400 m^2/g, pore size 2.34 nm) (Muzyka et al., 2023). The highly porous PCS800 facilitates diffusion of dyes and macromolecules such as starch during adsorption.

Table 2. Results of surface area (BET) analysis

Biochar	SBET (m^2/g)	Pore size (Å)	Pore size (in nm)	Pore volume (cm^3/g)
PCS 350	180	14.7985	1.4	0.0193
PCS 550	450	18.5654	1.8	0.0564
PCS 800	750	22.4588	2.2	0.0835

Phosphoric acid activation further promotes pore formation through structural swelling and amplification, explaining the higher porosity in PMCS compared to unmodified biochar (Zhao et al., 2017). Networks were observed in KOH-activated cotton stalk at 900°C.

SEM images of PCS800 at low (5.0 KX) and high (10.0 KX) magnification (Figure 3) reveal hollow, elongated pores that facilitate transport of COD contributing solutes. Similar mesoporous For H_3PO_4 treated biochar, micro/mesopores and fractured sheet-like surfaces have also been reported (Cui et al., 2024) supporting enhanced adsorption performance (Du et al., 2025).

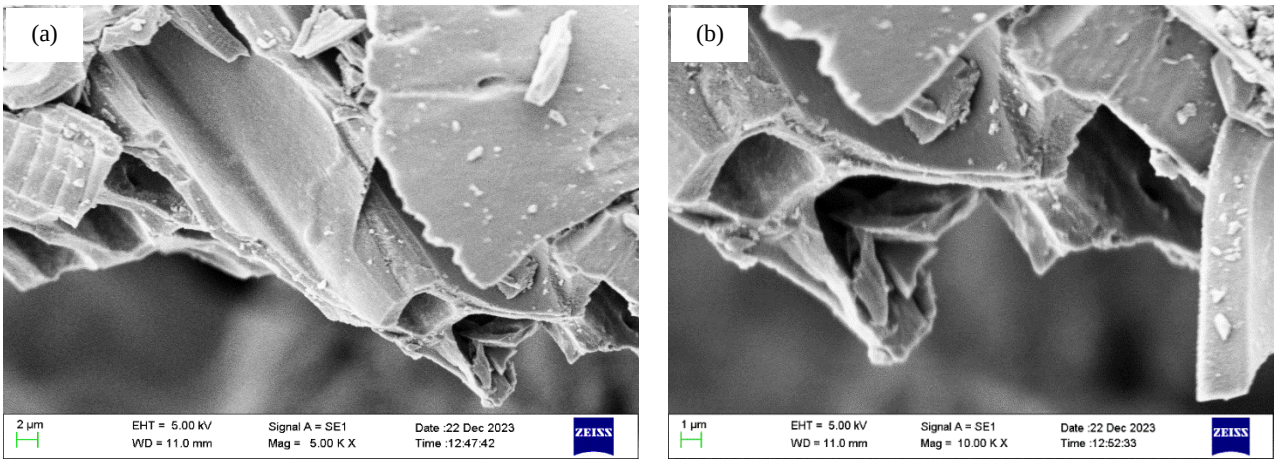

Figure 3. SEM images of PCS800 at (a) low (5.0 KX) and (b) High (10.0 KX) magnification

3.2 Results of change in surface functionality at varied temperature by FTIR

The spectra of PMCS biochar prepared at 350, 550, and 800°C (Figure 4(a-c)) showed a systematic development of surface functionalities with temperature. All the biochar showed deoxygenation and aromatization with redistribution of phosphate functionalities explain the transition from hydrogen bond dominated interactions to π-π interactions on more graphitized domains and phosphate modified biochar as mentioned in Table 3.

Here, FTIR graphs showed of carbonyl groups, weakening of aliphatic C-H, and stabilization of phosphate functionalities with increasing pyrolysis temperature. Phosphoric acid treated rice husk has also been documented the same results for weakening of C-H bands at higher pyrolysis temperature (Zeng et al., 2022). Whereas walnut shell (Heidarinejad et al., 2020), and sugarcane bagasse derived biochar (Kamran et al., 2022) has resulted that confirming that phosphate activation governs both surface chemistry and thermal stability across diverse biomass precursors.

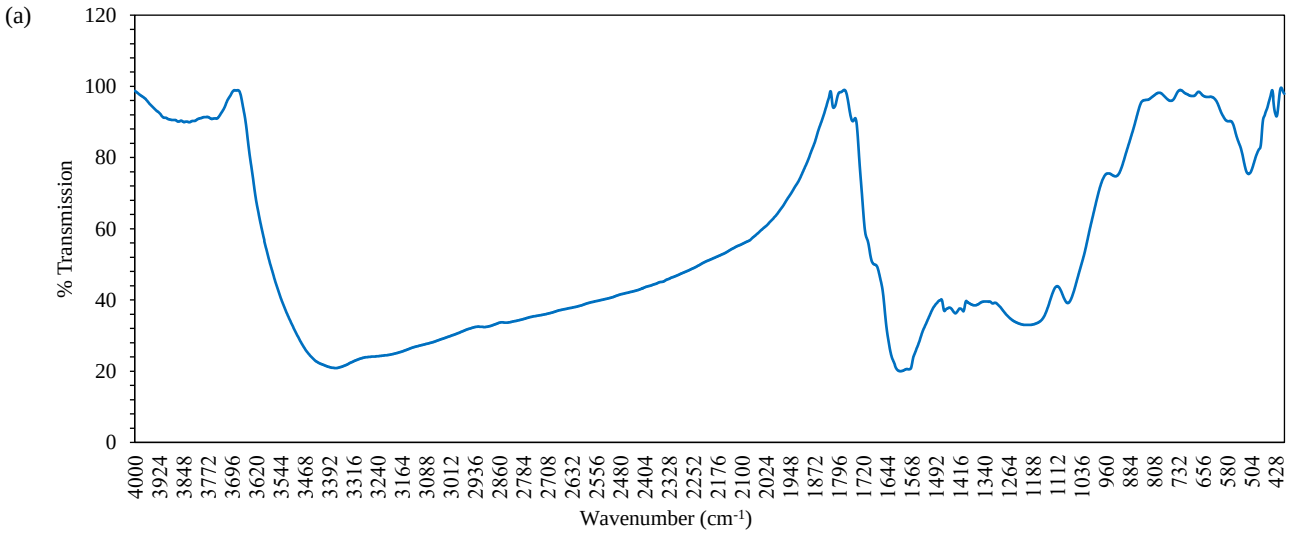

Figure 4. FTIR graph of phosphate modified cotton stalk biochar (a) PCS350, (b) PCS550, (c) PCS800

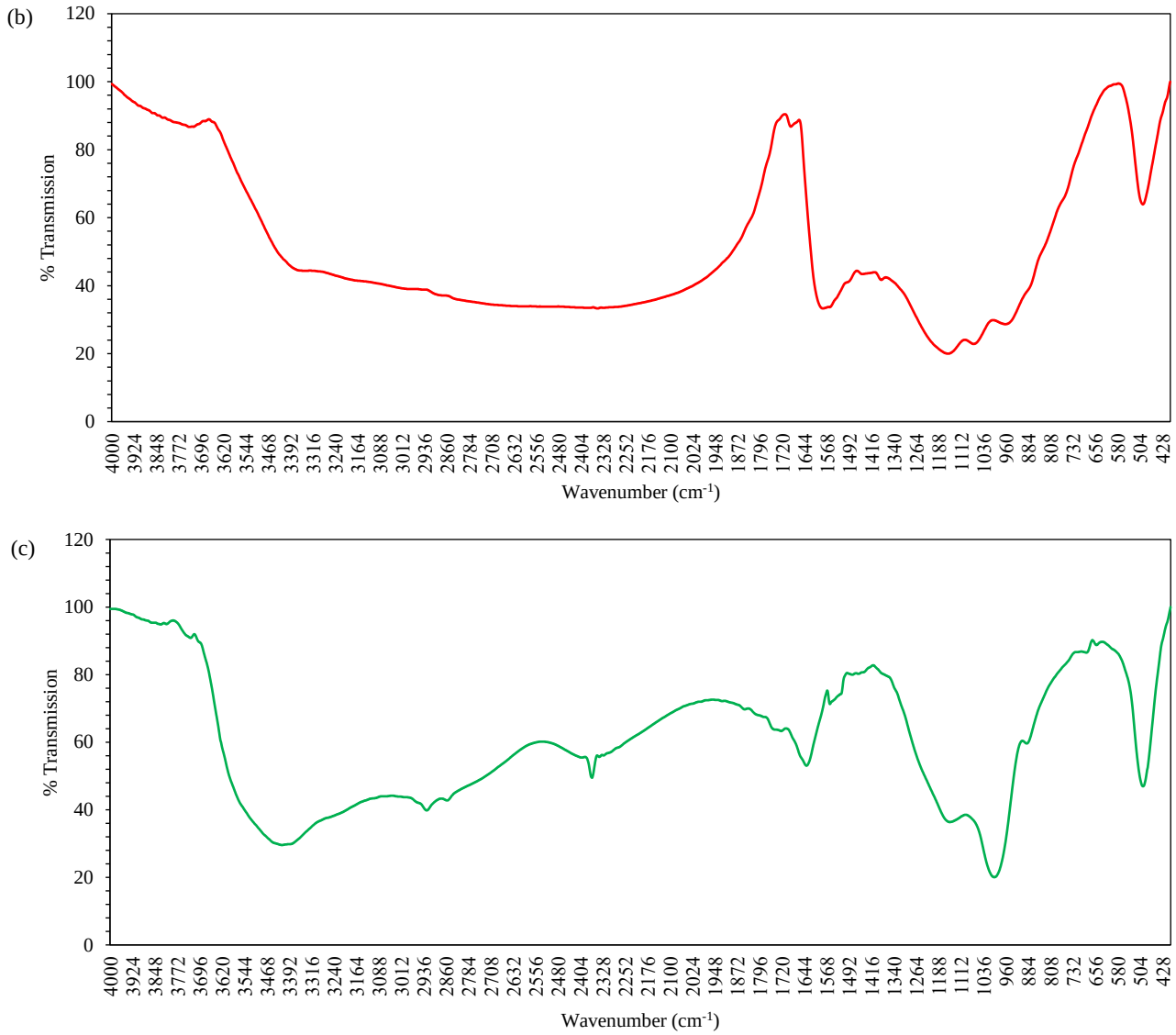

Figure 4. FTIR graph of phosphate modified cotton stalk biochar (a) PCS350, (b) PCS550, (c) PCS800

Table 3. Change in the functional groups in phosphate modified cotton stalk derived biochar

Wavenumber (cm^{-1})	Functional group	PCS350	PCS550	PCS800	Key process
3,300-3,500	O-H / N–H stretching	Strong (3370)	Narrow, shifted (3758)	Weak (3416)	De-hydroxylation, loss of H-bonding
2,925-2,850	Aliphatic C-H	Present	Reduced	Absent	Chain cracking, aromatization
1,700-1,800	C=O stretching	Present (1690)	Weakened (1636)	Absent	Decarboxylation, conjugation
1,580-1,620	Aromatic C=C	Weak	Stronger (1590)	Strong (1556)	Aromatization, ring condensation
1,400-1,450	C-H / phenolic O-H	Present (1445)	Reduced	Absent	Phenolic loss, condensation
1,150-1,200	P=O stretching	Present (1155)	Strong (1156)	Shifted (1148)	Phosphorylation, esterification
1,000-1,070	P-O-C stretching	1037	1068	998	Phosphate-C bonding, stabilization
~915	P-O-P (pyrophosphate)	Absent	Weak	Strong	Polycondensation, pyrophosphate
750-760	Aromatic C-H bending	Present	Present	Retained	Aromaticity, graphitization

3.3 Model performance and factor effects

The results of the total 33 results of experiments designed as per (Equation 2) are provided as supplementary material (Table S1) with this manuscript. Among various tested models, the quadratic model suggested by Design-Expert 23.1.6.0 was selected based on its superior statistical fit. The regression analysis yielded high coefficients of determination (R^2=0.9897, adjusted R^2=0.9897, and predicted R^2=0.9828), with less than 2% difference between adjusted and predicted R^2, confirming the adequacy of the model (Khan et al., 2021; Yusuff et al., 2023). The strong correlation between experimental and predicted COD reduction is mentioned in scattered plot Predicted vs actual for % COD reduction Figure 5, supporting the robustness of the quadratic equation (Equation 9) for process predictions.

$$\% \text{ COD Reduction} = 55.65 + 5.97\,A + 8.28\,B - 14.84\,C[1] - 2.90\,C[2] - 0.0417\,AB + 1.86\,AC[1] - 1.89\,AC[2] + 2.31\,BC[1] - 2.19\,BC[2] - 2.09\,A^2 + 1.33\,B^2 \quad (9)$$

The regression coefficients revealed that adsorbent dose (A) and mixing time (B) had significant positive effects on COD reduction, while the quadratic term of adsorbent dose was negative, indicating diminishing efficiency at higher levels. This trend is consistent with earlier adsorption studies reporting overdosing effects due to aggregation and active site masking (Beyan et al., 2021; Vakili et al., 2023). Interaction terms indicated that the adsorbent dose and mixing time (AB) interaction was antagonistic, while mixing time and temperature (BC) showed a synergistic effect. Here mixing time is the most crucial parameter, which aligns with previous reports highlighting the importance of contact time for molecular transport in adsorption studies. (Soleimani et al., 2023).

3.4 ANOVA results and model adequacy

The quadratic model was assessed through ANOVA (Table 4), and the results demonstrated the strong statistically significance ($p<0.0001$), that showed the selected factors adequately explained the observed variability in COD reduction. The adsorbent dose (A) and mixing time (B) alone and their quadratic terms were highly significant, while interaction effects AB have $p>0.05$ that is non-significant and negligible effect on COD removal. Since the lack of fit test returned $p>0.05$, the residual error was considered random supporting the adequacy of model in representing the observed data.

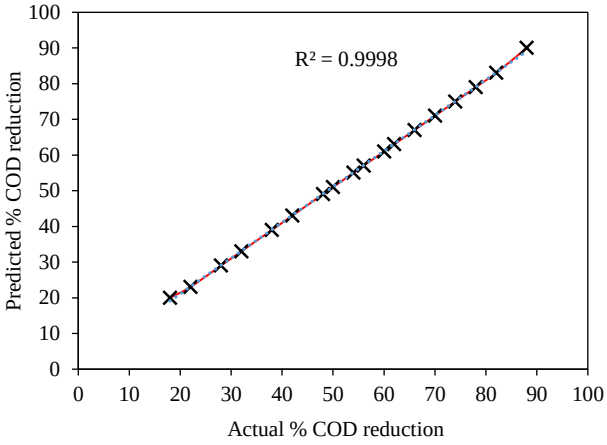

Figure 5. Scattered plot predicted vs actual for % COD reduction

3.5 Response surface evaluation by 3D plot

The three-dimensional response surface plots illustrated in Figure 6(a-c) the collective effects of adsorbent dose and mixing time on variation in COD reduction at different pyrolysis levels. COD removal increased with adsorbent dose but plateaued at higher values, indicating site saturation. Mixing time also enhanced removal, particularly at intermediate doses, highlighting its role in mass transfer. For PCS350 as per Figure 6(a), maximum COD removal reached between 55-60%, with a relatively flat surface suggesting a near-linear relationship between dose and time. PCS550 as showed in Figure 6(b) a flatter surface, indicating equilibrium conditions with limited improvement beyond approx. 62%. In contrast, PCS800 as per Figure 6(c) displayed strong positive interactions of dose and mixing time, achieving >80% COD removal at 10 g/L and 50 min.

These plots confirm the influence of pyrolysis temperature on adsorbent properties governing multicomponent adsorption. PCS800 achieved the highest efficiency (76.7% COD removal at 6.43 g/L, 33 min), while PCS550 offered balanced performance. Comparable studies, such as sugarcane bagasse activated carbon (96% COD removal at optimized conditions), also emphasize pH as a key factor (Beyan et al., 2021).

Table 4. ANOVA output of model

Factor	Sum of squares (SS)	Degree of freedom (df)	Mean square (MS)	F-ratio	Probability (P)
Model	7,995.28	11	726.84	279.26	<0.0001
A	642.01	1	642.01	246.66	<0.0001
B	1,233.39	1	1,233.39	473.87	<0.0001
C	5,978.74	2	2,989.37	1,148.53	<0.0001
AB	0.0208	1	0.0208	0.0080	0.9296
AC	42.19	2	21.10	8.11	0.0025
BC	60.86	2	30.43	11.69	0.0004
A^2	33.24	1	33.24	12.77	0.0018
B^2	13.35	1	13.35	5.13	0.0342
Residuals	54.66	21	2.60		
Lack of fit	48.13	15	1.09	2.95	0.0946
Pure error	6.53	6			
Cor Total	8,049.94	32			

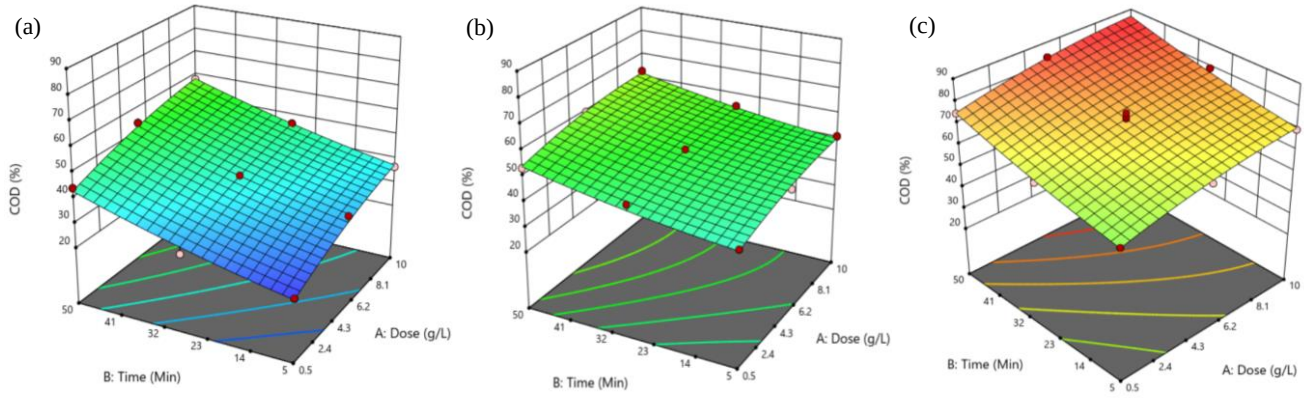

Figure 6. 3D Surface plot of PMCS biochar (a) 350, (b) 550 and (c) 800

3.6 Validation of the model results on real textile wastewater

To validate the CCD-RSM model, optimized conditions were applied to partially treated textile effluent (COD 200 mg/L and BOD 30 mg/L) from identified CETP of Ahmedabad. The optimized biochar (i.e., PCS800) was tested with 6.43 g/L of adsorbent dose and 33 min of mixing time at 150 rpm under batch adsorption and achieved 60% of COD reduction and >90% decolorization as shown in Figure 7.

Figure 7. Experimental photograph of treated real textile wastewater

The high efficiency for colour removal was due to chromophore part of dye adsorption, while COD reduction was achieved due to uptake of organic contaminants present in it. The treated effluent showed final COD<88 mg/L with complete colour removal. Unlike the synthetic wastewater, where the COD contributing components (EBT dye, starch and salts) are well defined, real textile wastewater contains unknown and variable dye mixtures, surfactants, sizing agents and auxiliary chemicals. Because different dyes exhibit different adsorption mechanisms and optimum pH ranges (Aritonang et al., 2025). The heterogeneity of the real effluent reduces the overall removal efficiency compared to the controlled synthetic matrix as reported in previous studies (Yaseen and Scholz, 2019; Castillo-Suárez et al., 2023). The COD removal performance of PMCS was compared with various biochar reported in literature Table 5.

Table 5. Recent studies on removal of chemical oxygen demand (COD) with biochar

Biochar	Feed stock modification	Wastewater type	% COD removal efficiency	References
Cotton Stalk	H_3PO_4-activated cotton stalk at 800°C	Textile wastewater	60	Present work
Walnut shell	Chemically activated with $FeCl_3$	Municipal wastewater	63.1	Rajabian et al. (2024)
Sugarcane baggase	Physical activation	Textile wastewater	55	da Costa et al. (2021)
Rice husk	$ZnCl_2$-activated rice husk	Wastewater	45.9	Mortada et al. (2023)
Corn stalk	$ZnCl_2$-activated corn stalk	Hospital wastewater	71.4	Walanda et al. (2022)
Lemon peels	$ZnCl_2$-activated at 800°C	Oil palm wastewater	82.72	Ahmad Ridzuan et al. (2025)
Tea waste	H_3PO_4 treated and H_2O_2 oxidized	Produced water	95.5	Khurshid et al. (2021a)

Previous studies show that COD removal using biochar varies widely, generally between 45-95%, depending on feedstock, activation method, and wastewater complexity. Activated sugarcane bagasse and rice-husk biochar achieved 55% and 45.9% COD removal in textile and industrial wastewater, respectively, while $FeCl_3$-activated walnut shell biochar reached 63.1% in municipal wastewater. Although highly modified systems such as tea waste biochar achieved 95.5% removal in produced water, these were tested on less complex matrices. In comparison, the 60% COD removal obtained with PMCS in real textile wastewater is competitive and aligns with the range reported for real, multi-component wastewaters, confirming the suitability of PMCS under practical treatment conditions. Hence, application of PMC treated effluent is safe for discharge and suitable for reuse when combined with advanced treatments like ultrafiltration (UF) or reverse osmosis (RO).

3.7 Isotherm results

The Langmuir and Freundlich adsorption isotherms of PCS350, PCS550, and PCS800 for % COD removal are shown in Figure 8(a-f). The corresponding isotherm constants are summarized in Table 6.

As shown in the Figure 8(a) for the PCS350, Langmuir fit was poor (R^2=0.7521, q_{max}=183.8 mg/g, K_L=0.0024 L/mg), indicating non-uniform adsorption, whereas Freundlich fit was stronger (R^2=0.9573, K_f=1.43 $mg^{-1}\frac{1}{n} \times L\frac{1}{n}.g^{-1}$ n=1.42) as shown in Figure 8(d), confirming favourable multilayer adsorption via electrostatic attraction, H-bonding and pore filling. For PCS550, Langmuir gave R^2=0.8864 with q_{max}=126.1 mg/g, K_L=0.0061 L/mg (Figure 8(b)), while Freundlich showed better correlation (R^2=0.8663, K_f=4.46 $mg^{-1}\frac{1}{n} \times L\frac{1}{n}.g^{-1}$, n=1.93) Figure 8(e), again suggesting heterogeneous adsorption, consistent with cotton stalk biochar reported by (Gao et al., 2021). In contrast, PCS800 fitted best to Langmuir (R^2=0.9994, q_{max}=90.2 mg/g, K_L=0.049 L/mg) as per Figure 8(c), while Freundlich (K_f=32.2 $mg^{-1}\frac{1}{n} \times L\frac{1}{n}.g^{-1}$, n=5.52, R^2=0.8715) also confirmed favourable adsorption as per Figure 8(f).

Table 6. Summary of isotherm constants

Biochar	Langmuir constants			Freundlich Constants		
	q_{max} (mg/L)	K_L (L/mg)	R^2	K_f ($mg^{-1} \cdot L \cdot g^{-1}$)	n	R^2
PCS350	183.8	0.0024	0.7521	1.43	1.42	0.9573
PCS550	126.1	0.0061	0.8864	4.46	1.93	0.8663
PCS800	90.2	0.0490	0.9994	32.2	5.52	0.8715

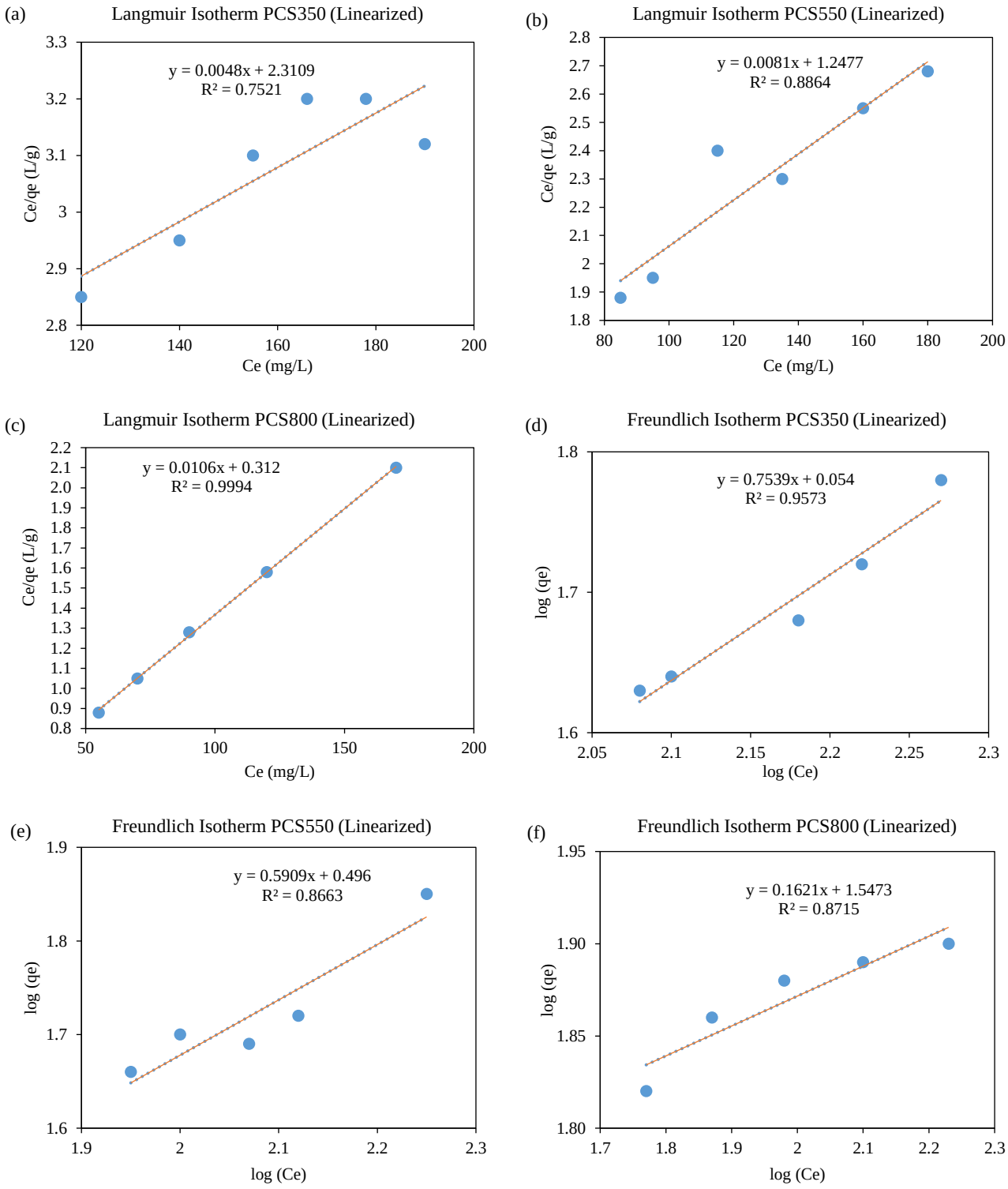

Figure 8. Adsorption isotherm at varied temperatures Langmuir at (a) 350°C, (b) 550°C, (c) 800°C; Freundlich at (d) 350°C, (e) 550°C, (f) 800°C

This transition can be attributed to the development of surface chemistry and porosity with pyrolysis temperature (Park et al., 2019). At 350°C, the biochar surface contains abundant oxygenated groups (-COOH, -OH) and a highly disordered carbon matrix, which produce heterogeneous surface energies capable of interacting with a wide spectrum of organic molecules. This explains the higher Langmuir q_{max} of PCS350, as these polar sites readily bind both EBT dye and larger macromolecular components i.e. starch through hydrogen bonding, electrostatic attraction and weak van der Waals forces. At 550°C, partial aromatization and moderate pore development create a balance of polar and aromatic domains, supporting mixed adsorption processes and resulting in intermediate q_{max} and model behaviour. In contrast, PCS800 exhibits highly aromatized carbon, greatly reduced surface polarity and well developed microporosity, favouring uniform monolayer adsorption through π-π interactions and hydrophobic effects. These interactions strongly promote the uptake of smaller aromatic dye molecules such as EBT, while the reduced number of polar sites and narrower pores restrict adsorption of bulky starch molecules, explaining the lower q_{max} but higher K_L observed for PCS800. This progressive shift in adsorption pathway from heterogeneous multilayer adsorption to uniform monolayer adsorption is fully consistent with the kinetic trend (PFO → PSO) and reflects increasing structural refinement and selectivity with pyrolysis temperature.

3.8 Kinetic results

The kinetic behaviour of COD adsorption onto PCS350, PCS550, and PCS800 was evaluated using the pseudo first order (PFO) and pseudo second order (PSO) models. These models help to determine whether the rate controlling step is primarily diffusion controlled or surface-interaction controlled. The Figure 9 showed the kinetic fit while Table 7 summarizes the fitted kinetic parameters.

Table 7. Summary of fitted kinetic parameters

Biochar	Pseudo first order (PFO) fitted parameters			Pseudo second order (PSO) fitted parameters		
	q_e (mg/g)	k_1 (min^{-1})	R^2	q_e (mg/g)	k_2 (g/mg·min)	R^2
PCS350	24	0.0582	0.988	24	2.54×10^{-3}	0.988
PCS550	29.6	0.0755	0.976	--	3.35×10^{-3}	0.995
PCS800	--	0.0814	0.976	30	3.41×10^{-3}	0.994

For PCS350, an initial rapid phase lasting 30-45 min was followed by equilibrium at around 60-90 min (q_e≈24 mg/g). PFO fit slightly better (R^2=0.988, k_1=0.0582 min^{-1}) than PSO (R^2=0.988, $k_2=2.54\times10^{-3}$ g/mg·min), indicating diffusion-controlled physisorption on a heterogeneous surface, consistent with earlier low-temperature biochar where external diffusion dominates.

The results of the PFO and PSO kinetic results for COD uptake onto PMCSB at varied temperature (Jegan et al., 2020; Li et al., 2023). Similarly, for PCS550, COD reduction reached equilibrium at ~90 min with PSO showing superior fit (R^2=0.995, q_e=29.6 mg/g, $k_2=3.35\times10^{-3}$ g/mg·min) compared to PFO (R^2=0.976, k_1=0.0755 min^{-1}). This indicates stronger surface interactions and site-specific adsorption, in agreement with previous COD adsorption studies on biochar (Dada et al., 2021; Khurshid et al., 2021b; Patel, 2024)

PCS800 exhibited the highest capacity (q_e=30 mg/g) and equilibrium at ~120 min. PSO fitted best (R^2=0.994, $k_2=3.41\times10^{-3}$ g/mg·min), while PFO fit was weaker (R^2=0.937). The dominance of PSO at higher temperature reflects increased aromaticity, pore development, and specific binding, as similarly reported for 800°C biochar from soybean straw and orange peel.

Overall, the adsorption behaviour across PCS350, PCS550, and PCS800 reflects the progressive structural evolution of biochar with increasing pyrolysis temperature. PCS350, rich in oxygenated functional groups and possessing limited porosity, exhibits diffusion-controlled physisorption and heterogeneous multilayer adsorption, consistent with its PFO and Freundlich fits. As temperature increases to 550°C, partial aromatization and moderate pore development introduce a balance of polar and aromatic sites, yielding mixed kinetic behaviour but a stronger PSO fit due to the emergence of more reactive adsorption sites. PCS800, characterized by extensive aromatization, reduced surface polarity and well-developed microporosity,

supports uniform, site-specific adsorption dominated by π-π and hydrophobic interactions, which aligns with its strong Langmuir and PSO fits. Thus, the transition from PFO to PSO and Freundlich to Langmuir is a direct consequence of increasing aromaticity, pore accessibility and the loss of surface oxygenated groups during pyrolysis (Elnour et al., 2019; Tomczyk et al., 2020). Similarly low cost biochar such as rice husk, tea waste and biogas residue derived biochar reported the same trend for COD removal by Langmuir behaviour and pseudo second order which can be explained by chemisorption rather than physical forces of adsorption (Khurshid et al., 2021a; Mortada et al., 2023; Wang et al., 2023).

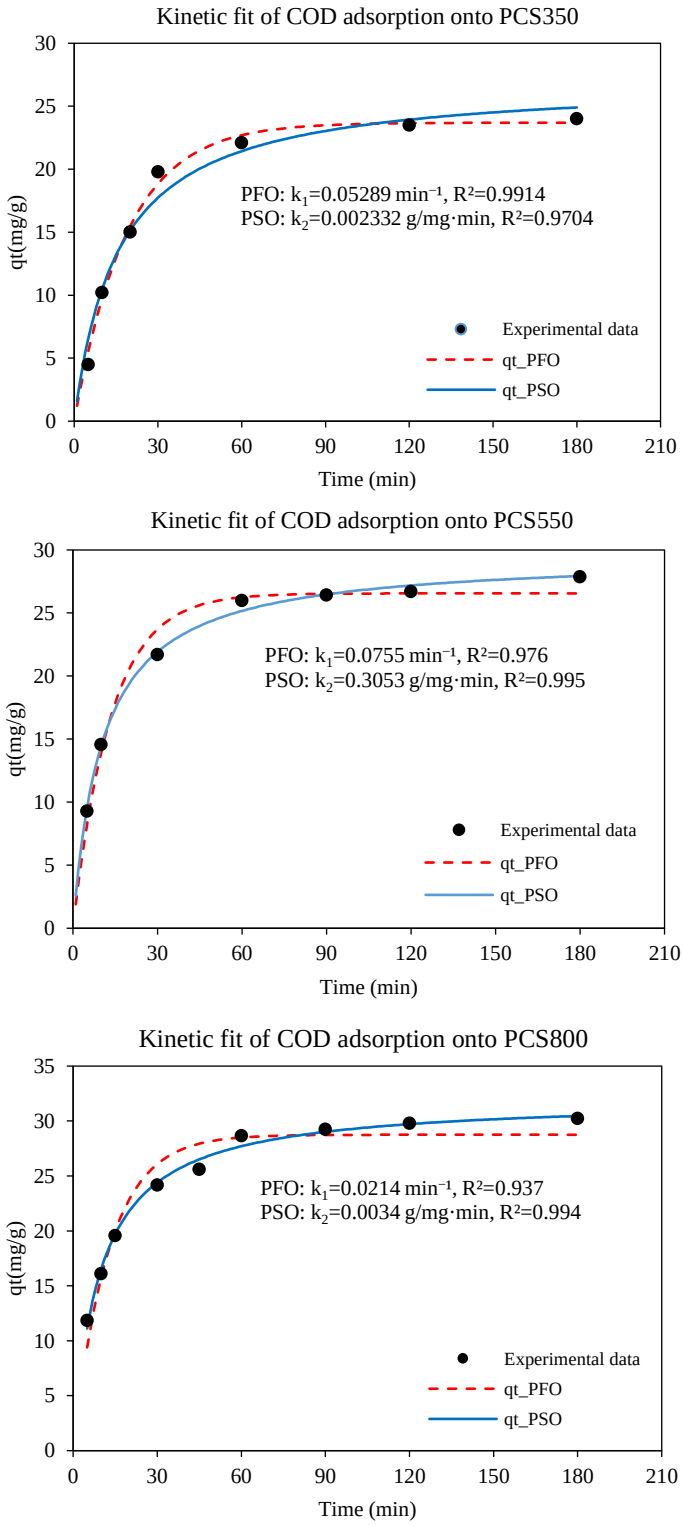

Figure 9. Kinetic fit graphs for PFO and PSO of (a) PCS350, (b) PCS550, (c) PCS80

3.9 Proposed adsorption mechanism in multi component synthetic wastewater

As the synthetic wastewater contains EBT dye, starch, and dissolved salts, the adsorption behaviour must be interpreted in a multi-component context. EBT, an anionic aromatic dye, binds preferentially to PCS550 and PCS800 through π-π stacking, hydrophobic interactions, and electrostatic attraction when pH < pHpzc, owing to their more developed aromatic domains. Similar interaction pathways have been reported for EBT adsorption onto carbonaceous materials, where monolayer adsorption on aromatic surfaces and strong dye carbon affinity were observed for activated carbon derived from rice hulls (de Luna et al., 2013). Likewise, tea-waste biochar has shown that π-π stacking, hydrophobic forces, van der Waals interactions, and pH-dependent electrostatic effects govern EBT uptake, with equilibrium behaviour following Langmuir and kinetics following pseudo-second-order models (Bansal et al., 2020). These literature results are consistent with the interaction mechanisms proposed for PMCS.

In contrast to EBT, starch being a large non-aromatic polysaccharide adsorbs mainly through hydrogen bonding and pore entrapment and therefore shows higher uptake on PCS350, which retains abundant oxygenated functional groups and larger accessible pores. The salts present (NaCl, Na_2CO_3, $NaHCO_3$) influence ionic strength and partially shield surface charges, reducing electrostatic interactions while enhancing hydrophobic pathways.

The pHpzc values of PCS350, PCS550, and PCS800 (5.8, 6.2, and 6.7) indicated in Figure 10, that at the operating pH 7 all surfaces are weakly negative. This behaviour aligns with (Ndoun et al., 2023), who reported that lignocellulosic biochar remain negatively charged over environmentally relevant pH ranges, with zeta potential becoming more negative as pH increases and typical pHpzc values below 4. Their findings support the interpretation that at neutral pH, electrostatic repulsion toward anionic dyes such as EBT is expected, making π-π and hydrophobic interactions the dominant pathways for adsorption.

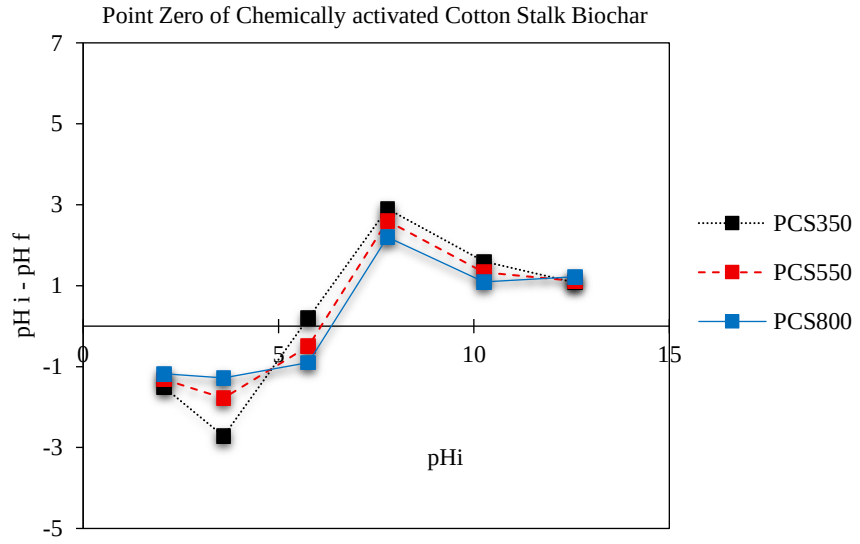

Figure 10. Point of zero charge graph of PCS350, PCS550, and PCS800

Hence, adsorption of EBT in this multi-component matrix is governed mainly by π-π stacking, hydrophobic attraction, and localized electrostatic interactions, whereas starch removal relies on polar functional groups. This selective and competitive site occupation explains why PCS800 shows higher affinity (high KL) despite lower q_{max}, while PCS350 exhibits higher theoretical capacity but weaker specific binding. These interaction pathways are summarised in Figure 11, which provides a graphical representation of the proposed adsorption mechanism. At higher temperature pore development and partial aromatization enhance pore filling and mixed interactions.

At 800°C, stabilized phosphate functionalities provide acidic sites, while graphitic domains favour π-π stacking and hydrophobic interactions, consistent with Langmuir monolayer adsorption and pseudo-second-order kinetics. Thus, synergistic effects of surface chemistry and pore structure govern COD reduction by PMCS.

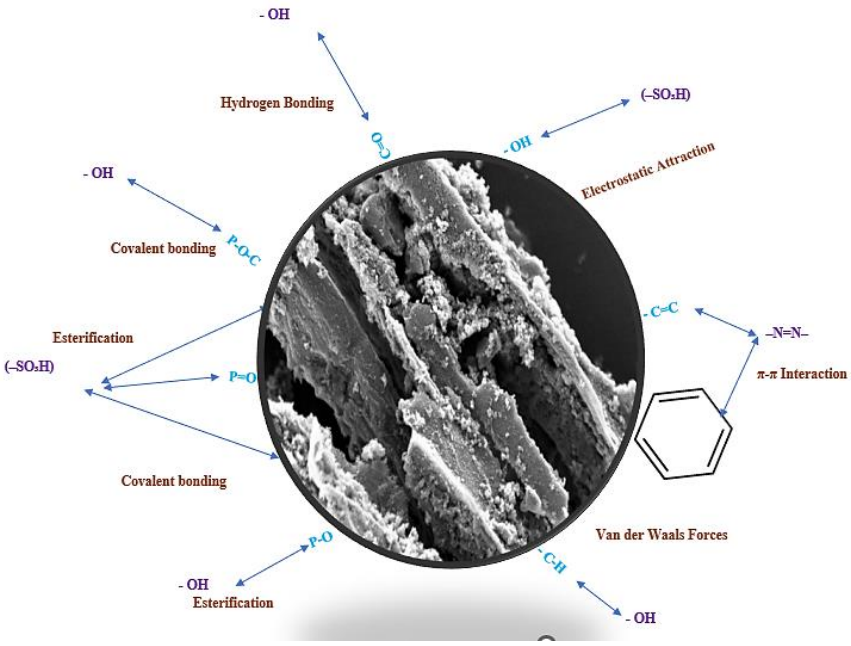

Figure 11. Possible mechanism of PCS800 in multi component synthetic wastewater

4. CONCLUSION

This study demonstrates a scalable circular economy pathway for converting cotton stalk into phosphate modified biochar (PMCS) and relates pyrolysis temperature to COD removal from textile wastewater. Using Central Composite Design, optimization revealed that adsorption shifted from heterogeneous multilayer behaviour at 350-550°C (best described by Freundlich, R^2=0.85-0.95) to uniform monolayer adsorption at 800°C (Langmuir, R^2=0.999). Kinetic analysis showed pseudo-first-order control at 350°C (k_1=0.0582 min^{-1}) and pseudo-second-order at 550-800°C (k_2=0.0033-0.0034 g/mg·min; R^2=0.994-0.995). Optimization achieved 76.7% COD reduction with PCS800 at pH 7, dose 6.43 g/L, and 33 min mixing, attributed to micropore driven uptake, while PCS550 offered the most balanced removal of small and large organics. The transition in behaviour reflects progressive aromatization, micropore development, and loss of labile oxygen groups with increasing temperature. Practically, PCS550 is recommended for treating complex effluents, whereas PCS800 is suited for polishing applications. Future work should extend this framework to column studies, regeneration, and techno-economic assessment to fully establish circular economy benefits. Overall, phosphate modification of cotton stalk biochar provides a technically rigorous and sustainable route for textile wastewater treatment, aligning waste valorization with environmental protection.

ACKNOWLEDGEMENTS

The authors sincerely acknowledge Central University, Gandhinagar for providing the laboratory facilities and support in conducting SEM and FTIR analyses, which were essential for this research work. The authors also thank the faculty members of the Department of Environmental Engineering, L.D. College of Engineering for their continuous encouragement, valuable suggestions, and support throughout the study.

AUTHOR CONTRIBUTIONS

Vishwa Vraj Shah, Ph.D. scholar, contributed to the conceptualization of the study, adoption of methodology, execution of research work, and preparation of the manuscript. Dr. Narendra Madhavlal Patel reviewed the manuscript and provided critical suggestions for its improvement.

DECLARATION OF CONFLICT OF INTEREST

The authors declare no conflict of interest.

REFERENCES

Agyemang E, Ofori-Dua K, Dwumah P, Forkuor JB. Towards responsible resource utilization: A review of sustainable vs. unsustainable reuse of wood waste. PLoS One 2024;19(12):e0312527.

Ahmad I, Farwa U, Khan ZUH, Imran M, Khalid MS, Zhu B, et al. Biosorption and health risk assessment of arsenic contaminated water through cotton stalk biochar. Surfaces and Interfaces 2022;29:Article No. 101806.

Ahmad Ridzuan NAN, Kasmuri N, Hamid KA, Nayono SE, Mojiri A, Selim H, et al. Remediation of palm oil mill effluent using citrus peel–based activated carbon. IOP Conference Series: Earth and Environmental Science 2025;1548:Article No. 1012030.

Ali J, Bakhsh EM, Hussain N, Bilal M, Akhtar K, Fagieh TM, et al. A new biosource for synthesis of activated carbon and its potential use for removal of methylene blue and eriochrome black T from aqueous solutions. Industrial Crops and Products 2022;179:Article No. 114676.

Arampatzidou AC, Voutsa D, Deliyanni EA, Matis KA. Adsorption of endocrine disruptor bisphenol A by carbonaceous materials: Influence of their porosity and specific surface area. Desalin Water Treat 2017;76:232-40.

Aritonang B, Ritonga AH, Harefa K, Herlina H. Reduction of BOD, COD, and TSS in textile wastewater using bentonite activated charcoal adsorbent. Jurnal Farmsimed 2025;7:381-9.

Arous F, Pinelli D, Bessadok S, Boudagga S, Hamdi C, Li W, et al. Performance and cost-benefit analyses of an integrated process for advanced treatment of highly saline textile wastewater at a semi-industrial scale. Euro-Mediterranean Journal for Environmental Integration 2024;9:605-20.

Bansal M, Patnala PK, Dugmore T. Adsorption of eriochrome Black-T(EBT) using tea waste as a low cost adsorbent by batch studies: A green approach for dye effluent treatments. Current Research in Green and Sustainable Chemistry 2020;3:Article No. 100036.

Beyan SM, Prabhu SV, Sissay TT, Getahun AA. Sugarcane bagasse based activated carbon preparation and its adsorption efficacy on removal of BOD and COD from textile effluents: RSM based modeling, optimization and kinetic aspects. Bioresource Technology Reports 2021;14:Article No. 100664.

Bhuvaneshwari S, Hettiarachchi H, Meegoda JN. Crop residue burning in India: Policy challenges and potential solutions. International Journal of Environmental Research and Public Health 2019;16(5):Article No. 832.

Castillo-Suárez LA, Sierra-Sánchez AG, Linares-Hernández I, Martínez-Miranda V, Teutli-Sequeira EA. A critical review of textile industry wastewater: Green technologies for the removal of indigo dyes. International Journal of Environmental Science and Technology 2023;20:10553-90.

Colmenares JC, Varma RS, Lisowski P. Sustainable hybrid photocatalysts: Titania immobilized on carbon materials derived from renewable and biodegradable resources. Green Chemistry 2016(21);18:5736-50.

da Costa WKOC, Gavazza S, Duarte MMMB, Freitas SKB, de Paula NTG, Paim APS. Preparation of activated carbon from sugarcane bagasse and removal of color and organic matter from Real Textile Wastewater. Water, Air, and Soil Pollution 2021;232:Article No. 358.

Cui Q, Huang Y, Ma X, Li S, Bai R, Li H, et al. Research on the adsorption mechanism and performance of cotton stalk-based biochar. Molecules 2024;29(24):Article No. 5841.

Dada AO, Adekola FA, Odebunmi EO, Ogunlaja AS, Bello OS. Two-three parameters isotherm modeling, kinetics with statistical validity, desorption and thermodynamic studies of adsorption of Cu(II) ions onto zerovalent iron nanoparticles. Scientific Reports 2021;11:Article No. 16454.

Deshpande MV, Kumar N, Pillai D, Krishna VV, Jain M. Greenhouse gas emissions from agricultural residue burning have increased by 75% since 2011 across India. Science of the Total Environment 2023;904:Article No. 166944.

Dhanya MS. Perspectives of agro-waste biorefineries for sustainable biofuels. In: Nandabalan YK, Garg VK, Labhsetwar NK, Singh A, editors. Zero Waste Biorefinery. Energy, Environment, and Sustainability. Singapore: Springer; 2022. p. 207-32.

Díaz B, Sommer-Márquez A, Ordoñez PE, Bastardo-González E, Ricaurte M, Navas-Cárdenas C. Synthesis methods, properties, and modifications of biochar-Based materials for wastewater treatment: A review. Resources 2024;13:Article No. 8.

Dowlatshah S, Hay AO, Noreng L, Hansen FA. A practical tutorial for optimizing electromembrane extraction methods by response surface methodology. Advances in Sample Preparation 2025;14:Article No. 100170.

Du K-Q, Li J-F, Farid MA, Wang W-H, Yang G. Preparation of high-efficient phosphoric acid modified biochar toward ciprofloxacin removal from wastewater. Industrial Crops and Products 2025;226:Article No. 120649.

Elnour AY, Alghyamah AA, Shaikh HM, Poulose AM, Al-Zahrani SM, Anis A, et al. Effect of pyrolysis temperature on biochar microstructural evolution, physicochemical characteristics, and its influence on biochar/polypropylene composites. Applied Sciences 2019;9:Article No. 1149.

Gao L, Li Z, Yi W, Li Y, Zhang P, Zhang A, et al. Impacts of pyrolysis temperature on lead adsorption by cotton stalk-derived biochar and related mechanisms. Journal of Environmental Chemical Engineering 2021;9(4):Article No. 105602.

Grover D, Chaudhry S. Ambient air quality changes after stubble burning in rice-wheat system in an agricultural state of India. Environmental Science and Pollution Research 2019;26:20550-9.

He M, Xu Z, Hou D, Gao B, Cao X, Ok YS, et al. Waste-derived biochar for water pollution control and sustainable development. Nature Reviews Earth and Environment 2022;3:444-60.

Heidarinejad Z, Dehghani MH, Heidari M, Javedan G, Ali I, Sillanpää M. Methods for preparation and activation of activated carbon: A review. Environmental Chemistry Letters 2020;18:393-415.

Hussain M, Imran M, Abbas G, Shahid M, Iqbal M, Naeem MA, et al. A new biochar from cotton stalks for As (V) removal from aqueous solutions: its improvement with H_3PO_4 and KOH. Environmental Geochemistry and Health 2020;42:2519-34.

Jegan J, Praveen S, Bhagavathi Pushpa T, Gokulan R. Sorption kinetics and isotherm studies of cationic dyes using groundnut (*Arachis hypogaea*) shell derived biochar a low-cost adsorbent. Applied Ecology and Environmental Research 2020;18(1):1925-39.

Kamran U, Bhatti HN, Noreen S, Tahir MA, Park S-J. Chemically modified sugarcane bagasse-based biocomposites for efficient removal of acid red 1 dye: Kinetics, isotherms, thermodynamics, and desorption studies. Chemosphere 2022;291:Article No. 132796.

Khalid U, Inam MA. The influence of pyrolysis temperature on the performance of cotton stalk biochar for hexavalent chromium removal from wastewater. Water, Air, and Soil Pollution 2024;235:Article No. 114.

Khan H, Hussain S, Hussain SF, Gul S, Ahmad A, Ullah S. Multivariate modeling and optimization of Cr(VI) adsorption onto carbonaceous material via response surface models

assisted with multiple regression analysis and particle swarm embedded neural network. Environmental Technology and Innovation 2021;24:Article No. 101952.

Khurshid H, Mustafa MRU, Rashid U, Isa MH, Ho YC, Shah MM. Adsorptive removal of COD from produced water using tea waste biochar. Environmental Technology and Innovation 2021a;23:Artilce No. 101563.

Khurshid H, Mustafa MRU, Rashid U, Isa MH, Ho YC, Shah MM. Adsorptive removal of COD from produced water using tea waste biochar. Environmental Technology and Innovation 2021b;23:Article No. 101563.

Kwarciak-Kozłowska A, Fijałkowski KL. Efficiency assessment of municipal landfill leachate treatment during advanced oxidation process (AOP) with biochar adsorption (BC). Journal of Environmental Management 2021;287:Article No. 112309.

Li L, Zhang H, Liu Z, Su Y, Du C. Adsorbent biochar derived from corn stalk core for highly efficient removal of bisphenol A. Environmental Science and Pollution Research 2023;30(30):74916-27.

Li T, Li J-P, Li Z-P, Cheng X-W. Eco-friendly modified biochar for phosphate removal: Adsorption mechanism and application in pressed vegetable wastewater treatment. Environmental Engineering Science 2024a;41:401-12.

Li R, Zhang C, Hui J, Shen T, Zhang Y. The application of P-modified biochar in wastewater remediation: A state-of-the-art review. Science of the Total Environment 2024b;917:Article No. 170198.

Liu Q, Li D, Cheng H, Cheng J, Du K, Hu Y, et al. High mesoporosity phosphorus-containing biochar fabricated from Camellia oleifera shells: Impressive tetracycline adsorption performance and promotion of pyrophosphate-like surface functional groups (C-O-P bond). Bioresource Technology 2021;329:Article No. 124922.

Liu T, Fan X, Wu K, Tao C, Bai X, Sun X. Structural characteristics of biochars made from different parts of corn straw and their adsorption performances for methylene blue. Journal of Water Process Engineering 2024;68:Article No. 106562.

de Luna MDG, Flores ED, Genuino DAD, Futalan CM, Wan M-W. Adsorption of Eriochrome Black T (EBT) dye using activated carbon prepared from waste rice hulls—Optimization, isotherm and kinetic studies. Journal of the Taiwan Institute of Chemical Engineers 2013;44:646-53.

Manzar MS, Khan G, dos Santos Lins PV, Zubair M, Khan SU, Selvasembian R, et al. RSM-CCD optimization approach for the adsorptive removal of Eriochrome Black T from aqueous system using steel slag-based adsorbent: Characterization, Isotherm, Kinetic modeling and thermodynamic analysis. Journal of Molecular Liquids 2021;339:Article No. 116714.

Mortada W, Mohamed R, Monem A, Awad M, Hassan A. Effective and low-cost adsorption procedure for removing chemical oxygen demand from wastewater using chemically activated carbon derived from rice husk. Separations 2023;10:Article No. 43.

Muhammad A, Shafeeq A, Butt MA, Rizvi ZH, Chughtai MA, Rehman S. Decolorization and removal of cod and bodfrom raw and biotreated textile dye bath effluent through advanced oxidation processes (AOPS). Brazilian Journal of Chemical Engineering 2008;25:453-9.

Muzyka R, Misztal E, Hrabak J, Banks SW, Sajdak M. Various biomass pyrolysis conditions influence the porosity and pore size distribution of biochar. Energy 2023;263:Article No. 126128.

Ndoun MC, Knopf A, Preisendanz HE, Vozenilek N, Elliott HA, Veith TL, et al. Physicochemical characterization of biochar derived from the pyrolysis of cotton gin waste and walnut shells. Journal of the American Society of Agricultural and Biological Engineers 2023;66:1163-74.

Okafor CC, Madu CN, Ajaero CC, Ibekwe JC, Nzekwe CA. Sustainable management of textile and clothing. Clean Technologies and Recycling 2021;1(1):70-87.

Ou W, Lan X, Guo J, Cai A, Liu P, Liu N, et al. Preparation of iron/calcium-modified biochar for phosphate removal from industrial wastewater. Journal of Cleaner Production 2023;383:Article No. 135468.

Oyekanmi AA, Ahmad A, Hossain K, Rafatullah M. Adsorption of Rhodamine B dye from aqueous solution onto acid treated banana peel: Response surface methodology, kinetics and isotherm studies. PLoS One 2019;14:e0216878.

Park J-H, Wang JJ, Meng Y, Wei Z, DeLaune RD, Seo D-C. Adsorption/desorption behavior of cationic and anionic dyes by biochars prepared at normal and high pyrolysis temperatures. Colloids and Surfaces A: Physicochemical and Engineering 2019;572:274-82.

Patel H. Removal of COD, BOD and color of different industrial effluents using activated neem char. Environmental Advances 2024;16:Article No. 100553.

Rajabian E, Sharififard H, Bonyadi M, Boostani F, Moradialvand M. COD reduction of municipal wastewater using mesoporous walnut shell-activated carbon: One step synthesis-modification via chemical activation with $FeCl_3$. Biomass Conversion and Biorefinery 2024;14:30627-40.

Roy H, Prantika TR, Riyad M, Paul S, Islam MS. Synthesis, characterizations, and RSM analysis of Citrus macroptera peel derived biochar for textile dye treatment. South African Journal of Chemical Engineering 2022;41:129-39.

Sadeghi S, Zakeri HR, Saghi MH, Ghadiri SK, Talebi SS, Shams M, et al. Modified wheat straw-derived graphene for the removal of Eriochrome Black T: Characterization, isotherm, and kinetic studies. Environmental Science and Pollution Research 2021;28:3556-65.

Sathya K, Nagarajan K, Carlin Geor Malar G, Rajalakshmi S, Raja Lakshmi P. A comprehensive review on comparison among effluent treatment methods and modern methods of treatment of industrial wastewater effluent from different sources. Applied Water Science 2022;12:Article No. 70.

Shah AJ, Soni B, Karmee SK. Application of cotton stalk biochar as a biosorbent for the removal of malachite green and its microwave-assisted regeneration. Energy, Ecology and Environment 2022;7:88-96.

Shao M, Ding ZC, Yang YZ, Zhang ZP, Wan YS. Phosphoric acid-modified biochar enhances electrokinetic in situ leaching technology to remediate Pb^{2+} contaminated soil. International Journal of Environmental Science and Technology 2024;21:8507-18.

Soleimani H, Sharafi K, Amiri Parian J, Jaafari J, Ebrahimzadeh G. Acidic modification of natural stone for Remazol Black B dye adsorption from aqueous solution- central composite design (CCD) and response surface methodology (RSM). Heliyon 2023;9(4):e14743.

Srivastav AL, Rani L, Sharda P, Patel A, Patel N, Chaudhary VK. Sustainable biochar adsorbents for dye removal from water:

present state of art and future directions. Adsorption 2024;30:1791-804.

Susaimanickam A, Manickam P, Joseph AA. A Comprehensive review on RSM-Coupled optimization techniques and its applications. Archives of Computational Methods in Engineering 2023;30:4831-53.

Tan W-T, Zhou H, Tang S-F, Zeng P, Gu J-F, Liao B-H. Enhancing Cd(II) adsorption on rice straw biochar by modification of iron and manganese oxides. Environmental Pollution 2022;300:Article No. 118899.

Tomczyk A, Sokołowska Z, Boguta P. Biochar physicochemical properties: Pyrolysis temperature and feedstock kind effects. Reviews in Environmental Science and Bio/Technology 2020;19:191-215.

Tzanakakis VA, Capodaglio AG, Angelakis AN. Insights into global water reuse opportunities. Sustainability 2023;15(17):Article No. 13007.

Vakili A, Zinatizadeh AA, Rahimi Z, Zinadini S, Mohammadi P, Azizi S, et al. The impact of activation temperature and time on the characteristics and performance of agricultural waste-based activated carbons for removing dye and residual COD from wastewater. Journal of Cleaner Production 2023;382:Article No. 134899.

Venkatesan A, Srividhya B, Alajmi A, Sadeq AM, Chava RK, Habila MA, et al. High adsorption capacities of rhodamine B dye by activated carbon synthesized from cotton stalks agricultural waste by chemical activation. Ceramics International 2025;51(10):13345-54.

Walanda DK, Anshary A, Napitupulu M, Walanda RM. The utilization of corn stalks as biochar to adsorb BOD and COD in hospital wastewater. International Journal of Design and Nature and Ecodynamics 2022;17:113-8.

Wang M, Wang G, Qian L, Yong X, Wang Y, An W, et al. Biochar production using biogas residue and their adsorption of ammonium nitrogen and chemical oxygen demand in wastewater. Biomass Convers Biorefinery 2023;13:3881-92.

Wu S, Wu H. Incorporating biochar into wastewater eco-treatment systems: Popularity, reality, and complexity. Environmental Science and Technology 2019;53:3345-6.

Xiang W, Zhang X, Cao C, Quan G, Wang M, Zimmerman AR, et al. Microwave-assisted pyrolysis derived biochar for volatile organic compounds treatment: Characteristics and adsorption performance. Bioresource Technology 2022;355:Article No. 127274.

Xu J, Fu M, Ma Q, Zhang X, You C, Shi Z, et al. Modification of biochar by phosphoric acid via wet pyrolysis and using it for adsorption of methylene blue. RSC Advances 2023;13(22): 15327-33.

Xu Q, Li C, Sumita, Pang W. Study on the removal efficacy and mechanism of phosphorus from wastewater by eggshell-modified biochar. Water Environment Research 2024;96(3): e10998.

Yaseen DA, Scholz M. Textile dye wastewater characteristics and constituents of synthetic effluents: a critical review. International Journal of Environmental Science and Technology 2019;16:1193-226.

Yusuff AS, Ishola NB, Gbadamosi AO, Epelle EI. Modeling and optimization of hexavalent chromium adsorption by activated eucalyptus biochar using response surface methodology and adaptive neuro-fuzzy inference system. Environments 2023;10(3):Article No. 55.

Zafar S, Razzaq A, Khalid S, Tariq TZ, Fatima R, Rabbani F, et al. Recent Advances in Applications of Engineered Biochar for Wastewater Treatment. In: Catalytic Applications of Biochar for Environmental Remediation: A Green Approach Towards Environment Restoration (Vol. 1). American Chemical Society Pubilcations; 2024. p. 109-30.

Zeng X-Y, Wang Y, Li R-X, Cao H-L, Li Y-F, Lü J. Impacts of temperatures and phosphoric-acid modification to the physicochemical properties of biochar for excellent sulfadiazine adsorption. Biochar 2022;4:Article No. 14.

Zeng Y, Lin Y, Ma M, Chen H. A review on the removal of heavy metals from water by phosphorus-enriched biochar. Minerals 2024;14(1):Article No. 61.

Zhao A, Liu S, Yao J, Huang F, He Z, Liu J. Characteristics of bio-oil and biochar from cotton stalk pyrolysis: Effects of torrefaction temperature and duration in an ammonia environment. Bioresource Technology 2022;343:Article No. 126145.

Zhao L, Zheng W, Mašek O, Chen X, Gu B, Sharma BK, et al. Roles of phosphoric acid in biochar formation: Synchronously improving carbon retention and sorption capacity. Journal of Environmental Quality 2017;46 (2):393-401.

Zhou F, Li K, Hang F, Zhang Z, Chen P, Wei L, et al. Efficient removal of methylene blue by activated hydrochar prepared by hydrothermal carbonization and NaOH activation of sugarcane bagasse and phosphoric acid. RSC Advances 2022;12(3): 1885-96.

Zhu X, Labianca C, He M, Luo Z, Wu C, You S, et al. Life-cycle assessment of pyrolysis processes for sustainable production of biochar from agro-residues. Bioresource Technology 2022;360:Article No. 127601.

INSTRUCTION FOR AUTHORS

Publication and Peer-reviewing processes of Environment and Natural Resources Journal

Environment and Natural Resources Journal is a peer reviewed and open access journal that is published in six issues per year. Manuscripts should be submitted online at https://ph02.tci-thaijo.org/index.php/ennrj/about/submissions by registering and logging into this website. Submitted manuscripts should not have been published previously, nor be under consideration for publication elsewhere (except conference proceedings papers). A guide for authors and relevant information for the submission of manuscripts are provided in this section and also online at: https://ph02.tci-thaijo.org/index.php/ennrj/author. All manuscripts are refereed through a **single-blind peer-review** process.

Submitted manuscripts are reviewed by outside experts or editorial board members of **Environment and Natural Resources Journal**. This journal uses double-blind review, which means that both the reviewer and author identities are concealed from the reviewers, and vice versa, throughout the review process. Steps in the process are as follows:

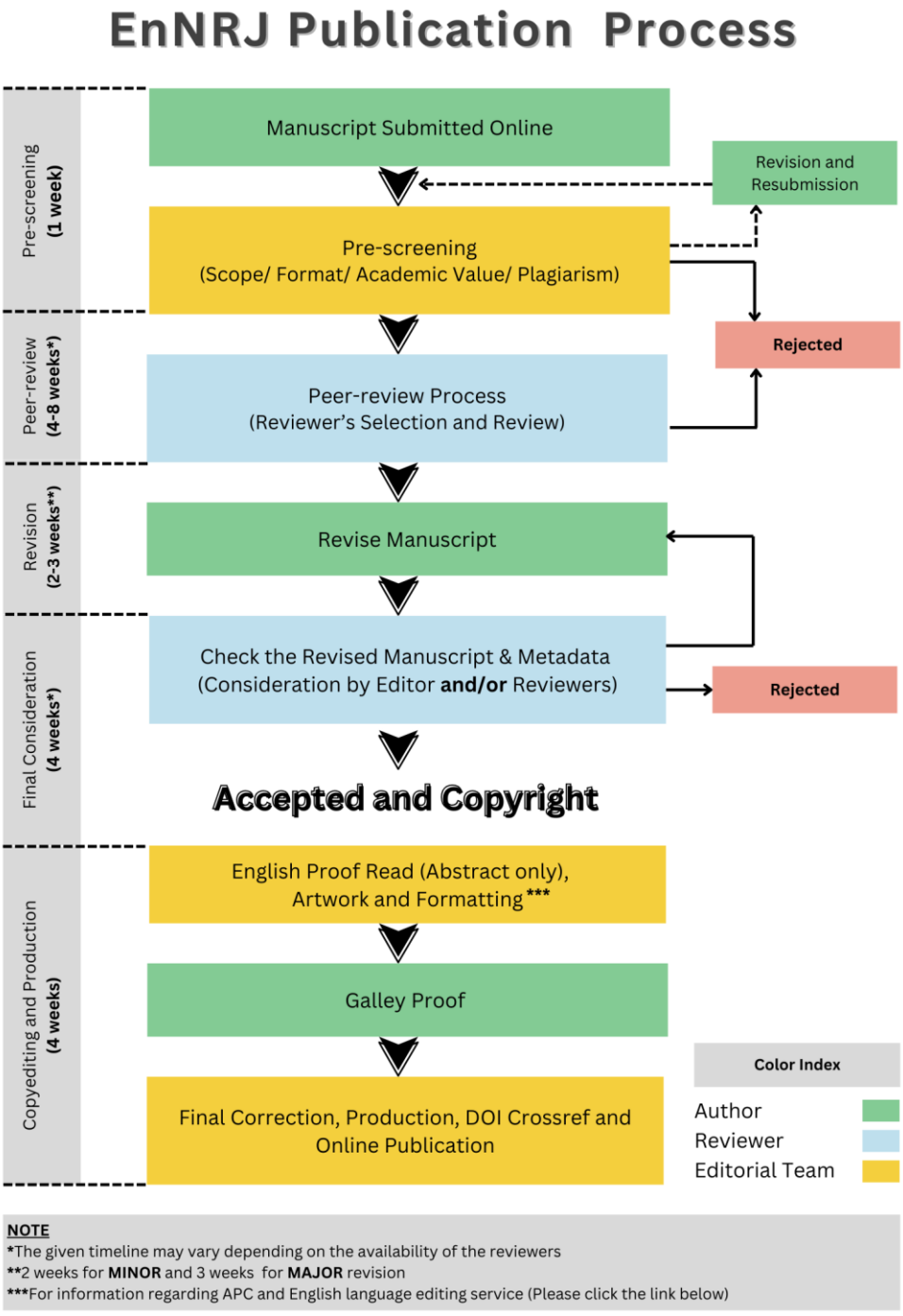

NOTE
*The given timeline may vary depending on the availability of the reviewers
2 weeks for **MINOR and 3 weeks for **MAJOR** revision
***For information regarding APC and English language editing service (Please click the link below)

The Environment and Natural Resources Journal (EnNRJ) considers and accepts two types of articles for publication as follows:

- *Original Research Article*: This is the most common type of article. It showcases new, innovative or unique findings surrounding a focused research question. Manuscripts should not exceed 4,000 words (excluding references) - see more details in the Preparation of Manuscript section below.
- *Review Article (by invitation)*: This type of article focuses on the in-depth critical review of a special aspect of an environmental-related research question, issue, or topic. It provides a synthesis and critical evaluation of the state of the knowledge of the subject. Manuscripts should not exceed 6,000 words (excluding references).

Submission of Manuscript

The items that the author needs to upload for the submission are as follows:

Manuscript: The manuscript must be submitted as a Microsoft Word file (.doc or .docx). Refer to the **Preparation of Manuscript** section below for detailed formatting instructions.

Cover Letter: The letter should address the Editor and include the following: a statement declaring that the author's paper has not been previously published and is not currently under consideration by another journal.

- a brief description of the research the author reports in the paper, including why the findings are important and why the journal readers should be interested
- contact information of the author and any co-authors
- a confirmation that the author has no competing interests to disclose

Graphical Abstract (Optional): The author is encouraged to submit a graphical abstract with the manuscript. The graphical abstract depicts the research and findings with visuals. It attracts more potential readers as it lets them understand the overall picture of the article within a few glances. Note that the graphical abstract must be original and unpublished artwork. It should be a high-quality illustration or diagram in any of the following formats: TIFF, PDF, JPEG, or PNG. The minimum required size is 750 × 750 pixels (height × width). The size should be of high quality (600 dpi or larger) in order to reproduce well.

Reviewers Suggestion (mandatory): Please provide the names of three potential reviewers, with information about their affiliations as well as their email addresses. The recommended reviewers should not have any conflict of interest with the authors. Each reviewer must represent a different affiliation and not have the same nationality as the author. Please note that the editorial board retains the sole right to decide whether or not the recommended reviewers will be selected.

Declaration of Competing Interest: The author must include a declaration of competing interest form during submission. If there is no conflict of interest, please state, "The authors declare no conflict of interest." Otherwise, authors should declare all interests to avoid inappropriate influence or bias in their published work. Examples of potential conflicts of interest in research projects include but are not limited to financial interests (such as employment, consultancies, grants, and other funding) and non-financial interests (such as personal or professional relationships, affiliations, and personal beliefs).

CrediT (Contributor Roles Taxonomy) Author Statement or Author Contributions: For research articles with several authors, we require corresponding authors to provide co-author contributions to the manuscript using the relevant CRediT roles. CRediT is a taxonomy that shows the contributions of the author and co-author(s), reduces possible authorship disputes, and facilitates collaboration among research team members. The CRediT taxonomy includes 14 different roles describing each contributor's specific contribution to the scholarly output.

The roles are: Conceptualization; Data curation; Formal analysis; Funding acquisition; Investigation; Methodology; Project administration; Resources; Software; Supervision; Validation; Visualization; Roles/Writing – original draft; and Writing – review & editing.

Note that authors may have contributed through multiple roles, and those who contributed to the research work but do not qualify for authorship should be listed in the acknowledgments.

An example of a CRediT author statement is given below:
"Conceptualization, X.X. and Y.Y.; Methodology, X.X.; Software, X.X.; Validation, X.X., Y.Y. and Z.Z.; Formal Analysis, X.X.; Investigation, X.X.; Resources, X.X.; Data Curation, X.X.; Writing – Original Draft Preparation, X.X.; Writing – Review & Editing, X.X.; Visualization, X.X.; Supervision, X.X.; Project Administration, X.X.; Funding Acquisition, Y.Y."

Artwork for the Journal Cover: The author may provide and propose a piece of artwork (with a description) for the journal issue cover. This is an excellent opportunity for the author to promote their article, if accepted, on the cover of a published issue. Alternatively, the editorial team may invite the author to submit a piece of artwork for the cover after their manuscript has been accepted for publication. The final cover artwork selection will be made by the editorial team.

Final Author Checks: In addition to the basic requirements, the author should review this checklist before submitting their manuscript. Following it ensures the manuscript is complete and in accordance with all standards.

Preparation of Manuscript

Format and Style

The manuscript should be prepared strictly as per the guidelines given below. Any manuscript with an incorrect format will be returned, and the corresponding author may have to resubmit a new manuscript with the correct format.

Overall Format

The manuscript must be submitted as a Microsoft Word file (.doc or .docx). The formatting should be as follows:

- File format - .doc or .docx
- Page size - A4
- Page orientation - portrait (some landscape pages are accepted if necessary)
- Page margin - 2.54 cm (left and the right margin) and 1.9 cm (bottom and the top margin)
- Page number (bottom of the page)
- Line number
- Line spacing - 1.5
- Font - 12 point, Times New Roman (unless stated otherwise)

Unit - The use of abbreviation must follow the International System of Units (SI Unit) format.

- The unit separator is a virgule (/) and not a negative coefficient: 10 mg/L not 10 mgL^{-1}
- Liter always has a capital letter: mg/L

Equations

- Insert equations using the dedicated tool in Microsoft Word. Do not use pictures or text boxes.
- Equations that are referenced in the text should be identified by parenthetical numbers, such as (1), and should be referred to in the manuscript as “Equation 1”.

Inclusive Language: The language used in the manuscript acknowledges diversity, promotes equal opportunity, respects all people, and is sensitive to all aspects of differences. The manuscript content should not make assumptions about the beliefs or commitments of any individual. It should not imply superiority regarding age, race, ethnicity, culture, gender, sexual orientation, disability, or health conditions. Moreover, the manuscript must be free from bias, stereotypes, slang, and derogatory terms.

Reference Style: Vancouver style should be used for the reference list and in-text citations throughout the manuscript. Please follow the format of the sample references and citations, as shown in the Body Text Sections portion below.

Front Page

Title: The title of the manuscript should be concise and not longer than necessary. The title should be bold, 12-point size, and Times New Roman. The first letter of major words should be capitalized (as in standard title case).

Author(s) Name: The first and last names of all authors must be given, in bold, Times New Roman, and 12-point font.

Affiliation of All Author(s): Affiliation(s) must be in italics, Times New Roman, and 11-point font. Specify the Department/School/Faculty, University, City/Province/or State, and Country of each affiliation. Do not include positions or fellowships, or postal zip codes.
Each affiliation should be indicated with superscript Arabic numerals. The Arabic numeral(s) should appear immediately after the author’s name, and represent the respective affiliation(s).

Corresponding Author: One author should be responsible for correspondence, and their name must be identified in the author list using an asterisk (*).

- All correspondence with the journal, including article submission and status updates, must be handled by the corresponding author.

- The online submission and all associated processes should be operated by the corresponding author.

*Corresponding author: followed by the corresponding author's email address.

Example:

Papitchaya Chookaew[1], Apiradee Sukmilin[2], and Chalor Jarusutthirak[1*]
[1]Department of Environmental Technology and Management, Faculty of Environment, Kasetsart University, Bangkok, Thailand
[2]Environmental Science and Technology Program, Faculty of Science and Technology, Phranakhon Rajabhat University, Bangkok, Thailand
**Corresponding author: abcxx@xx.ac.th*

Abstract Page

Abstract: The abstract should include the significant findings paired with relevant data. A good abstract is presented in one paragraph and is limited to 250 words. Do not include a table, figure, or references.
Keywords - Up to six keywords are allowed, and they should adequately index the subject matter.

Highlights: Please include 3-5 concise sentences describing innovative methods and the findings of the study. Each sentence should contain at most 85 characters (not words).

Body Text Sections
The main body text of the manuscript normally includes the following sections: 1. Introduction 2. Methodology 3. Results and Discussion 4. Conclusions 5. Acknowledgments 6. Author Contributions 7. Declaration of Competing Interests 8. References

Introduction should include the aims of the study. It should be as concise as possible, with no subheadings. The significance of the problem and the essential background should also be given.

Methodology is sufficiently detailed so that the experiments can be reproduced. The techniques and methods adopted should be supported with standard references.
There should be no more than three levels of headings in the **Methodology and Results and Discussion** sections. Main headings are in bold letters, second-level headings are in bold and italic letters, and third-level headings are in normal letters.

Here is an example:

2. Methodology
2.1 Sub-heading
2.1.1 Sub-sub-heading

Results presents the key findings in figures and tables with descriptive explanations in the text.

Tables
- Tables - look best if all the cells are not bordered; place horizontal borders only under the legend, the column headings, and the bottom.

Figures
- Figures - should be submitted in color. The author must ensure that the figures are clear and understandable. Regardless of the application used to create them, when electronic artworks are finalized, please 'save as' or convert the images to TIFF or JPG and send them separately to EnNRJ. Images require a resolution of at least 600 dpi (dots per inch) for publication. The labels of the figures and tables must be Times New Roman, and their size should be adjusted to fit the figures without borderlines.
- Graph - The font style in all graphs must be Times New Roman, 9-10 size, and black color. Please avoid bold formatting, and set the border width of the graphs to 0.75 pt.

- Graph from MS Excel: Please attach an editable graph from MS Excel within your manuscript. Then please also submit the full MS Excel file used to prepare the graph as a separate document. This helps us customize our layout for aesthetic beauty.
- Graph from another program: Feel free to use whichever program best suits your needs. But as noted above, when your artwork is finalized, please convert the image to TIFF or JPG and send them separately Again, images should be at least 600 dpi. Do not directly cut and paste.

***All figures and tables should be embedded in the text, and also mentioned in the text.**

Discussion shows the interpretation of findings with supporting theory and comparisons to other studies. The Results and Discussion sections can be either separated, or combined. If combined, the section should be named Results and Discussion. **Conclusions** should include a summary of the key findings and take-home messages. This should not be too long, or repetitive but this section is absolutely necessary so that the argument of the manuscript is not uncertain or left unfinished.

Acknowledgments should include the names of those who contributed substantially to the work, but do not fulfill the requirements for authorship. It should also include any sponsor or funding agency that supported the work.

Author Contributions: For research articles with several authors, we require corresponding author contributions listed using the relevant CRediT roles. This should be done by the author responsible for correspondence.

Declaration of Competing Interest: The author must include a declaration of competing interest form during submission. If there is no conflict of interest, please state, "The authors declare no conflict of interest." Otherwise, authors should declare all interests to avoid inappropriate influence or bias in their published work.

References should be cited in the text by the surname of the author(s) and the year. This journal uses the author-date method of citation. The author's last name and date of publication are inserted in the text in the appropriate place. If there are more than two authors, “et al.” must be added after the first author’s name. Examples: (Frits, 1976; Pandey and Shukla, 2003; Kungsuwas et al., 1996). If the author’s name is part of the sentence, only the date is placed in parentheses: “Frits (1976) argued that . . .”

Please ensure that every reference cited in the text is also in the reference list (and vice versa).

In the list at the end of the manuscript, complete references must be arranged alphabetically by the surnames of the first author in each citation. Examples are given below.

Book

Tyree MT, Zimmermann MH. Xylem Structure and the Ascent of Sap. Heidelberg, Germany: Springer; 2002.

Chapter in a book

Kungsuwan A, Ittipong B, Chandrkrachang S. Preservative effect of chitosan on fish products. In: Steven WF, Rao MS, Chandrkachang S, editors. Chitin and Chitosan: Environmental and Friendly and Versatile Biomaterials. Bangkok: Asian Institute of Technology; 1996. p. 193-9.

Journal article

Muenmee S, Chiemchaisri W, Chiemchaisri C. Microbial consortium involving biological methane oxidation in relation to the biodegradation of waste plastics in a solid waste disposal open dump site. International Biodeterioration and Biodegradation 2015;102(3):172-81.

Journal article with Article Number

Sah D. Concentration, source apportionment and human health risk assessment of elements in $PM_{2.5}$ at Agra, India. Urban Climate 2023;49:Article No. 101477.

Non-English articles

Suebsuk P, Pongnumkul A, Leartsudkanung D, Sareewiwatthana P. Predicting factors of lung function among motorcycle taxi drivers in the Bangkok metropolitan area. Journal of Public Health 2014;44(1):79-92 (in Thai).

Article in press

Dhiman V, Kumar A. Biomass and carbon stock estimation through remote sensing and field methods of subtropical Himalayan Forest under threat due to developmental activities. Environment and Natural Resources Journal 2024. DOI: 10.32526/ennrj/22/20240018.

Published in conference proceedings

Wiwattanakantang P, To-im J. Tourist satisfaction on sustainable tourism development, Amphawa floating market Samut Songkhram, Thailand. Proceedings of the 1st Environment and Natural Resources International Conference; 2014 Nov 6-7; The Sukosol hotel, Bangkok: Thailand; 2014.

Ph.D./Master thesis

Shrestha MK. Relative Ungulate Abundance in a Fragmented Landscape: Implications for Tiger Conservation [dissertation]. Saint Paul, University of Minnesota; 2004.

Website

Orzel C. Wind and temperature: why doesn't windy equal hot? [Internet]. 2010 [cited 2016 Jun 20]. Available from: http://scienceblogs.com/principles/2010/08/17/wind-and-temperature-why-doesn/.

Report organization

Intergovernmental Panel on Climate Change (IPCC). IPCC Guidelines for National Greenhouse Gas Inventories: Volume 1-5. Hayama, Japan: Institute for Global Environmental Strategies; 2006.

Royal Gazette

Royal Gazette. Promotion of Marine and Coastal Resources Management Act 2059. Volume 132, Part 21, Dated 26 Mar B.E. 2558. Bangkok, Thailand: Office of the Council of State; 2015a. (in Thai).

Remark

** Please be note that manuscripts should usually contain at least 15 references and some of them must be up-to-date research articles.*

** Please strictly check all references cited in text, they should be added in the list of references. Our Journal does not publish papers with incomplete citations.*

Changes to Authorship

This policy of journal concerns the addition, removal, or rearrangement of author names in the authorship of accepted manuscripts:

Before the accepted manuscript

For all submissions, that request of authorship change during review process should be made to the form below and sent to the Editorial Office of EnNRJ. Approval of the change during revision is at the discretion of the Editor-in-Chief. The form that the corresponding author must fill out includes: (a) the reason for the change in author list and (b) written confirmation from all authors who have been added, removed, or reordered need to confirm that they agree to the change by signing the form. Requests form submitted must be consented by corresponding author only.

After the accepted manuscript

The journal does not accept the change request in all of the addition, removal, or rearrangement of author names in the authorship. Only in exceptional circumstances will the Editor consider the addition, deletion or rearrangement of authors after the manuscript has been accepted.

Copyright transfer

The copyright to the published article is transferred to Environment and Natural Resources Journal (EnNRJ) which is organized by Faculty of Environment and Resource Studies, Mahidol University. The accepted article cannot be published until the Journal Editorial Officer has received the appropriate signed copyright transfer.

Online First Articles

The article will be published online after receipt of the corrected proofs. This is the official first publication citable with the Digital Object Identifier (DOI). After release of the printed version, the paper can also be cited by issue and page numbers. DOI may be used to cite and link to electronic documents. The DOI consists of a unique alpha-numeric character string which is assigned to a document by the publisher upon the initial electronic publication. The assigned DOI never changes.

Mahidol University

Wisdom of the Land

Faculty of Environment and Resource Studies, Mahidol University, Thailand
999 Phutthamonthon Sai 4 Rd, Salaya, Phutthamonthon District, Nakhon Pathom 73170
E-mail: ennrjournal@gmail.com